

VALIDATION OF STRESSES CAUSED BY THERMAL GRADIENTS IN SEGMENTAL
CONCRETE BRIDGES

By

FAROUK MAHAMA

A DISSERTATION PRESENTED TO THE GRADUATE SCHOOL
OF THE UNIVERSITY OF FLORIDA IN PARTIAL FULFILLMENT
OF THE REQUIREMENTS FOR THE DEGREE OF
DOCTOR OF PHILOSOPHY

UNIVERSITY OF FLORIDA

2007

© 2007 Farouk Mahama

To Mom and Dad

ACKNOWLEDGMENTS

I would first like to thank Dr. G. R. Consolazio and Dr. H.R. Hamilton for their help and guidance throughout the course of my study at The University of Florida. I would also like to thank the members of my supervisory committee: Dr. B. Sankar of the mechanical and aerospace engineering department, Dr. R. Cook and Dr. K. Gurley of the civil and coastal engineering department, for their insightful suggestions. I would like to acknowledge and thank the Florida Department of Transportation for funding this research. I would especially like to thank Mr. Marcus Ansley of the FDOT Structures Research Center, Tallahassee, for his invaluable support and contributions to this study. Sincere thanks to Mr. Frank Cobb, Mr. David Allen, Mr. Steve Eudy, Mr. Tony Johnston, and Mr. Paul Tighe also of the FDOT Structures Research Center, Tallahassee, for their help in constructing and transporting the laboratory specimen from Tallahassee to Gainesville, Florida. Thanks to DYWIDAG Systems Incorporated (DSI) for donating the post-tensioning bars which were used to post-tension the laboratory specimen. In addition, I would like to thank Mr. Richard M. DeLorenzo of the FDOT Materials Laboratory, Gainesville, for his assistance in determining material properties of the test specimen. Finally, I would like to express my sincere gratitude to Mr. Charles “Chuck” Broward of the University of Florida Structures Laboratory, his staff of undergraduate students, and Mr. Hubert “Nard” Martin for their various contributions towards the successful execution of experiments in the laboratory.

TABLE OF CONTENTS

	<u>page</u>
ACKNOWLEDGMENTS	4
LIST OF TABLES	8
LIST OF FIGURES	10
ABSTRACT.....	20
CHAPTER	
1 INTRODUCTION	22
2 SCOPE AND OBJECTIVES.....	24
3 BACKGROUND	26
Thermal Gradients	26
Structural Response to Thermal Gradients	29
Selected Field Studies on Thermal Gradients.....	33
The North Halawa Valley Viaduct Project.....	34
The San Antonio “Y” Project	35
Northbound IH-35/Northbound US 183 Flyover Ramp Project	36
Summary	39
4 BEAM DESIGN	47
Cross Section Design.....	47
Segment Design	49
Design of Segment Heating System	50
Prestress Design.....	51
5 BEAM CONSTRUCTION	61
Placement of Steel Reinforcement, Thermocouple Cages, and Copper Tubes	61
Casting of Concrete	62
Material Tests and Properties	62
Application of Prestress.....	65
6 INSTRUMENTATION	74
Thermocouples	74
Electrical Resistance Concrete Strain Gauges and Strain Rings	75
Linear Variable Displacement Transducers (LVDT)	76
Load Cells.....	76

	Data Acquisition	77
7	SETUP AND PROCEDURES FOR MECHANICAL LOADING	87
	Opening of Joint between Segments 2 and 3	88
8	SETUP AND PROCEDURES FOR THERMAL LOADING	93
	Uniform Temperature Distribution	93
	Linear Thermal Gradient	95
	AASHTO Positive Thermal Gradient	95
	AASHTO Negative Thermal Gradient	96
9	IN-SITU COEFFICIENT OF THERMAL EXPANSION	102
10	RESULTS – PRESTRESSING	116
11	RESULTS – MECHANICAL LOADING	129
	Detection of Joint Opening – Strain Gauges Close to Joint at Midspan	129
	Detection of Joint Opening – LVDTs Across Joint at Midspan	135
	Strains at Mid-Segment	137
	Deflection	138
	Summary	139
12	RESULTS – UNIFORM TEMPERATURE CHANGE	151
13	RESULTS – AASHTO POSITIVE THERMAL GRADIENT	163
	Elastic Modulus Derived Stresses (E stresses)	164
	Joint – Opening Derived Stresses (J Stresses)	169
14	RESULTS – AASHTO NEGATIVE THERMAL GRADIENT	195
	Elastic Modulus Derived Stresses (E stresses)	196
	Joint – Opening Derived Stresses (J Stresses)	201
15	SUMMARY AND CONCLUSIONS	222
APPENDIX		
A	BEAM SHOP DRAWINGS	227
B	LOADING FRAME DRAWINGS	231
C	LOAD RESPONSE CURVES AT MID-SEGMENT (MECHANICAL LOADING)	236
D	LOAD RESPONSE CURVES (POSITIVE THERMAL GRADIENT)	241

E LOAD RESPONSE CURVES (NEGATIVE THERMAL GRADIENT).....	246
LIST OF REFERENCES	251
BIOGRAPHICAL SKETCH	253

LIST OF TABLES

<u>Table</u>	<u>page</u>
3-1 Positive thermal gradient magnitudes.....	40
3-2 Modulus of elasticity values for selected Ramp P segments	40
3-3 Coefficient of thermal expansion values for selected Ramp P segments	40
3-4 Comparison of measured and calculated stresses from measured thermal gradients	40
3-5 Comparison of measured and design Stresses	41
4-1 Approximate Service I stresses in Santa Rosa Bay Bridge.....	53
5-1 Segment cast dates	67
5-2 Concrete pump mix proportions	67
5-3 Compressive strengths and moduli of elasticity of Segment 1	67
5-4 Compressive strengths and moduli of elasticity of Segment 2.....	67
5-5 Compressive strengths and moduli of elasticity of Segment 3.....	67
5-6 Compressive strengths and moduli of elasticity of Segment 4.....	67
5-7 Coefficient of thermal expansion (CTE) of Segment 3 (AASHTO TP 60-00)	68
5-8 Selected post-tensioning force increments.....	68
9-1 Experimentally determined coefficients of thermal expansion	107
10-1 Prestress magnitudes and horizontal eccentricities.....	121
11-1 Comparison of measured strains due to prestress and measured strains when joint opens	140
12-1 Average measured coefficients of thermal expansion (CTE) of concrete segments	156
12-2 Calculated modulus of elasticity (MOE) of concrete segments.....	156
12-3 Changes in prestress due to heating of Segments 2 and 3	156
12-4 Changes in prestress due to cooling of Segments 2 and 3	156
13-1 Comparison of E stresses and extrapolated stresses on top of segment flanges near joint J2 (laboratory positive thermal gradient).....	178

13-2	Comparison of E stresses and predicted self-equilibrating thermal stresses caused by laboratory positive thermal gradient near joint J2	178
13-3	J stresses in top 4 in. of flange	178
13-4	Comparison of J stresses and predicted stresses in top 4 in. of flange	178
13-5	Comparison of J stresses and E stresses in top 4 in. of flange.....	179
14-1	Comparison of E stresses and extrapolated stresses on top of segment flanges near joint J2 (laboratory negative thermal gradient).....	205
14-2	Comparison of E stresses and predicted self-equilibrating thermal stresses caused by laboratory negative thermal gradient near joint J2	205
14-3	J stresses in top 4 in. of flange	205
14-4	Comparison of J stresses and predicted stresses in top 4 in. of flange	205
14-5	Comparison of J stresses and E stresses in top 4 in. of flange.....	206

LIST OF FIGURES

<u>Figure</u>		<u>page</u>
3-1	Conditions for the development of positive thermal gradients.....	42
3-2	Conditions for the development of negative thermal gradients	42
3-4	Comparison of AASHTO gradients for zone 3 (for superstructure depths greater than 2 ft).....	43
3-5	Positive vertical temperature gradient for concrete superstructures	43
3-6	Decomposition of a nonlinear thermal gradient.....	44
3-7	Development of self-equilibrating thermal stresses for positive thermal gradient.....	44
3-8	Development of self-equilibrating thermal stresses for negative thermal gradient	45
3-9	Thermocouple locations.....	45
3-10	Comparison of maximum daily positive temperature differences and negative temperature differences with design gradients	46
3-11	Thermocouple locations.....	46
4-1	Typical cross-section of Santa Rosa Bay Bridge.....	54
4-2	I-section representation of SRB bridge cross section	54
4-3	Self-equilibrating stresses due to AASHTO positive thermal gradient.....	54
4-4	Self-equilibrating stresses due to AASHTO negative thermal gradient	55
4-5	Cross section of laboratory beam with analytically determined self-equilibrating thermal stresses due AASHTO design gradients	55
4-6	Location of shear keys on beam cross section and detailed elevation view of shear key.....	56
4-7	Beam segments	56
4-8	Copper tube layouts for prototype beam and laboratory segmental beam.....	57
4-9	Copper tube layouts in relation to shape of AASHTO design thermal gradients.....	57
4-10	Typical manifold in flange.....	58
4-11	Typical manifold in web	58

4-12	Typical flow rates through web manifolds	58
4-13	Typical flow rates through flange manifolds	59
4-14	Heating system.....	59
4-15	Cross section view of prestress assembly	59
4-16	Elevation view of prestress assembly	60
4-17	Mild steel reinforcements in Segments 1 and 4.....	60
4-18	Mild steel reinforcement.....	60
5-1	Open form with mild steel reinforcement, closed form with mild steel reinforcement and lifting hooks.	69
5-2	Form for shear keys	69
5-3	Heated segment with copper tubes, thermocouple cages and thermocouples	70
5-4	Beam layout with casting sequence	70
5-5	Match-casting of segment.....	70
5-6	Finished concrete pours for Segment 1, Segment 2, Segment 3, Segment 4.....	71
5-7	Compressive strength test setup, elastic modulus test setup.....	71
5-8	AASHTO TP 60-00 test setup	72
5-9	Bar designations and design eccentricities (West).....	72
5-10	Prestress assembly (East).....	73
5-11	Elevation view of prestress assembly (North)	73
6-1	Thermocouple cage with attached thermocouples.....	78
6-2	Layout of thermocouples in relation to shape of positive thermal gradient and negative thermal gradient.....	78
6-3	Location of thermocouple cages in Segments 2 and 3.....	79
6-4	Thermocouple labels in Segments 2 and 3	80
6-5	Strain (foil) gauge	81

6-6	Strain gauges close to joint at midspan on North flange, South flange, North web, and South web.....	81
6-7	Strain ring.....	82
6-8	Instrumentation details (North side)	82
6-9	Instrumentation details (South side)	83
6-10	Instrumentation at midspan (top flange).....	83
6-11	Typical labeling convention for strain gauges	83
6-12	Typical labeling convention for strain rings	84
6-13	LVDT for measuring deflection at cantilevered-end of beam.....	84
6-14	LVDTs mounted across joint at midspan on South side and top flange.....	84
6-15	LVDT labeling convention	84
6-16	Load cell layout.....	85
6-17	Load cells for measuring applied load, prestress, mid-support reaction, and end-support reaction.....	85
6-18	Instrumentation layout (North)	86
6-19	Instrumentation layout (South)	86
6-20	DAQ System; Connection of instrumentation to DAQ System.....	86
7-1	Test setup	90
7-2	Segmental beam in laboratory	90
7-3	Loading frame and 60-ton jack.....	91
7-4	Ideal stress diagrams without thermal loads	91
7-5	Ideal stress diagrams with positive thermal gradient.....	91
7-6	Ideal stress diagrams with negative thermal gradient.....	92
8-1	Pipe layers.....	98
8-2	Thermocouple locations in heated segments	98
8-3	Thermocouples used at each section.....	99

8-4	Insulated heated segments.....	99
8-5	Piping configuration used to impose initial condition	100
8-6	Piping configuration used to impose uniform temperature differential.....	100
8-7	Piping configuration used to impose linear thermal gradient	100
8-8	Piping configuration used to impose AASHTO nonlinear positive thermal gradient	101
8-9	Piping configuration used to impose AASHTO nonlinear negative thermal gradient	101
9-1	Typical in-situ CTE test setup; Photograph and Details.....	108
9-2	Uniform temperature change imposed on Segment 2.....	109
9-3	Measured end-displacements due to uniform temperature change imposed on Segment 2.....	109
9-4	Uniform temperature change imposed on Segment 3.....	110
9-5	Measured end-displacements due to uniform temperature change imposed on Segment 3.....	110
9-6	Measured concrete temperatures in Segment 2 (uniform profile)	111
9-7	Measured concrete temperatures in Segment 3 (uniform profile)	111
9-8	Orientation of Segment 2 during testing (South elevation)	112
9-9	Orientation of Segment 3 during testing (South elevation)	112
9-10	Linear temperature gradient imposed on Segment 2	113
9-11	Measured displacements due to linear thermal gradient imposed on Segment 2	113
9-12	Linear thermal gradient imposed on Segment 3	114
9-13	Measured displacements due to linear thermal gradient on Segment 3.....	114
9-14	Measured concrete temperatures in Segment 2 (linear profile)	115
9-15	Measured concrete temperatures in Segment 3 (linear profile)	115
10-1	Segment support during prestressing	122
10-2	Beam support for mechanical and thermal load tests	122

10-3	Post-tensioning bar designations and eccentricities.....	123
10-4	Measured concrete strains near joint J2 due to prestress (Segment 2, North)	123
10-5	Measured concrete strains near joint J2 due to prestress (Segment 3, North)	124
10-6	Measured concrete strains near joint J2 due to prestress (Segment 2, South)	124
10-7	Measured concrete strains near joint J2 due to prestress (Segment 3, South)	125
10-8	Measured concrete strains near joint J2 due to prestress (Top flange).....	125
10-9	Effect of differential shrinkage on top flange strains.....	126
10-10	Measured concrete strains due to prestress through depth of segments near joint J2.....	126
10-11	Measured concrete strains due to prestress across width of segment flanges near joint J2 (Top flange).....	127
10-12	Variation of prestress forces with time	127
10-13	Change in total prestress force with time.....	128
11-1	Expected behavior of strain gauges on side of beam near joint.....	141
11-2	Expected behavior of strain gauges on top of flange near joint.....	141
11-3	Load vs. Strain near joint at midspan (North side)	142
11-4	Load vs. Strain near joint at midspan (South side).....	142
11-5	Load vs. Strain near joint at midspan (Top flange)	143
11-6	Condition of joint J2 on top of flange.....	143
11-7	Measured strain distributions near joint at midspan (North side).....	144
11-8	Measured strain distributions near joint at midspan (South side).....	144
11-9	Estimated progression of joint-opening with load (based on strain gauge data)	145
11-10	Movement of neutral axis (N.A.) with load.....	145
11-11	Changes in prestress force with load	146
11-12	Expected behavior of LVDTs across joint on side of beam	146
11-13	Expected behavior of LVDTs across joint on top of flange	147

11-14	Load vs. Joint opening (Side LVDTs)	147
11-15	Load vs. Joint opening (Top flange LVDTs).....	148
11-16	Measured strain distributions at middle of Segment 3 (30 in. from joint J2) on North side of beam	148
11-17	Measured strain distributions at middle of Segment 3 (30 in. from joint J2) on South side of beam	149
11-18	Forces and moments acting at mid-segment.....	149
11-19	Measured vertical deflection near cantilevered end of beam.....	150
12-1	Laboratory beam	157
12-2	Laboratory imposed temperature changes on Segment 2	157
12-3	Laboratory imposed temperature changes on Segment 3	158
12-4	Measured concrete temperatures in Segment 2	158
12-5	Measured concrete temperatures in Segment 3	159
12-6	Measured temperature changes at Section C (Heating phase).....	159
12-7	Measured temperature changes at Section D (Heating phase).....	160
12-8	Measured strain distribution on Segment 2 (Section C) due to temperature changes.....	160
12-9	Measured strain distribution on Segment 3 (Section D) due to temperature changes.....	161
12-10	Comparison of measured and calculated strains at Section C due to moderately nonuniform temperature distribution (Segment 2, Heating).....	161
12-11	Comparison of measured and calculated strains at Section D due to moderately nonuniform temperature distribution (Segment 3, Heating).....	162
13-1	Sequence of load application (positive gradient test)	180
13-2	Laboratory beam	181
13-3	Laboratory imposed positive thermal gradient	181
13-4	Typical field measured positive thermal gradient.....	182
13-5	Measured temperatures in heated segments (positive thermal gradient)	182

13-6	Calculated strain components of the AASHTO positive thermal gradient.....	183
13-7	Measured and predicted strains near joint J2 (Segment 2)	183
13-8	Measured and predicted strains near joint J2 (Segment 3)	184
13-9	Plan view of measured and predicted strains near joint J2 (Top Flange).....	184
13-10	Comparison of measured thermal gradient profiles with average	185
13-11	E stresses near joint J2 (Segment 2)	185
13-12	E stresses near joint J2 (Segment 3)	186
13-13	Difference in magnitude of imposed thermal gradients at location of maximum slope change (elevation 32 in.).....	186
13-14	Superposition of component stress blocks (Mechanical loads only).....	187
13-15	Superposition of component stress blocks (Mechanical loads with positive thermal gradient).....	187
13-16	Uniform opening of joint across section width.....	188
13-17	Non-uniform opening of joint across section width	188
13-18	Load vs. strain at reference temperature (Segment 3, North).....	189
13-19	Load vs. strain with positive thermal gradient (Segment 3, North).....	189
13-20	Load vs. strain at reference temperature (Segment 3, South).....	190
13-21	Load vs. strain with positive thermal gradient (Segment 3, South).....	190
13-22	Load vs. strain at reference temperature (Top flange).....	191
13-23	Load vs. strain with positive thermal gradient (Top flange).....	191
13-24	Comparison of strain differences on North and South sides of joint J2 (Positive thermal gradient).....	192
13-25	Joint opening loads detected from strain gauges near joint J2.....	192
13-26	Sign convention for moments and curvature	193
13-27	Contact areas at joint J2 at incipient opening of joint on South side at elevation 35.5 in.....	193

13-28	Contact areas at joint J2 at incipient opening of joint on North side at elevation 33.5 in.	193
13-29	Contact areas at joint J2 at incipient opening of joint on South side at elevation 32.0 in.	194
14-1	Sequence of load application (negative gradient test)	207
14-2	Laboratory beam	208
14-3	Laboratory imposed negative thermal gradient	208
14-4	Measured temperatures in heated segments (negative thermal gradient)	209
14-5	Calculated strain components of the AASHTO negative thermal gradient.....	209
14-6	Measured and predicted strains near joint J2 (Segment 2)	210
14-7	Measured and predicted strains near joint J2 (Segment 3)	210
14-8	Plan view of measured and predicted strains near joint J2 (Top Flange)	211
14-9	Measured and predicted strains at midspan and mid-segment (Segment 2, North).....	211
14-10	Measured and predicted strains at midspan and mid-segment (Segment 3, North).....	212
14-11	Comparison of measured thermal gradient profiles with average profile.....	212
14-12	E stresses near joint J2 (Segment 2)	213
14-13	E stresses near joint J2 (Segment 3)	213
14-14	E stresses at mid-segment and midspan (Segment 2, North).....	214
14-15	E stresses at mid-segment and midspan (Segment 3, North).....	214
14-16	Difference in magnitude of imposed thermal gradients at location of maximum slope change (elevation 32 in.).....	215
14-17	Superposition of component stress blocks (mechanical with uniform temperature increase)	215
14-18	Superposition of component stress blocks (mechanical with uniform temperature increase and negative thermal gradient)	216
14-19	Load vs. strain at reference temperature (Segment 3, North).....	216
14-20	Load vs. strain with negative thermal gradient (Segment 3, North).....	217

14-21	Load vs. strain at reference temperature (Segment 3, South).....	217
14-22	Load vs. strain with negative thermal gradient (Segment 3, South).....	218
14-23	Load vs. strain at reference temperature (Top flange).....	218
14-24	Load vs. strain with negative thermal gradient (Top flange).....	219
14-25	Comparison of strain differences on North and South sides of joint J2 (Negative thermal gradient).....	219
14-26	Joint opening loads detected from strain gauges near joint J2.....	220
14-27	Sign convention for moments and curvature	220
14-28	Contact areas at joint J2 at incipient opening of joint on South side at elevation 35.5 in.	220
14-29	Contact areas at joint J2 at incipient opening of joint on North side at elevation 33.5 in.	221
14-30	Contact areas at joint J2 at incipient opening of joint on South side at elevation 32.0 in.	221
A-1	Prestress reinforcement details	228
A-2	Manifold and copper tube details.....	229
A-3	Shear key details	230
B-1	Loading frame details	232
B-2	Details of cross channels.....	233
B-3	Mid-support details	234
B-4	End-support details	235
C-1	Load vs. strain at middle of Segment 2 on North side.....	237
C-2	Load vs. strain at middle of Segment 2 on South side.....	237
C-3	Measured strain distributions at middle of Segment 2 on North side.....	238
C-4	Measured strain distributions at middle of Segment 2 on South side.....	238
C-5	Load vs. strain at middle of Segment 3 on North side.....	239
C-6	Load vs. strain at middle of Segment 3 on South side.....	239

C-7	Measured strain distributions at middle of Segment 3 on North side.....	240
C-8	Measured strain distributions at middle of Segment 3 on South side.....	240
D-1	Load vs. strain at reference temperature (Segment 2, North).....	242
D-2	Load vs. strain with positive thermal gradient (Segment 2, North).....	242
D-3	Load vs. strain at reference temperature (Segment 2, South).....	243
D-4	Load vs. strain with positive thermal gradient (Segment 2, South).....	243
D-5	Load vs. joint opening at reference temperature (Top flange).....	244
D-6	Load vs. joint opening with positive thermal gradient (Top flange)	244
D-7	Load vs. joint opening at reference temperature (South side)	245
D-8	Load vs. joint opening with positive thermal gradient (South side).....	245
E-1	Load vs. strain at reference temperature (Segment 2, North).....	247
E-2	Load vs. strain with negative thermal gradient (Segment 2, North).....	247
E-3	Load vs. strain at reference temperature (Segment 2, South).....	248
E-4	Load vs. strain with negative thermal gradient (Segment 2, South).....	248
E-5	Load vs. joint opening at reference temperature (Top flange).....	249
E-6	Load vs. joint opening with negative thermal gradient (Top flange)	249
E-7	Load vs. joint opening at reference temperature (South side)	250
E-8	Load vs. joint opening with negative thermal gradient (South side)	250

Abstract of Dissertation Presented to the Graduate School
of the University of Florida in Partial Fulfillment of the
Requirements for the Degree of Doctor of Philosophy

VALIDATION OF STRESSES CAUSED BY THERMAL GRADIENTS IN SEGMENTAL
CONCRETE BRIDGES

By

Farouk Mahama

December 2007

Chair: Gary R. Consolazio

Cochair: H. R. Hamilton

Major: Civil Engineering

This dissertation presents the results of a series of tests aimed at quantifying self-equilibrating thermal stresses caused by AASHTO design nonlinear thermal gradients in segmental concrete bridges. Negative gradients (deck cooler than web) can cause significant tensile stresses to develop in the top few inches of bridge decks, leading to requirements for large prestressing forces to counteract this tension.

Design gradients are based on field measurement of temperature variations on both a seasonal and diurnal basis. There is, however, little data in which actual stresses have been measured during these peak gradients to verify that the stresses are indeed as high as predicted by analysis. One reason for this is the difficulty of stress measurement in concrete. Stress is generally estimated by measuring strain, which is then converted to stress by applying an elastic modulus. This works well for homogeneous elastic materials but there is less confidence in this procedure when applied to concrete due to material variability at the scale of the strain gauge, temperature compensation of strain gauges, creep, and shrinkage.

A 20 ft-long 3 ft-deep segmental T beam was constructed and tested in the laboratory for the purpose of quantifying self-equilibrating thermal stresses caused by the AASHTO design

nonlinear thermal gradients. The beam was made of four 5 ft segments externally post-tensioned together with four high-strength steel bars. By embedding rows of copper tubing into two of the beam segments, and passing heated water through the tubes, the desired thermal gradients were imposed on the heated segments.

Two independent methods were used to measure stresses at the dry joint between the heated segments. The first was to convert measured stress-inducing thermal strains to stresses using the elastic modulus. Stresses determined using this method were referred to as elastic modulus derived stresses (E stresses). The second method was a more direct measure of stress using the known stress state at incipient opening of the joint. This method of determining stresses was referred to as joint opening derived stresses (J stresses). Stresses determined using both methods are compared with AASHTO predicted self-equilibrating thermal stresses and discussed.

CHAPTER 1 INTRODUCTION

Thermal stresses are the result of restraint to deformations caused by temperature changes. In general, stresses are generated in bridges when the temperature of all or part of the superstructure varies significantly from the temperature at which it was constructed. Seasonal and diurnal variations in temperature are usually the cause of these temperature changes. In typical beam-slab concrete bridges, temperature variations lead to uniform expansion and contraction of the superstructure. This is because the shallow decks of such bridges allow uniform heating and cooling of the superstructure under environmental conditions. Segmental bridges, however, are comprised of deep box-girder sections. Such bridges experience not only uniform temperature changes, but also nonlinear distributions of temperature through the depth of the superstructure cross-section, known as nonlinear thermal gradients. Bridge deformations due to uniform temperature changes are well understood and easily accounted for in design by providing sliding joints and flexible piers, among other methods, to accommodate such movements. Nonlinear temperature distributions, however, present a more complex engineering problem. In simply-supported spans, nonlinear thermal gradients lead to internal self-equilibrating thermal stresses that cannot be relieved through support conditions. In continuous spans, nonlinear gradients lead to continuity stresses due to restraint to curvature in addition to self-equilibrating thermal stresses.

Designing continuous segmental concrete bridges for stresses due to thermal gradients is typically accomplished by making use of the American Association of State Highway and Transportation Officials (AASHTO) Load and Resistance Factor Design (LRFD) Specifications (AASHTO 2004) and the AASHTO Guide Specifications for Design and Construction of Segmental Concrete Bridges (AASHTO 1999). These specifications require the consideration of

nonlinear thermal gradient load cases when analyzing a segmental bridge for serviceability. Gradients that must be considered are positive (deck warmer than web) and negative (deck cooler than web). Stresses due to thermal gradients are analytically determined using concepts from classical mechanics. The magnitudes of thermal stresses determined in this manner can sometimes equal those due to live loads. This is of particular concern in the negative gradient case, which causes high tensile stresses to develop in the top few inches of the bridge deck. Due to limitations on the allowable tensile stress in segmental bridges, as stipulated by design codes, large prestress forces are needed to counteract the tension generated by the negative gradient. From the perspective that nonlinear thermal gradients are considered only in serviceability checks, and do not affect the ultimate strength condition of a bridge, designing for thermal stresses as high as those determined analytically can produce overly-conservative and costly structures.

To gain a better understanding of the effects of nonlinear thermal gradients on concrete bridges, it is first necessary to accurately quantify stresses that are generated by such gradients. This will not only aid in the development of improved methods for predicting thermal stresses in segmental concrete bridges (e.g. should actual stresses be less severe than predicted with current analysis procedures), but will also aid in investigating the effects of stresses caused by nonlinear thermal gradients on the durability of concrete (e.g. cracking and associated crack widths).

CHAPTER 2 SCOPE AND OBJECTIVES

Past research leading to the determination of design thermal gradients for segmental concrete bridges has focused mainly on collection of temperature data over varying periods of time, and selection of the maximum observed gradients as design gradients. There is, however, little data with which to determine whether the peak gradients produce stresses that are as high as those predicted analytically. One reason for this is the difficulty of stress measurement in concrete. Stress is generally estimated by measuring strain, which is then converted to stress by applying an elastic modulus. This works well for homogeneous elastic materials but there is less confidence in this procedure when applied to concrete due to material variability at the scale of the strain gauge.

A primary objective of this research was to determine whether experimentally determined self-equilibrating thermal stresses caused by application of the AASHTO nonlinear thermal gradients, are as severe as predicted by analysis. To this end an experimental program was carried out to quantify self-equilibrating stresses caused by the thermal gradients.

A 20 ft-long, 3 ft-deep segmental concrete T-beam was constructed and laboratory-tested for this study. The beam was made of four 5 ft segments externally post-tensioned together with four high-strength steel bars. By embedding rows of copper tubing into two of the beam segments, and passing heated water through the tubes, the desired thermal gradients were imposed on the heated segments. These segments were also instrumented with thermocouples to monitor concrete temperatures during the application of thermal loads. The beam was supported on one end and at midspan. Mechanical loads were applied at the cantilevered end with the objective of creating a known (zero) stress state at the dry joint (at midspan) between the two heated segments from which the effects of thermal gradients could be determined.

In-situ tests utilizing non-stress-inducing temperature profiles (uniform and linear temperature distributions) were performed on selected simply supported segments of the beam, to determine coefficients of thermal expansion. The post-tensioned beam was initially tested under the action of mechanical loads to establish a baseline condition from which the effect of thermal loads could be determined. Data from these tests were also used to evaluate the most suitable method of determining loads at which the dry joint at the midspan of the beam opened at specified depths. Accurate determination of loads at which the joint opened was important in quantifying stresses at the joint caused by nonlinear thermal gradients. A uniform temperature increment was imposed to investigate the expansion behavior of the beam under thermal loading. Though the beam was statically determinate with respect to support conditions, expansion or contraction of the concrete segments relative to the post-tensioning bars was expected to lead to the development of additional stresses that had to be accounted for in quantifying self-equilibrating thermal stresses. Subsequently a combination of AASHTO nonlinear thermal gradients and mechanical loads were applied to the beam. Self-equilibrating thermal stresses determined with results from these tests were then compared with corresponding thermal stresses determined using the AASHTO recommended method for calculating stresses caused by nonlinear thermal gradients.

CHAPTER 3 BACKGROUND

Thermal Gradients

Thermal gradients in concrete bridges are largely the result of the low thermal conductivity of concrete. By convention, a positive gradient is defined as a condition in which the temperature of the top deck is higher than the temperature of the webs. A negative gradient exists when the temperature of the web is warmer than that of the top deck and bottom flange.

Climate, bridge material, and the shape of the cross section all affect the shape and magnitude of thermal gradients. Climatic factors of importance include solar radiation, ambient temperature, wind speed, and precipitation. Climatic conditions leading to the development of positive and negative thermal gradients in concrete bridges are illustrated in Figure 3-1 and Figure 3-2, respectively. Material properties such as thermal conductivity, density, absorptivity, and specific heat influence thermal gradients in concrete. The effect of cross sectional shape on the development of thermal gradients is complex and has not been the focus of extensive research. However, from thermocouple data taken from existing segmental box-girder bridges, it is known that in addition to vertical temperature gradients, box girder sections also experience transverse temperature gradients due to the effects of differential temperature inside and outside the section (see points A and B in Figure 3-1 and Figure 3-2). Furthermore, the effect of enclosed air inside concrete box girders causes slightly different temperatures between the deck above the cavity and the exposed (cantilevered) deck overhang (points C and D in Figure 3-1 and Figure 3-2).

AASHTO specifications for the design of bridges for thermal gradients were first introduced in 1989. In 1983 Potgieter and Gamble developed a two-dimensional finite difference program to calculate the distribution of temperature in a concrete section using

weather station data from around the United States. They determined conditions at each site that would produce the maximum temperature differences, shapes, and magnitudes of nonlinear (positive) temperature gradients. The analytical model was validated with data taken from the Kishwaukee River Bridge in Illinois. In 1985 the National Cooperative Highway Research Program (NCHRP) published Report 276, *Thermal Effects in Concrete Bridge Superstructures* (Imbsen et al. 1985), which provided guidelines for the consideration of thermal gradients in the design of concrete bridges. The recommendations in NCHRP Report 276 were based largely on the work by Potgieter and Gamble (1983). In 1989 AASHTO published their *Guide Specifications, Thermal Effects in Concrete Bridge Superstructures* (AASHTO 1989a), which was based on NCHRP Report 276. The AASHTO *Guide Specifications for Design and Construction of Segmental Concrete Bridges* (AASHTO 1989b), a derivative of the AASHTO (1989a) specifications, required the consideration of thermal gradients in the design of all segmental bridges.

In the AASHTO *Guide Specifications, Thermal Effects in Concrete Bridge Superstructures* (AASHTO 1989a), the United States is divided into four solar radiation zones (see Figure 3-3), and a positive and negative gradient magnitude is specified for each zone. At the time of publication of the AASHTO (1989a) Guide Specifications, very little field data were available to substantiate the nonlinear thermal gradients utilized by the specifications. Since then, several field studies have been conducted on existing segmental bridges in the United States (e.g. Shushkewich 1998) that generally agree with the positive gradients stipulated by AASHTO.

Negative gradients in the AASHTO (1989a) Guide Specifications were based on the British Standard BS 5400 (1978). The shape of negative thermal gradients has since been modified and the magnitudes reduced to both simplify the design process and reduce the

magnitude of stresses caused by these gradients, which are tensile in the top few inches of superstructure cross sections. The AASHTO *Guide Specifications for Design and Construction of Segmental Concrete Bridges* (AASHTO 1999), and the AASHTO *LRFD Bridge Design Specifications* (AASHTO 1998a) specify the negative gradient as a fractional multiple of the positive gradient (-0.30 for plain concrete surfaces and -0.20 for surfaces with 2-in. asphalt topping). Magnitudes of the negative gradients in each geographic zone depend on categorization into one of two superstructure surface conditions: plain concrete surface, and 2-in. asphalt topping. Asphalt toppings tend to insulate the flanges of bridge superstructures. This reduces loss of heat from the surface of the flange, thereby reducing the severity of the thermal gradient. Thermal gradient shapes are essentially the same for all cross sections.

Thermal gradients in the AASHTO *Guide Specifications, Thermal Effects in Concrete Bridge Superstructures* (AASHTO 1989b) are applicable only to superstructure depths greater than 2 ft. Thermal gradients in the AASHTO *Guide Specifications for Design and Construction of Segmental Concrete Bridges* (AASHTO 1999), and the AASHTO *LRFD Bridge Design Specifications* (AASHTO 1994a), which are derivatives of the AASHTO (1989b) Guide Specifications, are not restricted to superstructure depths greater than 2 ft. (see Figure 3-4 for a comparison of AASHTO gradients). Instead, different superstructure depths are taken into account by means of a vertical dimension, “A” (see Figure 3-5). The dimension “A” is taken as 12 in. for superstructure depths greater than 16 in. For superstructures with depth less than 16 in., “A” is taken as 4 in. less than the depth of the superstructure.

Magnitudes of T_1 and T_2 for the four solar radiation zones into which the United States is divided (see Figure 3-3) are shown in Table 3-1 (Florida is located in zone 3). The AASHTO (1999) Guide Specifications specify the value of T_3 as zero, unless a site-specific study is

conducted to determine an appropriate value. Furthermore, should a site-specific study be conducted, the maximum value of T_3 as required by the specifications is 5 °F. It is worth mentioning that T_3 is usually taken as zero in design since it is unlikely that design engineers will have the necessary site data to determine otherwise.

Nonlinear thermal gradients in AASHTO specifications published after 1999 are identical to the gradients in the AASHTO (1999) Guide Specifications. The AASHTO (1999) thermal gradients were therefore used in this study since they are currently being used in the design of segmental concrete bridges.

Structural Response to Thermal Gradients

Nonlinear thermal gradients are usually divided into three components for analysis purposes (Figure 3-6): uniform temperature, linear thermal gradient and, self-equilibrating temperature distribution. The uniform temperature component causes uniform expansion or contraction of the unrestrained superstructure. If the structure is restrained against this deformation, axial forces may develop. A linear temperature gradient causes uniform curvature in an unrestrained superstructure. If the structure is restrained against curvature (restraints from vertical supports, e.g. bridge piers), then secondary moments develop as the result of a linear gradient.

The self-equilibrating temperature gradient, as the name implies, leads to the development of stresses in the structure that are internally in self-equilibrium. The resultant force and moment due to these stresses are both zero because the stresses are developed as the result of inter-fiber compatibility and are not associated with external forces and moments. The development of self-equilibrating thermal stresses is discussed in the following paragraphs.

Consider the beam cross section shown in Figure 3-7 and assume the fibers of the section are free to deform independently. Under the action of a nonlinear positive thermal gradient the

section fibers would deform in the shape of the gradient with the top fibers undergoing greater elongations than the middle and bottom fibers. In a real beam, however, inter-fiber bonds resist the free deformation of section fibers. If the cross section of the beam is able to resist out-of-plane flexural distortion (which is the case for a beam made of a homogeneous isotropic material undergoing uniform bending), the fibers of the beam will undergo a uniform curvature plus elongation. For deformations of the fibers to be consistent with the resistance of the cross section to out-of-plane flexural distortion, stresses are developed. These stresses, which are self-equilibrating, are compressive in the top and bottom fibers and tensile in the middle fibers of the cross section.

The development of self-equilibrating thermal stresses under the action of a nonlinear negative thermal gradient is illustrated in Figure 3-8. In this case, if the fibers of the section are free to deform independently, they would shorten with the top fibers undergoing greater shortening than the middle and bottom fibers. For deformations of the fibers of the beam to be consistent with the resistance of the cross section to out-of-plane flexural distortion, self-equilibrating stresses are developed. These stresses are tensile in the top and bottom fibers and compressive in the middle fibers of the beam.

The AASHTO approach to calculating stresses due to thermal gradients, which is based on one-dimensional Bernoulli beam theory, is outlined in the *AASHTO Guide Specifications, Thermal Effects in Concrete Bridge Superstructures* (AASHTO 1989b). The following assumptions regarding concrete material behavior (for segmental box girder bridges, the construction material typically used is concrete) are made in the calculations:

1. Concrete is homogeneous and isotropic.
2. The material properties of concrete are independent of temperature.
3. Concrete has linear stress-strain and temperature-strain relationships.

4. The Navier-Bernoulli hypothesis; that initially plane sections remain plane after bending, is valid.
5. Temperature varies vertically with depth, but is constant at all points of equal depth.
6. Longitudinal and transverse thermal stress fields are independent of each other.

The shape of box-girder sections leads to the development of transverse thermal gradients because of differential temperatures between parts of the section that are inside and outside the box. Analysis for the effects of transverse thermal gradients is generally considered unnecessary (AASHTO 1999). For relatively shallow bridges with thick webs, however, such an analysis may be necessary. The AASHTO 1999 specifications recommend a plus or minus 10 °F transverse temperature differential in such cases. Generally, the primary stresses of interest in design are usually longitudinal stresses. To determine self-equilibrating longitudinal stresses using the AASHTO approach, a sectional analysis is performed. The structure is first assumed to be fully restrained against rotation and translation and the thermal stresses determined using Equation 3-1:

$$f_{RT}(y) = -1 \cdot (E \cdot \alpha \cdot TG(y)) \quad (3-1)$$

where; $f_{RT}(y)$ is the thermal stress assuming a fully restrained structure, y is the vertical distance measured from the z axis, E is the elastic modulus, α is the coefficient of thermal expansion, and $TG(y)$ is the vertical thermal gradient. Axial force and bending moment required to maintain full restraint are then determined from the resulting stress distribution using Equation 3-2 and Equation 3-3:

$$N_R = \int f_{RT}(y) \cdot b(y) dy \quad (3-2)$$

$$M_{z_R} = \int f_{RT}(y) \cdot b(y) \cdot y dy \quad (3-3)$$

where; N_R is the restraining axial force, M_{z_R} is the restraining moment about the z axis, and $b(y)$ is the width of the cross section. Stresses due to the axial force and bending moment are then

subtracted from the fully restrained thermal stresses to give self-equilibrating thermal stresses as shown in Equation 3-4:

$$f_{SE}(y) = f_{RT}(y) - \frac{N_R}{A} - \frac{M_{z_R} \cdot y}{I_z} \quad (3-4)$$

where; A is the area of the cross section and I_z is the moment of inertia of the cross section about the z axis. In statically determinate structures, this superposition yields the complete internal stress state. The strain distribution and curvature of the structure are given by Equation 3-5 and Equation 3-6, respectively:

$$\varepsilon(y) = \frac{-1}{E} \cdot \left(\frac{N_R}{A} + \frac{M_{z_R} \cdot y}{I_z} \right) \quad (3-5)$$

$$\phi = -\frac{M_{z_R}}{E \cdot I_z} \quad (3-6)$$

Strains the structure does not undergo (i.e. strains corresponding to self-equilibrating thermal stresses) are calculated from Equation 3-7:

$$\varepsilon_{SE}(y) = \varepsilon(y) - \alpha \cdot TG(y) \quad (3-7)$$

where $\varepsilon_{SE}(y)$ is the strain distribution corresponding to the self-equilibrating thermal stresses. In statically indeterminate (continuous) structures, additional continuity stresses must be determined by performing a structural analysis using the negative of the restraining axial force and bending moment as loads at the ends of the continuous structure. This is usually done using structural analysis software. Stresses computed from the structural analysis are then superimposed on stresses due to the restraining axial force and bending moment in the primary (sectional) analysis to give continuity stresses. Alternatively, the indeterminate structure can be allowed to undergo continuity deformations due to the nonlinear gradient (which can be obtained from Equation 3-5) by removing enough redundant supports to make the structure statically

determinate. Reactions necessary to enforce displacement compatibility and accompanying continuity stresses can then be subsequently determined (e.g. using the flexibility method). The sum of the self-equilibrating stresses (determined previously via sectional analysis) and continuity stresses gives the total stress state in the continuous structure due to the nonlinear thermal gradient.

If the thermal gradient varies through the depth and width of the cross section, self-equilibrating thermal stresses are determined using Equation 3-8 through Equation 3-12, which are two-dimensional versions of Equation 3-1 through Equation 3-4, respectively.

$$f_{RT}(z, y) = -1 \cdot (E \cdot \alpha \cdot TG(z, y)) \quad (3-8)$$

$$N_R = \int \int_{z \ y} f_{RT}(z, y) dz dy \quad (3-9)$$

$$M_{zR} = \int \int_{z \ y} f_{RT}(z, y) \cdot y dz dy \quad (3-10)$$

$$M_{yR} = \int \int_{z \ y} f_{RT}(z, y) \cdot z dz dy \quad (3-11)$$

$$f_{SE}(z, y) = f_{RT}(z, y) - \frac{N_R}{A} - \frac{M_{zR} \cdot y}{I_z} - \frac{M_{yR} \cdot z}{I_y} \quad (3-12)$$

Where $TG(z,y)$ is the two dimensional thermal gradient in the cross section, $f_{RT}(z,y)$ is the thermal stress distribution assuming a fully restrained structure, M_{zR} is the restrained moment about the z axis, M_{yR} is the restrained moment about the y axis, I_z is the moment of inertia of section about the z axis, I_y is the moment of inertia of the section about the y axis, and $f_{SE}(z,y)$ is the two dimensional self-equilibrating thermal stress distribution.

Selected Field Studies on Thermal Gradients

Past studies on thermal gradients in continuous concrete segmental bridges have focused on determining the magnitude and shape of positive and negative thermal gradients. The frequencies at which maximum positive and negative gradients occur, due to variations in environmental heating, have also been investigated. The studies vary in location, duration,

number and type of thermocouples, and placement of thermocouples. Bridge cross sections most frequently considered were of the concrete box-girder type. Three such field studies are discussed here.

The North Halawa Valley Viaduct Project

The North Halawa Viaduct consists of twin prestressed concrete segmental bridges on the island of Oahu in Hawaii. As part of the instrumentation set up to measure various bridges responses, two sections along a five-span unit were heavily instrumented with thermocouples (Shushkewich, 1998). One section, E, with 26 gauges, was near midspan (location of maximum positive moment under service loads), while another section, F, with 32 gauges, was near a support (location of maximum negative moment under service loads).

Thermocouple readings were first recorded in late 1994 and were to be recorded through the end of 1999. Initially readings were taken at 2-hour intervals but this was increased to 6-hour intervals when it was felt that too much data was being gathered. When it became apparent that the critical positive thermal gradient was being underestimated the recording interval was again reduced to 2 hours (for design gradients in Hawaii, see Figure 3-5 and Table 3-1, zone 3). According to Shushkewich (1998), negative gradient readings were not as sensitive to the time interval as positive gradient readings. Thus, all the negative gradient readings were considered useful. Positive gradient readings taken during the period when the time interval between readings was 6 hours were considered unreliable. A 2-in. thick concrete topping was later placed on the instrumented sections. The topping was instrumented with thermocouples at the top, middle, and bottom.

Monthly and daily positive thermal gradient data were seen to be slightly higher for Section E than they were for Section F. Shushkewich (1998) attributed this to the higher thermal inertia of Section F (larger depth). Critical positive and negative thermal gradient profiles

determined during the study were plotted for gauges along the centerlines of the web, top and bottom slabs. The gradients were also compared to design gradients in the then-proposed AASHTO (1998b) Segmental Guide Specifications. Because construction traffic interfered with the gauges at the top of the deck, Shushkewich (1998) considered readings from those gauges unreliable and suggested that readings at the deck surface be obtained by extrapolating data from gauges 2.5 in. from the deck surface. Considering the positive and negative thermal gradient profiles, it was clear that in general, the slab readings were very close to the design gradients. The same could not be said for the web readings. The overall measured positive thermal gradient profile matched the design gradient more than the measured negative gradient profile matched the design negative gradient. The results of this study substantiated the reduction of the negative thermal gradient from -0.5 (AASHTO 1994a) to -0.3 times the positive gradient: the value used in the AASHTO Segmental Guide Specifications (AASHTO 1998b) and the AASHTO *LRFD Bridge Design Specifications* (AASHTO 1998a).

The San Antonio “Y” Project

As part of a field study (Roberts, C. L.; Breen J. E.; Cawrse J. (2002)), four segments of a three-span continuous unit in the extensive upgrade to the intersection of interstate highways I-35 and I-10 in downtown San Antonio, Texas (the San Antonio “Y” project) were heavily instrumented with thermocouples. The instrumented segments were part of elevated viaducts comprised of precast segmental concrete box girders constructed using span-by-span techniques. Thermocouples in a web of one instrumented segment (Figure 3-9) were connected to a data logger. Temperatures were recorded every 30 minutes for 2 years and 6 months. There were gaps in the data due to limited memory of the data logger.

Maximum positive and negative temperature differences were determined for each day that thermocouple readings were recorded. Maximum positive temperature differences were

computed from the difference between the largest top thermocouple reading (located 1 inch from the deck surface) and the coolest web thermocouple reading. Maximum negative temperature differences were computed from the difference between the coolest top thermocouple reading and the warmest web thermocouple reading.

Measured positive thermal gradient magnitudes were found by Roberts et al. (2002) to be smaller than the design gradients in the AASHTO (1994a) LRFD specifications and the AASHTO (1999) segmental guide specifications (for design gradients in Texas, see Figure 3-5 and Table 3-1, zone 2). The gradient shapes were found to be similar to the older tri-linear shape in the *Guide Specifications for Thermal Effects in Concrete Superstructures* (AASHTO 1989b). Measured maximum negative thermal gradients were also compared to the design gradient. It was found that the field measured magnitudes were less than the AASHTO (1994b) LRFD specifications but slightly greater than the AASHTO (1999) segmental specifications. Figure 3-10 shows a comparison between design gradient magnitudes and the recorded maximum positive and negative temperature difference for each day in the data record, respectively. Data from the top most thermocouple (1 in. below the deck surface) were extrapolated to estimate deck surface temperatures using a fifth order polynomial equation based on earlier work by Priestley (1978).

Northbound IH-35/Northbound US 183 Flyover Ramp Project

A field study was conducted by Thompson et al. (1998) on a five-span continuous precast segmental horizontally curved concrete bridge erected using balanced cantilever construction. The bridge was part of a flyover ramp between interstate highway I-35 and US highway 183 in Austin, Texas. Three segments designated P16-2, P16-10, and P16-17 in one span of the structure were instrumented with thermocouples (see Figure 3-11). Segment P16-2 was at the base of the cantilever where the maximum negative moment (tension in the top fiber of the

section) occurred during construction. Segment P16-10 was near the quarter point of the completed span where an inflection point in the load moment diagram was expected to occur. Segment P16-17 was located near the midpoint of the completed span where the maximum moment from gravity load was expected to occur. Response of the structure was studied under the actions of daily thermal gradients that occurred over a 9-month period.

From the temperature data gathered during the course of monitoring the bridge, daily temperature gradients were evaluated. The average temperature at the junction between the webs and the top flange was used as baseline reference and deducted from the measured average top and bottom temperatures. These resulting temperatures were taken as the basis for determining the thermal gradients.

Longitudinal stresses from the design gradients and stresses from the maximum measured thermal gradients were calculated. The calculations were based on the technique recommended in the AASHTO *LRFD Bridge Design Specifications* (1994a). The calculated stresses were compared to *measured thermal gradient stresses*. The measured stresses were determined by making use of measured concrete strains (from strain gauges), a determined coefficient of thermal expansion, and elastic modulus determined from concrete test cylinders. To make calculated stresses comparable to measured stresses, calculated stress results were adjusted by adding a uniform temperature to the nonlinear AASHTO gradients. According to the investigators, measured stresses came from readings taken between the time of peak gradient occurrence and some baseline time when the temperature distribution in the section was fairly uniform. Since a uniform change in temperature occurred within this time, the adjustment was necessary to make comparisons between measured and calculated stresses reasonable. Average values of elastic modulus and coefficient of thermal expansion determined during the course of

the field study are shown in Table 3-2 and Table 3-3, respectively. Table 3-4 compares measured stresses with stresses calculated from the measured thermal gradients (tension is positive and compression is negative). Table 3-5 compares measured stresses with stresses calculated from application of the design gradients. It can be seen that measured stresses for P16-10 and P16-17 are high compared to those at P16-2. Furthermore, they do not compare well with the stresses determined using the AASHTO design technique. Thompson et al. (1998) attributed this to warping of the box girder. Of the three sections, P16-2 was the only one restrained by an anchorage diaphragm from section distortion. Since the AASHTO design specifications assume plane sections remain plane, stresses at P16-10 and P16-17, which were free to undergo out-of-plane distortion, could not be expected to match stresses computed using the AASHTO recommended design technique.

In spite of the observed high stresses, Thompson et al. (1998) did not observe any distress in the structure that could be attributed to thermal effects. The maximum and minimum top flange stresses, under load combinations of dead load, prestress, live load, and thermal gradient were computed. The field load combinations were not necessarily the same for each segment. From the computations, it was clear that no tension existed in the bridge under the load combinations considered. A design 28-day concrete compressive strength, f'_c , of 6.5ksi was used in the design of the bridge. However, compressive strength cylinder tests revealed that concrete strengths of 10 ksi were common. The maximum allowable compressive stress, $0.45f'_c$, was exceeded in P16-10 and P16-17 under full service loads. The approximate limit of elastic behavior in concrete, $0.7f'_c$, was also exceeded in a small (about 1 foot wide) part of P16-10. Based on the range of compressive strengths obtained from tests, the investigators felt the true compressive strength of concrete in the segments was probably much greater than the average

design compressive strength. They therefore decided the stress distributions needed no adjustment.

Summary

The subsequent chapters will discuss the study conducted at the University of Florida that is the subject of this dissertation. Previous studies have confirmed the existence of nonlinear thermal gradients in segmental concrete bridges. The shape and magnitudes of the positive thermal gradients have also, in large measure, been verified with field measurements on existing segmental concrete bridges in the United States. However, few attempts at measuring stresses caused by nonlinear thermal gradients have been made. This indicates a need to further investigate stresses caused by nonlinear thermal gradients.

In the following chapters, design of the laboratory setup and a series of tests aimed at quantifying stresses caused by the AASHTO design nonlinear thermal gradients are presented and discussed. Stresses quantified from laboratory test data are then compared with stresses predicted with the AASHTO recommended method.

Table 3-1. Positive thermal gradient magnitudes

Plain Concrete Surface or Asphalt Topping		
Zone	T ₁ (°F)	T ₂ (°F)
1	54	14
2	46	12
3	41	11
4	38	9

*AASHTO (1999)., “Guide Specifications for Design and Construction of Segmental Concrete Bridges,” 2nd Ed., Washington, D.C., Table 6-1, pg. 10.

Table 3-2. Modulus of elasticity values for selected Ramp P segments

Test Date	P16-2 (Cast 5/24/96)	P16-10 (Cast 6/4/96)	P16-17 (Cast 6/10/96)
9/24/1996	6350 ksi	5900 ksi	5950 ksi
6/17/1997	6080 ksi	5470 ksi	5570 ksi

*Thompson, M. K., Davis, R. T., Breen, J. E., and Kreger, M. E. (1998)., “Measured Behavior of a Curved Precast Segmental Concrete Bridge Erected by Balanced Cantilevering,” Research Rep. 1404-2, Center for Transportation Research, Univ. of Texas at Austin, Texas, Table 3.1, pg. 55.

Table 3-3. Coefficient of thermal expansion values for selected Ramp P segments

	P16-2	P16-10	P16-17	Average
Coefficient of Thermal Expansion (α)	(5.0E-6/°F) 9.0E-6/°C	(5.4E-6/°F) 9.7E-6/°C	(5.2E-6/°F) 9.4E-6/°C	(5.2E-6/°F) 9.4E-6/°C

*Thompson, M. K., Davis, R. T., Breen, J. E., and Kreger, M. E. (1998)., “Measured Behavior of a Curved Precast Segmental Concrete Bridge Erected by Balanced Cantilevering,” Research Rep. 1404-2, Center for Transportation Research, Univ. of Texas at Austin, Texas, Table 3.2, pg. 56

Table 3-4. Comparison of measured and calculated stresses from measured thermal gradients

Segment	Positive Thermal Gradient			Negative Thermal Gradient		
	Average Measured	Average Calculated	Measured/ Calculated	Average Measured	Average Calculated	Measured/ Calculated
P16-2	(368 psi) 2.54 Mpa	(441 psi) 3.04 Mpa	0.836	(-251 psi) -1.73 Mpa	(-220 psi) -1.52 Mpa	1.138
P16-10	(669 psi) 4.61 Mpa	(458 psi) 3.16 Mpa	1.459	(-466 psi) -3.21 Mpa	(-225 psi) -1.55 Mpa	2.071
P16-17	(609 psi) 4.20 Mpa	(451 psi) 3.11 Mpa	1.350	(-316 psi) -2.18 Mpa	(-219 psi) -1.51 Mpa	1.444
	Peak Measured	Peak Calculated	Measured/ Calculated	Peak Measured	Peak Calculated	Measured/ Calculated
P16-2	(584 psi) 4.03 Mpa	(624 psi) 4.30 Mpa	0.937	(-426 psi) -2.94 Mpa	(-292 psi) -2.01 Mpa	1.463
P16-10	(1874 psi) 12.92 Mpa	(640 psi) 4.41 Mpa	2.930	(-1144 psi) -7.89 Mpa	(-297 psi) -2.05 Mpa	3.849
P16-17	(1291 psi) 8.90 Mpa	(627 psi) 4.32 Mpa	2.060	(-483 psi) -3.33 Mpa	(-287 psi) -1.98 Mpa	1.682

*Thompson, M. K., Davis, R. T., Breen, J. E., and Kreger, M. E. (1998)., “Measured Behavior of a Curved Precast Segmental Concrete Bridge Erected by Balanced Cantilevering,” Research Rep. 1404-2, Center for Transportation Research, Univ. of Texas at Austin, Texas, Table 7.1, pg. 138.

Table 3-5. Comparison of measured and design stresses (after Thompson et al. (1998))

Segment	Positive Thermal Gradient			Negative Thermal Gradient		
	Peak Measured	Design Calculated	Measured/ Design	Peak Measured	Design Calculated	Measured/ Design
P16-2	(584 psi) 4.03 Mpa	(518 psi) 3.57 Mpa	1.129	(-426 psi) -2.94 Mpa	(-264 psi) -1.82 Mpa	1.615
P16-10	(1874 psi) 12.92 Mpa	(518 psi) 3.57 Mpa	3.619	(-1144 psi) -7.89 Mpa	(-263 psi) -1.81 Mpa	4.359
P16-17	(1291 psi) 8.90 Mpa	515 psi (3.55 Mpa)	2.507	(-483 psi) -3.33 Mpa	(-260 psi) -1.79 Mpa	1.860

*Thompson, M. K., Davis, R. T., Breen, J. E., and Kreger, M. E. (1998)., “Measured Behavior of a Curved Precast Segmental Concrete Bridge Erected by Balanced Cantilevering,” Research Rep. 1404-2, Center for Transportation Research, Univ. of Texas at Austin, Texas, Table 7.2, pg. 138.

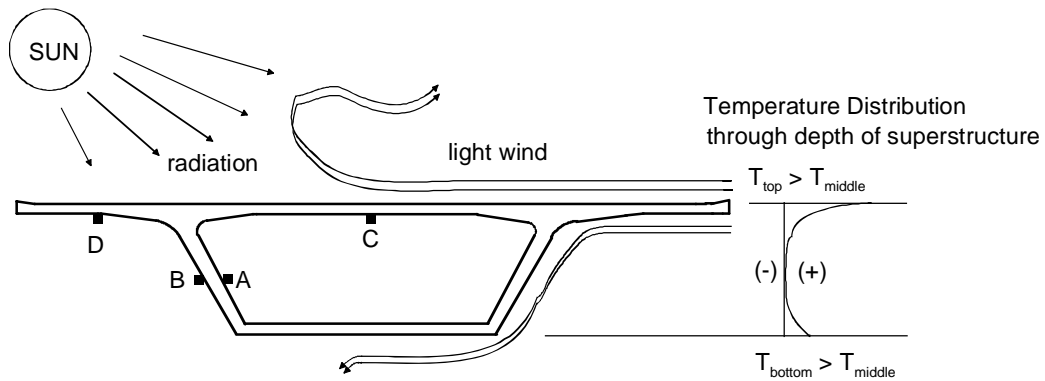


Figure 3-1. Conditions for the development of positive thermal gradients

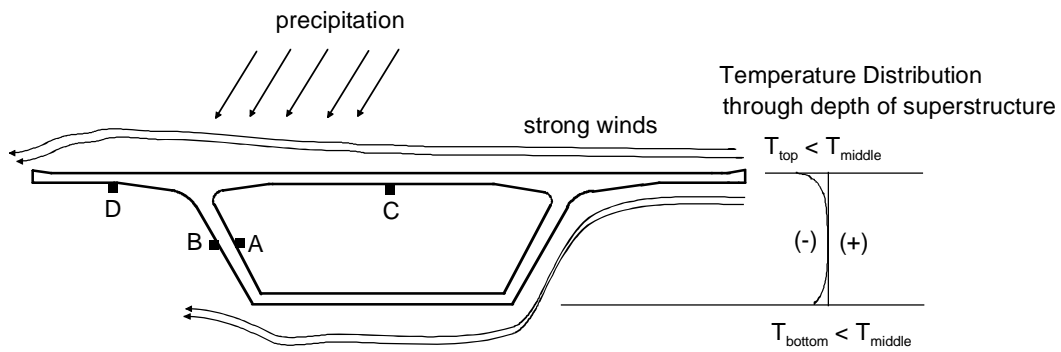


Figure 3-2. Conditions for the development of negative thermal gradients

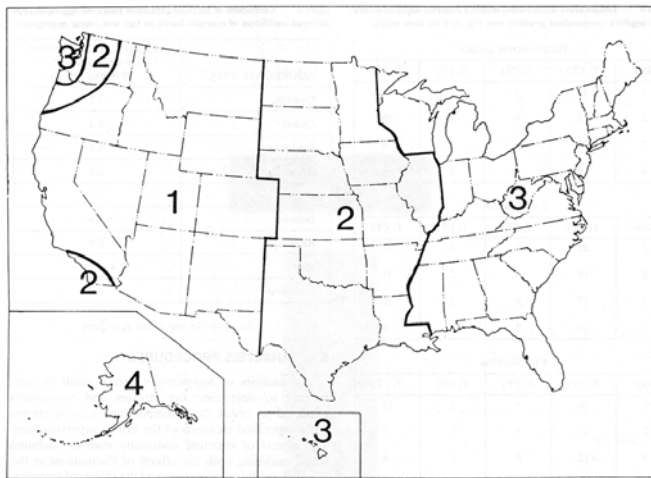
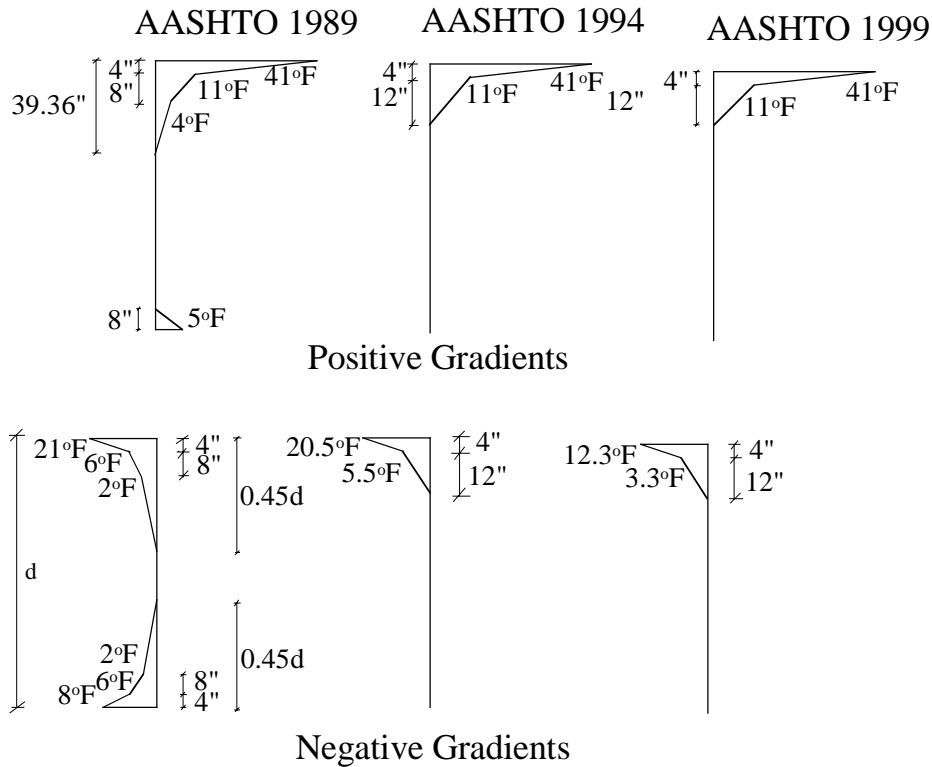


Figure 3-3. Solar radiation zones for the United States (AASHTO (1989a)., "AASHTO Guide Specifications, Thermal Effects in Concrete Bridge Superstructures," Washington D.C., Figure 4, pg. 5)



d = superstructure depth

Figure 3-4. Comparison of AASHTO gradients for zone 3 (for superstructure depths greater than 2 ft)

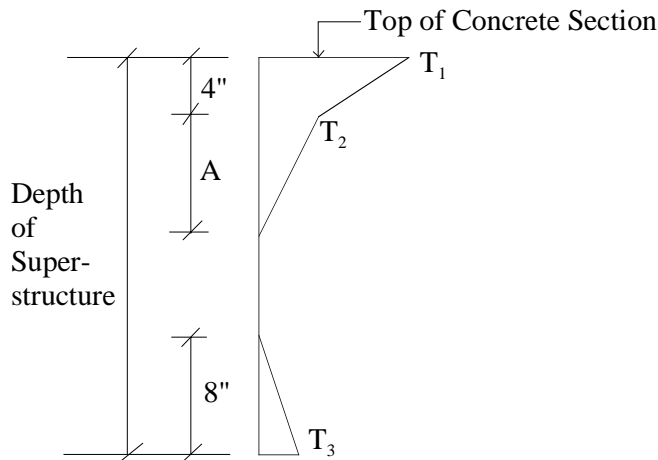


Figure 3-5. Positive vertical temperature gradient for concrete superstructures (AASHTO (1999)., "Guide Specifications for Design and Construction of Segmental Concrete Bridges," 2nd Ed., Washington, D.C., Figure 6-4, pg. 11.)

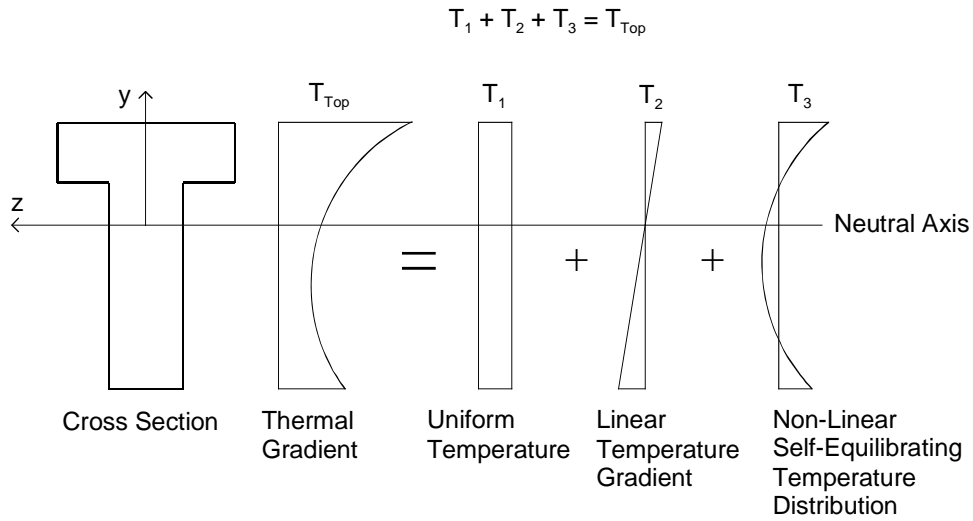


Figure 3-6. Decomposition of a nonlinear thermal gradient

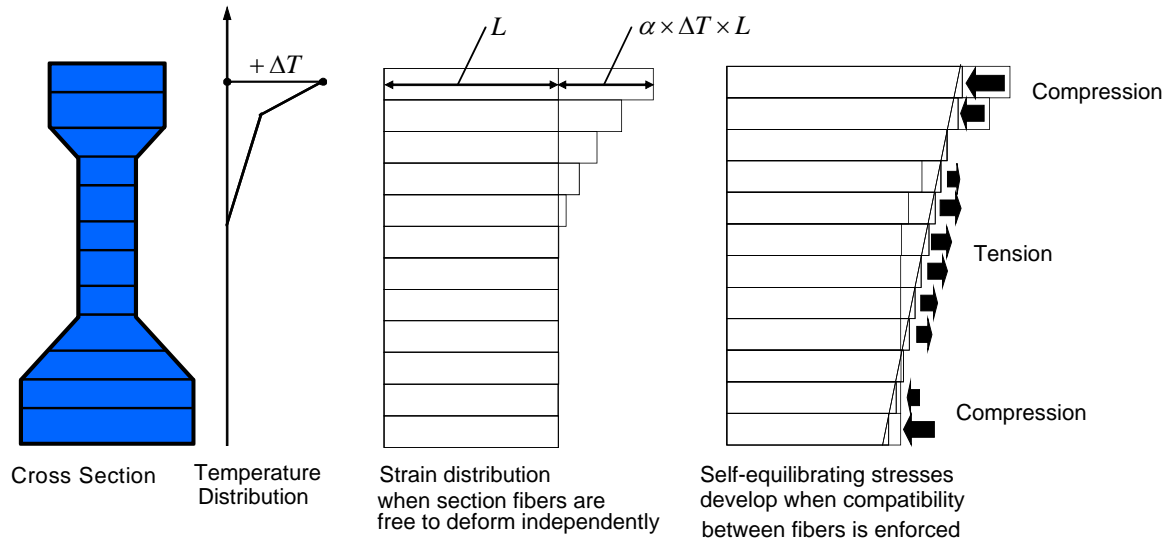


Figure 3-7. Development of self-equilibrating thermal stresses for positive thermal gradient

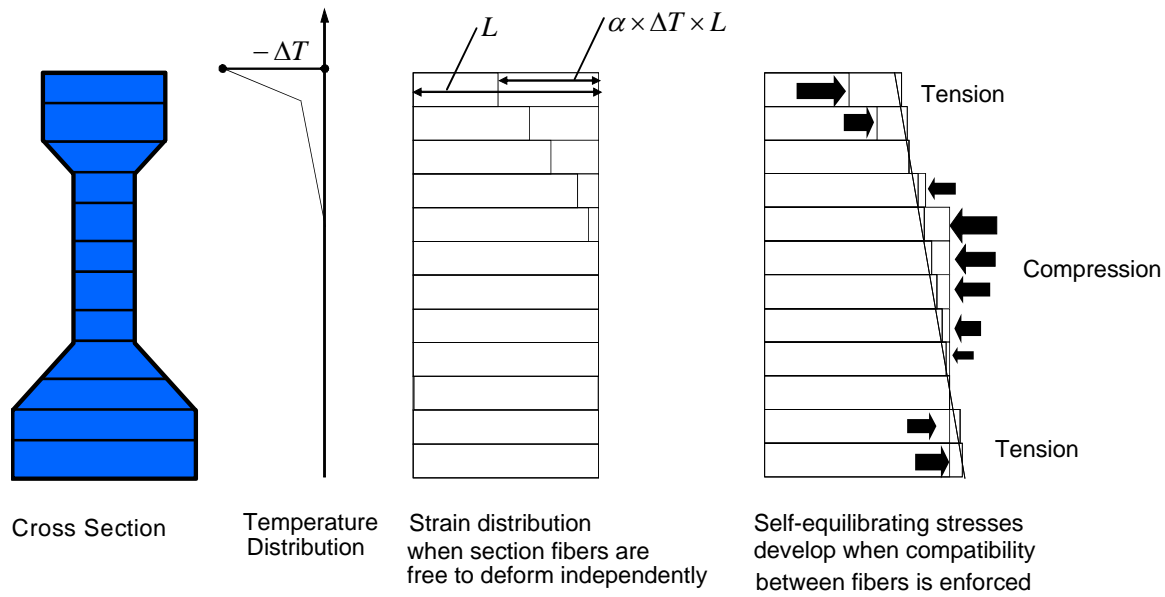


Figure 3-8. Development of self-equilibrating thermal stresses for negative thermal gradient

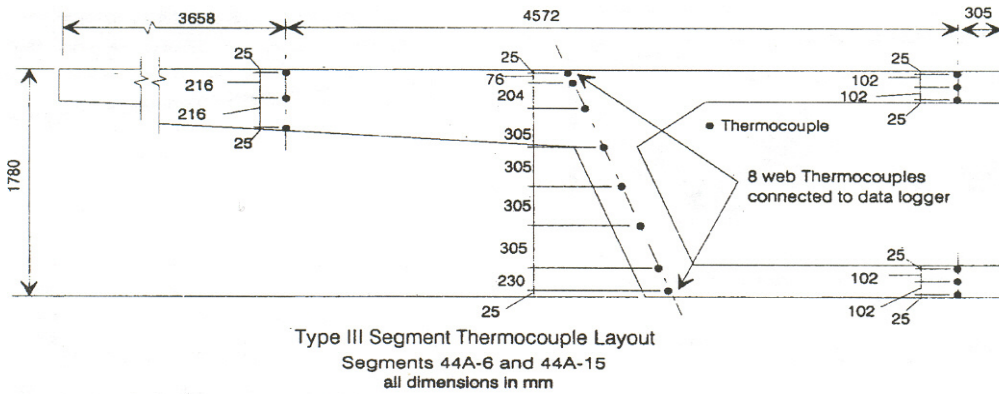


Figure 3-9. Thermocouple locations (Roberts, C. L., Breen, J. E., Cawrse J. (2002)., "Measurement of Thermal Gradients and their Effects on Segmental Concrete Bridge," ASCE Journal of Bridge Engineering, Vol. 7, No. 3, Figure 3, pg. 168.)

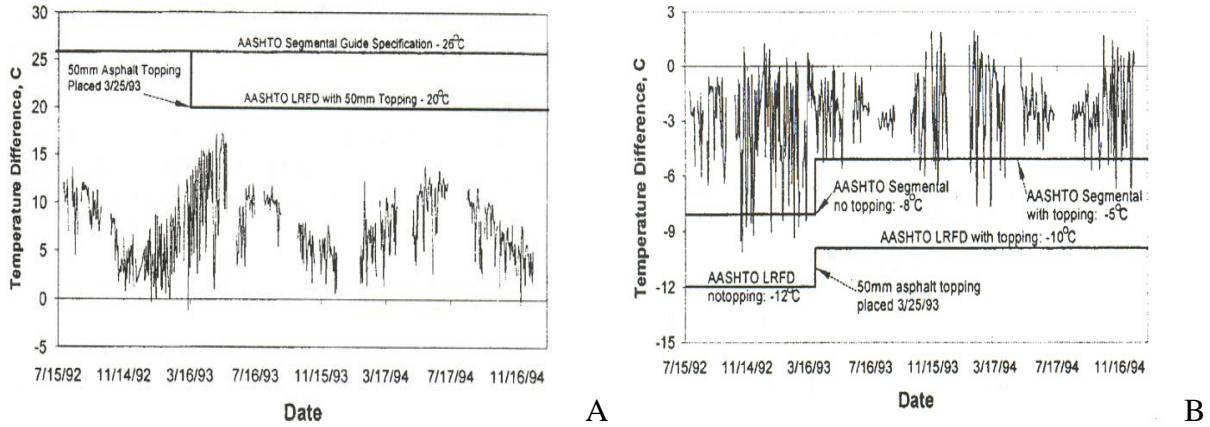


Figure 3-10. Comparison of maximum daily A) positive temperature difference. B) negative temperature difference with design gradients (Roberts, C. L., Breen, J. E., Cawrse J. (2002)., "Measurement of Thermal Gradients and their Effects on Segmental Concrete Bridge," ASCE Journal of Bridge Engineering, Vol. 7, No. 3, Figure 6 and Figure 7, pg. 169-170.)

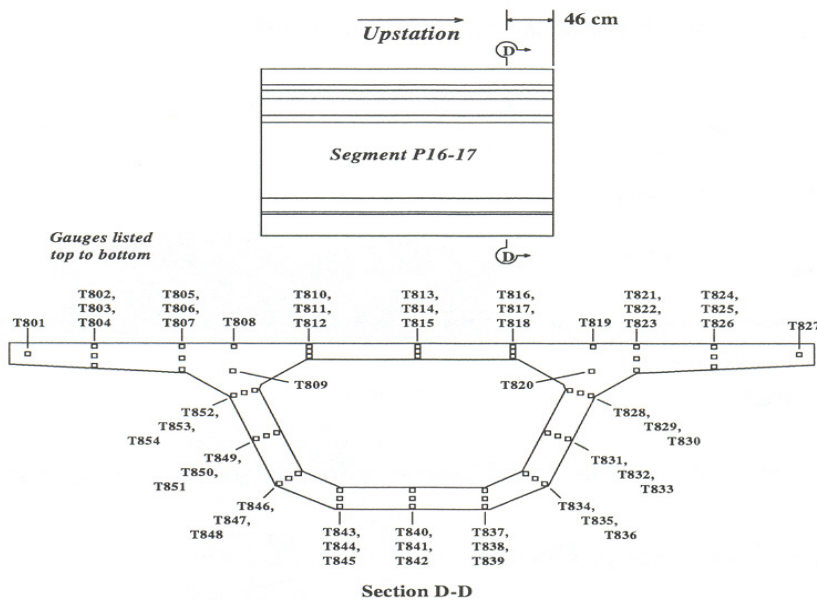


Figure 3-11. Thermocouple locations (Thompson, M. K., Davis, R. T., Breen, J. E., and Kreger, M. E. (1998)., "Measured Behavior of a Curved Precast Segmental Concrete Bridge Erected by Balanced Cantilevering," Research Rep. 1404-2, Center for Transportation Research, Univ. of Texas at Austin, Texas, Figure 3.14, pg. 53.)

CHAPTER 4 BEAM DESIGN

Cross Section Design

The Santa Rosa Bay (SRB) Bridge, located near Milton, Florida, was used as a prototype for design of the laboratory segmental beam that was tested in this study. Laboratory space and equipment constraints ruled out the use of a full scale replica of the cross-section of the bridge (see Figure 4-1) as the test specimen. A scaled model of the box-girder section was considered. This, however, required scaling of the AASHTO design thermal gradients such that self-equilibrating thermal stresses in the model, determined using the AASHTO recommended procedure, matched those in the full size bridge. The logistics of imposing scaled AASHTO thermal gradients on a scaled model of the bridge (e.g. difficulties of scaling aggregates, steel reinforcement, etc.) eliminated this as a viable option.

Past research constituting the basis of thermal gradients in the design codes were conducted mainly on segmental box girder bridges. The design codes, however, do not restrict the use of the gradients to box girder bridges. Furthermore, the codes assume that the gradients vary only through the depth of the section. This means two cross-sections of different shapes, with the same depths, section properties, and material properties will experience identical self-equilibrating thermal stresses due to a nonlinear thermal gradient (from classical Bernoulli beam theory). For the purpose of determining longitudinal stresses due to bending about the weak axis, the cross-section of the SRB Bridge can be simplified to that of an un-symmetric I-section (see Figure 4-2) with the same cross sectional area and flexural stiffness about the weak axis as the box-girder section. The results of an analysis on the simplified section for self-equilibrating thermal stresses under the action of the AASHTO positive and negative design thermal gradients (for Florida) are shown in Figure 4-3 and Figure 4-4, respectively. The

positive gradient leads to the development of compressive stresses (negative) in the top and bottom fibers of the section while tensile stresses (positive) develop in intermediate parts of the section. The negative gradient leads to the development of tensile stresses in the top and bottom fibers of the section and compressive stresses in the intermediate parts of the section.

Throughout this document tensile stresses will be considered positive, and compressive stresses negative. Of primary interest in this study were the tensile stresses created in the top few inches of the section by the negative thermal gradient. Consequently, a segmental T-beam with cross sectional geometry matching the top portion of the modified SRB Bridge section (illustrated by the hatching in Figure 4-3 and Figure 4-4) was constructed. Analytically determined self-equilibrating thermal stresses developed in the T-section by the AASHTO design gradients are also shown in the figures. The key aspects of the thermal stress profile in the SRB Bridge are captured in the laboratory segmental beam, including stress magnitudes in the top four inches of the flange, where the thermal gradient is steepest. Details of the cross-section of the laboratory beam together with analytically determined self-equilibrating thermal stresses due to the AASHTO design gradients are shown in Figure 4-5.

The flange width of the laboratory test beam was chosen based on recommendations in the AASHTO *LRFD Bridge Design Specifications* (AASHTO 2004), which are similar to recommendations in the ACI Committee 318, *Building Code Requirements for Structural Concrete and Commentary* (ACI 318-02). In prestressed beams with very wide flanges, shear deformations tend to relieve extreme fibers in the flange of longitudinal compressive stress, leading to a non-uniform distribution of stress (often referred to as “shear lag” effect). Therefore, for simplicity in design calculations it is recommended that an “effective flange width”, which may be smaller than the actual physical flange width, be used together with the assumption of

uniform stress distribution in the flange. For symmetrical T-beams it is recommended that the width of slab effective as a T-beam flange not exceed one-quarter of the span length of the beam, and the effective overhanging flange width on each side of the web not exceed eight times the slab thickness nor one-half the clear distance to the next web. A width of 2 ft was chosen so that the entire flange of the beam could be considered effective in resisting the prestress force. Heating time and thermal energy required to impose the AASHTO nonlinear thermal gradients on the beam were also considered in limiting the width of the flange to 2 ft.

Segment Design

A 20-foot long segmental beam was designed for use in laboratory testing. The length of the beam was chosen based on the length of a typical segment of the Santa Rosa Bay Bridge. The beam was constructed as four 5 ft segments that were post-tensioned together. Equal segment lengths allowed a single set of forms to be used in casting the segments. The design of the segments included shear keys (see Figure 4-6), which were used to fit the segments together and prevent relative vertical sliding during load tests. Details of the shear keys on each segment can be found in Appendix A. Figure 4-7 shows the segments as designed to fit together for laboratory testing. Two of the segments (segments 1 and 4) were designated “ambient” segments because they remained at the ambient laboratory temperature throughout testing. These segments were reinforced with steel to resist the high prestress forces arising in the anchorage zones. The remaining two segments (segments 2 and 3) were designated “heated” segments because they were thermally controlled during tests that involved the application of thermal loads. The heated segments contained copper tubes for thermal control but did not contain steel reinforcement, except for three thermocouple positioning steel cages.

Design of Segment Heating System

Thermal control was achieved by passing heated water through layers of copper tubes embedded in the heated segments of the beam. The number of copper tubes in each layer was minimized to reduce any reinforcing effect and reduction in concrete cross-sectional properties. Tests were first conducted on a 5 ft long, 2 ft deep prototype beam to optimize the number of copper tubes used in the laboratory segmental beam. AASHTO positive and negative design thermal gradients were imposed on the prototype beam using a varying number of copper tubes in each layer. The number of tubes in each layer that minimized piping while not sacrificing the ability to achieve the gradients in a reasonable amount of time, was chosen for use in the laboratory segmental beam. Copper tube layouts in the prototype and laboratory beam are shown in Figure 4-8 (A) and (B), respectively. As shown in Figure 4-9, layers 1, 2, and 4 were located near the slope changes in the AASHTO design thermal gradients. Additional layers of tubes were positioned to aid in heating the entire beam and in shaping the AASHTO gradients. The top layer of tubes was placed as close to top of the flange of the segments as possible while retaining adequate concrete cover (1 in.). This resulted in a slight kink in the thermal gradients near the top surface of the beam. Test results indicated that this may have affected the magnitude of measured strains caused by the AASHTO nonlinear thermal gradients in the extreme top flange fibers of the heated segments (see Chapter 13 and Chapter 14 for a complete discussion).

Manifold systems were designed to distribute approximately equal flow of heated water to each pipe, which was key in achieving a uniform distribution of temperature across the width of the beam. Typical manifolds in the flange and web of the heated segments are shown in Figure 4-10 and Figure 4-11, respectively. The web manifolds consisted of constant-diameter inlet and outlet pipes. The flange manifolds required the use of varying-diameter inlet and outlet pipes to

maintain approximately equal flow rates, due to the significant number of tubes in each layer in the flanges. Typical flow rates through the manifolds in the web and flange of the heated segments are shown in Figure 4-12 and Figure 4-13, respectively. Tests conducted on the manifolds showed that they were adequate in uniformly distributing heat across the web and along the length of the heated segments.

Heat energy was supplied to the beam by pumping water through on-demand electrical water heaters (see Figure 4-14). The heating system comprised of two S-H-7 Seisco electric heaters and one DHC-E Stiebel Eltron heater. The Seisco heaters (referred to as Heaters 1 and 2) could deliver water at temperatures as high as 135 °F. The Stiebel Eltron heater (referred to as Heater 3) could instantly deliver water at temperatures as high as 125 °F. Pressurized water was supplied to the heaters (and beam) by 0.5 horsepower Depco submersible pumps. The pumps were able to operate at temperatures as high as 200 °F, which was required to re-circulate hot water through the beam. Hoses used with the pumps and the heaters were flexible plastic braided tubing, which could also operate at high temperatures.

Prestress Design

An external post-tensioning system was designed for post-tensioning the segmental beam. The choice to use an external post-tensioning system, rather than an embedded internal system using ducts, was made to avoid problems with concrete void space and interference with internal instrumentation (thermocouples). Stress levels considered in the design of the post-tensioning system were AASHTO Service I stresses at the midspan and first interior support of a typical five-span unit of the Santa Rosa Bay Bridge (see Table 4-1). The Santa Rosa Bay Bridge was designed using HS20-44 vehicular loads, however, HL-93 vehicular loads (AASHTO LRFD) were considered in the prestress design of the laboratory beam. In Table 4-1, M/S_t and M/S_b

refer to stresses in the extreme top and bottom fibers of the cross section of the Santa Rosa Bay Bridge, respectively.

Four 1-3/8 in.-diameter high-strength DYWIDAG threaded bars were used to post-tension the beam. An anchorage system fabricated from structural steel shapes was designed to hold the bars in place during post-tensioning (see Figure 4-15 and Figure 4-16). Steel channels were placed back-to-back with sufficient space to allow for passage of the DYWIDAG bars. A pair of back-to-back channels was used for the top and another pair for the bottom bars. Stiffeners were welded to the channels under the bar bearing plates. The design of the channel systems allowed the prestress force to be evenly distributed over the web of the beam.

Steel reinforcement was required to resist the high post-tensioning forces in segments 1 and 4, where the post-tensioning systems were anchored. The AASHTO *LRFD Bridge Design Specifications* (AASHTO 2004a) was used in the design of reinforcement in the prestress anchorage zones. Number 3 vertical stirrups were placed 1.75 in. on center to resist principal tensile stresses that developed in the general anchorage zones. This reinforcement was placed within 27 in. from the bearing ends of the segments. The approximate method, which is permitted by the AASHTO LRFD specifications, was the basis of the design. Outside the anchorage zone, vertical stirrups were placed at 12 in. on center. Stresses in the local zones were determined using guidelines from the AASHTO (2004a) specifications. A set of three confinement spirals were used to resist the high local zone stresses. The reinforcement design is shown in Figure 4-17 and Figure 4-18.

Table 4-1. Approximate Service I stresses in Santa Rosa Bay Bridge

	Effective Prestress (psi)						Dead + Live Load (psi)			
	Support			Midspan			Support		Midspan	
	P/A	M/S _t	M/S _b	P/A	M/S _t	M/S _b	M/S _t	M/S _b	M/S _t	M/S _b
HS20-44	-700	-338	680	-700	460	-940	810	-1630	-610	1230
HL-93	-700	-338	680	-700	460	-940	810	-1735	-684	1380

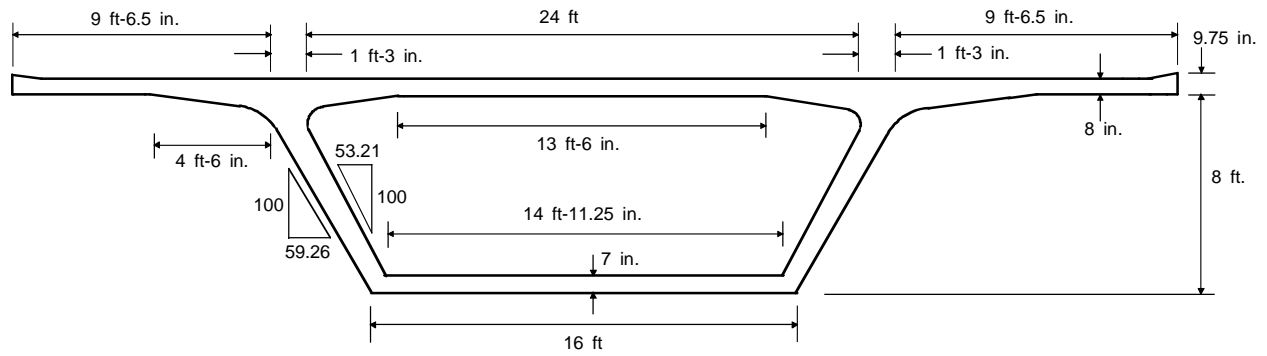


Figure 4-1. Typical cross-section of Santa Rosa Bay Bridge

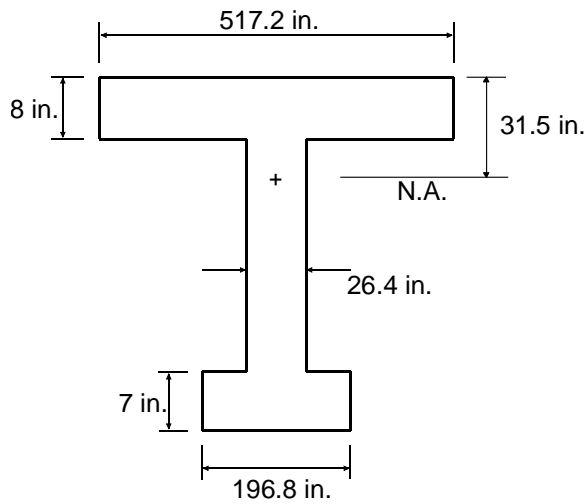


Figure 4-2. I-section representation of SRB bridge cross section

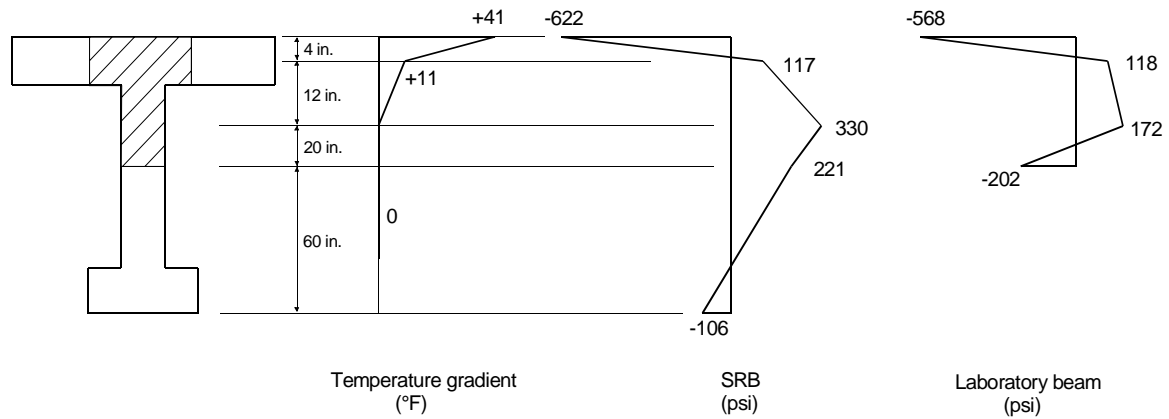


Figure 4-3. Self-equilibrating stresses due to AASHTO positive thermal gradient

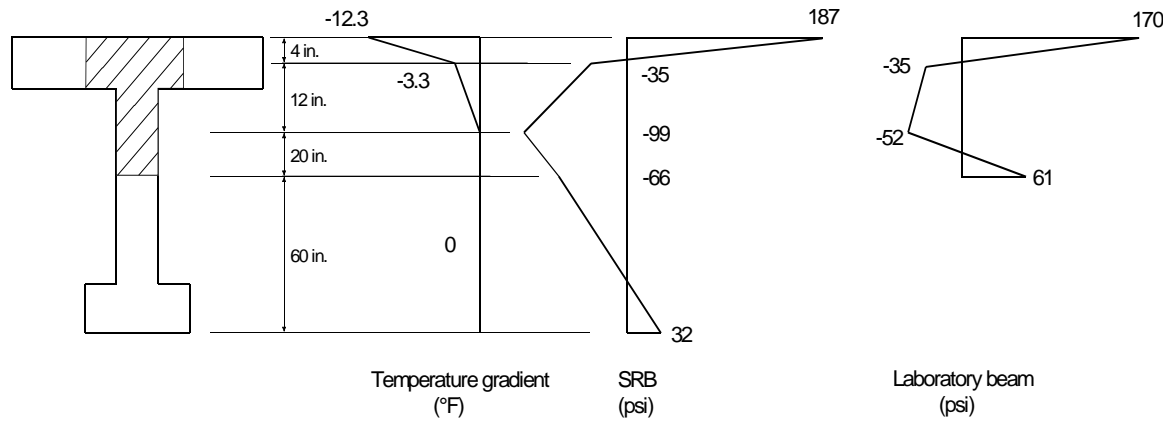


Figure 4-4. Self-equilibrating stresses due to AASHTO negative thermal gradient

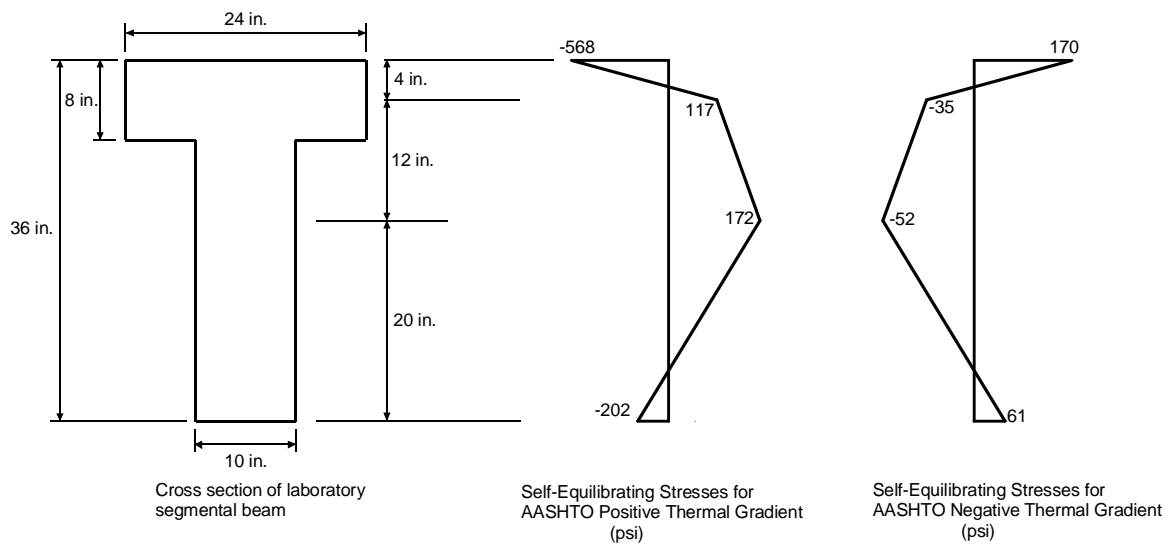


Figure 4-5. Cross section of laboratory beam with analytically determined self-equilibrating thermal stresses due to AASHTO design gradients

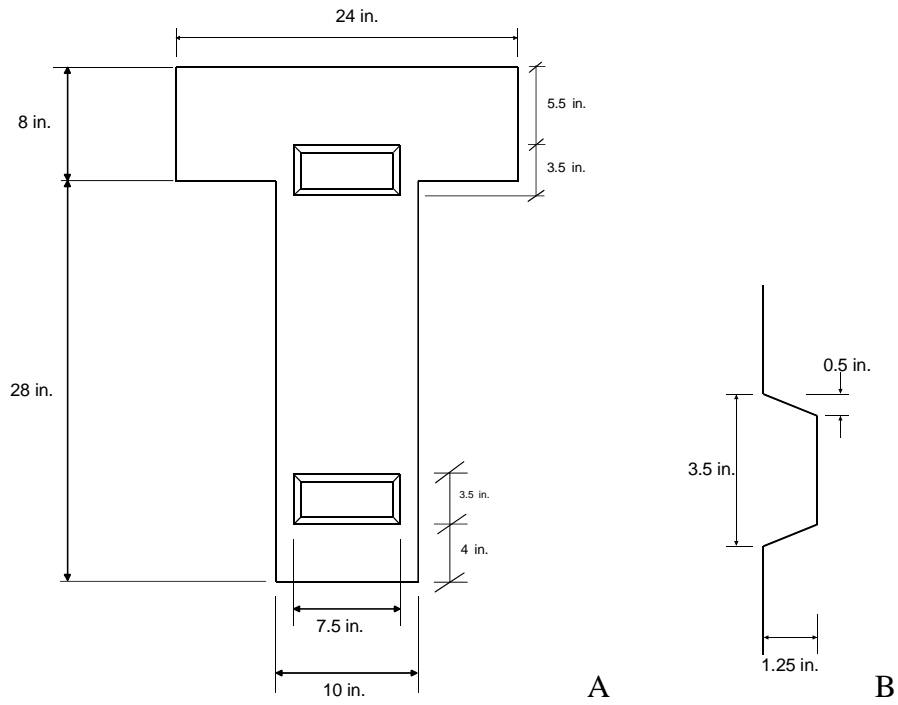


Figure 4-6. A) Location of shear keys on beam cross section. B) Detailed elevation view of shear key.

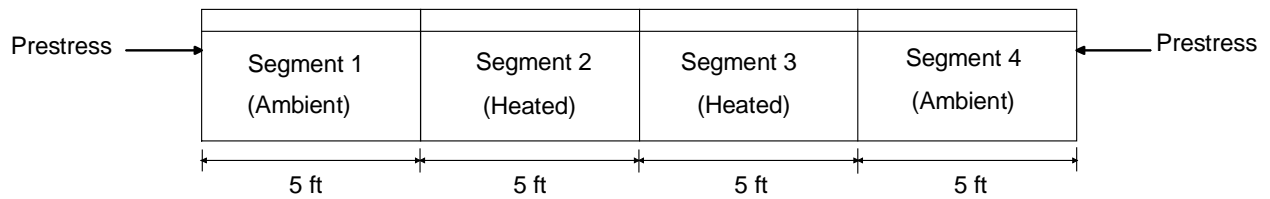


Figure 4-7. Beam segments

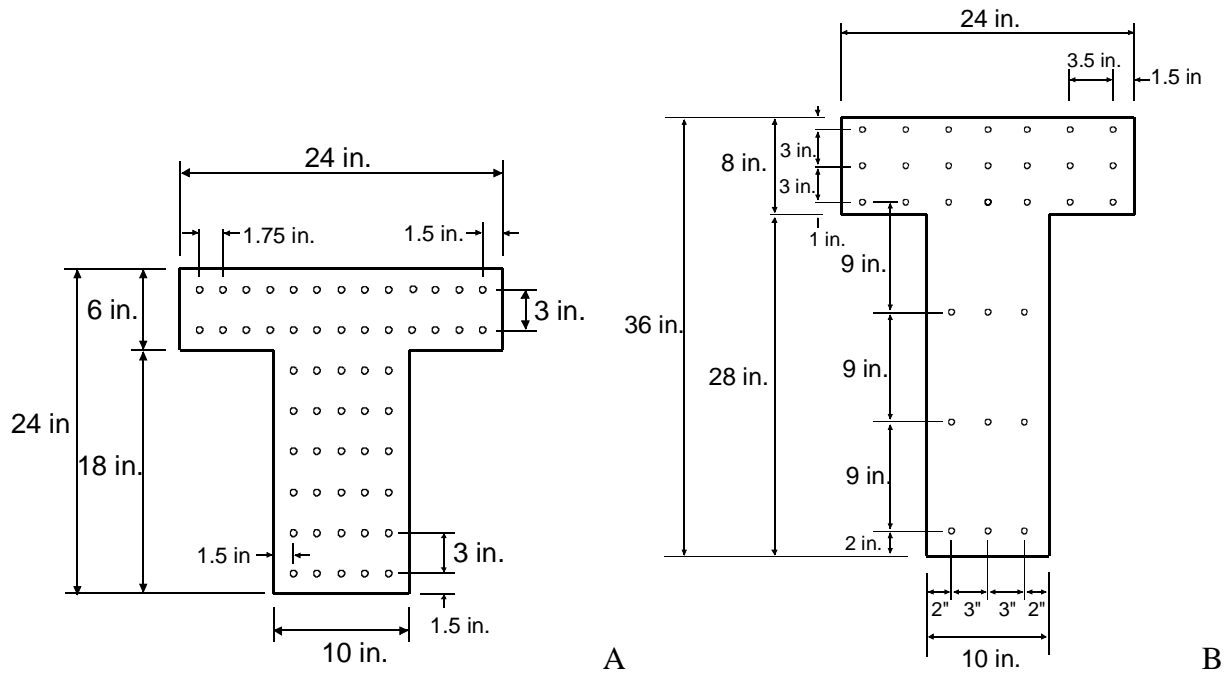


Figure 4-8. Copper tube layouts for A) Prototype beam. B) Laboratory segmental beam.

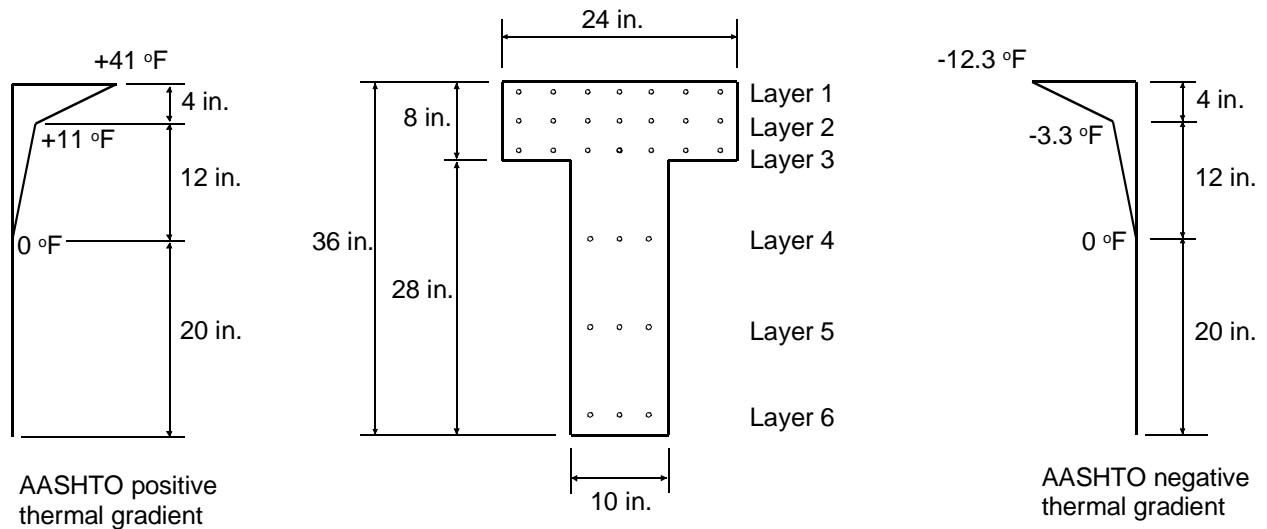


Figure 4-9. Copper tube layouts in relation to shape of AASHTO design thermal gradients

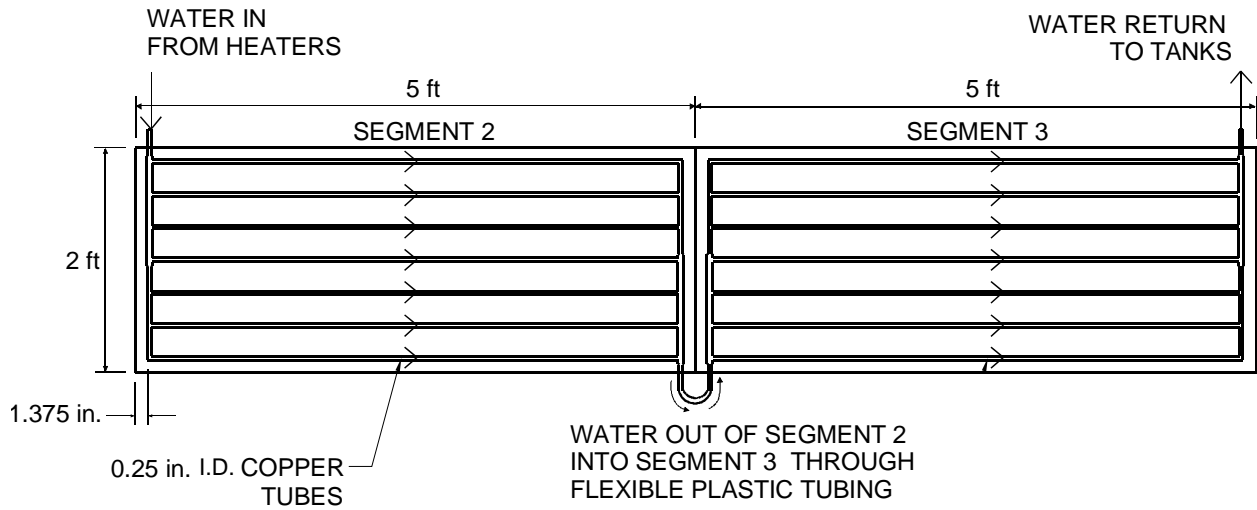


Figure 4-10. Typical manifold in flange

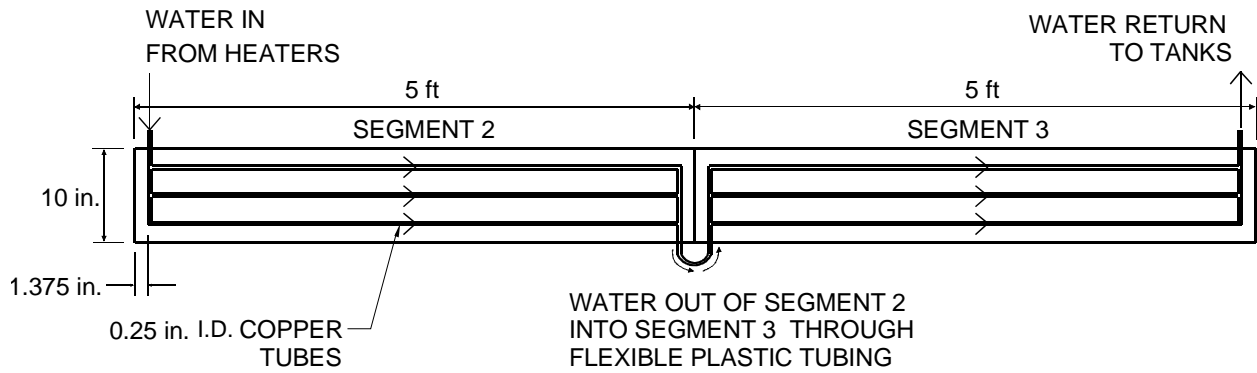


Figure 4-11. Typical manifold in web

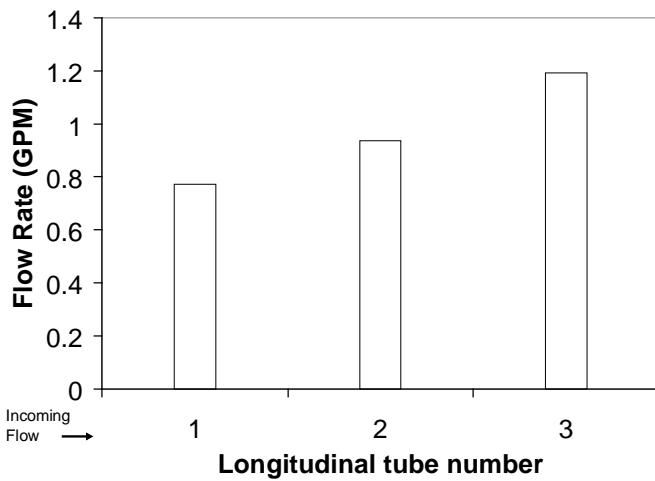


Figure 4-12. Typical flow rates through web manifolds

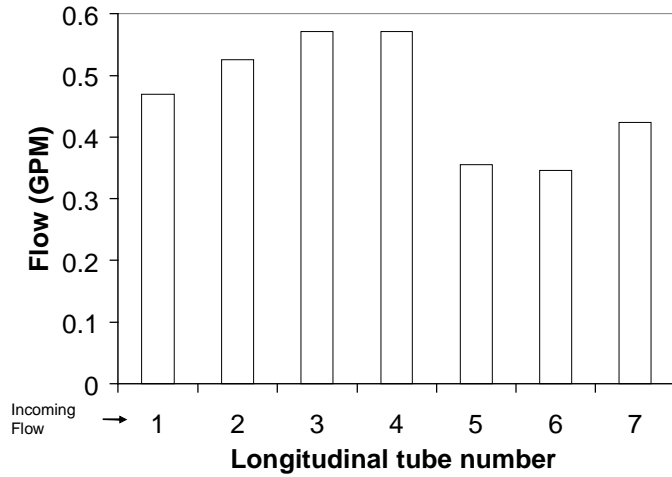


Figure 4-13. Typical flow rates through flange manifolds



Figure 4-14. Heating system

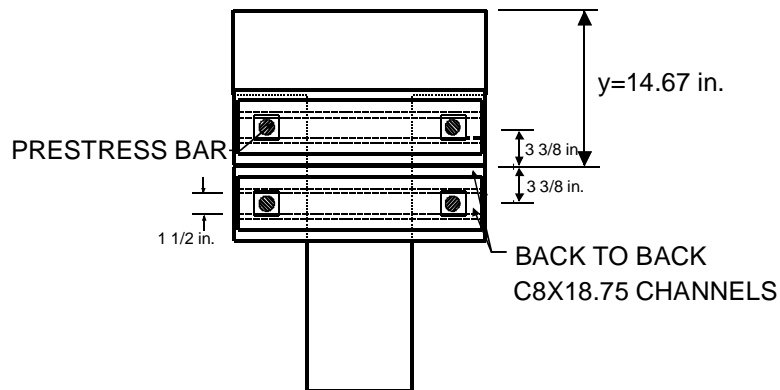


Figure 4-15. Cross section view of prestress assembly

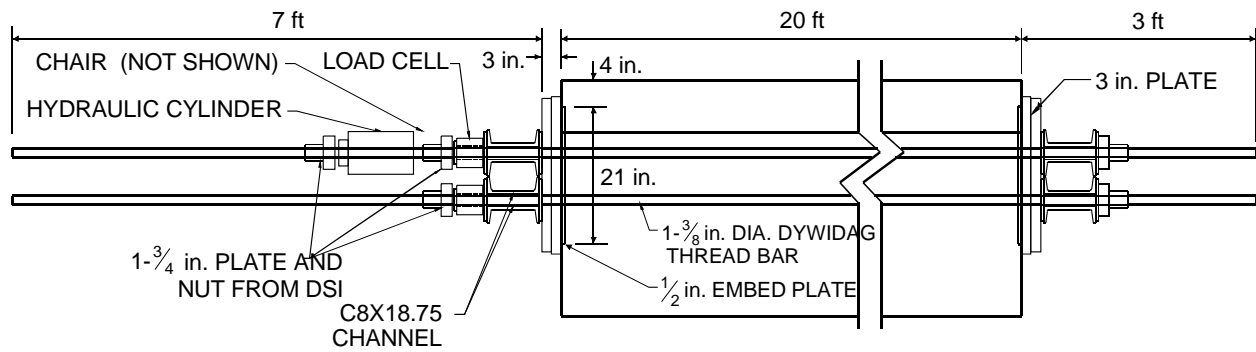


Figure 4-16. Elevation view of prestress assembly

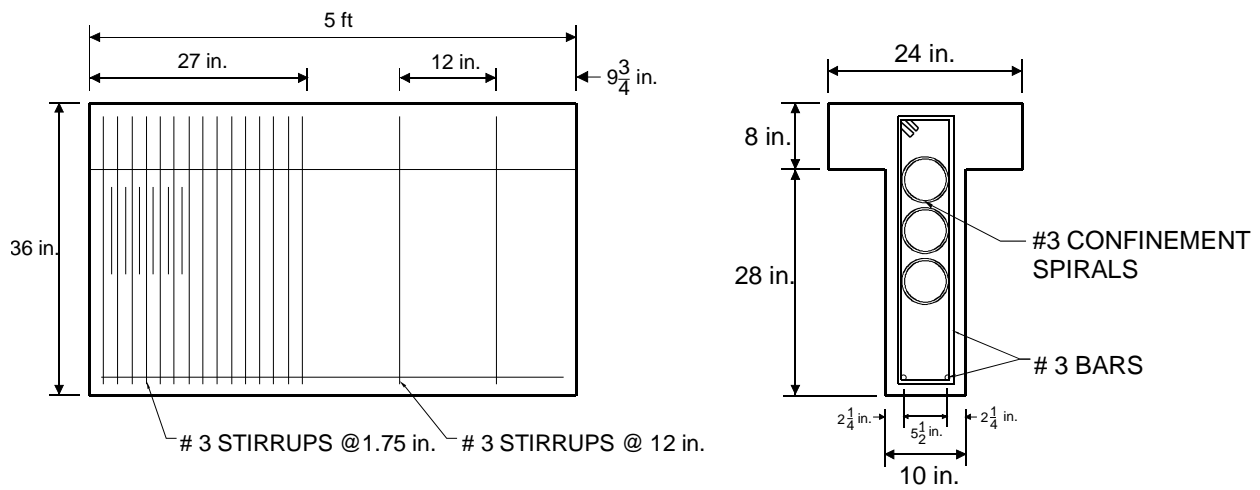


Figure 4-17. Mild steel reinforcements in Segments 1 and 4

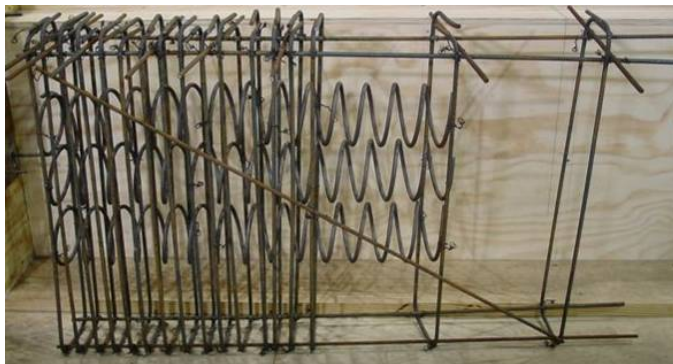


Figure 4-18. Mild steel reinforcement

CHAPTER 5 BEAM CONSTRUCTION

The segmental laboratory test beam was constructed at the Florida Department of Transportation (FDOT) Structures Research Center in Tallahassee, Florida. Beam design plans (see Appendix A) prepared by the University of Florida, were submitted to the FDOT personnel in the summer of 2005. Construction began in December, 2005 and was completed in February, 2006. Formwork, reinforcement, and thermocouple cages were fabricated by FDOT personnel. After the segments were cast and cured, they were transported to the University of Florida Civil Engineering Structures Laboratory in Gainesville.

Placement of Steel Reinforcement, Thermocouple Cages, and Copper Tubes

Because the segments were of equal length, a single set of re-usable wooden forms was used to cast each of the four segments of the beam. Segments 1 and 4 contained a steel bearing plate to distribute the anchorage force to the prestress anchorage zones, which contained mild steel confinement reinforcement (Figure 5-1 (A)). Two steel lifting hooks were placed 1 ft from each end of the segments as shown in Figure 5-1 (B). The segment joints contained two shear keys to assist in alignment during prestressing and to transfer shear during load tests (Figure 5-2). The heated segments (Segment 2 and 3) each contained three thermocouple positioning steel cages (Figure 5-3). In addition, six copper tube manifolds were tied to the thermocouple cages to ensure that their positions were maintained during concrete placement. Three manifolds were placed in the flange and three were placed in the web.

Casting of Concrete

The casting sequence of the segments of the laboratory beam is shown in Figure 5-4 and in Table 5-1 in ascending order. The ambient segments (1 and 4) were cast first so that the heated segments (2 and 3) could be match cast against them.

A 7000-psi concrete pump mix was used for all four segments. The design mix proportions are shown in Table 5-2. Delivery tickets for each mix are provided in Appendix C. Although the slump of the concrete is listed as 5 in. in Table 5-2, the mix was delivered with a slightly lower water content and slump to allow for adjustments prior to casting. Each segment was left in the forms for a week in the FDOT research laboratory before being removed and re-positioned for match-casting the next segment (see Figure 5-5). Finished pours for Segments 1 through 4 are shown in Figure 5-6 (A) through (D), respectively.

Material Tests and Properties

During the casting of each segment, fifteen 6 in. diameter by 12 in. long cylinders were cast for later use in determining material properties. The material properties determined for the ambient segments (1 and 4) were the compressive strength and modulus of elasticity (MOE). For the heated segments (2 and 3), the coefficient of thermal expansion (CTE) was determined in addition to the compressive strength and elastic modulus. The test setup for compressive strength and elastic modulus tests are shown in Figure 5-7 (A) and Figure 5-7 (B), respectively.

Compressive strength tests were conducted in accordance with the Standard Test Method for Compressive Strength of Cylindrical Concrete Specimens (ASTM C 39-01). Modulus of elasticity tests were conducted in accordance with the *Standard Test Method for Static Modulus of Elasticity and Poisson's Ratio of Concrete in Compression* (ASTM C 469-94). Coefficient of thermal expansion tests were conducted on each heated segment under laboratory conditions (in-situ CTE) and on 4 in. diameter by 8 in. long cylinders in accordance with the *Standard*

Method of Test for Coefficient of Thermal Expansion of Hydraulic Cement Concrete

(AASHTO TP 60-00). The in-situ CTE tests are discussed in Chapter 9. Cylinders meeting the specifications of the AASHTO TP 60-00 test method were not taken for Segment 2 therefore results from this test are only available for Segment 3. The AASHTO TP 60-00 test setup is shown in Figure 5-8. Tests were conducted in the FDOT Materials Testing Laboratory in Gainesville, Florida.

The results of compressive strength and modulus of elasticity tests for Segment 1 through Segment 4 are shown in Table 5-3 through Table 5-6, respectively. Three sets of compressive strength and elastic modulus tests were conducted for all segments except for Segment 3, the last segment to be cast. The first two sets of tests were conducted in early 2006 soon after the cylinders were transported from Tallahassee to Gainesville. The last set of tests was conducted in late 2006 during the course of conducting experiments on the laboratory segmental beam. In each test, one cylinder from each segment was used to determine the compressive strength and two cylinders were used for determining the elastic modulus. The elastic modulus values shown in the table are the average of elastic moduli determined from two cylinders. Because of scheduling conflicts, the ages of cylinders at the times tests were conducted were generally not the same. However, test results for segments 1 and 4 which were cast 11 days apart, match closely (maximum difference of 2% and 6% in compressive strength and modulus of elasticity values, respectively). The same is true for segments 2 and 3, which were also cast 11 days apart (maximum difference of 12% and 5% in compressive strength and modulus of elasticity values, respectively).

The coefficient of thermal expansion (CTE) of Segment 3 was determined using the AASHTO TP 60-00 test method. The focus of the test method is the measurement of the change

in length of a fully water-saturated concrete cylinder over a specified temperature range. The length change is then divided by the product of the original length of the specimen and the temperature change to give the CTE.

The AASHTO TP 60-00 test procedure is conducted as follows. The tests specimens consist of concrete cylinders that are 7.0 ± 1 in. long and 4 in. in diameter. The specimens are submerged in saturated limewater at 73 ± 4 °F for at least two days. After the cylinders are fully saturated, they are wiped dry and their lengths measured at room temperature to the nearest 0.004 in. The specimens are then placed in the measuring apparatus shown in Figure 5-8, which is positioned in a prepared water bath. The temperature of the water bath is set to 50 ± 2 °F. The bath is allowed to remain at this temperature until the specimen reaches thermal equilibrium, which is indicated by consistent readings of a linear variable displacement transducer (LVDT) to the nearest 0.00001 in. taken every 10 minutes over a half hour time period. The temperature of the water bath and the consistent LVDT readings are taken as initial readings. The temperature of the water bath is then set to 122 ± 2 °F. The bath is allowed to remain at this temperature until the specimen reaches thermal equilibrium in the same manner as for the initial readings. The temperature of the water bath and LVDT readings are taken as the second readings. The temperature of the water bath is finally set back to 50 ± 2 °F. After thermal equilibrium is reached the temperature of the water bath and LVDT readings are taken as final readings.

The CTE is calculated using the following equations:

$$CTE = (\Delta L_a / L_o) / \Delta T \quad (5-1)$$

$$\Delta L_a = \Delta L_m + \Delta L_f \quad (5-2)$$

$$\Delta L_f = C_f \times L_o \Delta T \quad (5-3)$$

where ΔL_a is the actual length change of the specimen during the temperature change, L_o is the measured length of specimen at room temperature, ΔT is the measured temperature

change (increase is positive, decrease is negative), ΔL_m is the measured length change of specimen during the temperature change (increase is positive, decrease is negative), ΔL_f is the length change of the measuring apparatus during the temperature change, and C_f is a correction factor accounting for the change in length of the measurement apparatus with temperature. The correction factor (C_f) in Equation 5-3 is usually taken as $9.6E-6/^{\circ}F$, the coefficient of thermal expansion of stainless steel. CTEs are determined from the expansion (initial and second readings) and contraction (second and final readings) segments of the test. The two CTE values thus obtained are averaged to give the CTE of the test specimen, provided the values are within $0.5E-6/^{\circ}F$ of each other. If the CTEs obtained from the expansion and contraction phases are not within $0.5E-6/^{\circ}F$ of each other, the test is repeated until this criterion is satisfied. Results for the coefficient of thermal expansion of Segment 3 determined using the AASHTO TP 60-00 test procedure are given in Table 5-7. Three cylinders were used for the test.

Application of Prestress

The goal of prestressing was to produce a net prestress with a selected vertical eccentricity and no net horizontal eccentricity. The magnitude and vertical eccentricity of prestress were chosen to impose a negative curvature (less compression in the extreme top fibers than in the bottom of the web) on the beam with stresses comparable to Service I stresses at a typical interior support of a four-span unit of the Santa Rosa Bay (SRB) bridge. The total prestress force was also required to provide sufficient compression in the extreme top fibers of the beam such that an appreciably high load at the cantilevered end of the beam, which could be accurately measured in the laboratory, would be required to open the joint at midspan. To achieve the stress state described above, a total prestress force of 376 kips (94 kips per bar) with a vertical eccentricity of 1.5 in. below the centroid of the beam was applied to the beam (see Figure 5-9).

Prior to post-tensioning, the segments were placed on wooden blocks at the same elevation with matching joint faces in contact. This reduced the possibility of excessive movement as the joints closed during post-tensioning. The prestress anchorage systems were suspended from the ends of Segments 1 and 4 using a pair of threaded bars connected to two steel channels, which were bolted to the ends of the segments (Figure 5-10 and Figure 5-11). This arrangement allowed the vertical eccentricity of prestress to be varied as necessary. Four DYWIDAG post-tensioning bars were then installed. Tandem 60-ton Enerpac hollow core single-acting jacks, pressurized with a manifold system attached to a single pump, were used to stress two bars on either side of the web at a time. The set of four bars were stressed sequentially, 2 bars on either side of the beam at a time. Prestressing was applied incrementally as shown in Table 5-8 with the force monitored using 200 kip hollow core load cells mounted on each bar (Figure 5-11). Prestressing forces in opposing bars were slightly different (less than 8%) due to construction imperfections and variations in bar placement.

Table 5-1. Segment cast dates

Segment Number	Date Cast
1	12/01/2005
4	12/12/2005
2	01/19/2006
3	02/02/2006

Table 5-2. Concrete pump mix proportions

Mix Number	FC82JC		
Strength (psi)	7000		
W/C Ratio	0.31		
Slump (in)	5 +/- 1"		
Air Content (%)	4.5 +/- 1.5%		
Plastic Unit Weight (lbs/cf)	140.1 +/- 1.5		
Material	ASTM	Type	
Cement	C 150	I/II	820
Cement	C 618	F. Ash	160
Water	--	--	304
Fine Aggregate	C 33	Sand	1095
Aggregate	C 33	#89STONE	1400
Admixture	C 260	AIR	Dosage rates vary with
Admixture	C 494	W/Reducer	manufacturers recommendations

Table 5-3. Compressive strengths and moduli of elasticity of Segment 1

SEGMENT 1 (Cast 12/01/2005)		
Age (days)	Compressive Strength (psi)	Modulus of Elasticity (ksi)
77	9300	4862
124	9820	5000
350	10210	5362

Table 5-4. Compressive strengths and moduli of elasticity of Segment 2

SEGMENT 2 (Cast 01/19/2006)		
Age (days)	Compressive Strength (psi)	Modulus of Elasticity (ksi)
28	7090	3785
75	8360	4000
319	9690	5180

Table 5-5. Compressive strengths and moduli of elasticity of Segment 3

SEGMENT 3 (Cast 02/02/2006)		
Age (days)	Compressive Strength (psi)	Modulus of Elasticity (ksi)
28	7150	3836
62	7950	4000
361	10970	5443

Table 5-6. Compressive strengths and moduli of elasticity of Segment 4

SEGMENT 4 (Cast 12/12/2005)		
Age (days)	Compressive Strength (psi)	Modulus of Elasticity (ksi)
66	9110	4575

Table 5-6. Continued

SEGMENT 4 (Cast 12/12/2005)		
Age (days)	Compressive Strength (psi)	Modulus of Elasticity (ksi)
113	10030	5000
339	10250	5158

Table 5-7. Coefficient of thermal expansion (CTE) of Segment 3 (AASHTO TP 60-00)

CTE (per °F)	
Cylinder 1	7.92E-6
Cylinder 2	7.77E-6
Cylinder 3	7.83E-6
Average	7.84E-6

Table 5-8. Selected post-tensioning force increments

Post-tensioning Step	Load Cell Readings(kips)			
	P1	P2	P3	P4
1	29.2	18	--	--
2	29.2	18	43.8	46.7
3	48.3	32.2	43.8	46.7
4	48.3	32.2	76.3	68.8
5	76.7	68.8	76.3	68.8
6	76.7	68.8	97.6	93.2
7	94.6	100.8	97.6	93.2
8	94.6	100.8	107.7	100.9
9	106.5	112.1	107.7	100.9
10	106.5	112.1	111.8	106.1
Final Loads	97.2	89.2	93.3	92.4



Figure 5-1. A) Open form with mild steel reinforcement. B) Closed form with mild steel reinforcement and lifting hooks.



Figure 5-2. Form for shear keys



Figure 5-3. Heated segment with copper tubes, thermocouple cages and thermocouples

SEGMENT 1 December 1, 2005	SEGMENT 2 January 19, 2006	SEGMENT 3 February 2, 2006	SEGMENT 4 December 12, 2005

Figure 5-4. Beam layout with casting sequence



Figure 5-5. Match-casting of segment



A



B



C



D

Figure 5-6. Finished concrete pours for A) Segment 1. B) Segment 2. C) Segment 3. D) Segment 4.



A



B

Figure 5-7. A) Compressive strength test setup. B) Elastic modulus test setup.

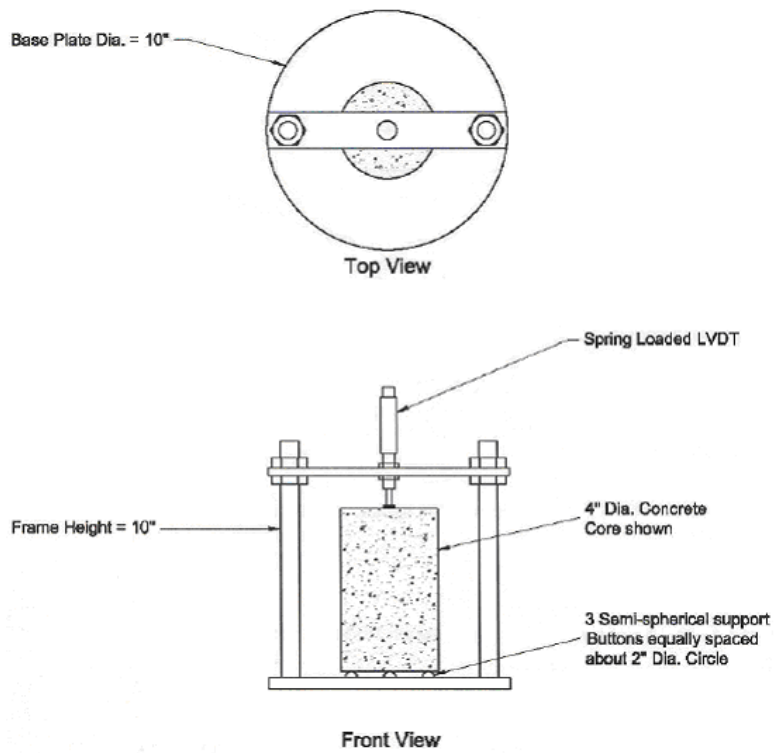


Figure 5-8. AASHTO TP 60-00 test setup

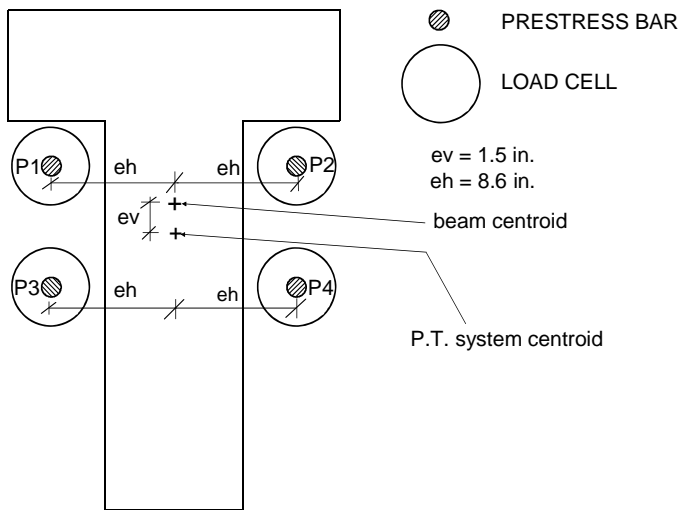


Figure 5-9. Bar designations and design eccentricities (West)



Figure 5-10. Prestress assembly (East)



Figure 5-11. Elevation view of prestress assembly (North)

CHAPTER 6 INSTRUMENTATION

Segments 2 and 3 of the laboratory segmental beam, designated “heated segments” because they were thermally controlled during testing, were internally instrumented with thermocouples prior to being cast, and externally instrumented with strain gauges, strain rings, and linear variable displacement transducers (LVDTs) prior to post-tensioning of the beam. Load cells were used to monitor reactions, applied mechanical loads, and prestress forces in the post-tensioning bars. This chapter presents a detailed description of the instrumentation used.

Thermocouples

Laboratory-fabricated thermocouples were embedded in the heated segments to monitor temperatures during thermal loading of the beam. The range of temperature that was to be measured was 50 °F to 130 °F. A Teflon-neoflon type T thermocouple wire, produced by OMEGA Engineering, Inc., was used for fabrication of the thermocouples due to its wide range of temperature sensitivity (-150 °F to 392 °F). Thermocouples were positioned in the segments with the aid of cages made of small-diameter steel, which were then placed in the forms at desired locations before concrete was cast (see Figure 6-1).

Thermocouples were vertically positioned to monitor temperature changes at heights corresponding to slope changes in the imposed thermal gradients. Additional thermocouples were placed at intermediate points between slope changes to facilitate control of the shape of the thermal gradient being imposed. The layout of thermocouples in relation to the shape of the AASHTO positive and negative thermal gradients is shown in Figure 6-2. Three thermocouple cages were embedded in each of the two heated segments and total of thirty nine thermocouples were attached to each cage. Thermocouple cages were placed 3 in. away from the ends and at the middle of each segment (see Figure 6-3). This arrangement was used to

ensure the thermal gradient being imposed was longitudinally uniform. Thermocouple labels at the sections in Figure 6-3 are shown in Figure 6-4.

Electrical Resistance Concrete Strain Gauges and Strain Rings

Foil type electrical resistance strain gauges (Figure 6-5) were bonded to the surfaces of the heated segments of the beam for monitoring beam behavior under mechanical and thermal loading (Figure 6-6). The strain gauges were of type PL-60-11-5LT, manufactured by Tokyo Sokki Kenkyujo Co., Ltd. The gauges had a gauge length of 60 mm (2.4 in.), and a temperature compensation number of 11, which is adequate for eliminating strains due to unrestrained thermal expansion/contraction of steel and concrete from measured strain values. To eliminate the influence of temperature variations (of the lead wires) on measured strains, three-wire type gauges were used.

In addition to strain gauges, four Strainstall Type-5745 sealed strain rings (Figure 6-7) were mounted at the centroid of the beam at midspan (Figure 6-6 (C) and (D)). Data from the strain rings were used to validate readings from strain gauges mounted at the same location. The detailed locations of strain gauges and strain rings through the depth of the beam on either side are shown in Figure 6-8, Figure 6-9, and Figure 6-10. The strain gauges located in the vicinity of the joint at midspan, (J2), were of particular importance in determining the load at which the joint opened. Strain gauges and strain rings located at the centroid of the beam at midspan were used to monitor movement of the neutral axis of the beam after the midspan joint began to open. With the exception of gauges located at the centroid of the beam, strain gauges located on the North and South of joint J2 were placed such that the center of each gauge was 2 in. away from the joint. Strain gauges located at the centroid at midspan were centered beneath strain rings, which had a greater gauge length (4.5 in.). Thus, the distance from the common center of these gauges to the joint at midspan was 3.6 in. Strain gauges on top of the flange were located 5.5 in.

away from the joint. Because of the presence of copper tubes protruding from the concrete on the North side of the beam, two strain gauges were installed on the North side of the flange while three were installed on the South side. Therefore, a total of three strain gauges were located above the neutral axis of the section on the North side compared with four on the South side. The labeling convention used for strain gauges is explained in Figure 6-11. Strain rings were labeled in a similar manner by replacing the “S” for strain gauge with “R” for strain ring (see Figure 6-12).

Linear Variable Displacement Transducers (LVDT)

DCTH Series LVDTs, produced by RDP Electrosense, were used in measuring deflections and opening of the joint at the midspan of the beam. The LVDTs had a stroke of 1 in. Four LVDTs were used to measure the vertical deflection at the cantilevered end of the beam (see Figure 6-13), relative sliding (if any) between Segments 2 and 3, deflections close to the mid-support, and deflections close to the end-support. To detect and track the depth of joint-opening at the midspan of the beam, six LVDTs were mounted on the South side and three were mounted on the top flange across the joint (see Figure 6-14). The labeling convention used for LVDTs is shown in Figure 6-15.

Load Cells

Load cells used to measure the magnitudes of applied loads and reactions were Model 3000 load cells, manufactured by Geokon, Inc. The layout of load cells on the post-tensioned beam is illustrated in Figure 6-16. The force in the hydraulic jack, which was used to load the beam at the cantilevered end, was measured using a 200-kip load cell (Figure 6-17 (A)). 200-kip load cells were mounted on each of the four DYWIDAG post-tensioning bars (Figure 6-17 (B)). These load cells were used to monitor prestress levels in the beam. 150-kip and 75-kip load cells

were installed at the mid-support (Figure 6-17 (C)) and end-support (Figure 6-17 (D)) of the beam, respectively, for measuring reactions under the effect of applied loads.

Data Acquisition

The instrumentation layout for the prestressed beam is shown in Figure 6-18 and Figure 6-19. Data from the variety of instruments shown in the figures were collected using the National Instruments model SCXI-1000DC Data Acquisition (DAQ) System (see Figure 6-20). Data were collected from a total of 192 thermocouples (32 per section), 15 LVDTs, and 7 load cells. Forty-one data acquisition channels were reserved for collecting data from strain gauges, which were connected to the DAQ system based on the cross section of interest in test being conducted. During the application of thermal loads, the DAQ system was set to acquire 3600 samples of data from each instrument in five minutes, which were then averaged and recorded at the end of each 5 minute interval. During the application of mechanical loads, the system was set to acquire 100 samples of data from each instrument, which were averaged and recorded every second. Compared with mechanical loading a lower data acquisition rate was used during thermal loading because of the longer time needed to heat or cool the concrete.



Figure 6-1. Thermocouple cage with attached thermocouples

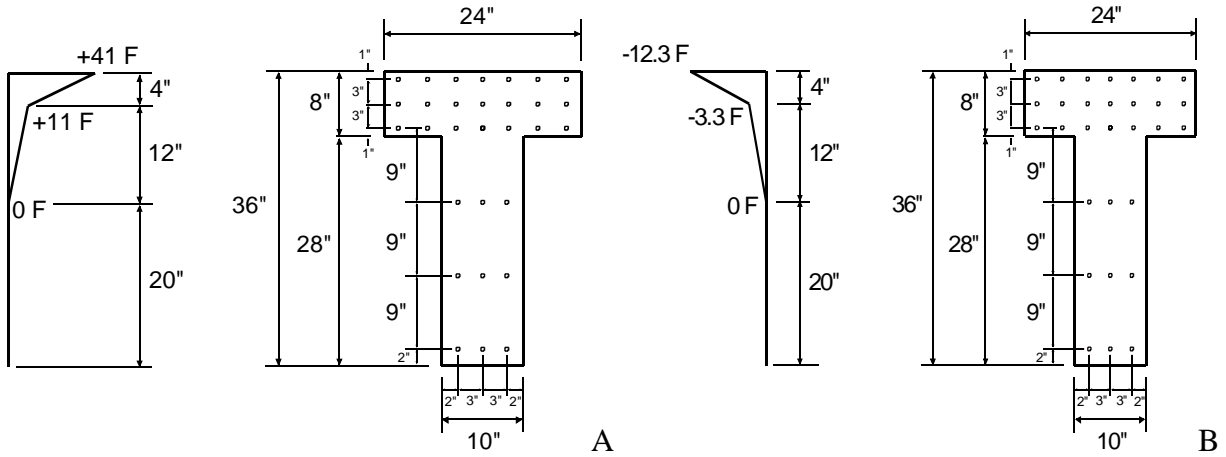


Figure 6-2. Layout of thermocouples in relation to shape of A) positive thermal gradient.
B) negative thermal gradient.

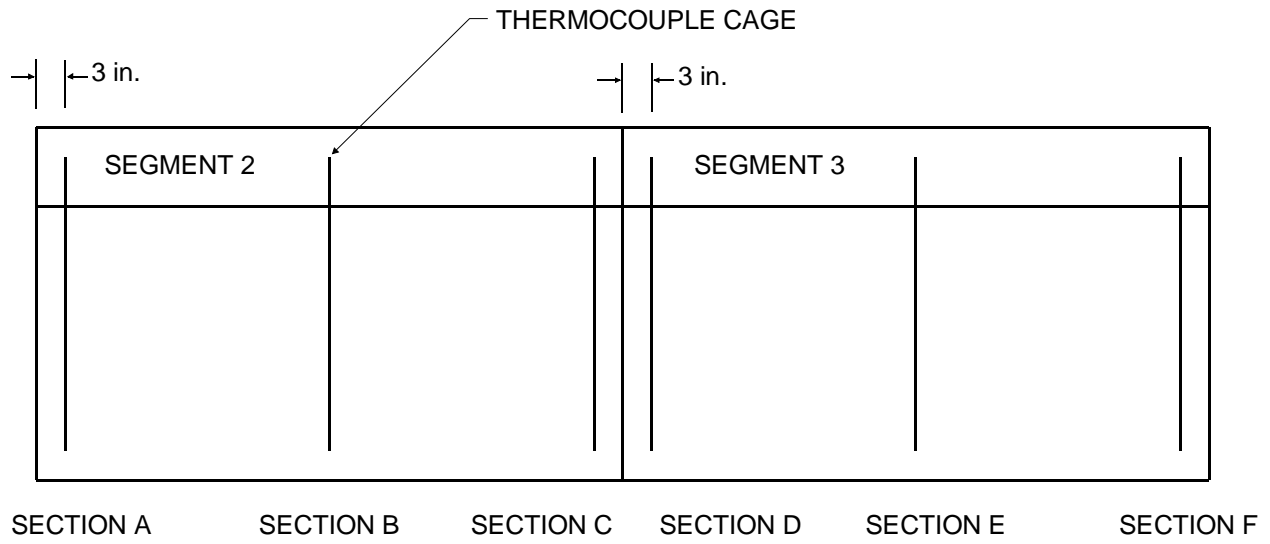
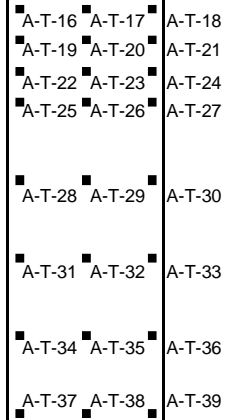
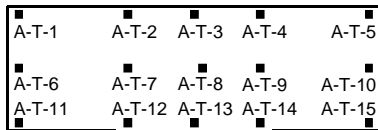
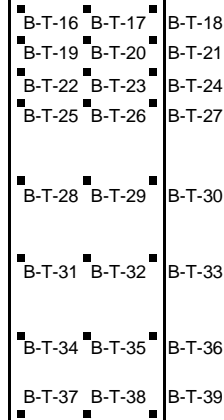
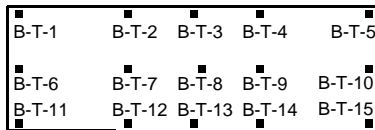


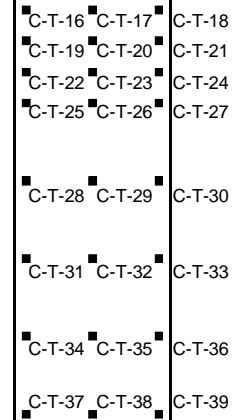
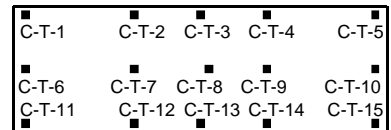
Figure 6-3. Location of thermocouple cages in Segments 2 and 3



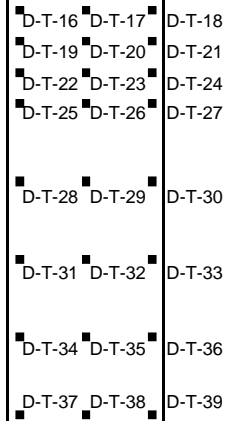
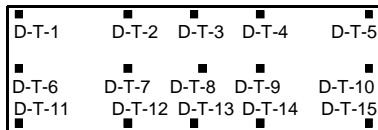
SECTION A



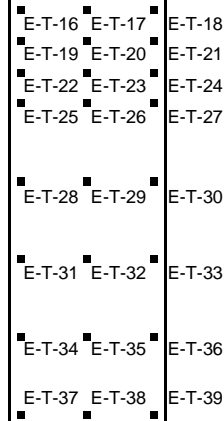
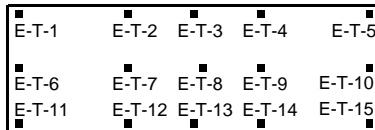
SECTION B



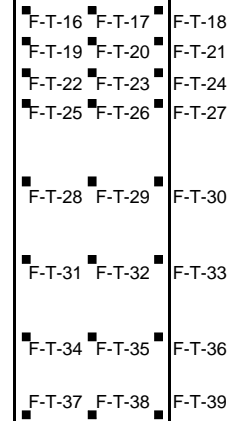
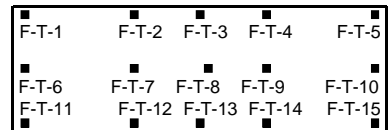
SECTION C



SECTION D



SECTION E



SECTION F

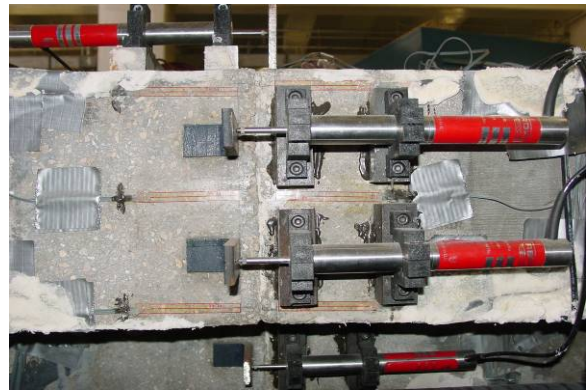
Figure 6-4. Thermocouple labels in Segments 2 and 3



Figure 6-5. Strain (foil) gauge



A



B



C



D

Figure 6-6. Strain gauges close to joint at midspan; A) North flange. B) South flange. C) North web. D) South web.



Figure 6-7. Strain ring

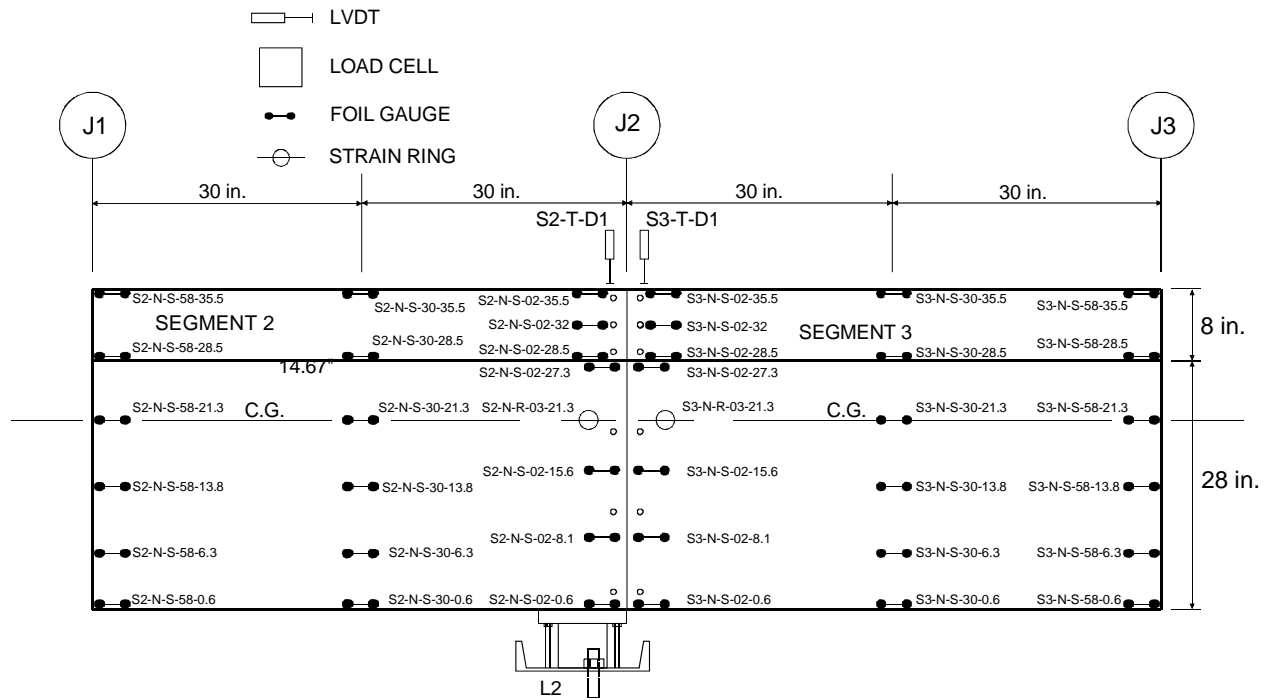


Figure 6-8. Instrumentation details (North side)

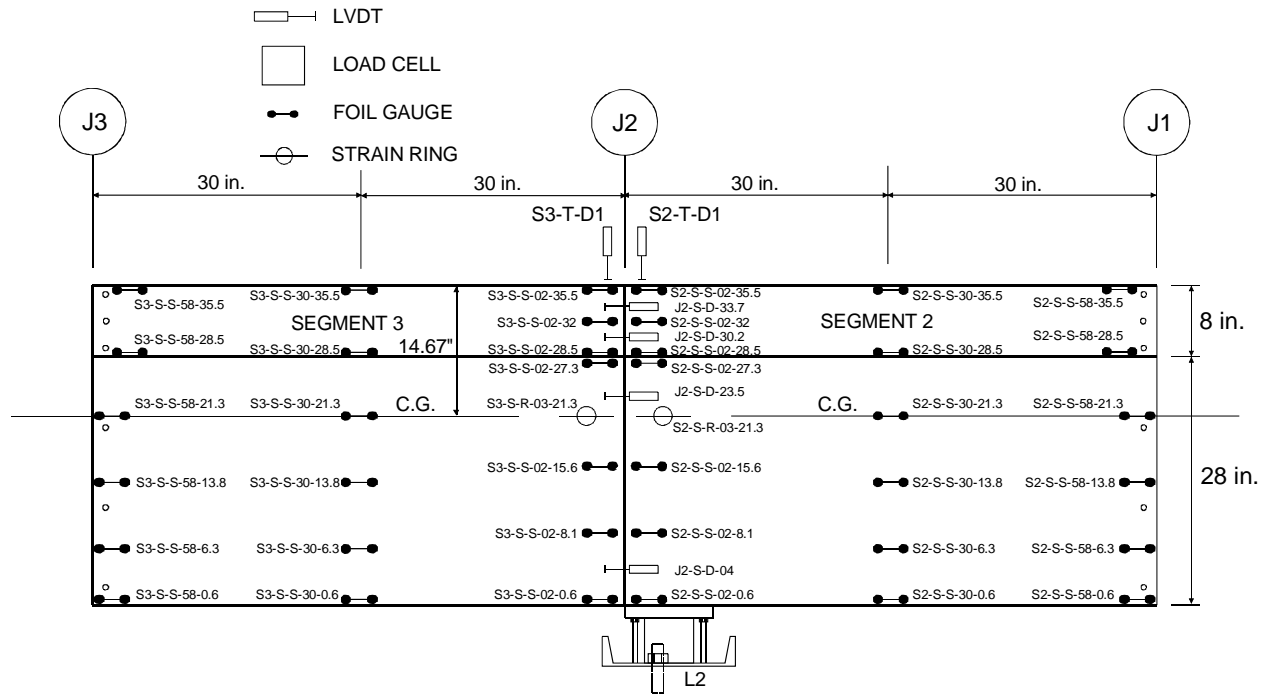


Figure 6-9. Instrumentation details (South side)

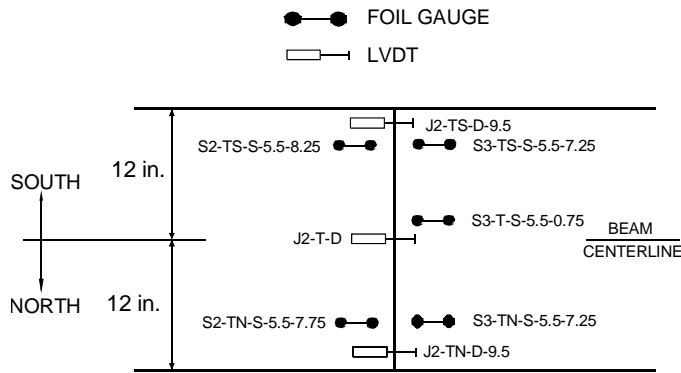


Figure 6-10. Instrumentation at midspan (top flange)

Segment Number	S
North (N) or South (S)	N
Strain Gauge	S
Distance from Joint 2	58
Distance Above Bottom of Beam	0.6

Figure 6-11. Typical labeling convention for strain gauges

Segment Number	S2 - N - R - 3.5 - 21.3
North (N) or South (S) Face	
Strain Gauge	
Distance from Joint 2	
Distance Above Bottom of Beam	

Figure 6-12. Typical labeling convention for strain rings



Figure 6-13. LVDT for measuring deflection at cantilevered-end of beam

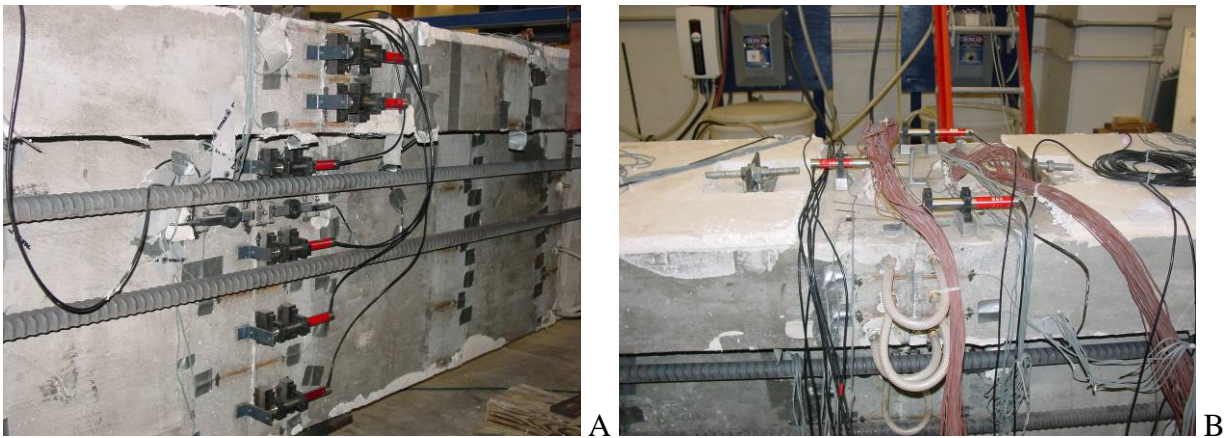


Figure 6-14. LVDTs mounted across joint at midspan on A) South side and B) top flange

Joint (J) or Seg. (S) Number	J2 - T - D1
Location (T = Top, S = Side)	
Displacement Device Number	

Figure 6-15. LVDT labeling convention

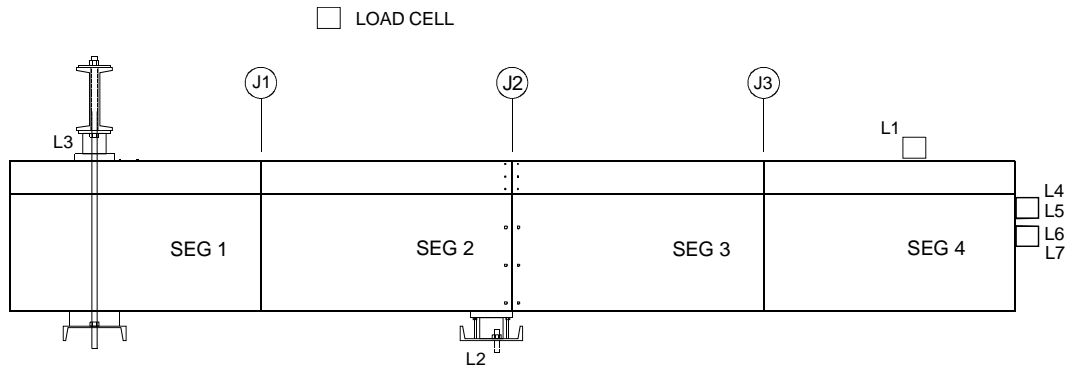


Figure 6-16. Load cell layout



Figure 6-17. Load cells for measuring; A) applied load. B) prestress. C) mid-support reaction. D) end-support reaction.

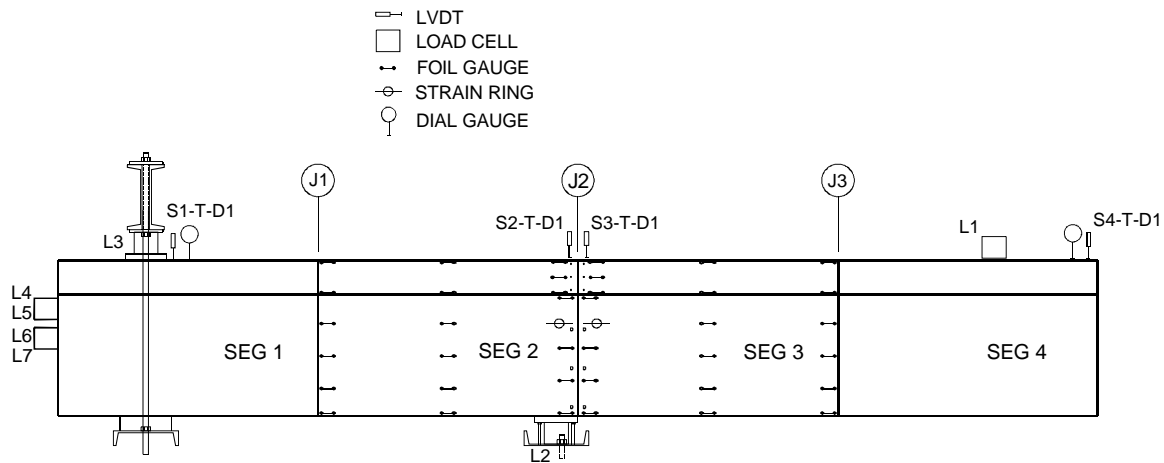


Figure 6-18. Instrumentation layout (North)

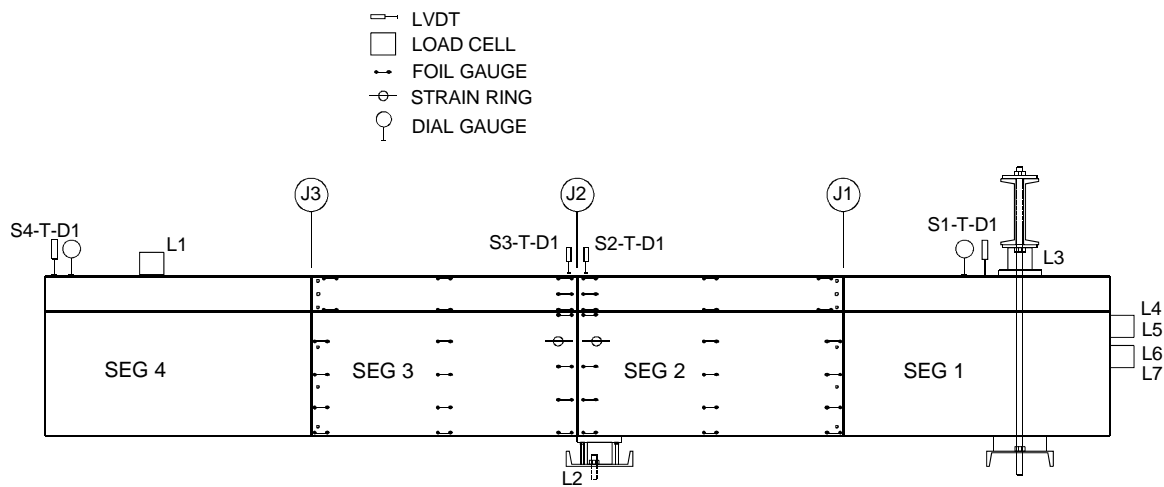


Figure 6-19. Instrumentation layout (South)



A



B

Figure 6-20. A) DAQ System. B) Connection of instrumentation to DAQ System.

CHAPTER 7 SETUP AND PROCEDURES FOR MECHANICAL LOADING

The setup for conducting laboratory experiments is illustrated in Figure 7-1. A picture of the post-tensioned beam in the laboratory is shown in Figure 7-2. The beam was supported 1.7 ft from the end of Segment 1 (end-support) and 10.5 ft from the cantilevered-end of the beam (mid-support). It was mechanically loaded 2.7 ft from the cantilevered-end. Fabrication details of the support systems and loading frame can be found in Appendix B.

The end-support consisted of back-to-back channels supported by four all-thread bars bolted to the laboratory strong floor. A 75-kip load cell was placed between the back-to-back channels and a 3/8-in. thick, 12 in. by 12 in. steel plate. Between the steel plate and the surface of the beam a 5/8-in. thick, 12 in. by 12 in. neoprene pad was used to distribute the reaction to the concrete. The mid-support consisted of a 1.5 in.-thick, 10 in. by 10 in. steel plate supported by four all-thread rods. The rods were 0.5 in. shorter than the 150-kip load cell at mid-support, which was placed between the steel plate and a C15 x 33.9 channel bolted to the laboratory strong floor. The 0.5 in. clearance between the load cell and the steel rods allowed the load cell to fully carry loads due to the self-weight of the beam and the actuator without any contribution from the steel rods. A 5/8-in. thick, 12 in. by 12 in. neoprene pad was placed between the steel plate and the bottom web of the beam to distribute the mid-support reaction to the concrete. The loading frame, which was designed to carry loads up to 400 kips, consisted of two steel columns and two deep channel beams. For convenience, a temporary I-section was bolted to the load frame columns below the deep channel beams, to support a 60 ton manually pressurized jack, which was used to apply mechanical loads to the beam (see Figure 7-3). A 200-kip load cell was placed directly under the jack to measure applied loads. A 3/8-in. thick, 12 in. by 12 in. steel

plate and 5/8-in. thick, 12 in. by 12 in. neoprene pad were used to distribute the applied load to the concrete.

Opening of Joint between Segments 2 and 3

The primary aim of applying mechanical loads to the beam was to open the joint between segments 2 and 3 (joint J2), creating zero stress conditions from which the effects of thermal loads could be quantified. This is illustrated in Figure 7-4 through Figure 7-6.

Stresses at joint J2 created by prestress and the self-weight of the beam were taken as the baseline or reference stresses. Stresses due to the AASHTO nonlinear thermal gradients, which were expected to be uniformly distributed across the width of joint J2, were quantified relative to the baseline stresses at joint J2. Quantifying average stresses caused by the AASHTO nonlinear thermal gradients in the extreme top fibers of the beam at joint J2 required the determination of the load corresponding to the average reference stress, Q_{NT} , (see Figure 7-4). In addition, loads corresponding to average stresses in the extreme top fibers created by the superposition of the AASHTO nonlinear positive thermal gradient on the reference stresses, Q_{PG} , (see Figure 7-5) and the AASHTO nonlinear negative thermal gradient on the reference stresses, Q_{NG} , (see Figure 7-6) had to be determined. Average stresses due to the thermal gradients were quantified from the difference in loads initiating joint opening ($Q_{PG} - Q_{NT}$ for the positive gradient and $Q_{NG} - Q_{NT}$ for the negative gradient) through back calculation. Though the concept of quantifying thermal stresses by opening the joint between segments 2 and 3 is illustrated for the extreme top fibers in Figure 7-4 through Figure 7-6, it is applicable at any depth at joint J2 where loads which cause the section fibers to lose contact at that depth can be determined.

It was determined from sectional analysis using conventional beam theory that a maximum load of about 40 kips was required to relieve the average longitudinal stress in the extreme top fibers of the beam at the joint (i.e. open the joint) created by the superposition of stresses due to

the self-weight of the beam, prestress, and the AASHTO nonlinear positive or negative thermal gradient. To allow for the possibility that the experimental setup might deviate somewhat from beam theory, loads of up to 60 kips were applied during the tests. The configuration of load and support points ensured that the maximum moment due to applied loads occurred at the joint at midspan (joint J2). This eliminated the development of high tensile stresses within the beam segments since tensile stresses could not be transmitted across the joint.

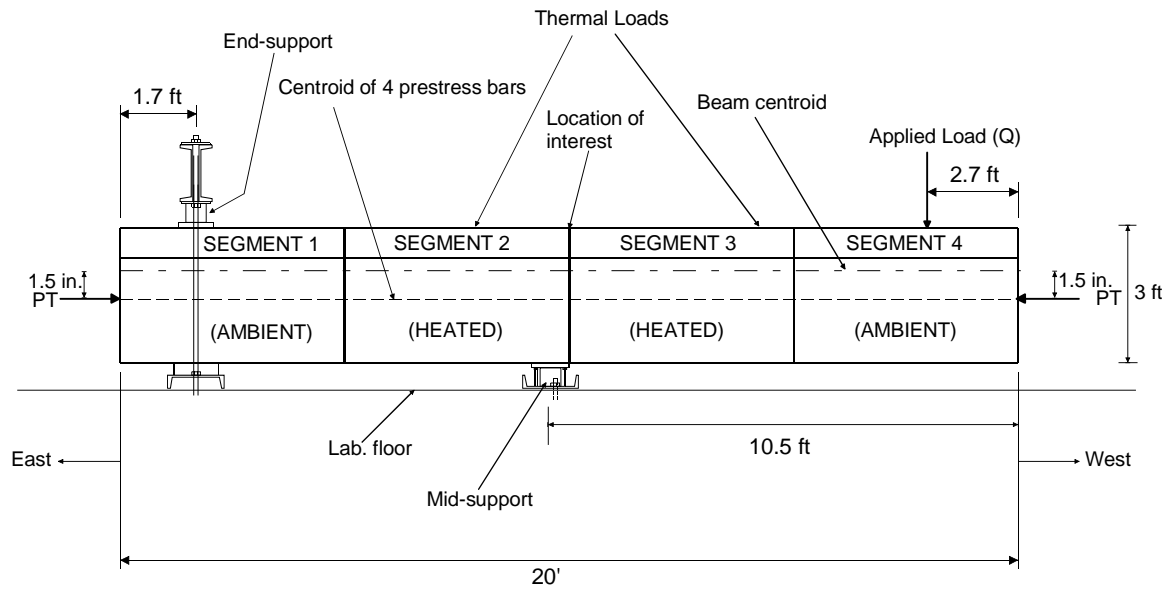


Figure 7-1. Test setup



Figure 7-2. Segmental beam in laboratory

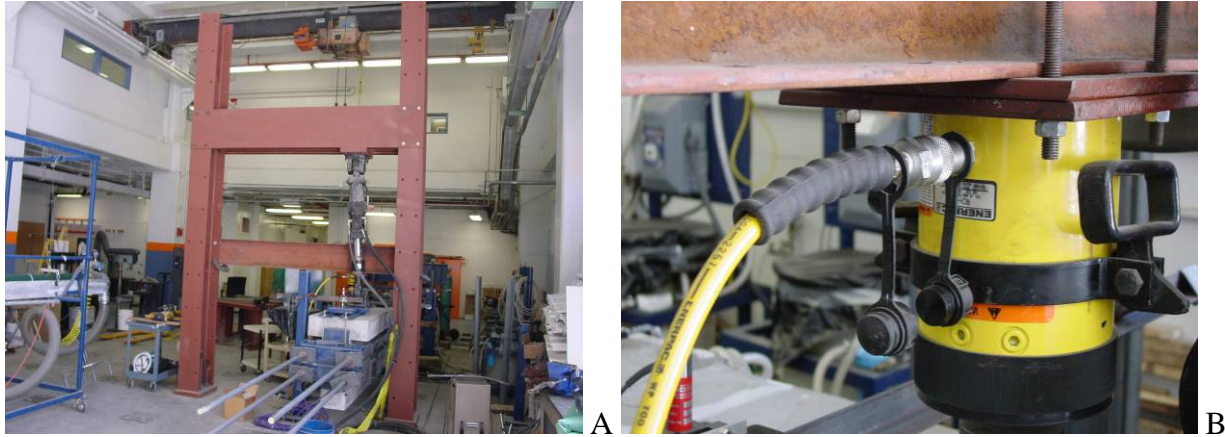


Figure 7-3. A) Loading frame. B) 60-ton jack

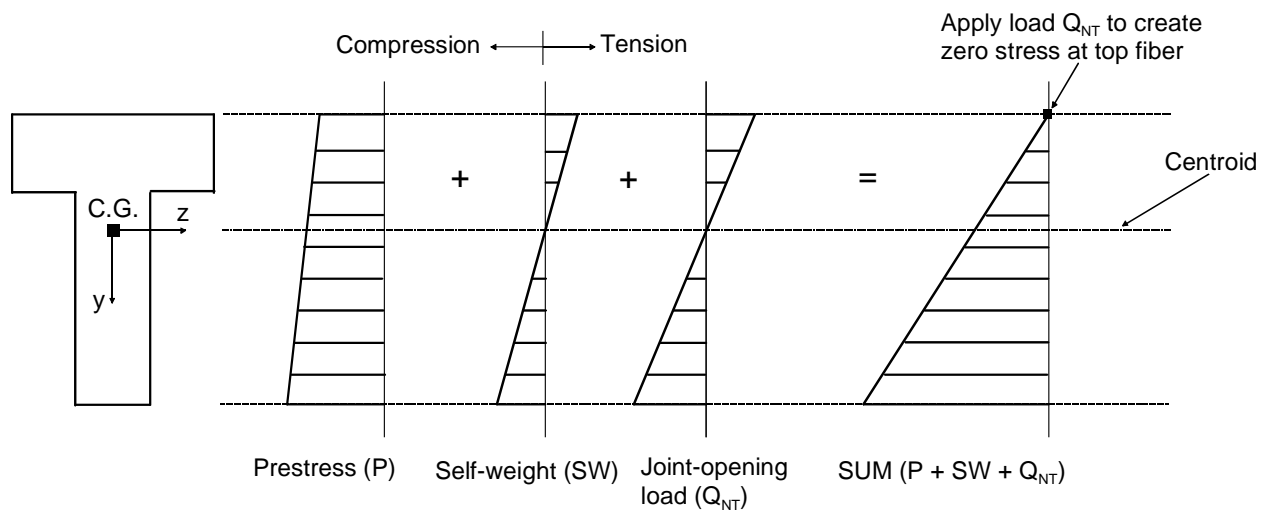


Figure 7-4. Ideal stress diagrams without thermal loads

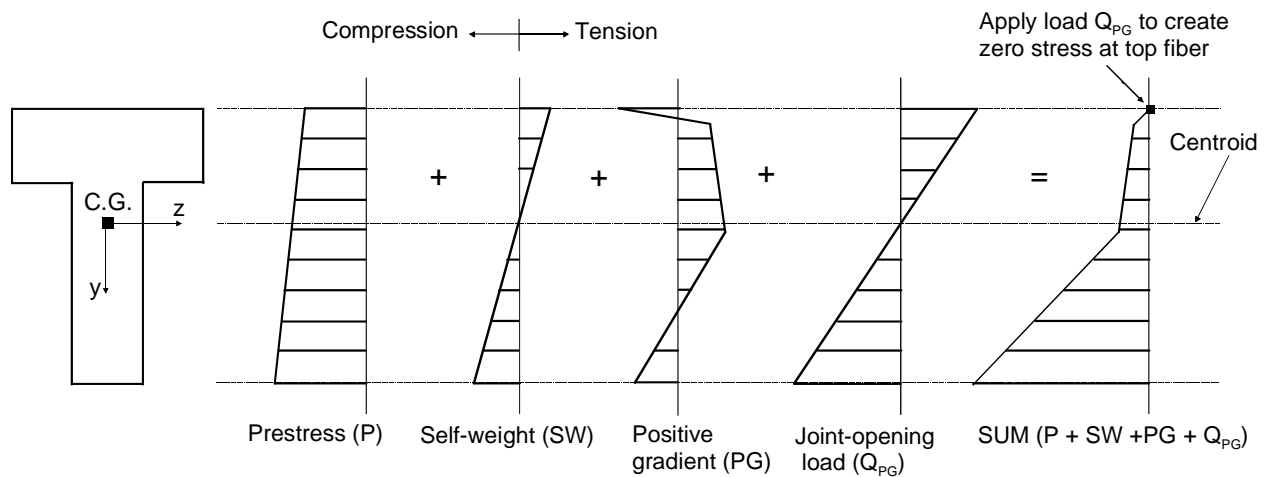


Figure 7-5. Ideal stress diagrams with positive thermal gradient

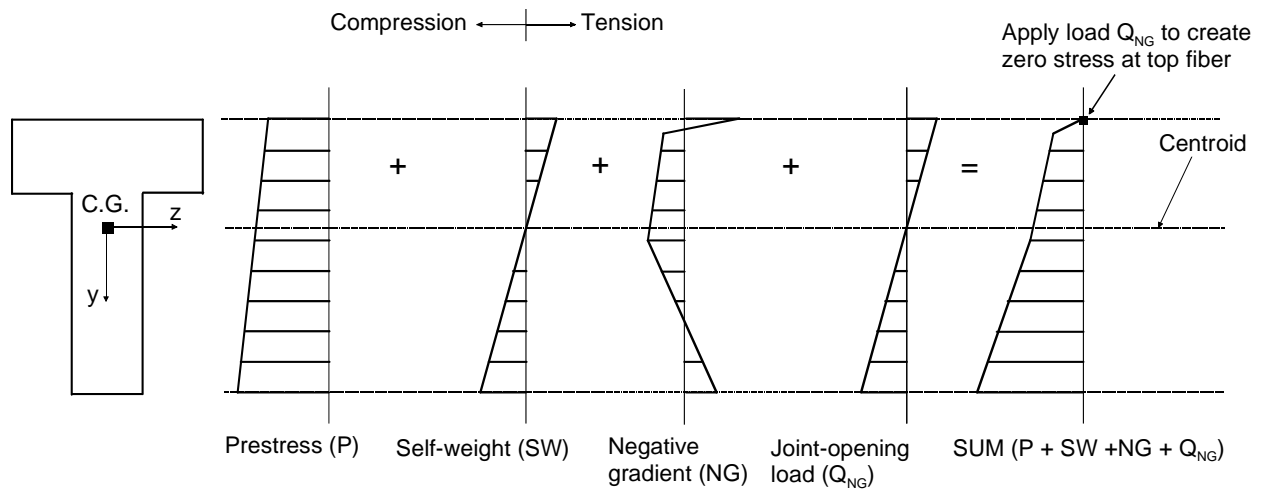


Figure 7-6. Ideal stress diagrams with negative thermal gradient

CHAPTER 8 SETUP AND PROCEDURES FOR THERMAL LOADING

Thermal profiles were imposed on the heated segments of the beam by passing heated water at laboratory controlled temperatures through strategically placed copper tubes embedded in the concrete. Four thermal profiles were imposed on the heated segments: uniform temperature distribution, linear thermal gradient, AASHTO nonlinear positive thermal gradient, and AASHTO nonlinear negative thermal gradient.

This chapter describes the methods and piping arrangements used to impose each thermal profile. Throughout this chapter, thermocouple locations, pipe layers, and heaters are referenced. Three water heaters were used to heat the water pumped through the beam. Heaters 1 and 2 (H1 and H2) were capable of supplying water at temperatures as high as 135 °F. These heaters were used to provide high temperatures typically ranging from 105 °F to 135 °F. Heater 3 (H3) was capable of supplying water at temperatures as high as 125 °F, and was utilized for temperatures ranging from 86 °F to 100 °F. Pipe layer designations, thermocouple section locations, and the layout of thermocouples at each section are shown in Figure 8-1 through Figure 8-3, respectively. The “x” markings in Figure 8-3 represent thermocouples that were not connected to the DAQ system because they were not needed to capture pertinent data. To minimize heat loss from the beam, 0.5-in. thick Styrofoam boards were used to insulate the surfaces of the beam (see Figure 8-4).

Uniform Temperature Distribution

Before the beam was prestressed, initial thermal testing was conducted that involved heating the segments uniformly to determine the in-situ CTE. The uniform heating was also one part of the AASHTO negative thermal gradient.

Changing laboratory temperatures (i.e. from early morning through noon till evening) and the fact that the heated segments were insulated prevented the segments from being at a uniform temperature prior to the start of imposing prescribed thermal profiles. This was because the large mass and low thermal conductivity of the concrete segments prevented them from rapidly adjusting to changing laboratory temperatures. In particular, the bottom webs of the segments were generally cooler than the top flanges of the segments. Tap water, which ranged in temperature from 74 °F to 85 °F, depending on the month in which tests were conducted, was used to bring the entire segments to a uniform reference temperature by circulating the water through the segments overnight using the piping configuration shown in Figure 8-5. After the desired thermal configuration had been imposed, this same approach was then used to cool the segments back to the reference temperature.

The piping configuration shown in Figure 8-6 was used to uniformly heat the segments. This created a temperature differential that was uniform over the height of the segment. With Heaters 1 and 2 set to the target temperature, water was continuously circulated through the segments. Heater 3 was not used in this setup primarily because of limitations on the heat energy that it could deliver at the high flow rates which were required to uniformly heat the segments longitudinally. Temperatures in the concrete were monitored from thermocouple readings. Thermal profiles at each section were also periodically plotted using an average of readings taken from each row of thermocouples throughout the depth of the beam. Heater settings were then updated to offset deviations from the target temperature. When the desired profile was achieved at each section, temperatures were held in steady state for about 30 to 45 minutes as readings were taken periodically. The segments were then cooled to the reference temperature.

The average time it took to impose a uniform profile on a single heated segment was about 10 hours. In the case of two segments, the system was kept running for between 20 to 30 hours.

Linear Thermal Gradient

A second set of thermal tests were conducted that involved imposing a linear thermal gradient from 0 °F at the bottom of the web to +41 °F at the top of the flange. This gradient, which leads to no stress development in a simply supported structure, was also used in determining the in-situ coefficients of thermal expansion of the heated segments.

The piping configuration shown in Figure 8-7 was used to impose the linear thermal gradient after circulating tap water through the segment to establish a uniform reference temperature. Heaters 1, 2, and 3 were set to temperatures 41 °F, 23 °F, and 12 °F above the reference temperature, respectively. Water from Heaters 1 and 2 was mixed and circulated through pipe layer 3. The temperature of mixed water was about 32 °F above the reference temperature. There was no flow in pipe layers 2 and 6. Thermocouple readings and thermal profiles at each section were monitored and changes to the heater settings made when necessary. When the target thermal gradient was achieved, temperatures were held in steady state for about 30 to 45 minutes as readings were taken periodically. The segment was then cooled back to the reference temperature. The average time it took to impose the linear profiles on a single heated segment was about 9 hours.

AASHTO Positive Thermal Gradient

The piping shown in Figure 8-8 was used to impose the AASHTO nonlinear positive thermal gradient on the heated segments of the beam. Before circulating heated water through the segments, tap water was circulated overnight to establish the reference temperature. Heaters 1 and 3 were set to 41 °F and 11 °F above the reference temperature, respectively. Although tap water was pumped from a reservoir through Heater 2, the heater was turned off for

the duration of the test. The water pumped through Heater 2 was mixed with water from Heater 1 and circulated through layer 3, which was required to be at a temperature about 7 °F above the reference temperature. The temperature of mixed water was regulated by controlling contributions to the mix from Heater 1 (turned on) and Heater 2 (turned off). The bottom 20-in. portion of the beam was maintained at the reference temperature by circulating tap water through layers 4, 5, and 6. This produced the 0 °F temperature change in the gradient (relative to the reference temperature). Thermocouple readings and the shape of the gradient at each section were monitored and changes to heater settings were made when necessary. When the AASHTO positive thermal gradient profile was achieved, temperatures were kept at steady state for about 30 to 45 minutes as readings were taken periodically. The beam was then cooled to the reference temperature. The average time it took to impose the AASHTO positive thermal gradient on the heated segments was about 7 hours.

AASHTO Negative Thermal Gradient

The AASHTO nonlinear negative thermal gradient was imposed on the heated segments using the setup shown in Figure 8-9. To impose this gradient, the segments had to be cooled from the reference temperature rather than heated. Since the setup for thermal control could only be used to heat the segments, two reference temperatures were involved in imposing the negative gradient. The first reference temperature (referred to as the low reference temperature) was imposed by circulating tap water through the segments using the piping configuration previously shown in Figure 8-5. The low reference temperature was imposed to maintain consistency with procedure for imposing the thermal profiles discussed previously. After establishing the low reference temperature, a uniform temperature increase of about 40 °F was imposed on the segments using the plumbing in Figure 8-6. The temperature of the segments after the 40 °F increase was referred to as the high reference temperature. Heater settings and layer

temperatures required to impose the gradient were based on the high reference temperature. Heater 1 was set to a temperature 12.3 °F below the high reference temperature. This corresponded to the -12.3 °F temperature change in the AASHTO nonlinear thermal gradient. The bottom 20-in. portion of the beam was maintained at the high reference temperature by circulating water at that temperature through layers 4, 5, and 6, using Heater 2. This corresponded with the 0 °F temperature change in the gradient. Heater 3 was connected to layer 2 and was only used when needed to bring the temperature of layer 2 to 3.3 °F below the high reference temperature. Water from heaters 1 and 2 was mixed and circulated through layer 3. Thermocouple readings and the shape of the gradient were monitored throughout the test, and changes to heater settings were made as necessary. When the target gradient was achieved, temperatures were kept in steady state for about 30 to 45 minutes as readings were periodically taken. The beam was then cooled to the low reference temperature. The average time required to impose the AASHTO negative thermal gradient after imposing the high reference temperature was about 7 hours.

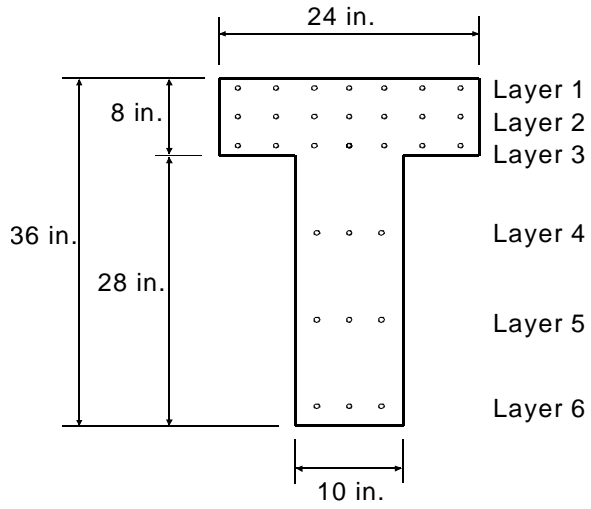


Figure 8-1. Pipe layers

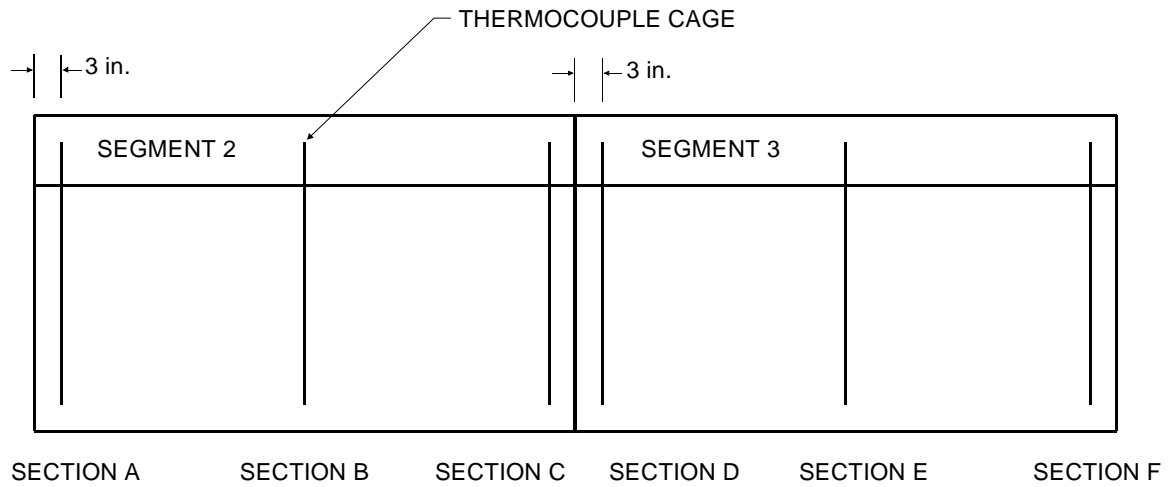


Figure 8-2. Thermocouple locations in heated segments

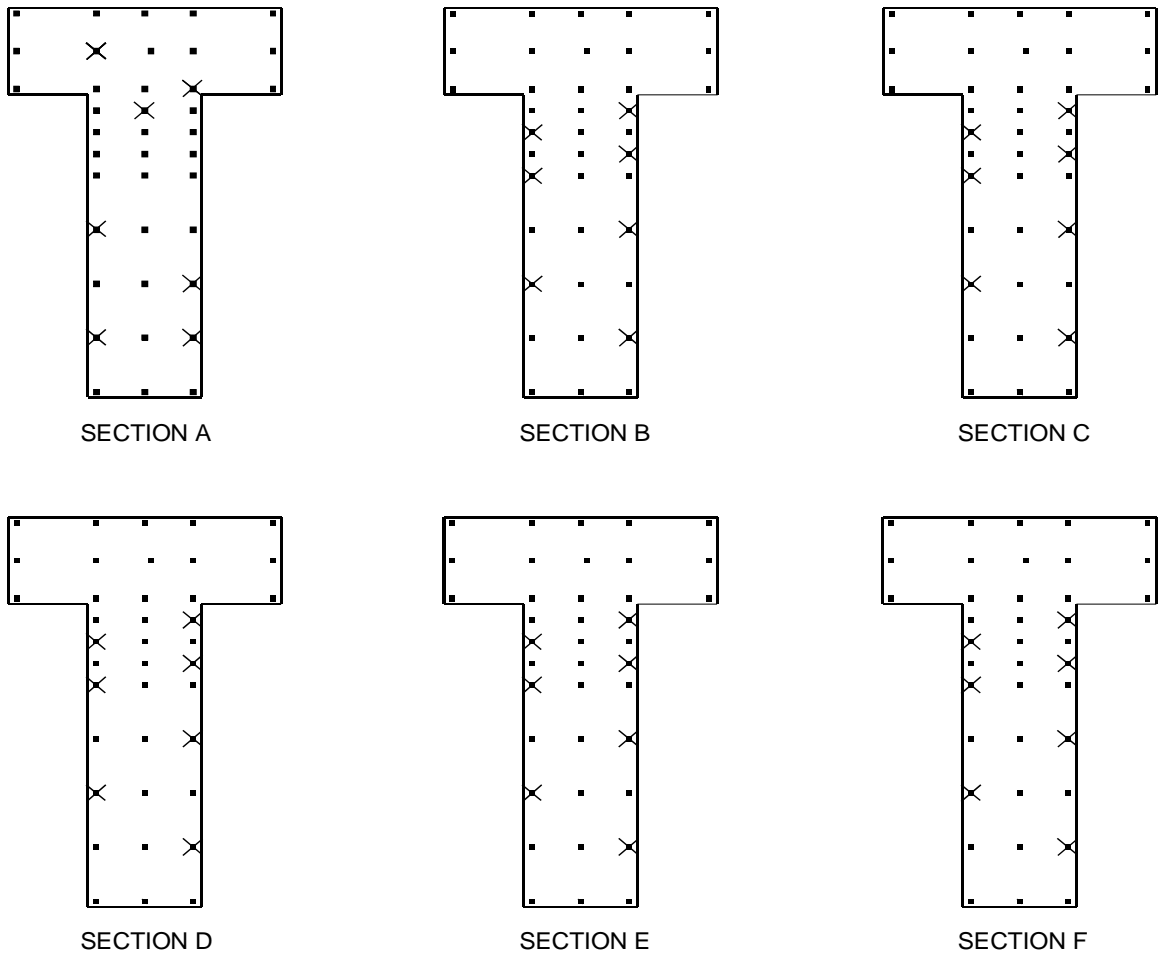


Figure 8-3. Thermocouples used at each section



Figure 8-4. Insulated heated segments

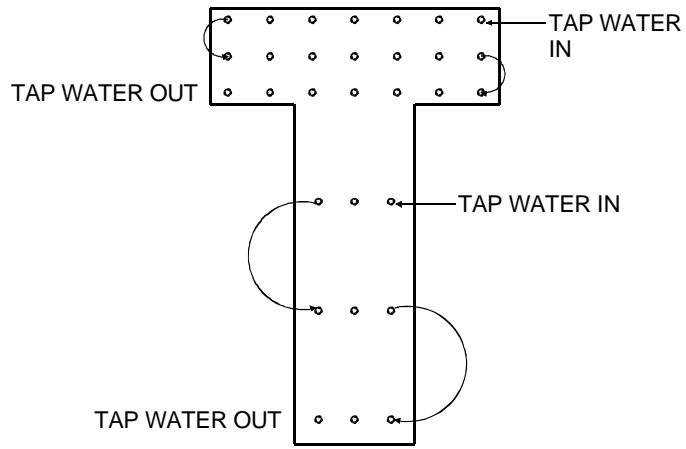


Figure 8-5. Piping configuration used to impose initial condition

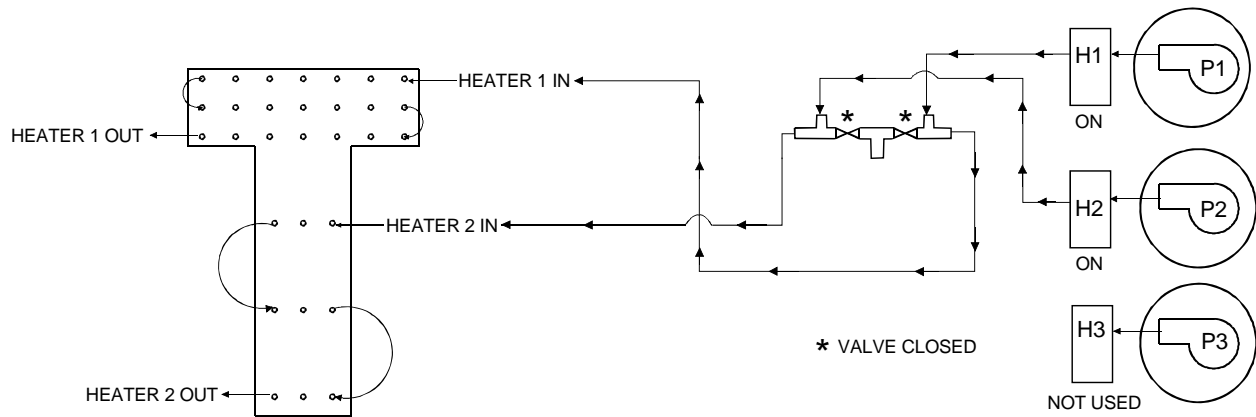


Figure 8-6. Piping configuration used to impose uniform temperature differential

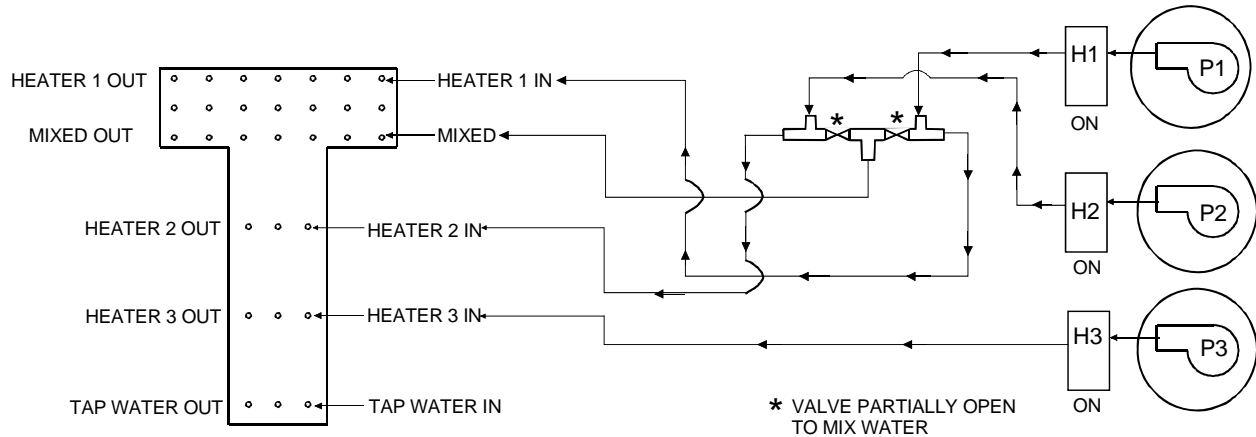


Figure 8-7. Piping configuration used to impose linear thermal gradient

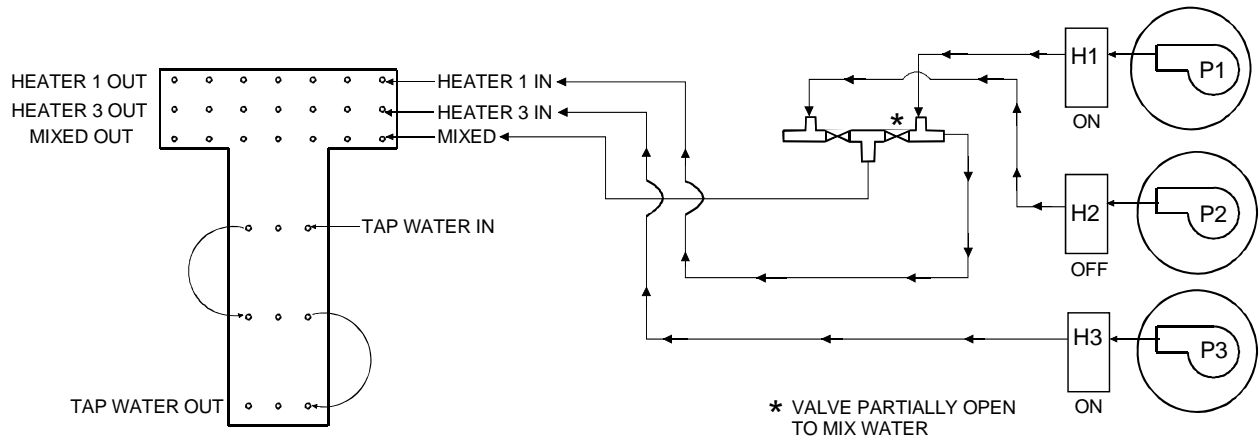


Figure 8-8. Piping configuration used to impose AASHTO nonlinear positive thermal gradient

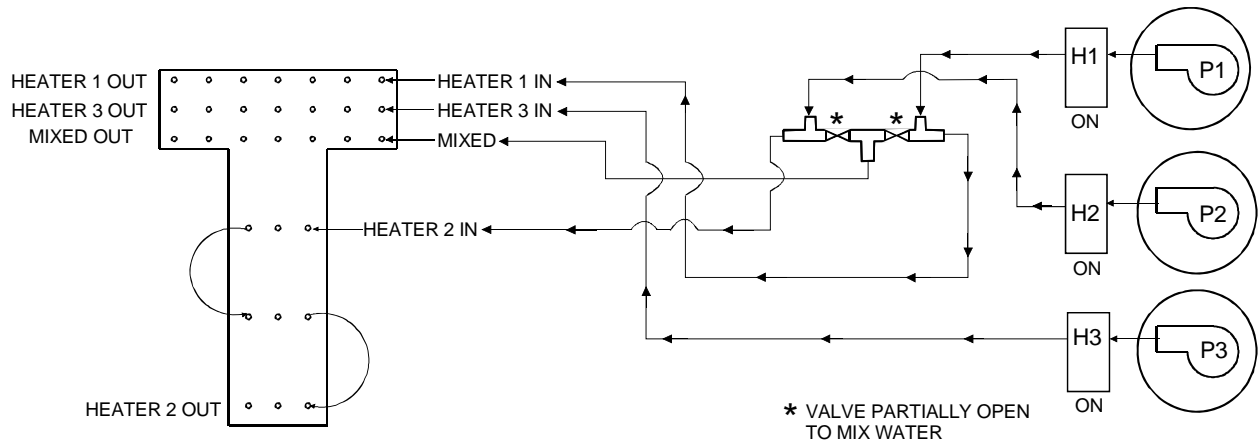


Figure 8-9. Piping configuration used to impose AASHTO nonlinear negative thermal gradient

CHAPTER 9
IN-SITU COEFFICIENT OF THERMAL EXPANSION

In-situ CTE tests were conducted to determine coefficients of thermal expansion that were representative of the composite behavior of the concrete segments, copper tubes, and thermocouple cages embedded in segments 2 and 3 of the laboratory test beam. The setup for the in-situ CTE tests is shown in Figure 9-1. The segment being tested was supported on two wooden blocks 6 in. away from the ends. LVDTs were placed vertically along the centerline of the cross section on both ends of the segment to record the elongation of the segment. Initially three LVDTs were used to record displacements at locations 0.5 in. below the top of the flange, at the centroid of the segment (21.3 in. from the bottom of the segment), and 0.5 in. above the bottom of the segment. Subsequently, with the acquisition of additional LVDTs, four and then five LVDTs were used in the testing. The three and four LVDT setups were used in tests conducted on Segment 2. The four LVDT setup was used in one test conducted on Segment 3. In the remaining tests conducted on Segment 3, the five LVDT setup was used.

Two non-stress inducing thermal profiles were imposed on the segment: a uniform temperature change of about 41 °F above the reference temperature (about 85 °F) of the segment, and a linear thermal gradient varying from 0 °F at the bottom of the web to +41 °F at the top of the flange. The uniform and linear thermal profiles were imposed using the piping setups in Figure 8-6 and Figure 8-7, respectively. The composite CTE of the segment was calculated as:

$$\Delta_{avg} = \frac{\int \delta_{total} dA_c}{A_c} \quad (9-1)$$

$$\epsilon_{avg} = \frac{\Delta_{avg}}{L} \quad (9-2)$$

$$TG_{avg} = \frac{\int T_{grad} dA_c}{A_c} \quad (9-3)$$

$$\alpha = \frac{\varepsilon_{avg}}{TG_{avg}} \quad (9-4)$$

where Δ_{avg} is the average axial elongation of the segment, ε_{avg} is the average engineering strain of the segment, TG_{avg} is the average temperature differential, α is the coefficient of thermal expansion, δ_{total} is the total measured axial elongation at the location of the LVDT, L is the length of the segment, T_{grad} is the temperature gradient/change imposed on the segment, and A_c is the cross sectional area of the segment.

It was expected that both uniform and linear temperature distributions would produce the same CTE values since neither involved nonlinearity of temperature profile, and since it was assumed that the segments had uniform distributions of moisture content.

A laboratory imposed uniform temperature change on Segment 2 and the corresponding measured end displacements are shown together with the target thermal profile and calculated longitudinal displacement in Figure 9-2 and Figure 9-3, respectively. A uniform temperature change imposed on Segment 3 and the corresponding measured end displacements are shown together with the target thermal profile and calculated longitudinal displacement in Figure 9-4 and Figure 9-5, respectively. Measured concrete temperatures after uniform profiles were imposed on segments 2 and 3 are shown in Figure 9-6 and Figure 9-7, respectively. Laboratory imposed thermal profiles were within 2% of the target profiles for both segments. In Figure 9-3 and Figure 9-5, calculated displacements were determined using CTEs determined from measured data and target temperature profiles. There was more variability in measured total displacements for Segment 3 (see Figure 9-5) about the calculated displacement than for Segment 2 (see Figure 9-3). This was partly because five LVDTs were used at each end of Segment 3 whereas only three LVDTs were used at each end of Segment 2. In addition, the

coefficient of variation of the temperature profile imposed on Segment 3 with respect to the target (1.9%) was higher than the coefficient of variation of the temperature profile imposed on Segment 2 (1.4%). The variability in measured displacements was also partially attributed to nonlinearities in the laboratory imposed thermal profiles and varying moisture contents throughout the volume of the segments.

It should be noted that in the AASHTO standard test method for determining the coefficient of thermal expansion of concrete (AASHTO TP 60-00) the influence of moisture content on CTE is eliminated by fully saturating the concrete test cylinders (and thus ensuring a uniform distribution of moisture in the test specimen). In the in-situ CTE tests, measured end displacements were higher at the ends where heated water entered the segments than at the ends where water exited the segments. The orientations of Segment 2 and Segment 3 together with the inlet and outlet of heated water during testing are shown in Figure 9-8 and Figure 9-9, respectively. Measured end displacements were higher on the West end of Segment 2 than on the East end of the segment (see Figure 9-3). For Segment 3 measured end displacements were higher on the East end than on the West end of the segment (see Figure 9-5). This was because prior to achieving a constant temperature profile longitudinally, the inlet sections of each segment experienced higher temperatures than the outlet sections, which led to higher measured elongations at the inlet ends than at the outlet ends of the segments.

A laboratory imposed linear temperature profile on Segment 2 and the corresponding measured end displacements are shown together with the target thermal profile and calculated longitudinal displacement in Figure 9-10 and Figure 9-11, respectively. A linear temperature change imposed on Segment 3 and the corresponding measured end displacements are shown together with the target thermal profile and calculated longitudinal displacement in Figure 9-12

and Figure 9-13, respectively. Measured concrete temperatures after linear profiles were imposed on segments 2 and 3 are shown in Figure 9-14 and Figure 9-15, respectively. Laboratory imposed linear temperature gradients were within 2% of the target temperature profile for both segments. The coefficients of variation of the laboratory imposed thermal gradients with respect to the target gradients were 3.7% and 4% for Segment 2 and Segment 3, respectively. This is in agreement with the closer match between calculated and measured total displacements for Segment 2 (see Figure 9-11) than for Segment 3 (see Figure 9-13). In calculating the coefficient of variation of laboratory imposed linear gradients, the standard error about the target gradient was used in place of the standard deviation about the mean. This explains the higher coefficients of variation for laboratory imposed linear temperature gradients compared with laboratory imposed uniform temperature changes. In Figure 9-11, measured displacements at the West end of Segment 2 were lower than measured displacements at the East end in the lower half of the segment, which was expected since the inlet of heated water to the segment was at the East end. In the upper half of the segment, however, measured displacements were higher at the West end than at the East end of the segment. This was because the target temperature at the top of the flange was exceeded in imposing the linear thermal gradient. In an attempt to cool the top flange to the target temperature it was slightly overcooled, leading to lower temperatures and corresponding lower elongations at sections close to the inlet (East end) of water to the segment than at sections close to the outlet (West end) of water from the segment. For Segment 3, measured displacements were higher at the East end than at the West end of the segment. This was consistent with higher temperatures developing at the inlet of heated water to the segment (East end) than at the outlet of heated water from the segment (West end) prior to achieving a constant thermal profile longitudinally.

The coefficients of thermal expansion determined from in-situ tests and the AASHTO TP 60-00 procedure, which was discussed in Chapter 5, are summarized in Table 9-1. In-situ CTEs determined with linear thermal gradients were generally higher than in-situ CTEs determined with uniform temperature distributions. The slight increase in CTE (an average of about 8%) associated with linear thermal gradients was attributed to the influence of copper tubes on the longitudinal expansion of the concrete segments and non-uniform moisture contents of the segments. The influence of thermocouple positioning steel cages on the longitudinal expansion of the segments was deemed insignificant since they were placed transversely in the segments.

The CTE for Segment 3, determined using the uniform temperature profile, was equal to the CTE of the segment determined using the AASHTO standard method (AASHTO TP 60-00). It is, however, likely that a repeat of the in-situ test would have yielded a slightly different CTE for the segment. In the AASHTO procedure, the tolerance within which two CTEs determined from the same cycle can be averaged is $0.5E-6/^{\circ}F$. The differences between CTEs determined with the linear profile and CTEs determined with the uniform temperature distribution were $0.7E-6/^{\circ}F$ and $0.5E-6/^{\circ}F$ for segments 2 and 3, respectively. Since the in-situ CTEs were determined from different tests using different temperature distributions, these differences were deemed acceptable. The arithmetic average of the CTEs of each segment determined using the procedures discussed above was used in predicting thermal stresses and strains later in this study.

Table 9-1. Experimentally determined coefficients of thermal expansion

	Uniform Temp. Distribution (In-situ)	Linear Thermal Gradient (In-situ)	AASHTO TP 60-00 Method
Segment 2	7.3E-6/°F	8.0E-6/°F	N/A
Segment 3	7.8E-6/°F	8.3E-6/°F	7.8E-6/°F

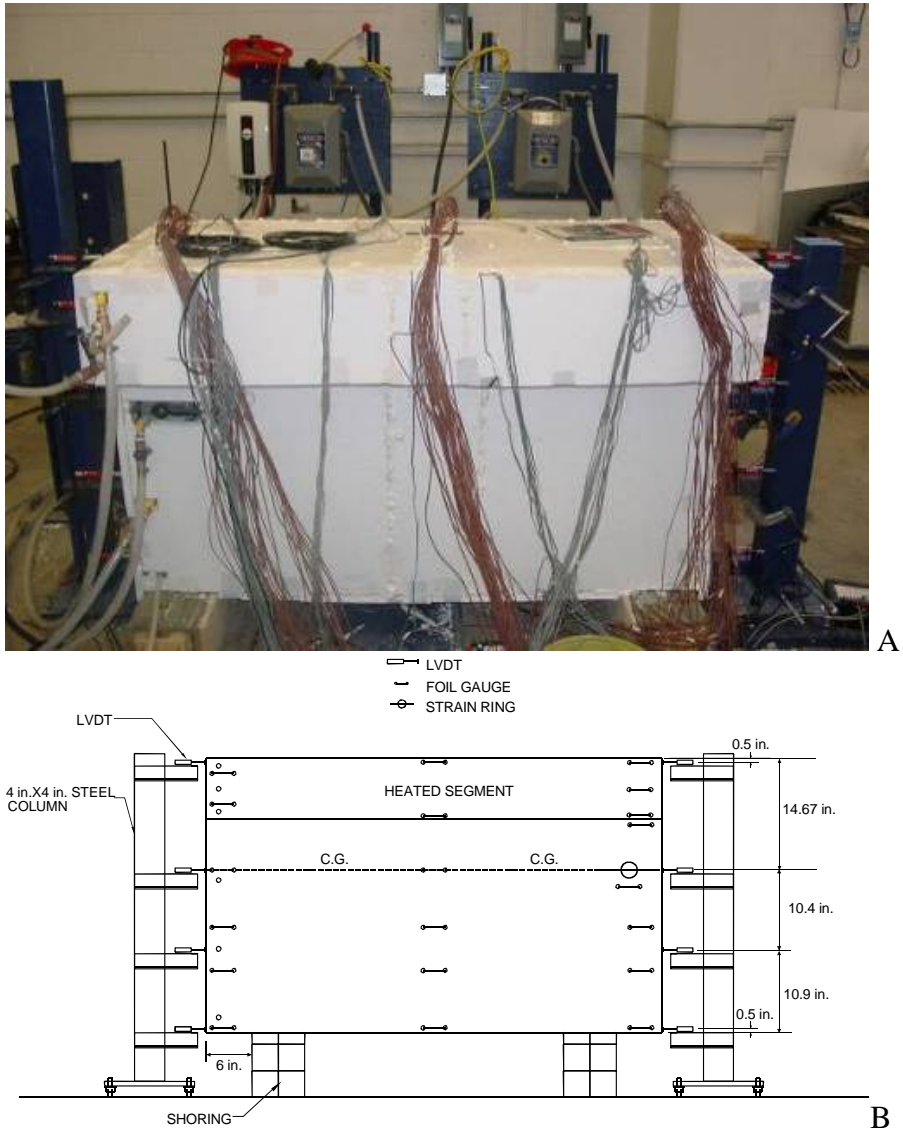


Figure 9-1. Typical in-situ CTE test setup; A) Photograph. B) Details.

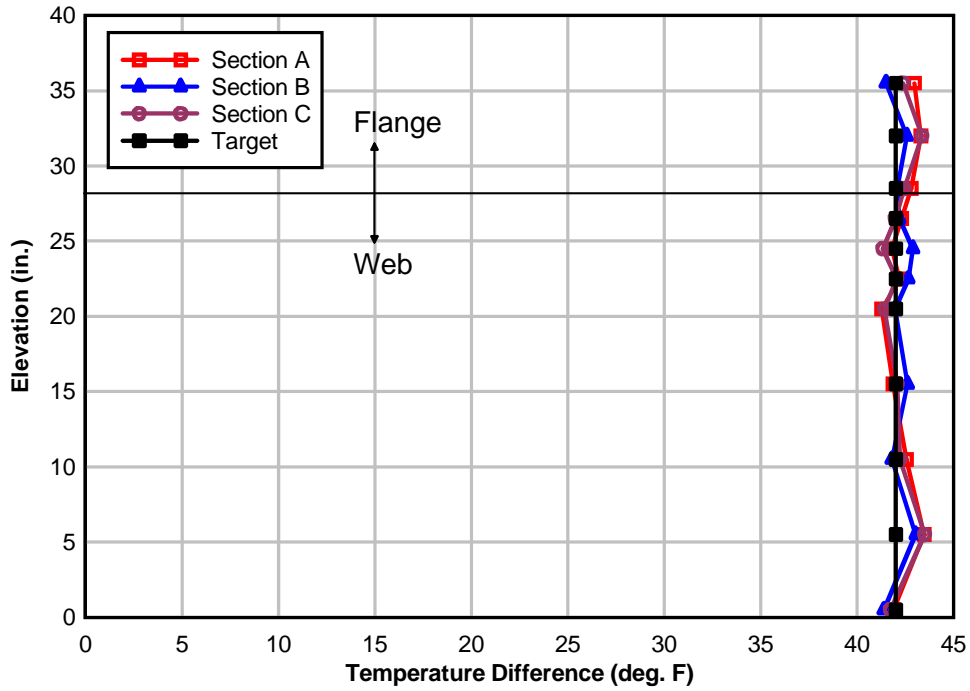


Figure 9-2. Uniform temperature change imposed on Segment 2

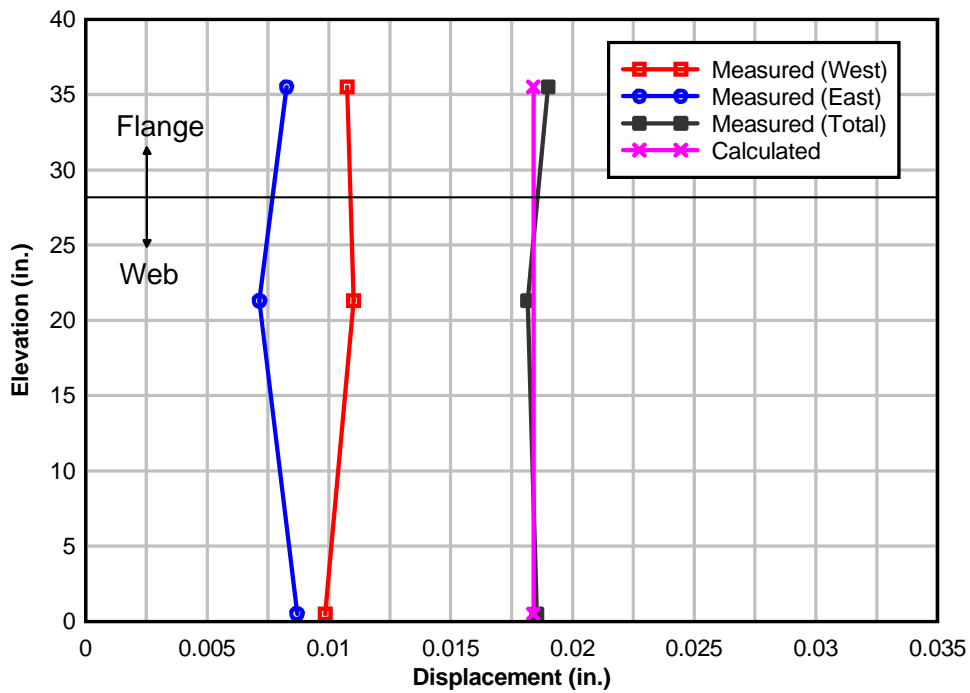


Figure 9-3. Measured end-displacements due to uniform temperature change imposed on Segment 2

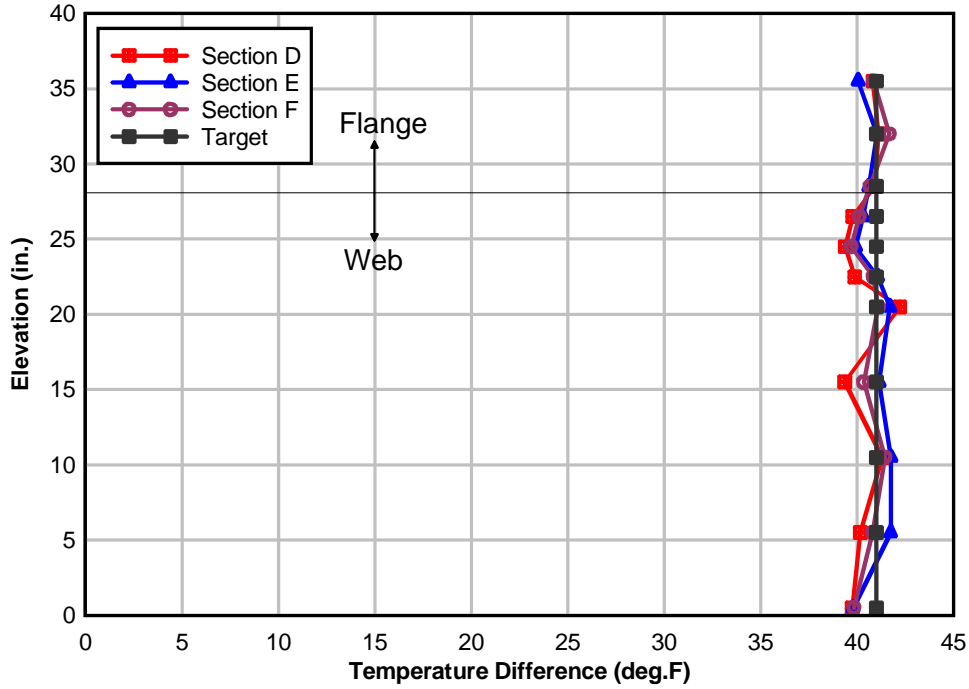


Figure 9-4. Uniform temperature change imposed on Segment 3

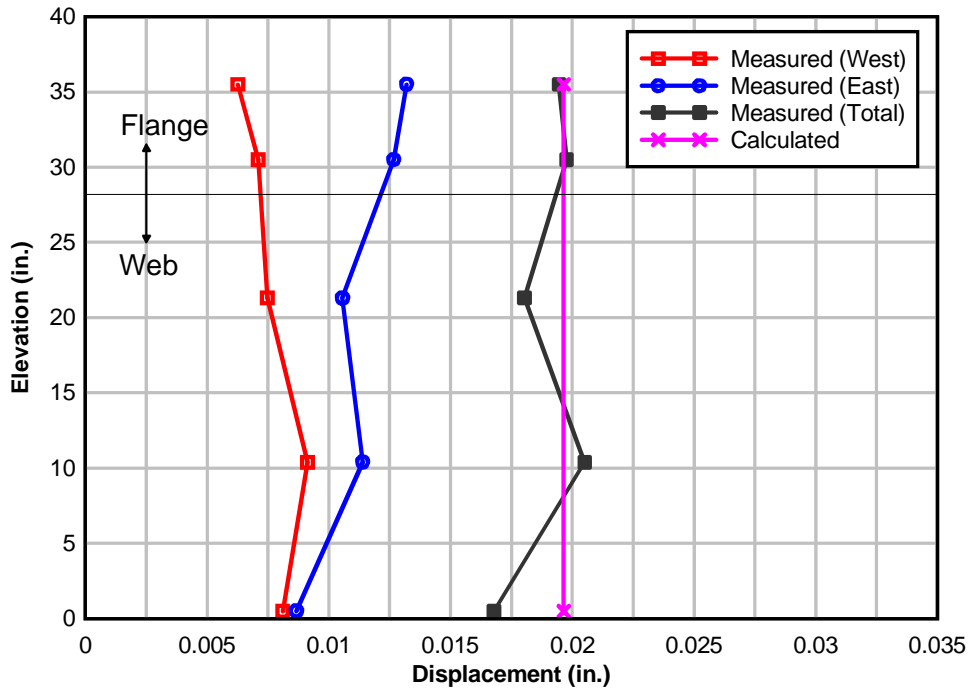


Figure 9-5. Measured end-displacements due to uniform temperature change imposed on Segment 3

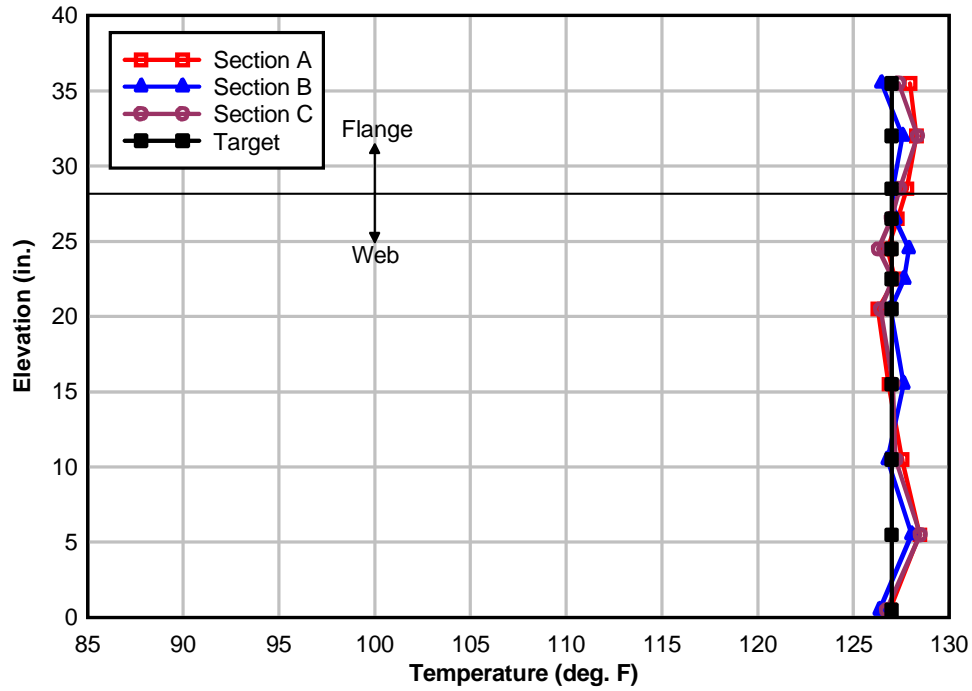


Figure 9-6. Measured concrete temperatures in Segment 2 (uniform profile)

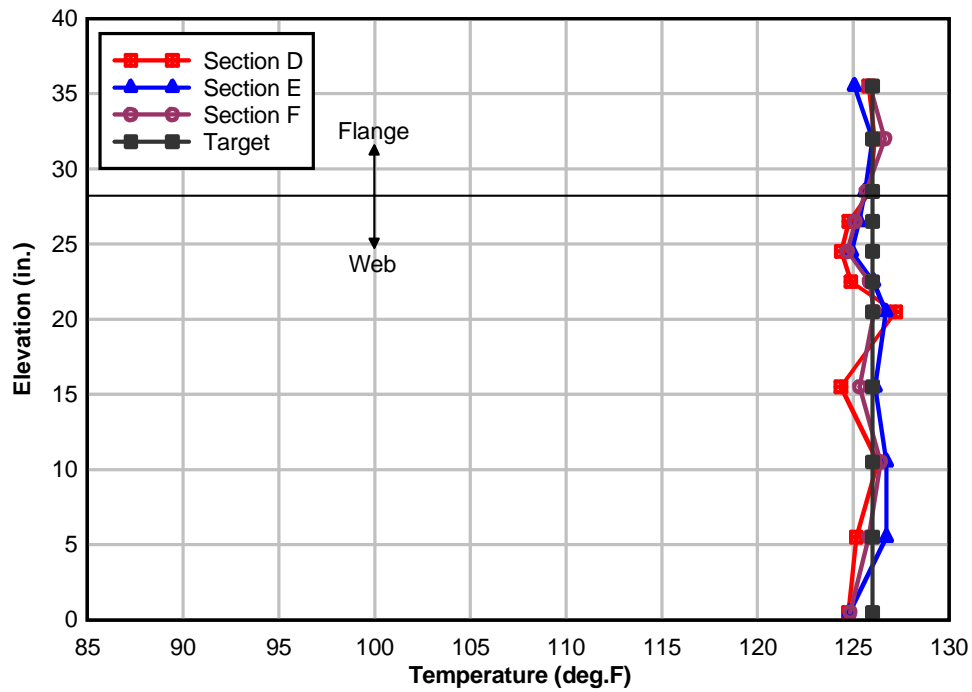


Figure 9-7. Measured concrete temperatures in Segment 3 (uniform profile)

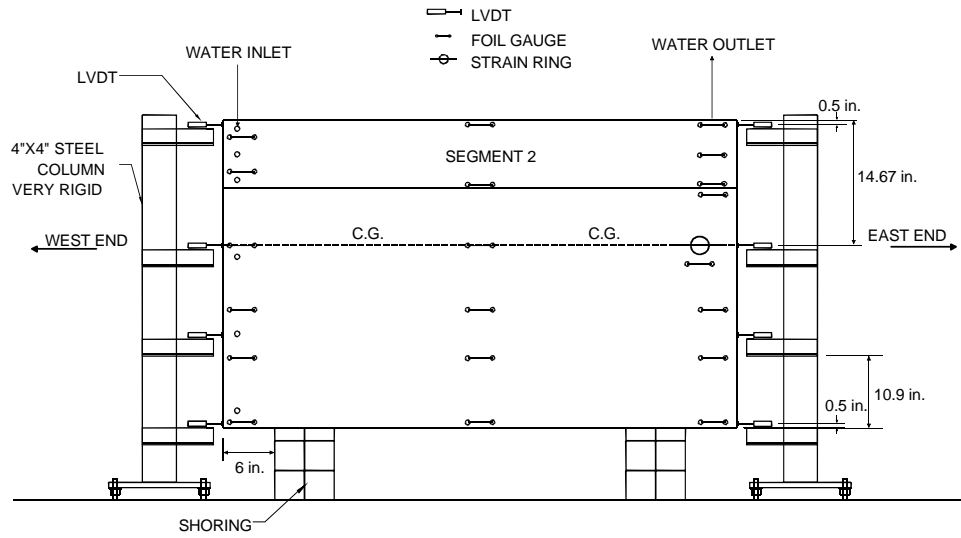


Figure 9-8. Orientation of Segment 2 during testing (South elevation)

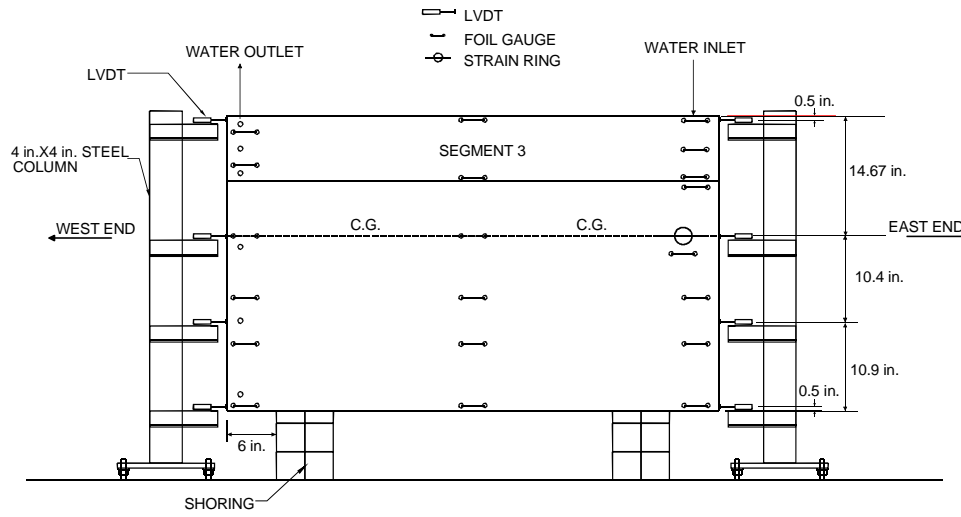


Figure 9-9. Orientation of Segment 3 during testing (South elevation)

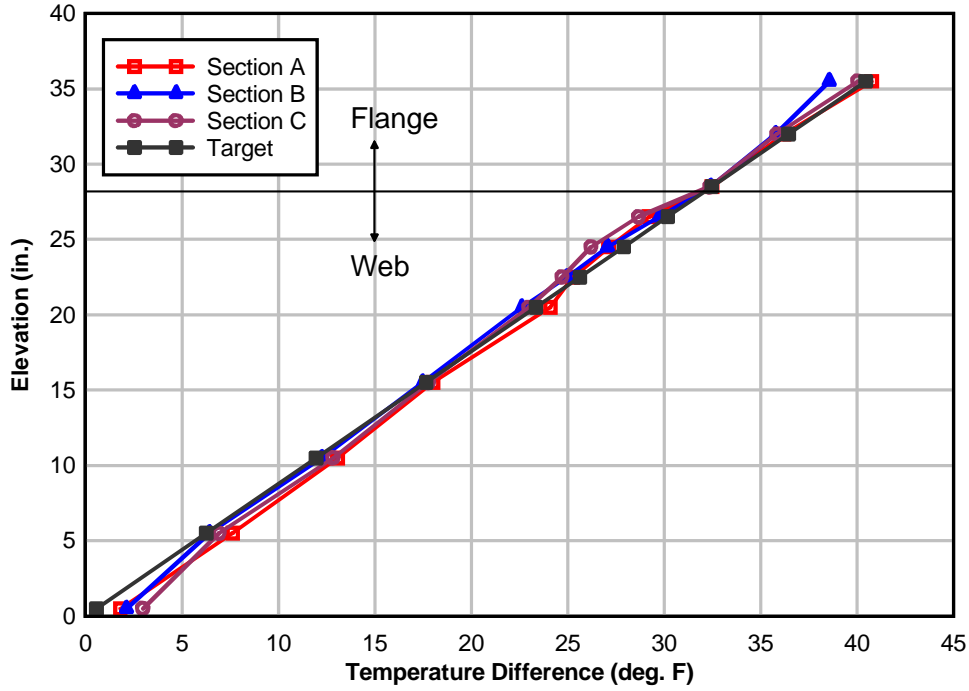


Figure 9-10. Linear temperature gradient imposed on Segment 2

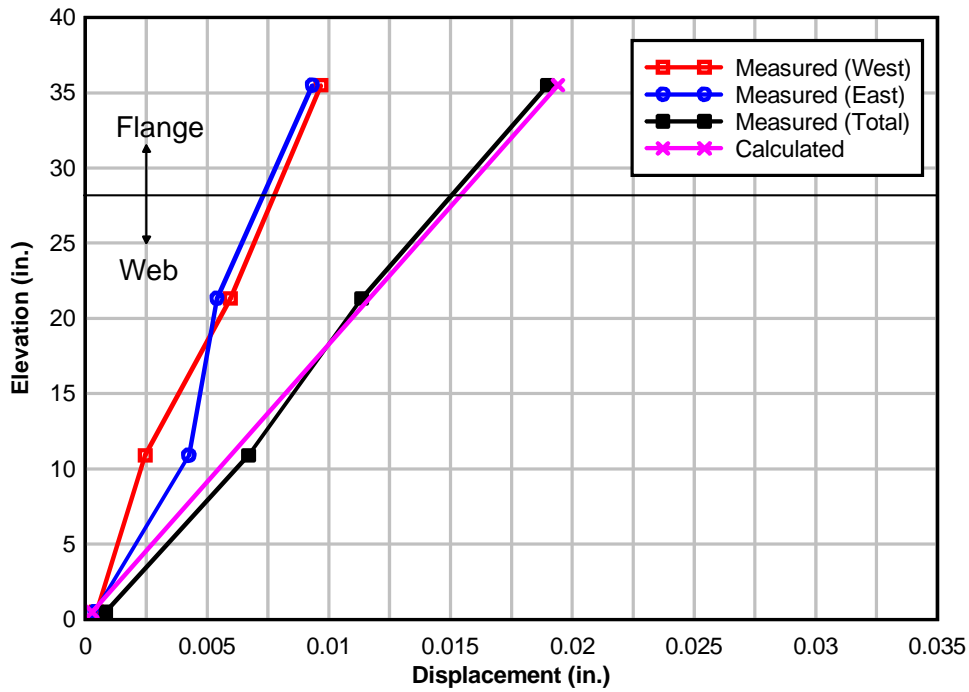


Figure 9-11. Measured displacements due to linear thermal gradient imposed on Segment 2

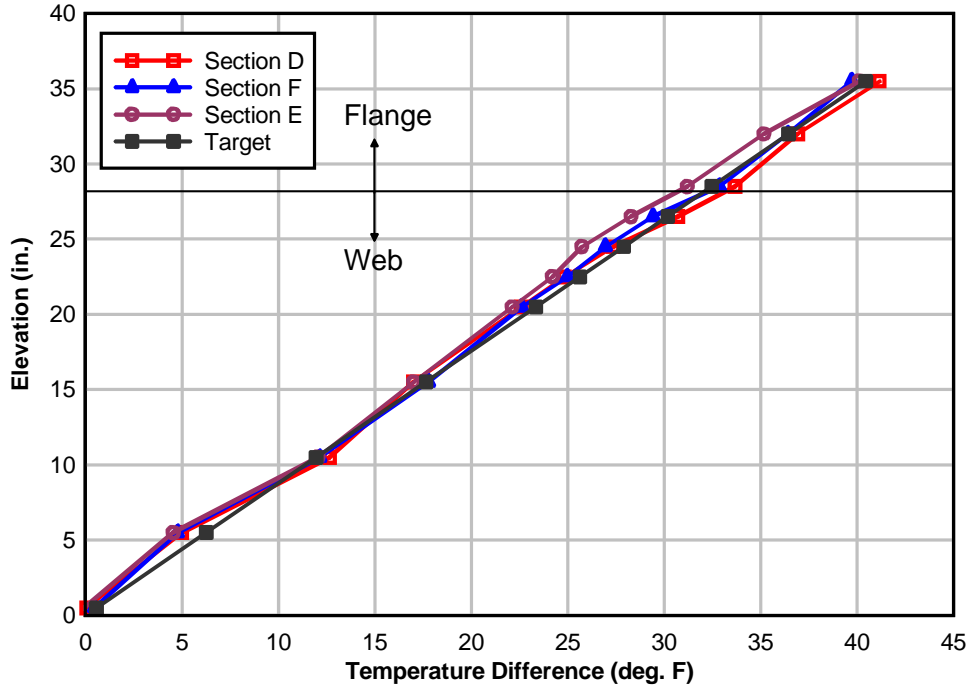


Figure 9-12. Linear thermal gradient imposed on Segment 3

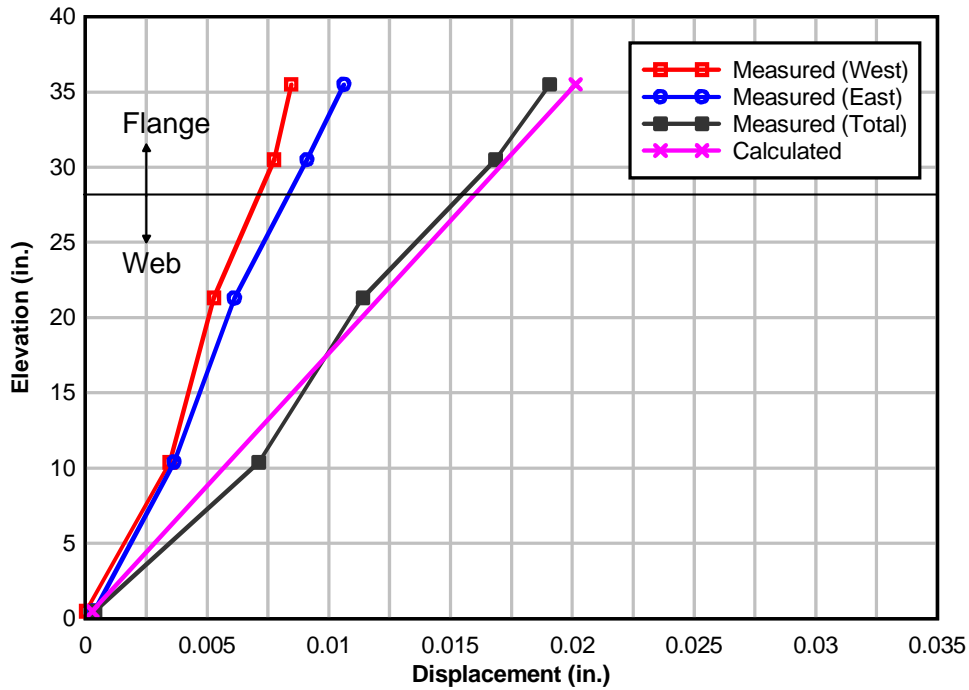


Figure 9-13. Measured displacements due to linear thermal gradient on Segment 3

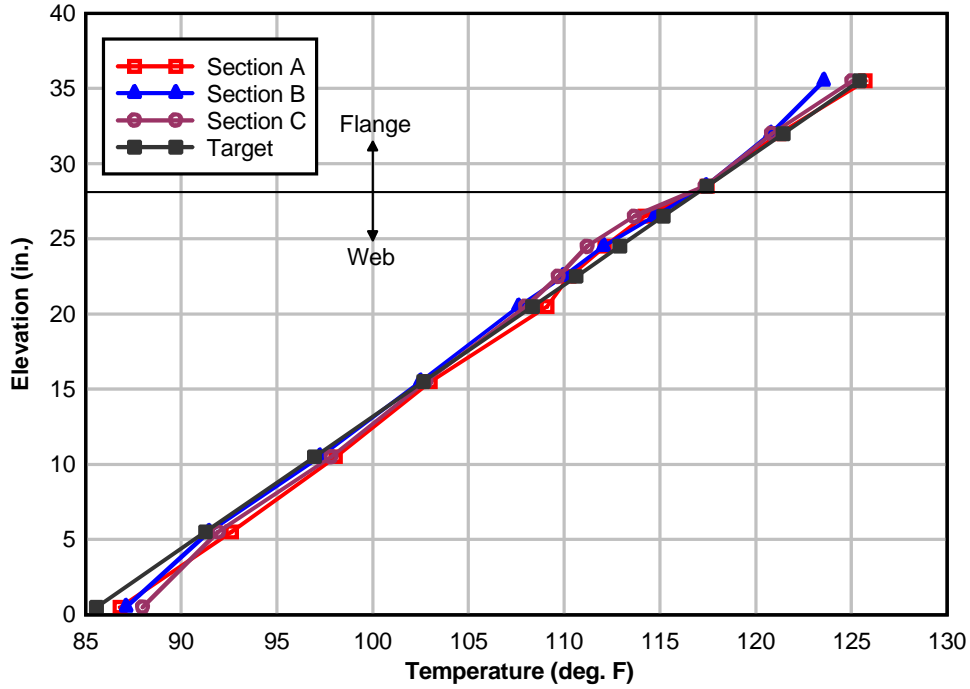


Figure 9-14. Measured concrete temperatures in Segment 2 (linear profile)

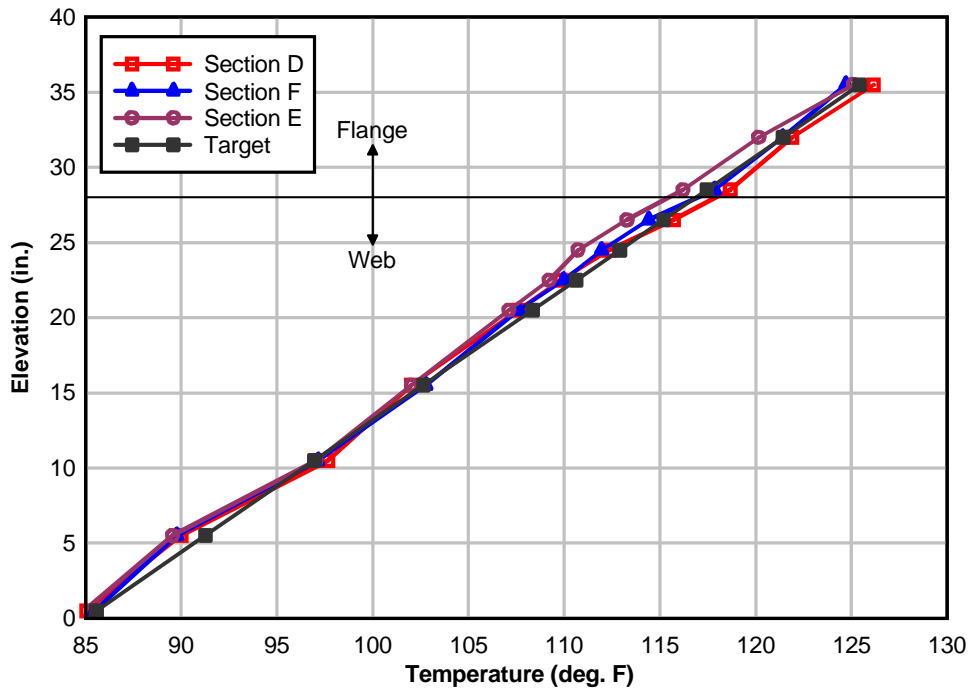


Figure 9-15. Measured concrete temperatures in Segment 3 (linear profile)

CHAPTER 10 RESULTS – PRESTRESSING

In this chapter strains recorded during prestressing of the laboratory segmental beam are presented and discussed. The four segments of the beam were supported on wooden blocks as shown in Figure 10-1 during prestressing. This support system was changed to that shown in Figure 10-2 prior to the beginning of mechanical and thermal load tests on the laboratory beam. Labels assigned to the DYWIDAG post-tensioning bars and the design eccentricities of the bars from the centroid of the beam were presented in Chapter 5. They are duplicated in Figure 10-3 for convenience. Final forces in the prestress bars and measured horizontal eccentricities immediately after tensioning are given in Table 10-1. The vertical eccentricity of the four-bar group was 1.5 in. below the centroid of the beam.

Concrete strains near (joint J2) were continuously recorded as the beam was prestressed. The strain data collected during prestressing provided important information regarding the distribution of strains at the joint. This information was vital in interpreting data collected during later mechanical load tests in which the joint was slowly opened to relieve stresses due to the initial pre-compression and self-weight of the beam. The locations of strain gauges on the beam can be found in Chapter 6.

Figure 10-4 and Figure 10-5 show the increase in strain at joint J2 on the North side of the beam. Figure 10-6 and Figure 10-7 show the strains at the same joint on the South side and Figure 10-8 shows the strains on top of the top flange. Also included in Figure 10-4 through Figure 10-8 are calculated strains at the top flange at joint J2. Strains were calculated using laboratory determined concrete material properties (e.g. elastic modulus) and measured prestress forces. Gaps, if any, at joint J2 prior to prestressing were neglected in the calculations. In these figures negative strains indicate compression. The top two bars, which were located above the

centroid of the beam, were tensioned first (up to a total prestress of about 50 kips). As shown in Figure 10-8 the top flange strain gauges detected very little strain until the prestress force was between 50 kips and 125 kips. One explanation for this behavior is differential shrinkage of concrete at the edges of the beam segments. As Figure 10-9, shows the top surfaces of the segments were exposed to the laboratory environment after segment casting. It is likely that shrinkage was greater in the exposed portion of the top flange than in other surfaces which remained covered during curing. It is believed that this differential shrinkage led to a narrow gap between the top flanges of segments 2 and 3. Consequently, no strain was detected until sufficient prestress force had been applied to close the gap.

Differential shrinkage is also believed to be the reason for the systematically lower strains measured at the top flange compared with calculated strains (see Figure 10-8). This may have been due to the assumption in the calculations, that contact surfaces at joint J2 were smooth and in full contact (with no gaps). Calculated strains at the top flange close to joint J2 were higher than measured strains at the top flange for all prestress levels. The same was not the case for measured strains close to the top flange on the sides of the joint (see Figure 10-4 through Figure 10-7). Comparison of data from gauges on the sides of the joint with calculated top flange strains was more representative of expected behavior. This was because the 1.5 in. vertical eccentricity in prestressing was expected to lead to the development of lower compressive strains on top of the flange than at lower elevations.

Measured concrete strains through the depth of the beam segments near joint J2 are shown in Figure 10-10. These readings were taken immediately after prestressing was completed. Also shown in the plot are calculated strain profiles determined with the measured prestress forces and eccentricities (horizontal as well as vertical) shown in Table 10-1. Two observations can be

made when comparing the measured and calculated strains. The first is that strains vary considerably with depth. The other is that the average measured strains on the North side are greater in magnitude than those on the South side with calculated strains along the vertical line of symmetry of the beam between the two.

Differences in the average measured strains on the North and South sides of the segments can be attributed to the unequal total prestress forces on the North (190.4 kips) and South (181.6 kips) sides of the beam, and the 0.5 in. net horizontal eccentricity in prestressing (see Figure 10-3 and Table 10-1). As Figure 10-10 shows, calculated strains on the North and South sides of joint J2 determined with measured prestress forces and measured horizontal and vertical eccentricities were higher on the North side than on the South side of the joint. It was explained in Chapter 5 that the goal of applying an equal prestress force to each bar was not achieved because the prestress anchorage system prevented independent post-tensioning of the DYWIDAG bars. The 0.5 in. net horizontal eccentricity was most likely the result of movement of the suspended post-tensioning anchorage system as the beam was prestressed. The moment due to the unintended horizontal eccentricity caused the development of compressive strains on the North side and tensile strains on the South side of the vertical axis of the beam. This moment, together with the moment developed as a result of the inequality in the total prestress on the North and South sides of the beam, led to the development of lower magnitude strains on the South side of the beam compared to the North side.

A likely explanation for the variation in measured strains through the depth of the segments is an imperfect fit (segment-to-segment contact) at joint J2. This could have occurred during the match-casting process or during positioning of the segments for prestressing. An imperfect fit would lead to data from the strain gauges being influenced by stress concentrations

in the surface fibers of the beam segments. The unusually high strains measured on the North side of Segment 3 from strain gauges located 1.1 in. and 21.3 in. from the bottom of the segment (see Figure 10-10) might have been due to localized effects at those points on the segment. The exact causes of the high measured strains at these locations are unknown, however, at about 7% of the total prestress force the strain gauges designated S3-N-S-02-1.1 and S3-N-S-3.6-21.3 (see Figure 10-5) had registered about 36% and 55% of the respective total measured strains at their locations. Except for the two high strain points in the profile of Segment 3 on the North side, strain profiles on identical sides of segments 2 and 3 compared quite well.

Strains measured transversely across the width of the flanges of segments 2 and 3 near joint J2 are shown in Figure 10-11. Also shown in the figure are calculated strains that take into account the vertical eccentricity in prestressing only (shown as *average calculated* strains in the legend) and calculated strains that take into account both vertical and net horizontal eccentricities in prestressing (shown as *calculated* strains in the legend). Data in Figure 10-11 were collected from three strain gauges on Segment 3 and two strain gauges on Segment 2. The presence of LVDT mounts on Segment 2 prevented the placement of a strain gauge close to the center of the flange of that segment. In an ideal situation, strains measured across the width of the flanges near joint J2 should be uniform (see the *average calculated* strains in Figure 10-11). Because of the measured net horizontal eccentricity in prestressing, the distribution of measured strains across the width of the flange was expected to look like the *calculated* strains in the figure. A possible reason for the nonlinear distribution of measured strains across the width of the flange is a lack of a full contact fit at the joint.

The nonlinearities in the measured strains were not expected to affect the quantification of thermal stresses caused by the AASHTO nonlinear thermal gradients. As discussed in Chapter 7,

stresses due to prestress, self-weight, and any additional forces that may have been induced at joint J2 when the support system of the beam was changed (see Figure 10-1 and Figure 10-2), were taken as reference stresses. These stresses were then relieved when joint J2 was opened, and therefore did not directly enter into calculations of thermally induced stresses.

Partial losses in prestressing force were initially measured over a period of approximately three weeks and are plotted for each bar in Figure 10-12. The percentage change in total prestress with time is shown in Figure 10-13. Fluctuations about the general downward trend in Figure 10-12 and Figure 10-13 were the result of daily temperature variations. Prestress levels were also checked before and after each mechanical and thermal load test conducted after the initial monitoring period. The maximum percentage reduction in total prestress over the course of the 4-month period during which tests were conducted on the laboratory segmental beam was about 3.5% of the initial total prestress.

Table 10-1. Prestress magnitudes and horizontal eccentricities

Bar Designation	Force (kips)	Horizontal Eccentricity Designation	Horizontal Eccentricity (in.)
P1	97.2	e1	8.6
P2	89.2	e2	8.1
P3	93.2	e3	8.6
P4	92.4	e4	8.1

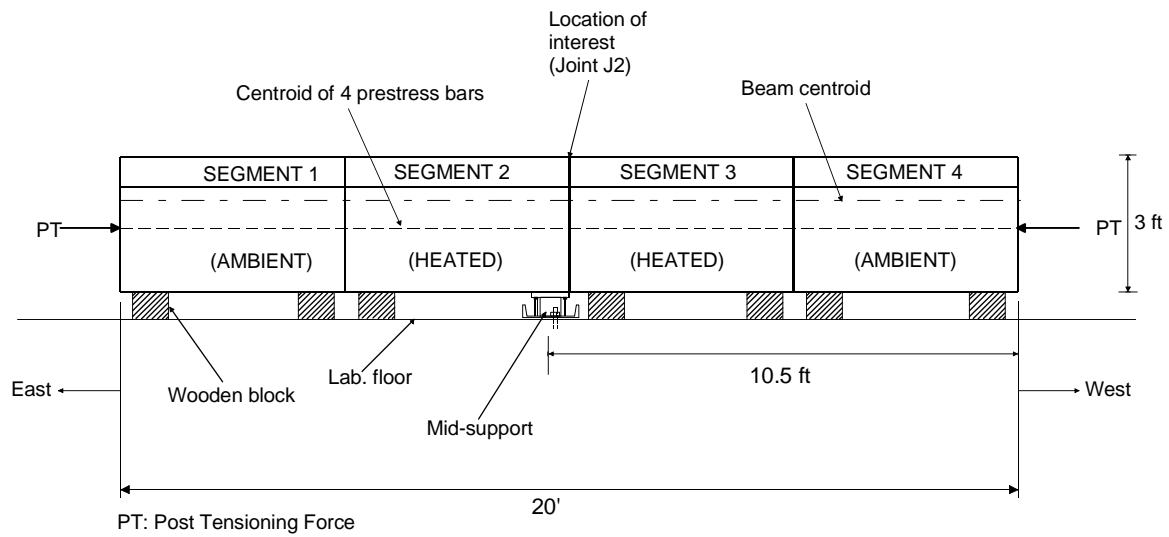


Figure 10-1. Segment support during prestressing

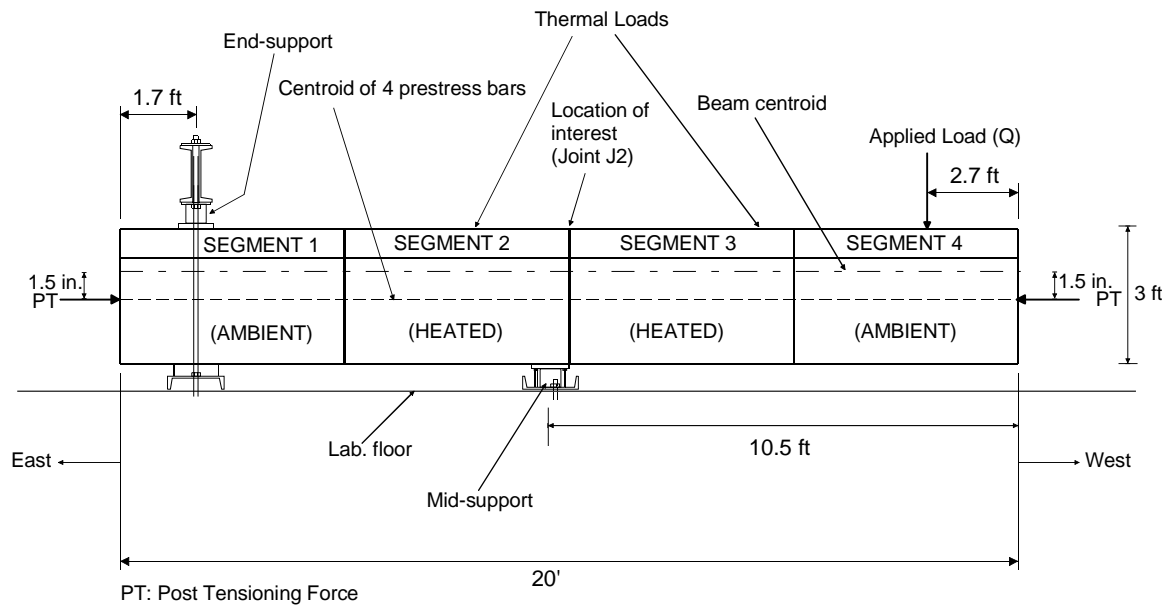


Figure 10-2. Beam support for mechanical and thermal load tests

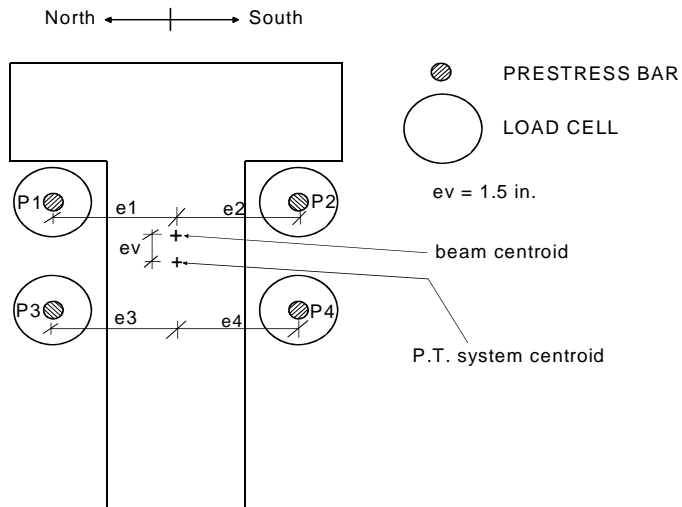


Figure 10-3. Post-tensioning bar designations and eccentricities

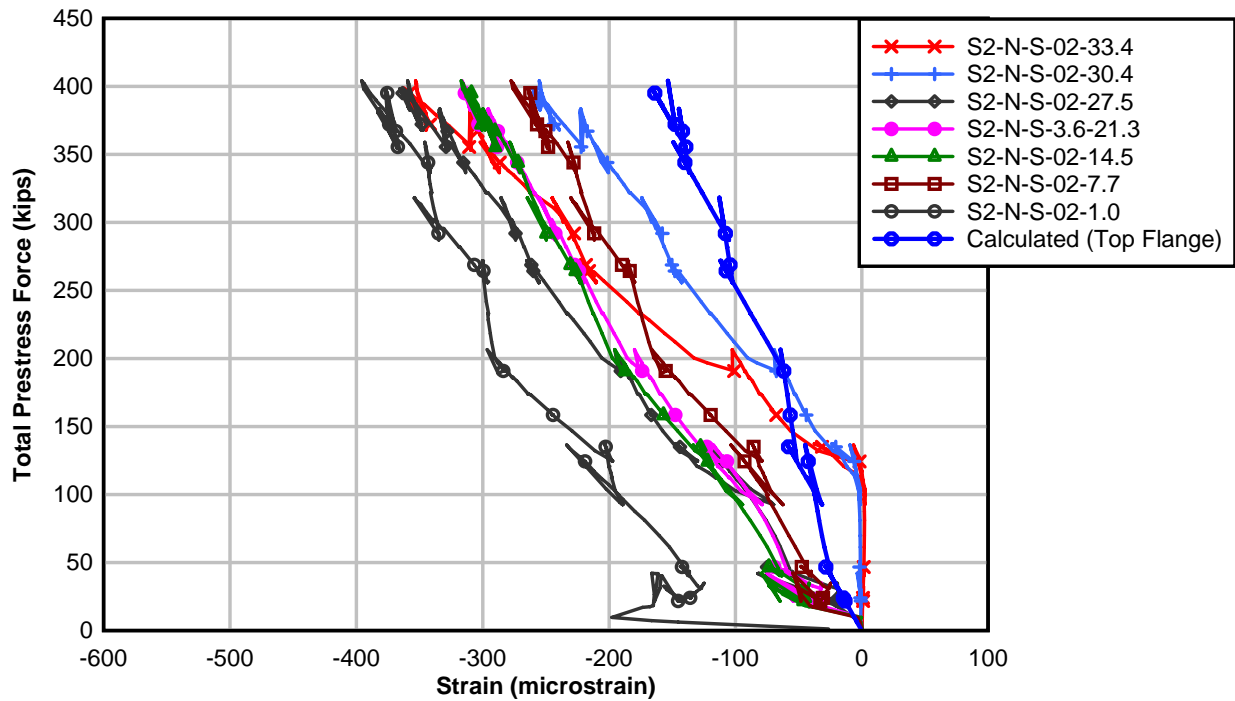


Figure 10-4. Measured concrete strains near joint J2 due to prestress (Segment 2, North)

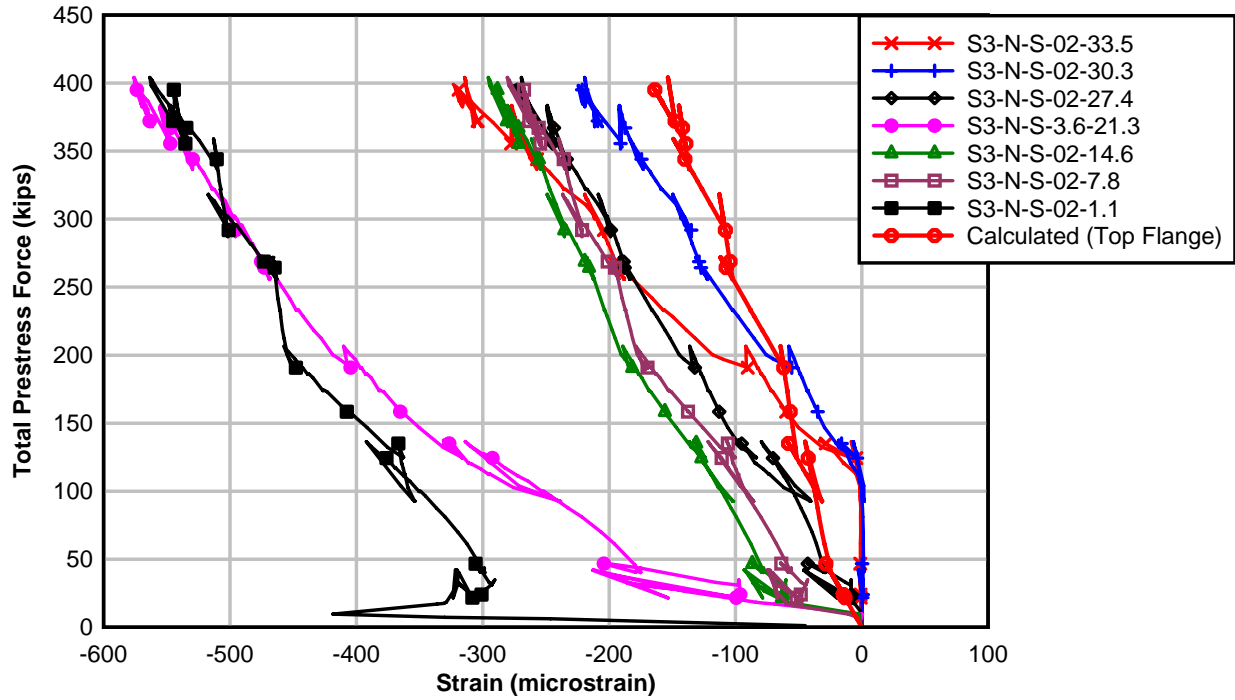


Figure 10-5. Measured concrete strains near joint J2 due to prestress (Segment 3, North)

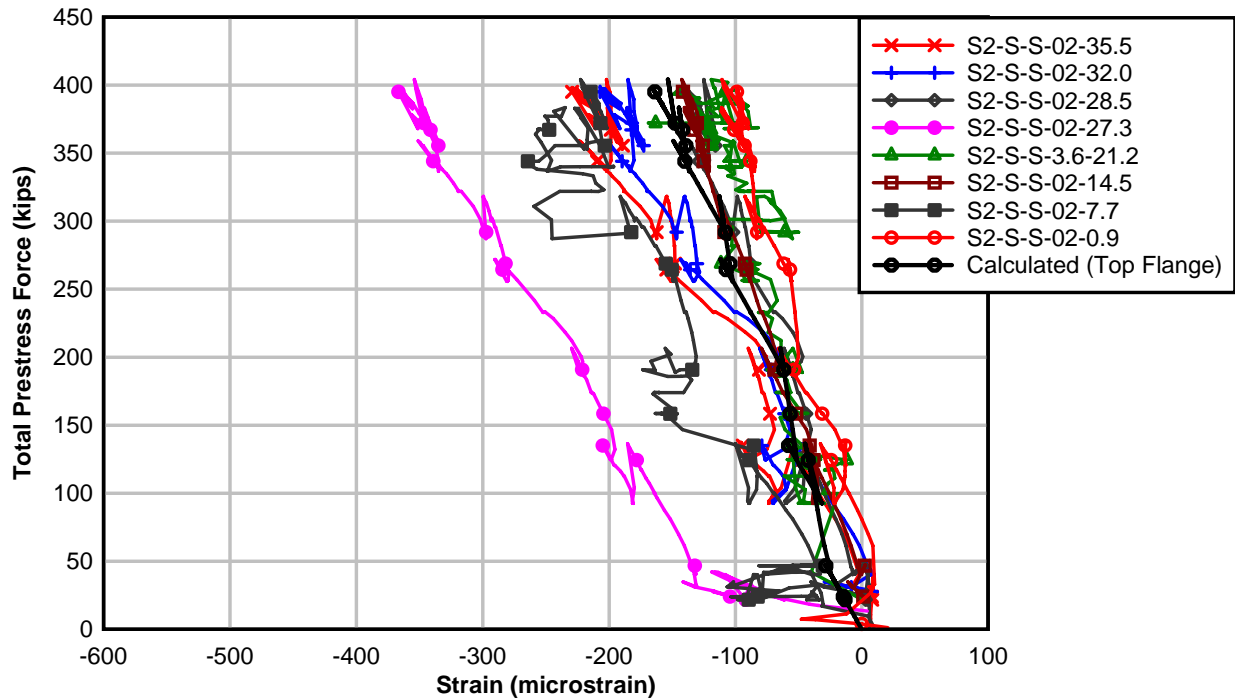


Figure 10-6. Measured concrete strains near joint J2 due to prestress (Segment 2, South)

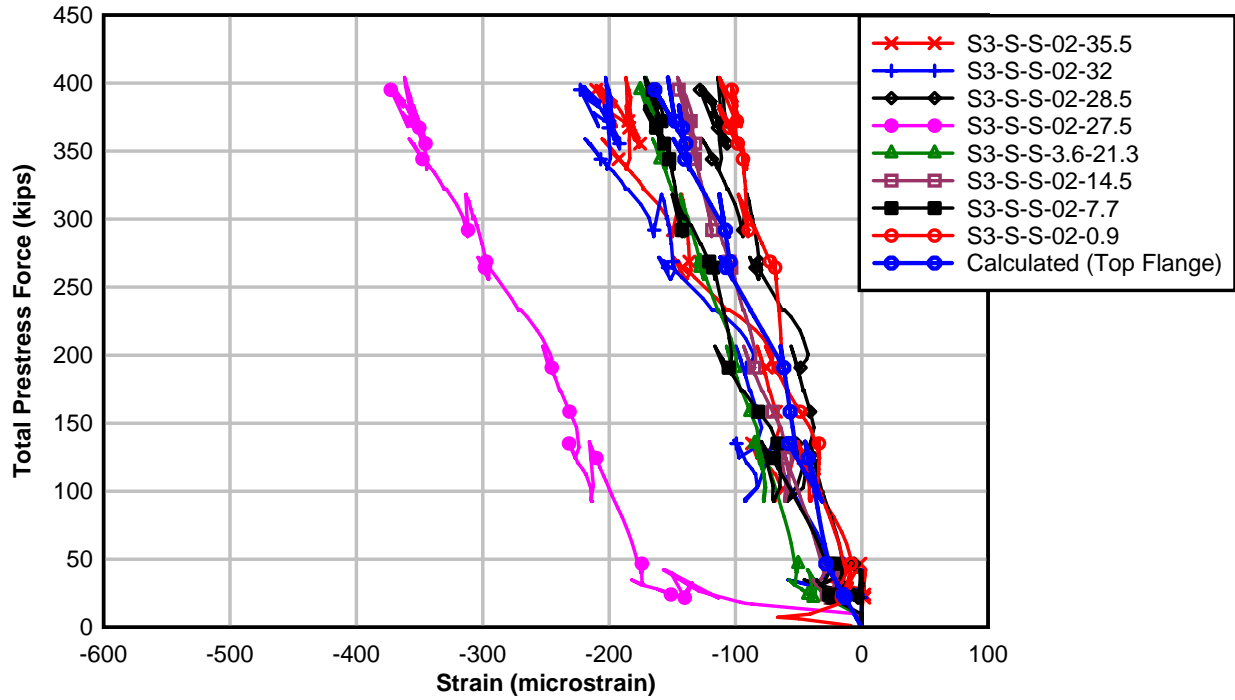


Figure 10-7. Measured concrete strains near joint J2 due to prestress (Segment 3, South)

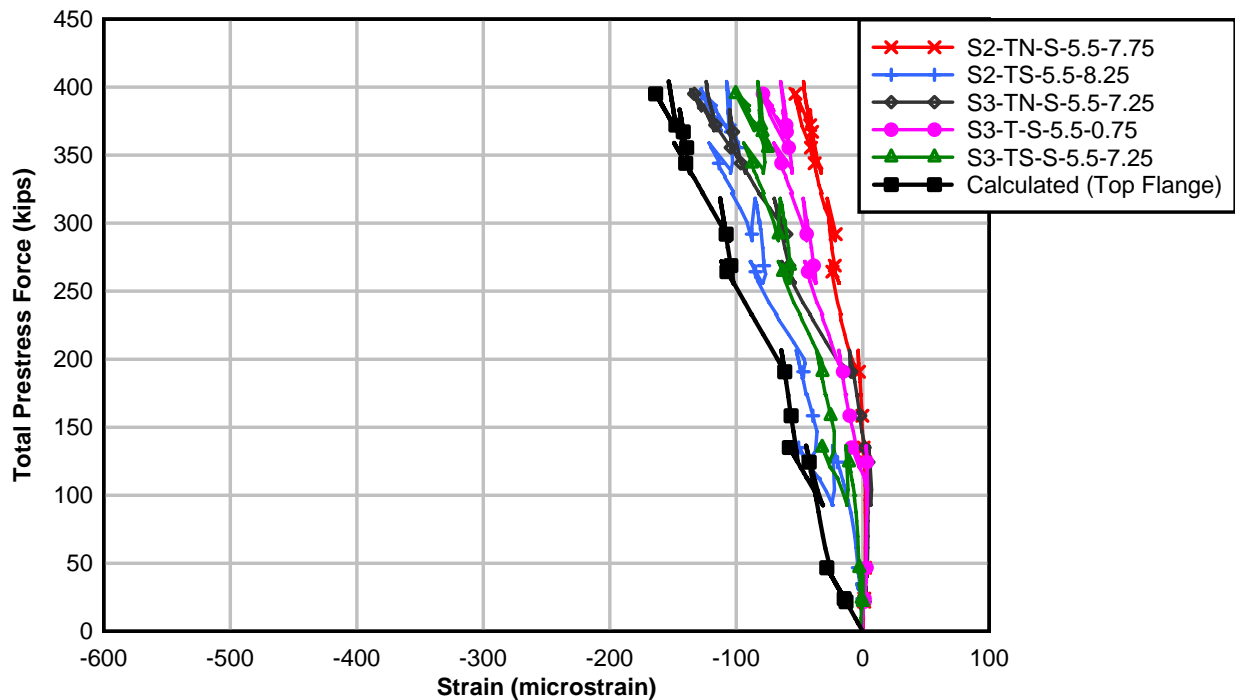


Figure 10-8. Measured concrete strains near joint J2 due to prestress (Top flange)

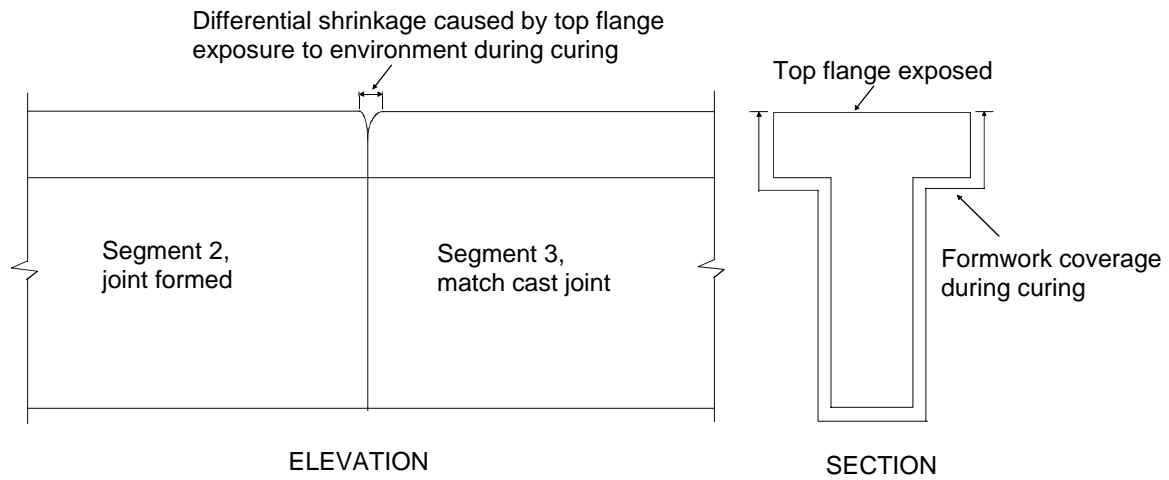


Figure 10-9. Effect of differential shrinkage on top flange strains

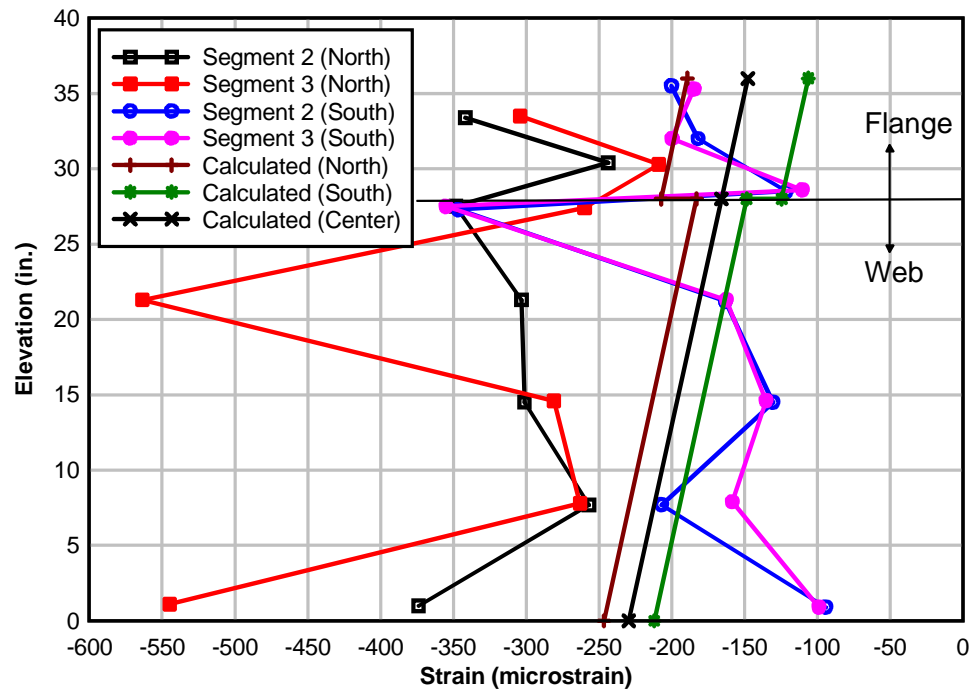


Figure 10-10. Measured concrete strains due to prestress through depth of segments near joint J2

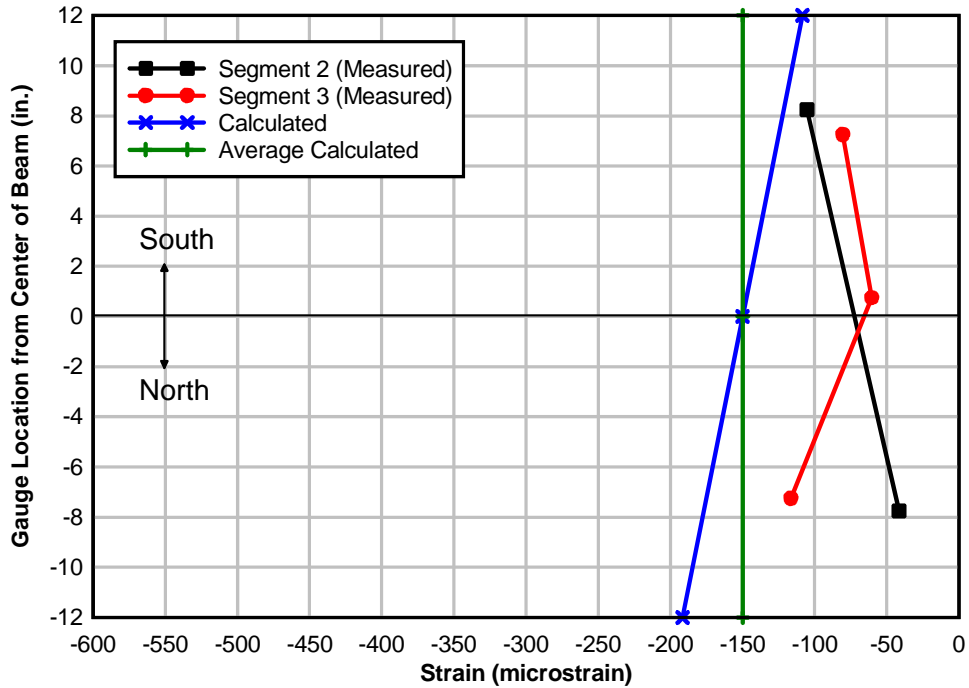


Figure 10-11. Measured concrete strains due to prestress across width of segment flanges near joint J2 (Top flange)

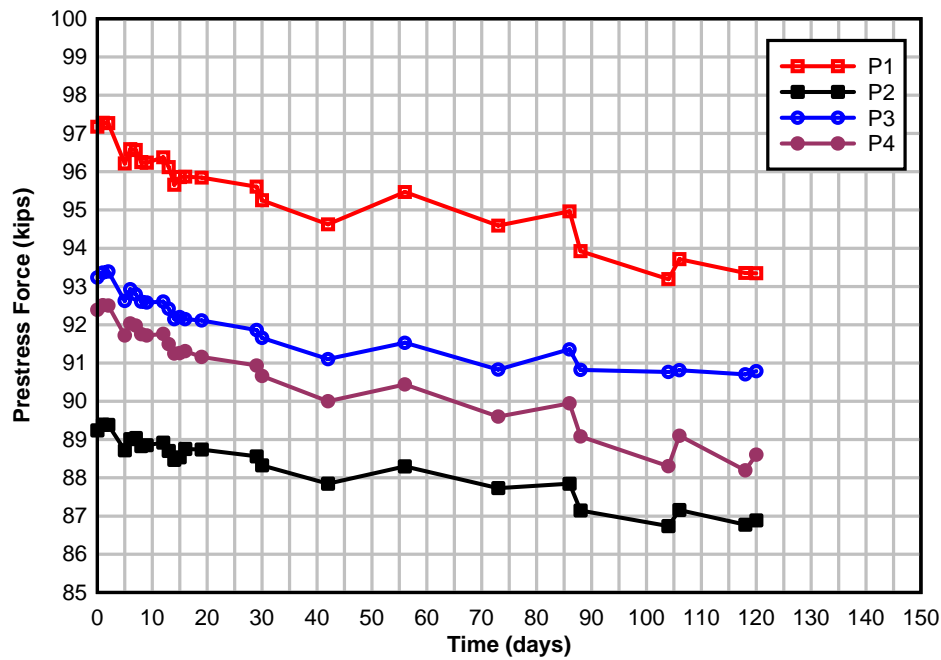


Figure 10-12. Variation of prestress forces with time

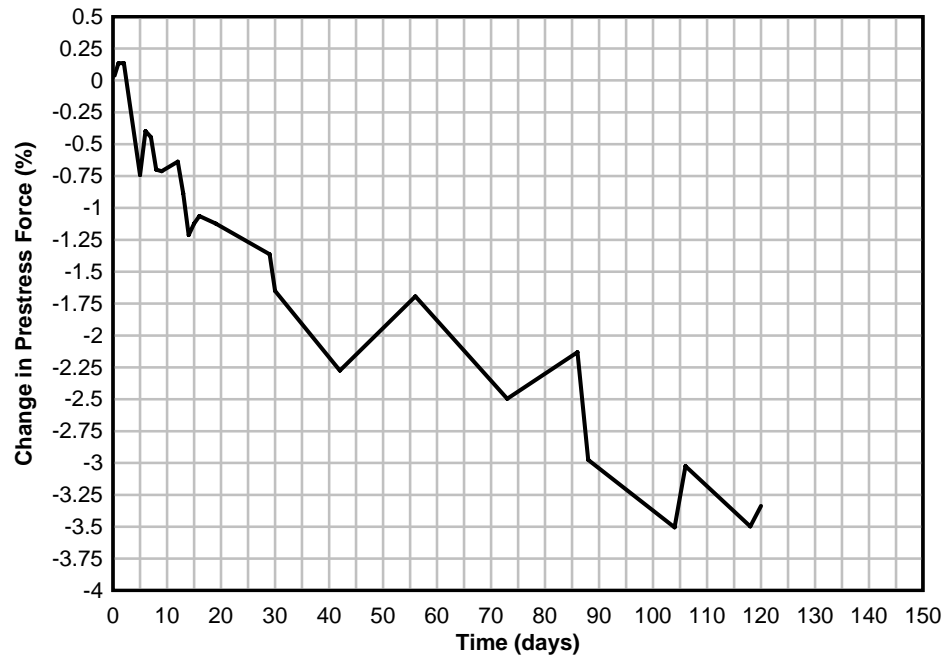


Figure 10-13. Change in total prestress force with time

CHAPTER 11 RESULTS – MECHANICAL LOADING

The behavior of the laboratory segmental beam under the action of mechanical loads applied at the cantilevered end of the beam is discussed in this chapter. The objective of the mechanical load tests was to determine: the load at which the joint at midspan (joint J2) opened; and the effect that this joint opening had on the overall behavior of the beam. As discussed in Chapter 7, opening of joint J2 was used to create zero reference stress conditions from which stresses due to the AASHTO nonlinear thermal gradients could later be quantified.

Two methods of detecting joint opening were used. One involved the use of strain gauges mounted close to joint J2. The other involved the use of LVDTs mounted across joint J2 at specified depths. Data collected from the LVDTs and strain gauges are presented and compared in the following sections. In addition, data collected from strain gauges located at the middle of segments 2 and 3 (30 in. away from joint J2 on both sides) and vertical deflection data will be presented and discussed.

In the plots presented in the following sections, loads refer to mechanical loads applied by the hydraulic jack. Beam response is also due to loads applied by the hydraulic jack. The total vertical mechanical load carried by the beam during tests was the sum of the self-weight of the beam (measured at about 11 kips) and the load applied by the hydraulic jack. Tensile strains plotted in this chapter represent relief of initial compressive strains (caused by prestressing) and are positive. Compressive strains represent additional increments of compression that add to the initial precompression and are negative.

Detection of Joint Opening – Strain Gauges Close to Joint at Midspan

The detection of joint opening with strain gauges is illustrated in Figure 11-1 and Figure 11-2. Prior to opening of the joint, the change in strain is linear with respect to applied load.

After the joint opens, concrete fibers initially in contact are unable to carry any significant additional strain. Strain gauges located at the level of joint opening therefore show no change in strain with increasing load, and the load vs. strain curve becomes almost vertical. The load at which strains initially stop increasing is the load that causes the joint to open at the location of the strain gauge. Strain at this load is equal in magnitude, but opposite in sign, to the initial strain at the same location that was caused by prestress and self-weight.

For strain gauges located on the side of the beam (see Figure 11-1), the initial slope of the load vs. strain curve is inversely proportional to the distance of the gauge from the neutral axis of the gross section. Strain gauges located farther away from the centroid of the contact area of the gross section indicate lower joint-opening loads than strain gauges located closer in distance to the centroid. In Figure 11-1, Q_1 is less than Q_2 because SG1 and SG2 are closer in distance to the centroid of the contact area than SG3 and SG4. This is because the joint starts opening at the top of the section and slowly progresses downward as indicated by the direction of the moment in Figure 11-1. The point at which the load vs. strain curve changes slope (becomes vertical) is dependent on the compressive strain at the location of the strain gauge. In Figure 11-1 it is assumed that the initial strain, ϵ_1 , at the location of SG1 and SG2 is less than the initial strain, ϵ_2 , at the location of SG3 and SG4 (due to the location of the line of action of the post-tensioning force, i.e. below the centroid of the contact area of the gross cross section).

Strain gauges located on top of the flange have identical load vs. strain curves (see Figure 11-2). This is because strain is uniformly distributed across the width of the flange. The strain at which the load vs. strain curve becomes vertical, ϵ_i , is the initial uniform strain in the top fibers of the flange before the application of mechanical loads.

Though the post-joint-opening curves are shown as vertical in Figure 11-1 and Figure 11-2, this is not always the case. In prestressed beams, the sudden increase in prestress associated with opening a joint may lead to a slight compression in fibers that are no longer in contact. The post-joint-opening curve then has a slight curvature, which diminishes as the depth of joint-opening moves farther away from the location of the fibers (with increasing load).

Typical load vs. strain curves on the North and South sides of joint J2, plotted with laboratory measured loads and concrete strains, are shown in Figure 11-3 and Figure 11-4, respectively. Opening of the joint at the location of each strain gauge was indicated by the point at which the curves initially became vertical. Generally, strain gauges located above the centroid of the contact area of the cross section prior to the joint opening (referred to simply as the centroid of the gross cross section in the figures) indicated opening of the joint. Strain gauges located below the centroid of the gross cross section registered compressive strains. This was expected since the moment at joint J2 due to the applied loads led to relief of existing compressive strains above, and the addition of compressive strains below the centroid of the contact area at the joint. The high decompression shown by the strain gauge located at the centroid of the gross cross section in Figure 11-3 (S3-N-S-3.6-21.3) as the depth of joint opening approached the centroid was consistent with the high compressive strain recorded by the same gauge during prestressing (see Figure 10-5 and the measured strain profile on the North side of Segment 3 at elevation 21.3 in. in Figure 10-10).

Figure 11-5 shows the variation of concrete strain with load on top of the flanges of segments 2 and 3 close to joint J2. Strain gauges located on the top flange generally detected very low strains with applied load compared with strain gauges on the sides of the segments. This was expected since low strains were recorded in the extreme top fibers of the segment

flanges during prestressing (see Figure 10-8 and Figure 10-11). Of the five strain gauges on the top flange, it was possible to detect joint-opening from two: one on the South of Segment 2 and the other on the North of Segment 3 (see Figure 11-5). The load vs. strain curves of the other three strain gauges were almost vertical throughout the entire loading process. Normally, the behavior of the three gauges with almost vertical load vs. strain curves would indicate that the joint opened at the top flange almost immediately after the beam was loaded. This, however, was not the case. As shown in Figure 11-6, some concrete at the top flange at joint J2 had broken off during transportation and handling of the segments. Gauges at the locations where a significant amount of concrete had broken off showed almost no change in strain with load even though the joint was not open. This was because concrete fibers on opposite sides of the joint at the locations were not in contact prior to loading the beam. Strain gauges at other locations where this condition was less severe registered some strain as the beam was loaded. The nonlinear behavior of measured strain with load in Figure 11-3 through Figure 11-5 was the result of the condition of joint J2 at the top flange as shown in Figure 11-6, and changes in the stiffness of the contact area at the joint as it was slowly opened.

As discussed in the beginning paragraphs of this section, the strain at which the joint opened at the location of a gauge was expected to be equal to the initial compressive strain at that location. Before beginning mechanical load tests on the beam, the supports were changed from the system shown in Figure 10-1 to that shown in Figure 10-2. The changes in strain that took place during this transition were not recorded. Hence the exact distribution of initial strain at joint J2 was not known prior to the application of mechanical loads. In spite of the unknown changes in strain that took place while changing the beam support conditions, the measured strains at which the joint opened, though not equal in magnitude, were still consistent with the

distribution of strains due to prestress. As shown in Table 11-1, strain gauges near joint J2 on the sides of the flange, which showed higher strains due to prestress, indicated opening of joint J2 at higher strains than gauges located in areas of lesser prestrain.

Strain gauges above the centroid of the contact area of the section and at identical locations on either side of the joint were expected to detect joint-opening at the same load. Furthermore, it was expected that gauges at higher elevations would indicate opening of the joint at lower loads than gauges at lower elevations (see Figure 11-1). However, strain gauges located above the centroid of the contact area showed the joint opening at higher loads on the North side (Figure 11-3) than on the South side (Figure 11-4). This was partly due to differences in the elevations of the gauges. The strain gauge designated S3-N-S-02-27.4 on the North side of the joint showed the joint opening at a load of about 48 kips (see Figure 11-3), while the strain gauge at the same location on the South (S3-S-S-02-27.5) showed the joint opening at a load of about 38 kips (see Figure 11-4). Furthermore, the strain gauge located at elevation 28.6 in. on the South side of the joint (see Figure 11-4) showed joint opening at a lower load (21 kips) than two strain gauges located above it on the North side of the joint as shown in Figure 11-3 (31 kips for the gauge at elevation 33.5 in. and 41 kips for the gauge at elevation 30.3 in.). This was indicative of the joint opening earlier on the South side than on the North side, and was consistent with the distribution of measured strains through the depth of the beam due to prestress (see Figure 10-10).

Because of the distinct change in strain that occurred when the joint opened, strain gauges were the instrument of choice in determining joint-opening loads.

Measured concrete strains through the depth of the beam near joint J2 on the North and South sides are shown in Figure 11-7 and Figure 11-8, respectively. Strain data shown in Figure

11-3 through Figure 11-5 were used in plotting the strain profiles in Figure 11-7 and Figure 11-8. In Figure 11-7 and Figure 11-8, joint-opening at each elevation within joint J2 is indicated when no further strain change with load occurs at that depth. As explained previously, the fact that top flange strains were nearly constant with respect to load in Figure 11-8 was not indicative of opening of joint J2, but was probably the result of the condition at the joint shown in Figure 11-6.

As shown in Figure 11-7 and Figure 11-8, the neutral axis of the contact area at joint J2 (point of intersection of strain profile with zero strain axis) gradually moved downward with increasing load. Furthermore, the movement of the neutral axis was smaller on the North side of the joint (see Figure 11-7) than on the South side (see Figure 11-8), indicating a rotation of the neutral axis about the centroid of the contact area. As illustrated in Figure 11-9, the downward movement of the centroid of the contact area at joint J2, as the beam was incrementally loaded, was due to opening of the joint. Rotation of the neutral axis about the centroid of the contact area was attributed to the net out-of-plane horizontal eccentricity in prestressing. Movement of the neutral axis with load is illustrated in Figure 11-10.

The change in prestress as the beam was incrementally loaded is shown in Figure 11-11. Bars 1 and 2 were expected to undergo the same change in force with load since they were at the same elevation. Similarly, bars 2 and 4 were expected to undergo the same change in force. However, because the opening of joint J2 was greater on the South side than on the North side, the change in force in the bars on the South side (P2 and P4) was greater than the change in force in the bars on the North side (P1 and P3, respectively) after the joint opened. The forces in bars 1 and 2 increased with load while forces in bars 2 and 3 generally decreased with load. This was because bars 1 and 2 were located above the centroid of the gross section and bars 3 and 4 were

located below the centroid of the gross section (see the position of prestress bars in Figure 11-11). At a load of about 40 kips (see Figure 11-9) the depth of joint opening caused the centroid of the contact area at joint J2 to move below the location of bars 3 and 4, leading to an increase in force with load in these bars.

Detection of Joint Opening – LVDTs Across Joint at Midspan

Determination of joint-opening using LVDTs mounted across the joint is illustrated in Figure 11-12 and Figure 11-13. LVDTs mounted across a joint indicate opening of the joint at the location of the LVDT when the initial slope of the load vs. displacement curve changes as a result of the reduction in stiffness of the section.

Prior to the joint opening, LVDTs measure the displacement between the mounts (supports) of the LVDT as a result of strain in concrete. The initial slope of the load vs. displacement curve is inversely proportional to the distance between the mounts of the LVDT and the distance of the LVDT from the centroid of the contact area at the joint prior to the application of mechanical loads (see Figure 11-12). The bending moment in Figure 11-12 causes the joint to start opening at the top flange and gradually progress downward. Therefore, LVDTs that are farther above the centroid of the contact area prior to the joint opening indicate lower joint-opening loads than LVDTs that are closer to the centroid of the contact area. LVDTs at identical distances from the centroid of the contact area of the gross section have the same load vs. displacement curves if the joint opens uniformly across the width of the section (see Figure 11-13). After the joint opens, fibers that were initially in contact separate and are unable to carry any significant additional strain. LVDTs then measure the distance between the separated fibers or the width of joint opening.

Figure 11-14 shows data from LVDTs distributed throughout the depth of joint J2 on the South side of the beam. In this figure, the last number in each LVDT label indicates the distance

of the LVDT from the bottom of the beam. The centroid of the contact area of the gross section at joint J2 was 21.3 in. from the bottom of the segments. As expected, LVDTs located at elevations above the centroid of the contact area of the gross section indicated lower joint-opening loads than LVDTs at lower elevations. Furthermore, LVDTs located close to the bottom of the joint indicated little or no joint-opening, and in the case of the LVDT at the lowest elevation (J2-S-D-4.275) some compression. This was because the moment at joint J2 due to applied mechanical loads caused the relief of compressive strains above the centroid of the contact area but increased the existing compressive strains below the centroid. At the level of each LVDT the initial compressive strains had to be relieved by strains due to the applied moment in order for the joint to open. It was therefore expected that only LVDTs located above the centroid of the contact area would indicate joint-opening. This was evident in data from the top three LVDTs, designated J2-S-D-33.75, J2-S-D-30.25, and J2-S-D-25.0 in Figure 11-14, which were located above the centroid of the contact area at joint J2 prior to opening of the joint.

Figure 11-15 shows data from LVDTs mounted across joint J2 on top of the flanges of segments 2 and 3. Unlike the ideal curve in Figure 11-13, the load vs. displacement curves in Figure 11-15 were essentially nonlinear from the beginning of load application. This was most likely caused by lack of contact between top flange concrete fibers at joint J2 (see Figure 11-6). Similar to the measured strain gauge data, the nonlinear form of the LVDT curves at higher loads was due to changes in stiffness of the contact area at joint J2 as it was opened. Opening of joint J2 at the flange top fibers was estimated from the curves in Figure 11-15 by locating the points at which the various curves initially deviated from one another.

Ideally, if the joint opened uniformly across the width of the flange, all three LVDTs would have indicated opening of the joint at the same load and would have had identical

load vs. displacement curves. As discussed in the previous chapter, however, joint J2 initially opened on the South side before opening on the North side. This caused displacements recorded by the LVDT on the South flange, designated J2-TS-D-9.5, to be larger than displacements recorded by the LVDT at the center of the flange (J2-T-D), and the LVDT at the North flange (J2-TN-D-9.5).

LVDTs mounted across joint J2 on top of the flanges of segments 2 and 3, and the LVDTs designated J2-S-D-33.75 and J2-S-D-30.25 in Figure 11-14 showed two distinct essentially linear regions after the joint initially opened. In the first linear region of the curves, which occurred after the joint initially opened at the location of each LVDT, the centroid of the concrete contact area was between the top and bottom post-tensioning bars. Thus, tensile stresses due to the applied moment were resisted by the post-tensioning bars and existing compressive stresses at the joint. In the second linear region, which began at a load of about 40 kips, the centroid of the concrete contact area was below the bottom post-tensioning bars (see Figure 11-9). Tensile stresses due to the applied moment were therefore effectively resisted by the post-tensioning bars with little contribution from existing concrete compressive stresses, leading to a significant change in slope (from the first linear region).

Due to nonlinearities in the load vs. displacement curves for LVDTs mounted across joint J2, there was less confidence in determining joint-opening loads with these instruments compared to strain gauges located close to the joint. LVDT data were, however, useful in checking joint-opening loads determined from strain gauge data.

Strains at Mid-Segment

During tests in which data were collected from strain gauges at the middle of segments 2 and 3, loads applied to the beam did not exceed 40 kips. This was because strain data from the middle of the segments were not needed for joint-opening analysis.

Strain distributions 30 in. away from the middle of Segment 3 on the North and South sides of the beam are shown in Figure 11-16 and Figure 11-17, respectively. Data obtained from gauges located at the middle of Segment 2 (see Appendix C) were nearly identical to the Segment 3 data and are therefore not shown here.

Opening of the joint at the beam midspan (at joint J2) did not affect on the location of the neutral axis at the middle of the segments, which remained at elevation 21.3 in. However, the non-uniform opening of joint J2 across the width of the section at the joint affected the distribution of strains at mid-segment. Lesser magnitude strains were detected in the North flange than the South flange, and higher strains were detected in the North web than the South web. This was indicative of bi-axial bending as illustrated in Figure 11-18. The horizontal component of the moment at mid-segment equilibrated the moment due to the applied load at the cantilevered end of the beam. The vertical component of the moment at mid-segment, which was the result of the net out-of-plane horizontal eccentricity in prestressing and the changes in prestress shown in Figure 11-11, formed a self-equilibrating system with the concrete.

Deflection

Vertical deflection of the beam, measured at a location 7.25 in. from the cantilevered end, is shown in Figure 11-19. The initial nonlinear part of the deflection curve was attributed to a slight deflection at the East end-support of the beam as it was initially loaded. Movement of the neutral axis at the midspan of the beam, as the joint opened, was expected to affect the vertical deflection of the beam. This is indicated by the deviation of the straight line drawn through the deflection curve from the nonlinear parts of the curve. The initial deviation of the straight line from the deflection curve occurred at a load of about 9 kips, the load at which the centroid of the contact area at joint J2 initially began to move downward. After this point the deflection curve was almost linear with load until the depth of joint opening was sufficient enough to cause the

centroid of the contact area to move below the bottom prestress bars (bars 3 and 4 in Figure 11-11) at a load of about 41 kips. Though the section stiffness at joint J2 continuously changed in the linear part of the deflection curve, the change in stiffness was local to the joint and did not affect the overall stiffness of the beam, and therefore the cantilever tip deflection.

Summary

Results from mechanical load tests on the laboratory beam indicated elastic behavior of the beam. The tests were also repeatable (i.e. neglecting small changes of prestress that occurred with time, the response of the beam under the action of mechanical loads was repeatable across tests). The distinct change in strain with load at incipient opening of the joint at midspan (joint J2) resulted in the use of strain gauges near the joint as instruments for detecting joint-opening loads. The contact area at joint J2 could also be estimated using joint-opening loads and elevations of strain gauges near the joint. The relative magnitude of joint-opening loads at identical elevations on the North side and South side of joint J2 together with the shape of contact areas at the joint showed that the beam underwent biaxial bending when mechanically loaded. Measured strain distributions through the height of contact areas at joint J2 showed that strain was a linear function of curvature.

These experimental observations made it possible for normal stresses at incipient opening of joint J2 to be determined without explicitly using material properties (e.g. elastic modulus and coefficient of thermal expansion) of segments 2 and 3.

Table 11-1. Comparison of measured strains due to prestress and measured strains when joint opens

Gauge Location	Gauge Designation	Strains due to Prestress ($\mu\epsilon$)	Strains measured at joint opening condition ($\mu\epsilon$)
North Flange	S3-N-S-02-33.5	-304	210
	S3-N-S-02-30.3	-209	151
South Flange	S3-N-S-02-35.3	-185	103
	S3-N-S-02-32.0	-200	115
	S3-N-S-02-28.6	-110	60

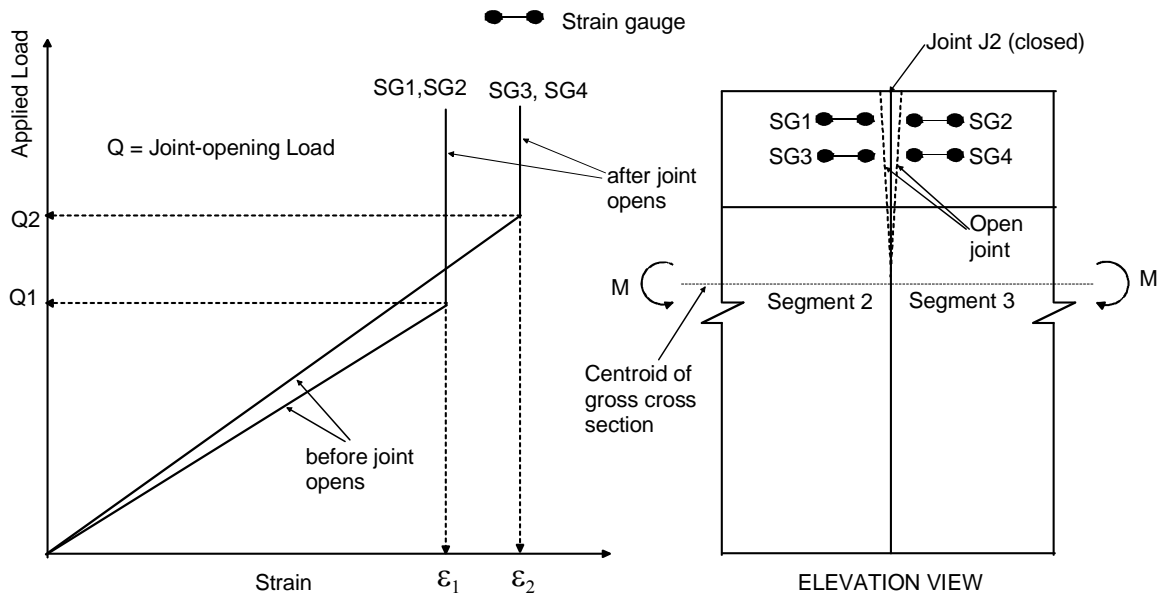


Figure 11-1. Expected behavior of strain gauges on side of beam near joint

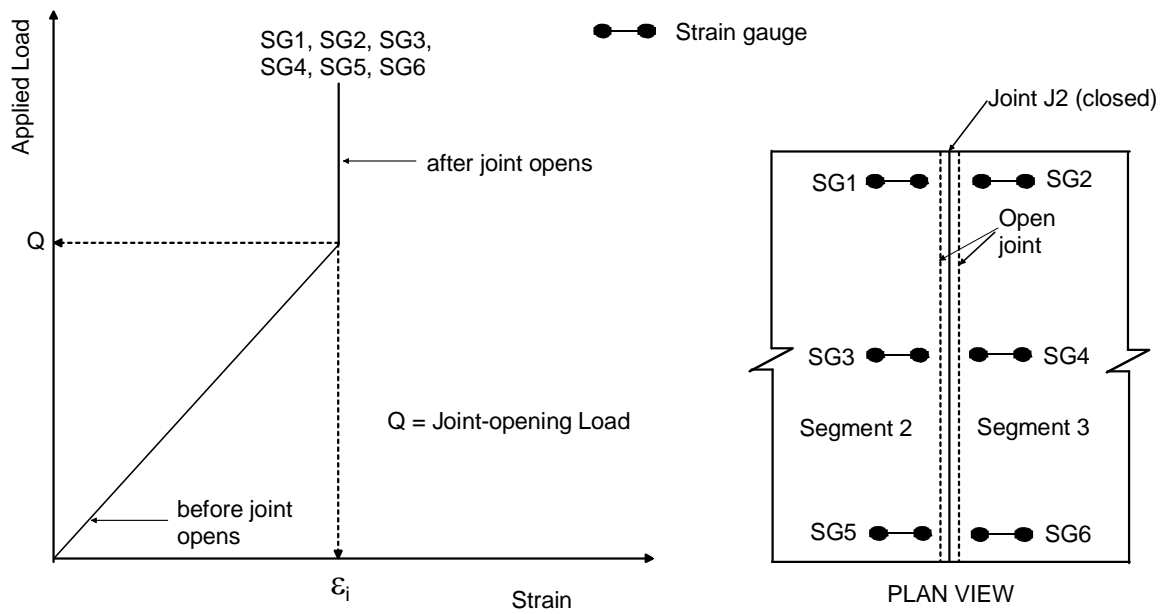


Figure 11-2. Expected behavior of strain gauges on top of flange near joint

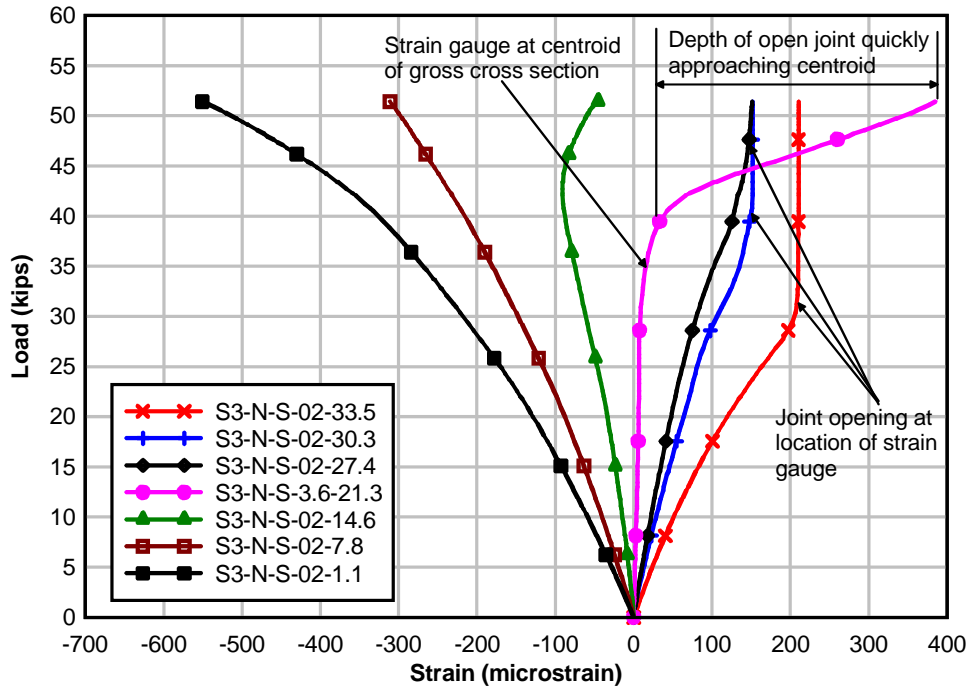


Figure 11-3. Load vs. Strain near joint at midspan (North side)

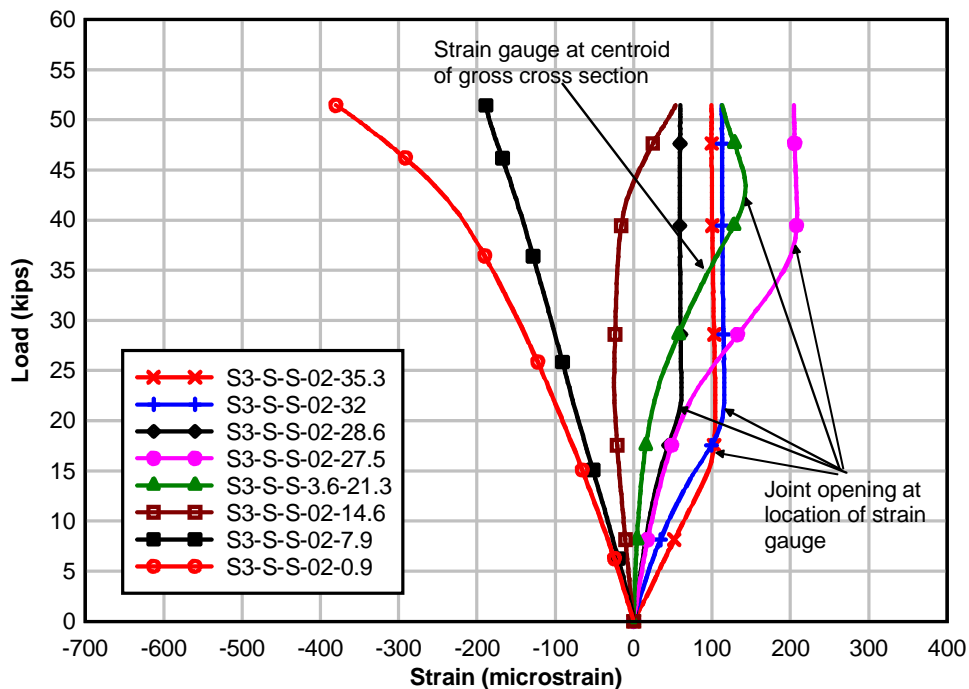


Figure 11-4. Load vs. Strain near joint at midspan (South side)

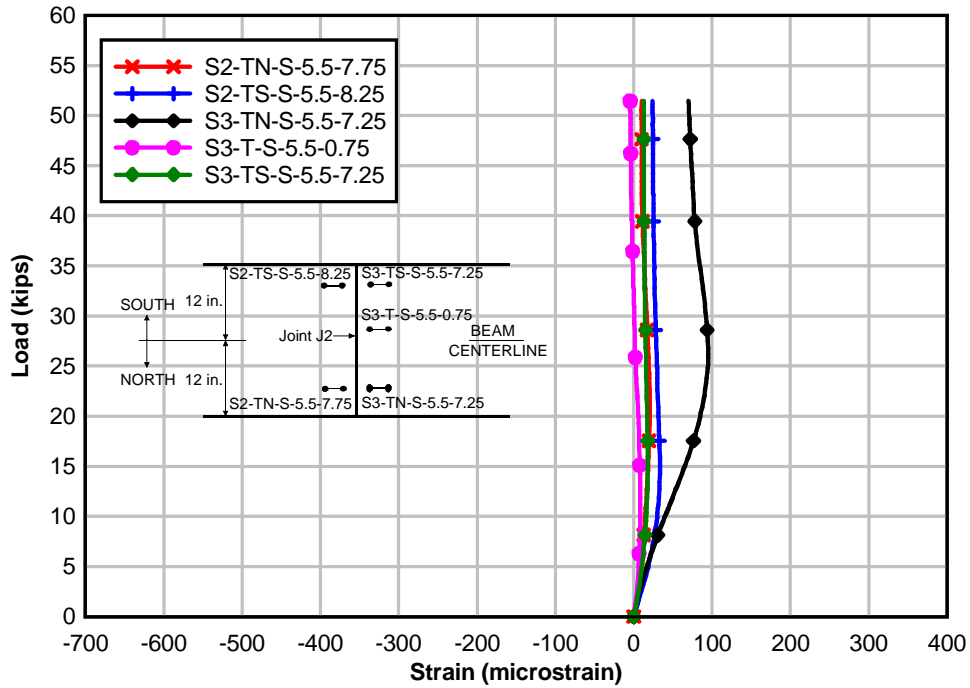


Figure 11-5. Load vs. Strain near joint at midspan (Top flange)

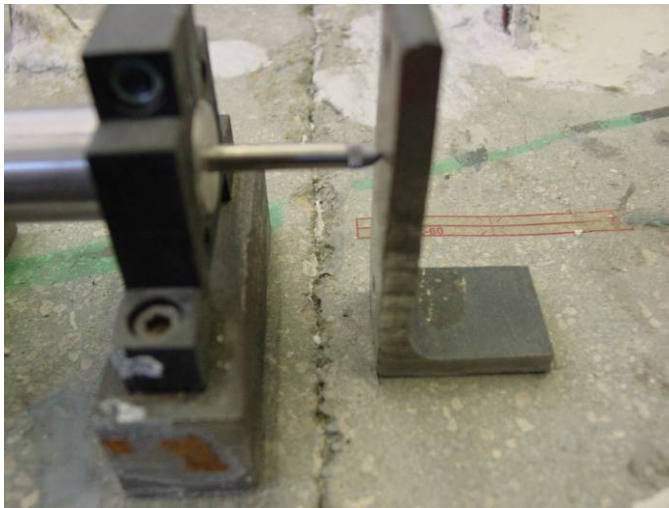


Figure 11-6. Condition of joint J2 on top of flange

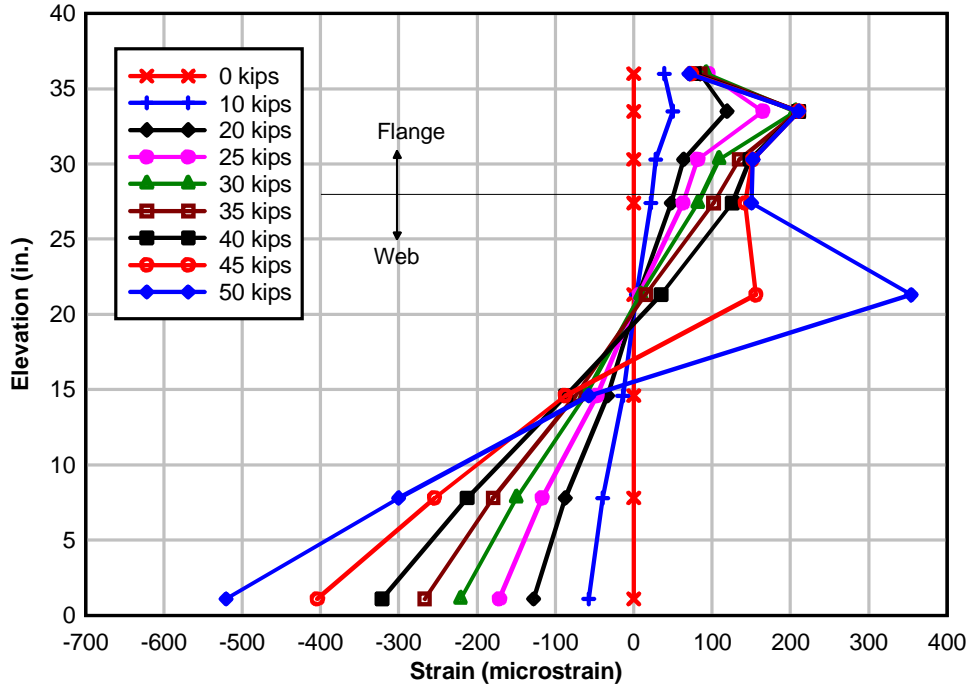


Figure 11-7. Measured strain distributions near joint at midspan (North side)

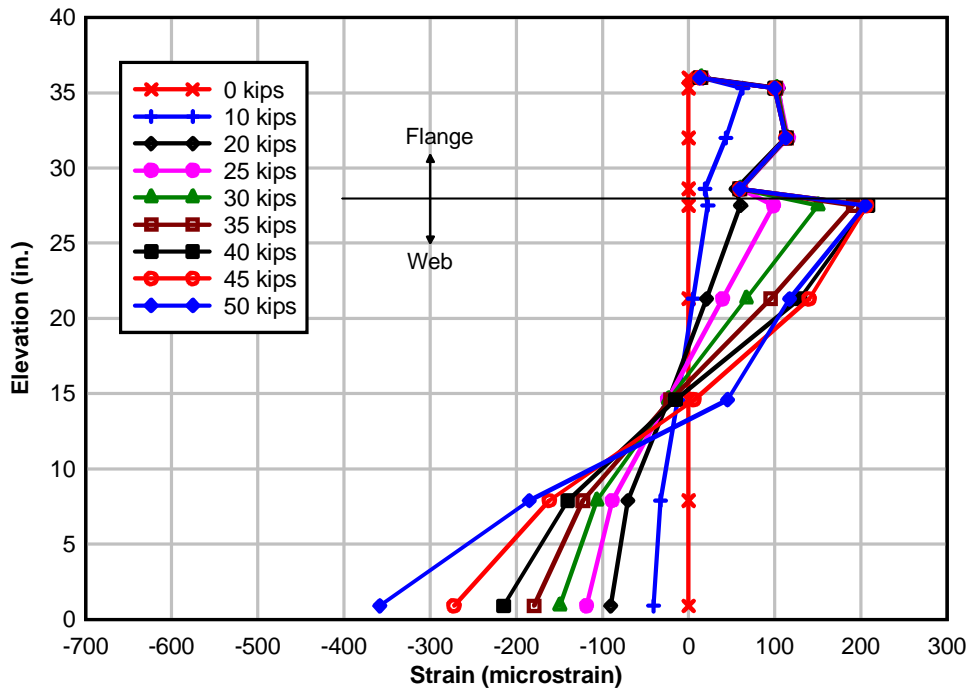


Figure 11-8. Measured strain distributions near joint at midspan (South side)

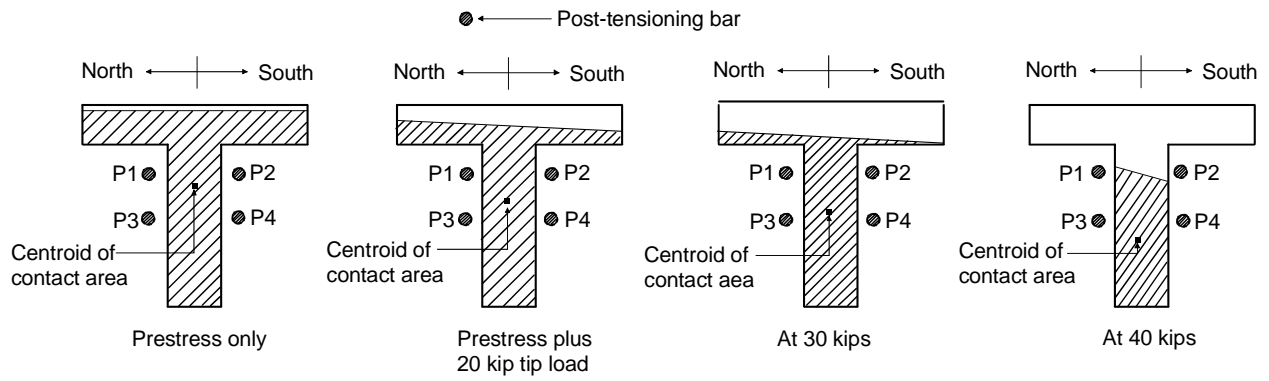


Figure 11-9. Estimated progression of joint-opening with load (based on strain gauge data)

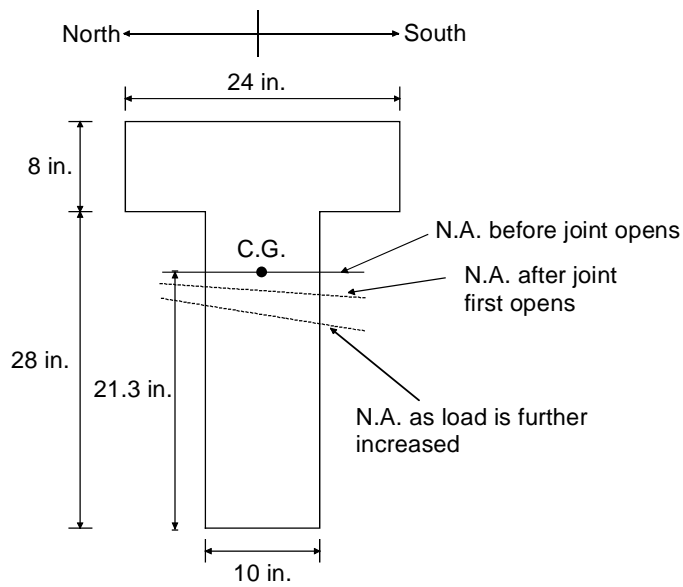


Figure 11-10. Movement of neutral axis (N.A.) with load

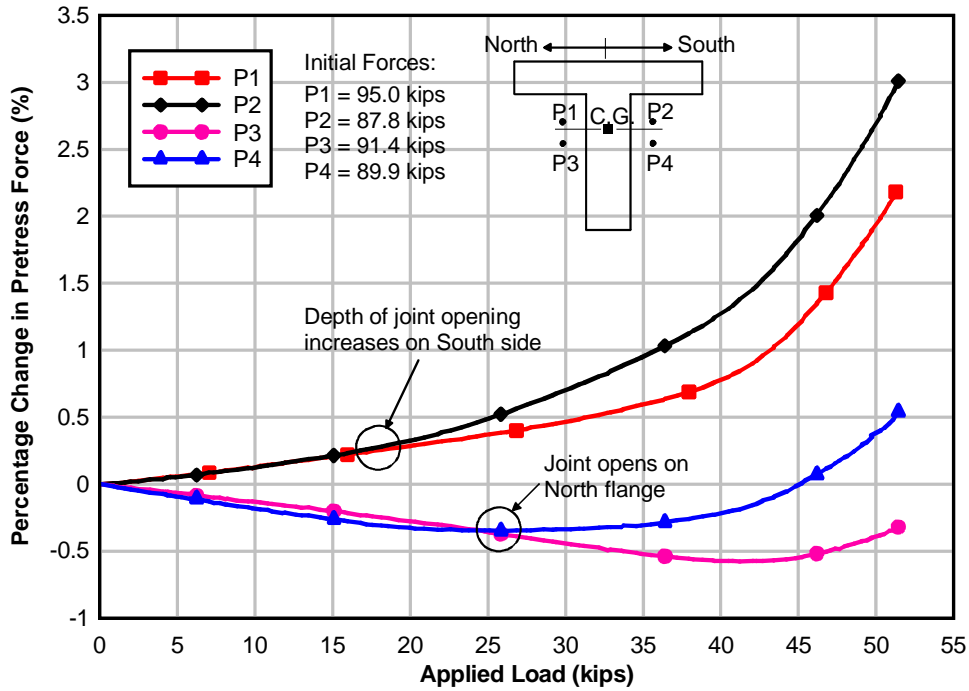


Figure 11-11. Changes in prestress force with load

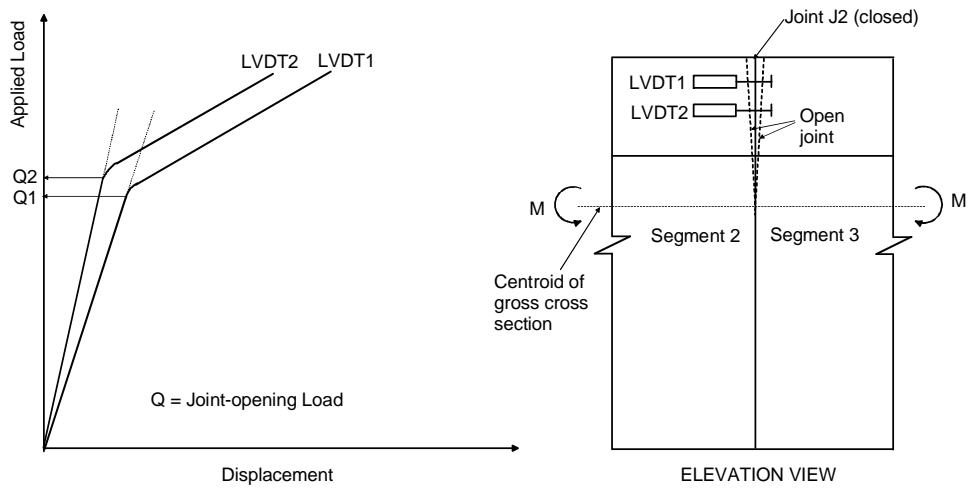


Figure 11-12. Expected behavior of LVDTs across joint on side of beam

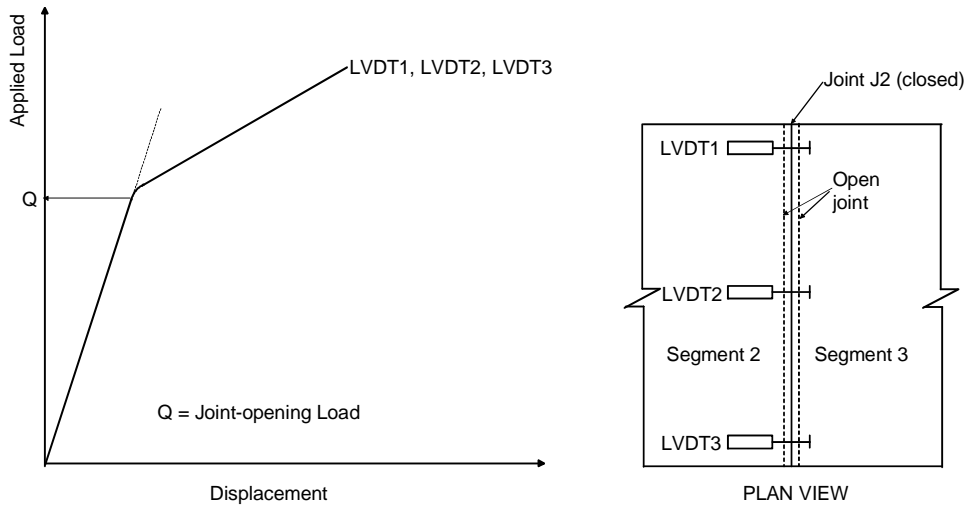


Figure 11-13. Expected behavior of LVDTs across joint on top of flange

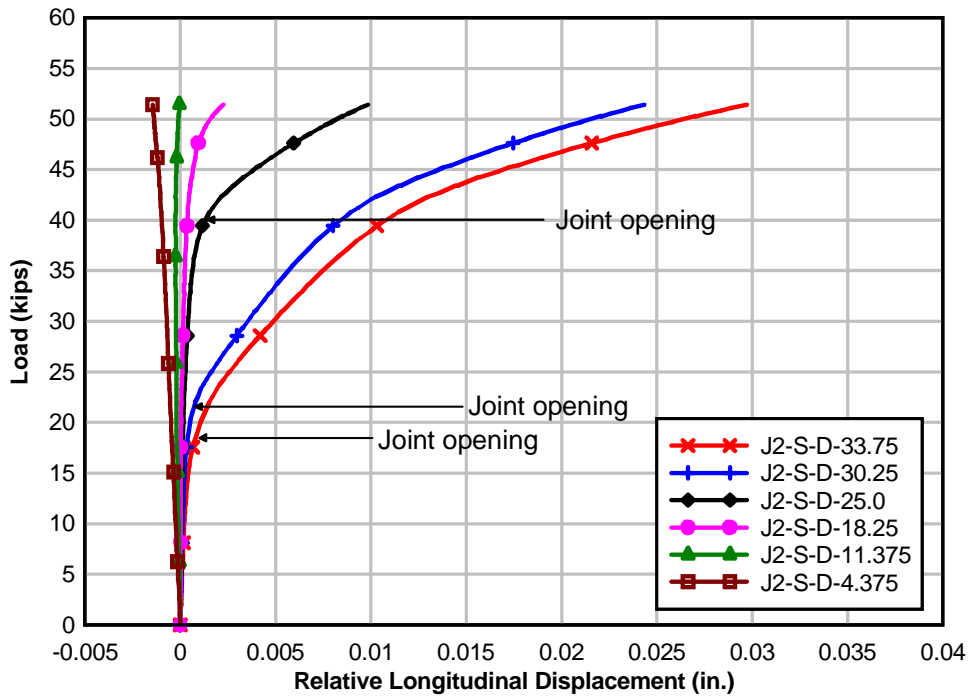


Figure 11-14. Load vs. Joint opening (Side LVDTs)

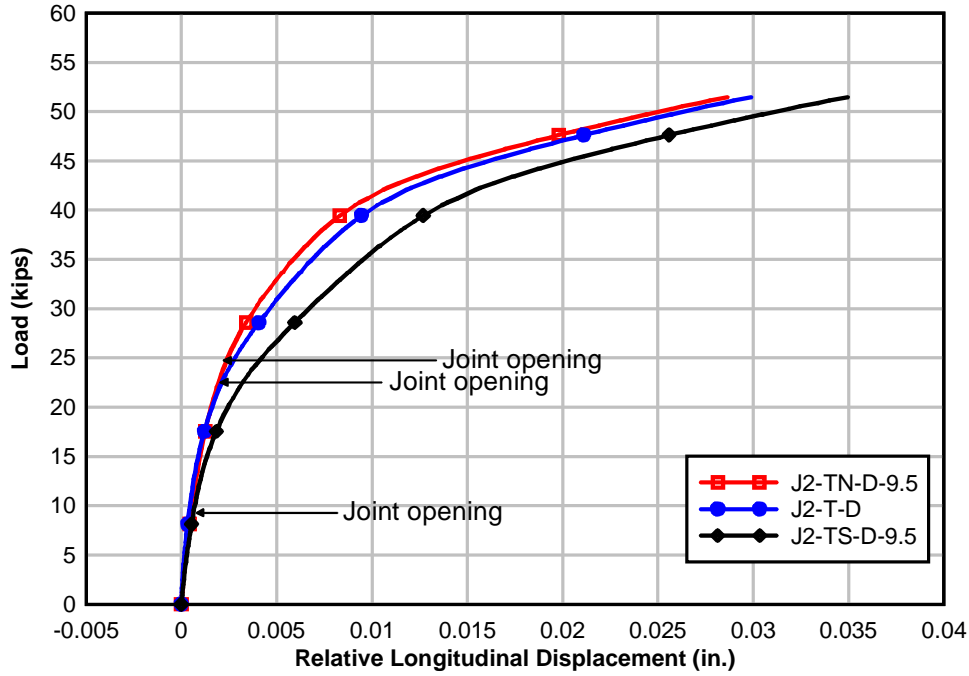


Figure 11-15. Load vs. Joint opening (Top flange LVDTs)

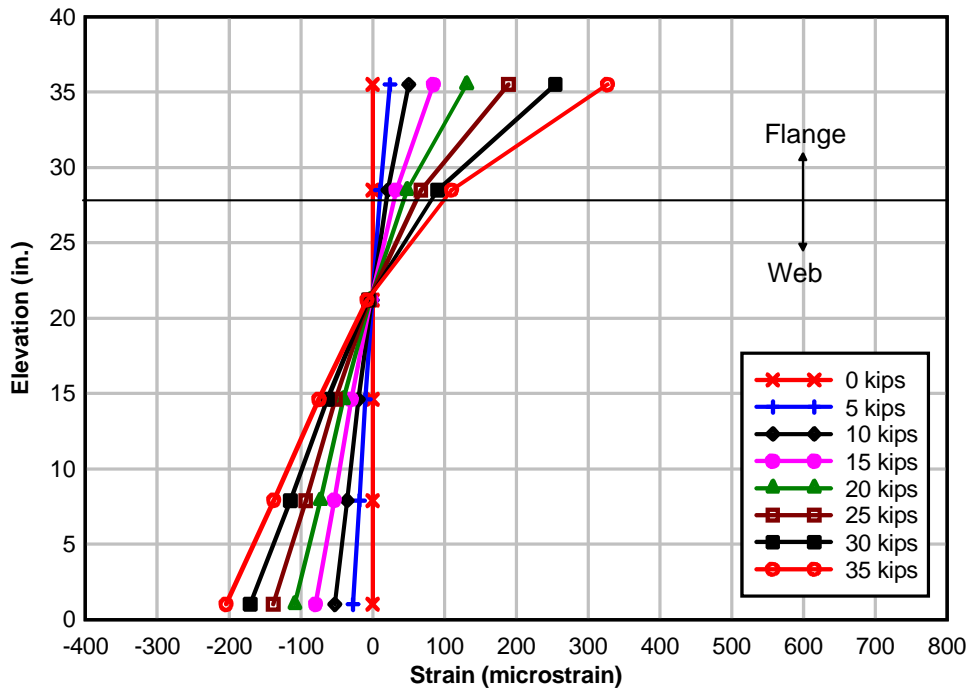


Figure 11-16. Measured strain distributions at middle of Segment 3 (30 in. from joint J2) on North side of beam

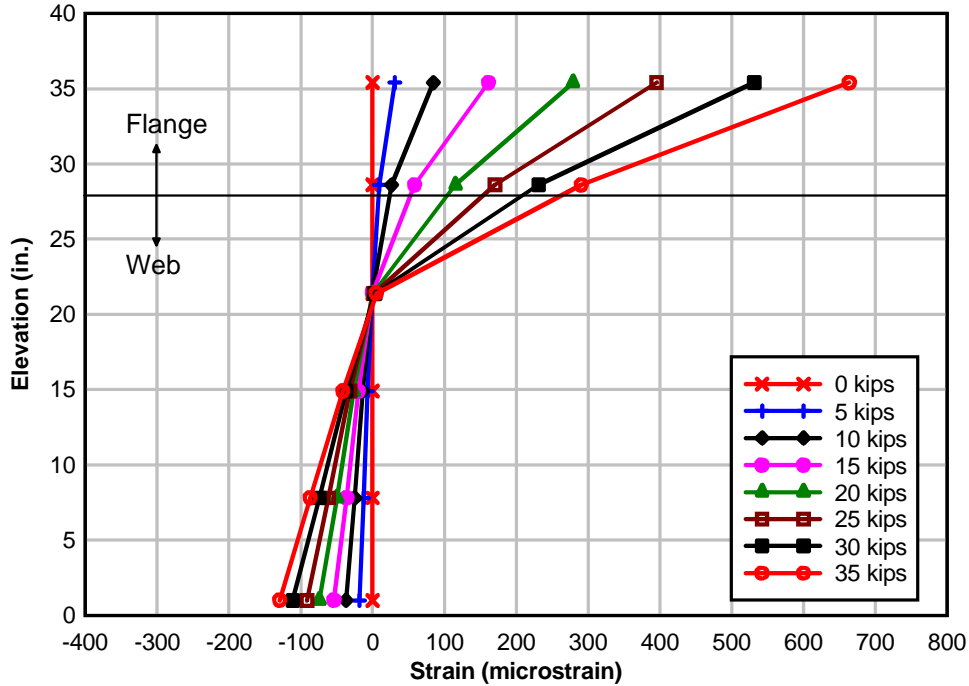


Figure 11-17. Measured strain distributions at middle of Segment 3 (30 in. from joint J2) on South side of beam

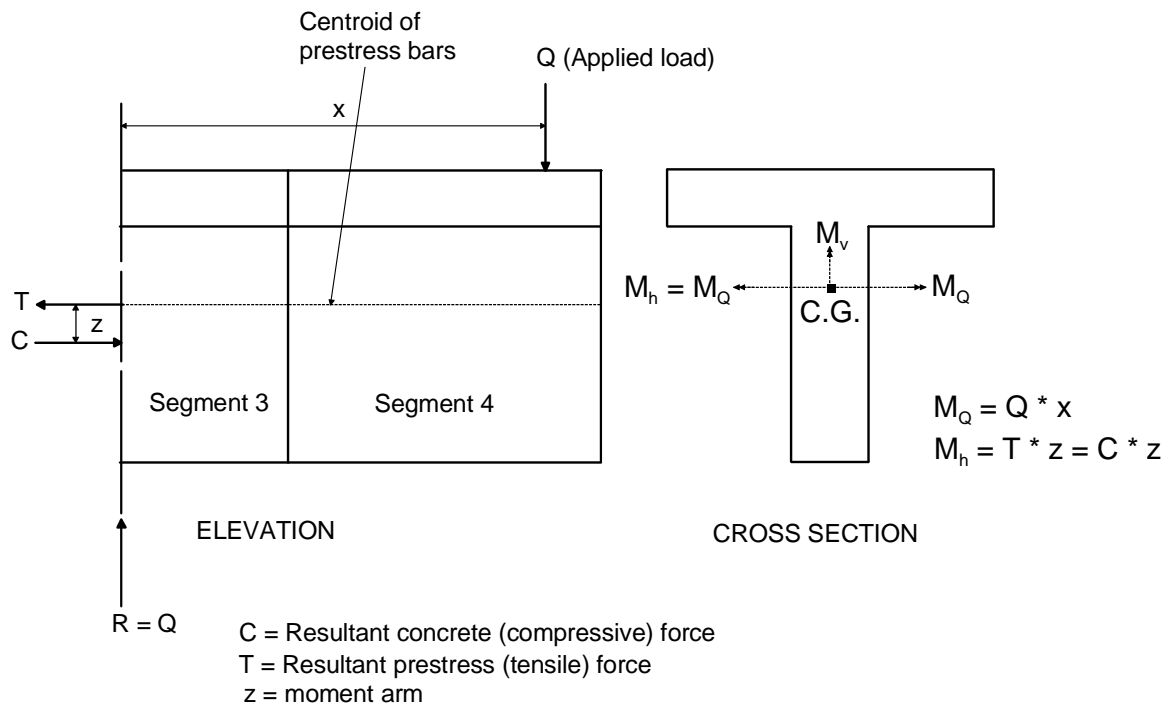


Figure 11-18. Forces and moments acting at mid-segment

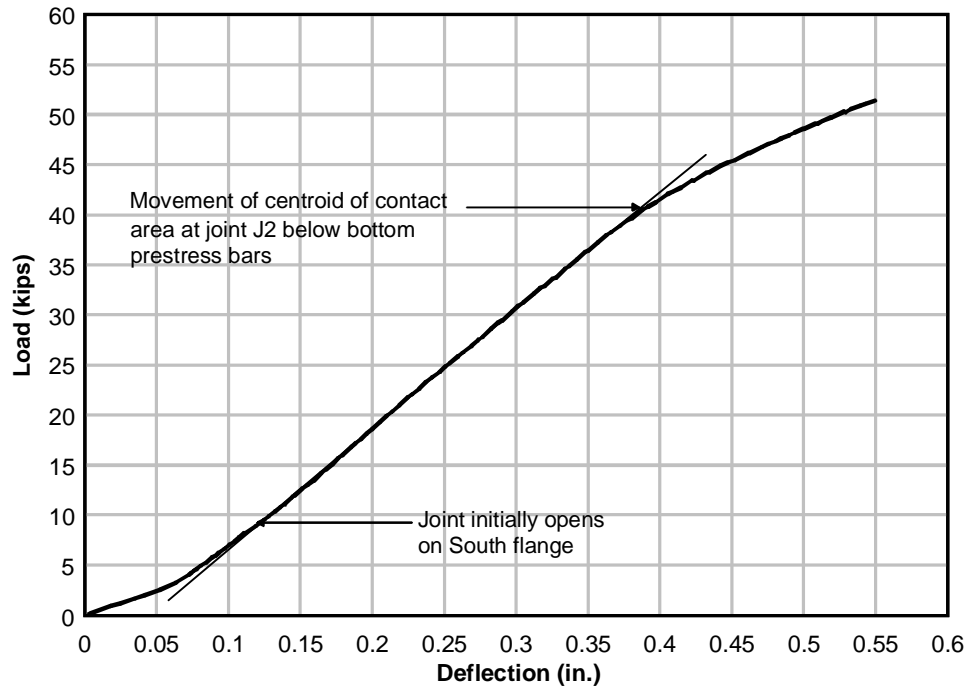


Figure 11-19. Measured vertical deflection near cantilevered end of beam

CHAPTER 12 RESULTS – UNIFORM TEMPERATURE CHANGE

A uniform temperature change was imposed on segments 2 and 3 of the laboratory beam (Figure 12-1) to investigate the behavior in the absence of self-equilibrating thermally induced stresses. The goal was to determine the maximum change in prestress that would result from application of thermal loads on the concrete segments while the DYWIDAG post-tensioning bars remained essentially at laboratory temperature. Though the beam was statically determinate with respect to the supports, expansion of the concrete segments relative to the post-tensioning bars was expected to lead to an increase in prestress and the development of net compressive stresses in the concrete. Conversely, contraction (due to cooling) of the concrete segments relative to the post-tensioning bars was expected to lead to a reduction in prestress and the development of net tensile stresses (i.e. a reduction in compressive stresses) in the concrete. Understanding how such changes in prestress affected concrete stresses was important in estimating the effects, if any, of thermally induced changes in prestress on self-equilibrating thermal stresses when the AASHTO nonlinear thermal gradients were later imposed on the beam.

The test sequence started with the circulation of tap water through segments 2 and 3 for about 24 hours to establish a uniform reference temperature of about 84 °F (low reference temperature). Segments 2 and 3 were then heated to an average temperature of about +41 °F above the low reference temperature using the piping configuration shown in Figure 8-6. Forces in the post-tensioning bars and concrete strains at joint J2 were continuously recorded during this period, which will subsequently be referred to as the “heating phase”. Following the heating phase, the temperature of the concrete segments, which was about 125 °F, was taken as the new reference temperature (high reference). With the data acquisition system still running, the segments were cooled from the high reference temperature back to the initial (low) reference

temperature using the piping configuration shown in Figure 8-5. This phase of the test will subsequently be referred to as the “cooling phase”. Laboratory imposed temperature changes in the heating and cooling phases of the test are shown together with target temperature changes for Segment 2 and Segment 3 in Figure 12-2 and Figure 12-3, respectively. Measured concrete temperatures in Segment 2 and Segment 3 are shown in Figure 12-4 and Figure 12-5, respectively. Temperature changes in the Figure 12-2 and Figure 12-3 are with respect to the low reference temperature (about 84 °F) for the heating phase and the high reference temperature (about 125 °F) for the cooling phase. The average (uniform) temperature increase during the heating phase of the test was about 40 °F and the average decrease in temperature during the cooling phase was about 38 °F. The difference between the average temperature changes in the heating and cooling phases was due to a slight increase in tap water temperature during the three day period over which the test was conducted. This slight increase caused segments 2 and 3 to be cooled to a temperature that was higher than the initial temperature from which they were heated.

Significant deviation from the target profile occurred at Section A (see Figure 12-1) and Section F (see Figure 12-3). These deviations were due to the fact that sections A and F were adjacent to the ambient segments (segments 1 and 4). These segments (1 and 4) acted as heat sinks because they remained essentially at laboratory temperature during application of the thermal profiles on the heated segments (Segments 2 and 3). Additionally, the bottom surfaces of segments 2 and 3 could not be adequately heated at sections C and D because these locations were close to the mid-support point and could not be adequately insulated with Styrofoam. This issue was resolved in later tests by using flexible fiberglass to insulate the mid-support area of the beam. Temperature profiles were non uniform not only through the height of the segments

but also across the width. The distribution of temperature change through the height and across the width of the beam at Section C and Section D during the heating phase are shown in Figure 12-6 and Figure 12-7, respectively. The color bar in each figure represents change in temperature (in °F) relative to the low reference temperature. These figures show that temperatures along the perimeter of each section were generally slightly lower than temperatures in the interior. This was more pronounced in the web, where the ratio of concrete area to copper tubes was only about a third of that in the flange. There were two main reasons for this. First, the segment heating system was designed to efficiently impose the AASHTO nonlinear gradients while keeping the number of copper tubes embedded in concrete to a minimum. Thus, there was a higher concentration of copper tubes in the flange (where the maximum temperature changes in the gradients occur) than in the web (where there was almost no change in temperature). Second, heating the two concrete segments, by approximately 40 °F, uniformly was the most thermally demanding situation imposed on the heating system, due to the total volume of concrete and temperature increase involved.

Average measured temperature changes in the heated segments were used together with the average measured coefficients of thermal expansion (CTE) in Table 12-1, elastic moduli (MOE) in Table 12-2, and DYWIDAG bar properties to predict anticipated changes in prestress. Concrete elastic moduli in Table 12-2 were obtained by linearly interpolating between MOEs which were derived from cylinder test data between test ages of 28 and 360 days. Moments caused by the vertical and horizontal eccentricities of the prestress bars and slight curvatures caused by non-uniformity of the imposed temperature profiles were neglected in the prediction of prestress change. It was also assumed that for the duration of the test, the prestress bars and ambient concrete segments did not undergo any changes in temperature. Predicted and measured

changes in prestress during the heating and cooling phases of the test are compared in Table 12-3 and Table 12-4, respectively. Measured total changes in prestress were within 11% of corresponding calculated values. Calculated changes were of higher magnitude than measured changes mainly because the ambient segments and prestress bars were subjected to a slight temperature increase due to an increase in laboratory temperature during the course of the test. It was expected that the steel prestress bars would respond to such non-stress-inducing temperature changes more rapidly than the ambient segments because of the relatively high thermal conductivity of steel and the small volume of steel compared with concrete (about 1%). Measured total changes in prestress even under this worst case thermal loading condition were less than 6% of the initial total prestress.

Measured concrete strains near joint J2 from strain gauges located on segments 2 and 3 during the heating and cooling phases of the test are shown in Figure 12-8 and Figure 12-9, respectively. Expected (calculated) strain distributions are also shown in the figures for comparison. Calculated strains were determined using measured prestress forces and eccentricities, concrete section properties, and the elastic moduli shown in Table 12-2. Concrete strains measured during the heating phase were essentially a mirror image of concrete strains measured during the cooling phase. This showed that strains induced in the heated segments when the beam was heated were relieved when the beam was cooled; evidence that the beam remained elastic under the action of the thermal loads. Because the strain gauges installed on the concrete segments were self-temperature-compensating (STC) gauges, it was expected that the measured strains (assuming uniformity of temperature distributions) would arise solely from changes in prestress, and therefore would be compressive during heating and tensile during cooling. It is, however, evident from Figure 12-8 and Figure 12-9 that the opposite was the case.

Measured concrete strains during the heating phase were instead tensile. A similar reversal was observed during the cooling phase. Furthermore, the measured strains were non-uniform through the height of the segments. The observed reversals were attributed to the fact that the temperature profiles imposed on the segments were somewhat non-uniform over the cross sectional area of the segments (recall Figure 12-6 and Figure 12-7). Thus, while the total change in prestress was a result of the average (uniform) temperature change imposed on the heated segments, strains measured on the surfaces of the sections were affected by non-uniform temperature changes. Concrete strains measured during the heating phase are compared with calculated strains which take into account both changes in prestress and the non-uniformity in temperature distributions in Figure 12-10 and Figure 12-11. The calculated strains in were determined by superimposing strains caused by the increase in prestress and stress-inducing strains caused by the non-uniform temperature distributions shown in Figure 12-6 and Figure 12-7, respectively. Stress-inducing strains caused by the two-dimensional thermal gradients in the figures were calculated using Eqns. 3-8 through 3-12 (see Chapter 3). Though the calculated strain magnitudes shown in Figure 12-10 and Figure 12-11 do not exactly match the measured strains they are consistent in sign (i.e. positive, tensile). A possible explanation for the difference in magnitude of measured and calculated strains is that precise measurements of temperature at the surface of the concrete sections, where the strains were measured, were not available. Instead surface temperatures were obtained by extrapolating data from thermocouples nearest to, but not exactly at, the surface of the concrete. Hence the extrapolated surface temperatures may have been less than the actual surface temperatures.

Table 12-1. Average measured coefficients of thermal expansion (CTE) of concrete segments

Segment	Average CTE
1	N/A
2	7.7E-6/°F
3	8.0E-6/°F
4	N/A

Table 12-2. Calculated modulus of elasticity (MOE) of concrete segments

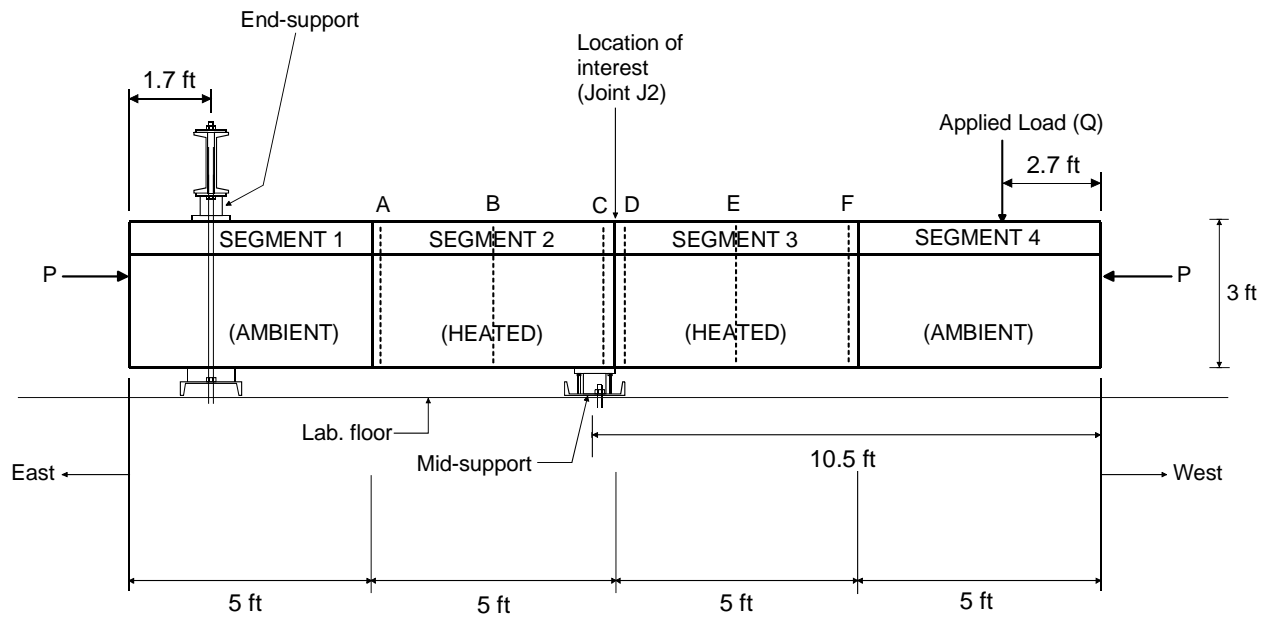
Segment	Age (days)	MOE (ksi)
1	268	5231
2	219	4696
3	206	4695
4	257	5101

Table 12-3. Changes in prestress due to heating of Segments 2 and 3

Bar Designation	Measured Initial Prestress (kips)	Increase in Measured Prestress (kips)	Percentage Increase in Measured Prestress (%)	Calculated Increase in Prestress (kips)	Difference b/n Measured and Calculated Increase in Prestress (%)
P1	94.6	5.6	5.9	5.9	-5.1
P2	87.7	5.2	5.9	5.9	-11.9
P3	90.8	4.5	5.0	5.9	-23.7
P4	89.6	5.8	6.5	5.9	-1.7
Total	362.7	21.1	5.8	23.6	-10.6

Table 12-4. Changes in prestress due to cooling of Segments 2 and 3

Bar Designation	Measured Initial Prestress (kips)	Decrease in Measured Prestress (kips)	Percentage Decrease in Measured Prestress (%)	Calculated Decrease in Prestress (kips)	Difference b/n Measured and Calculated Increase in Prestress (%)
P1	100.2	-5.5	-5.5	-5.6	-1.8
P2	93.0	-5.2	-5.6	-5.6	-7.1
P3	95.3	-4.1	-4.3	-5.6	-26.8
P4	95.4	-5.3	-5.6	-5.6	-5.4
Total	384.0	-20.0	-5.2	-22.4	-10.7



P: Post-tensioning force

Figure 12-1. Laboratory beam

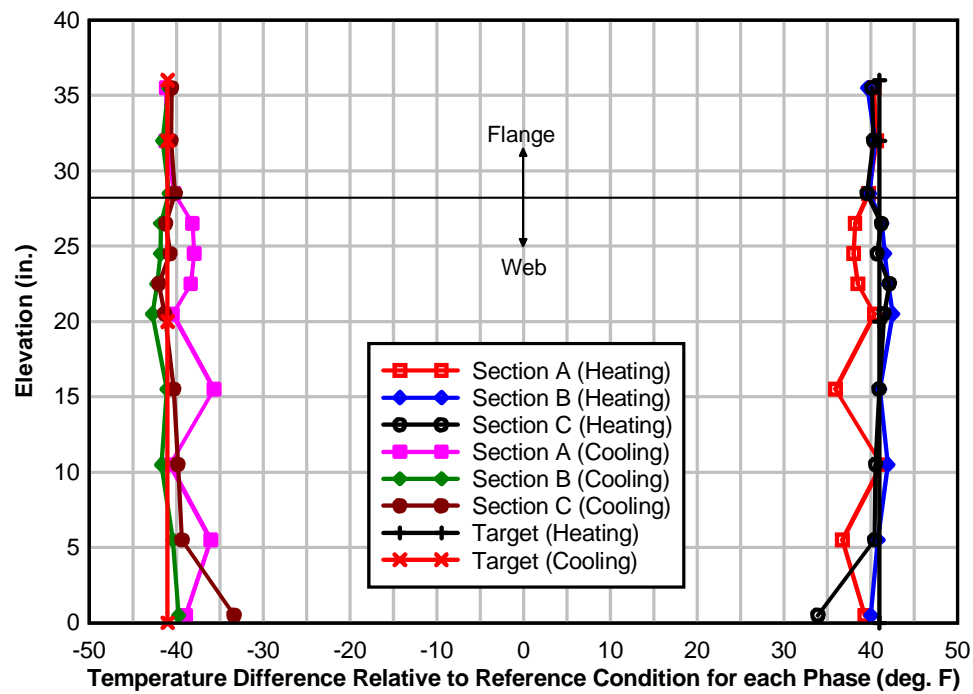


Figure 12-2. Laboratory imposed temperature changes on Segment 2

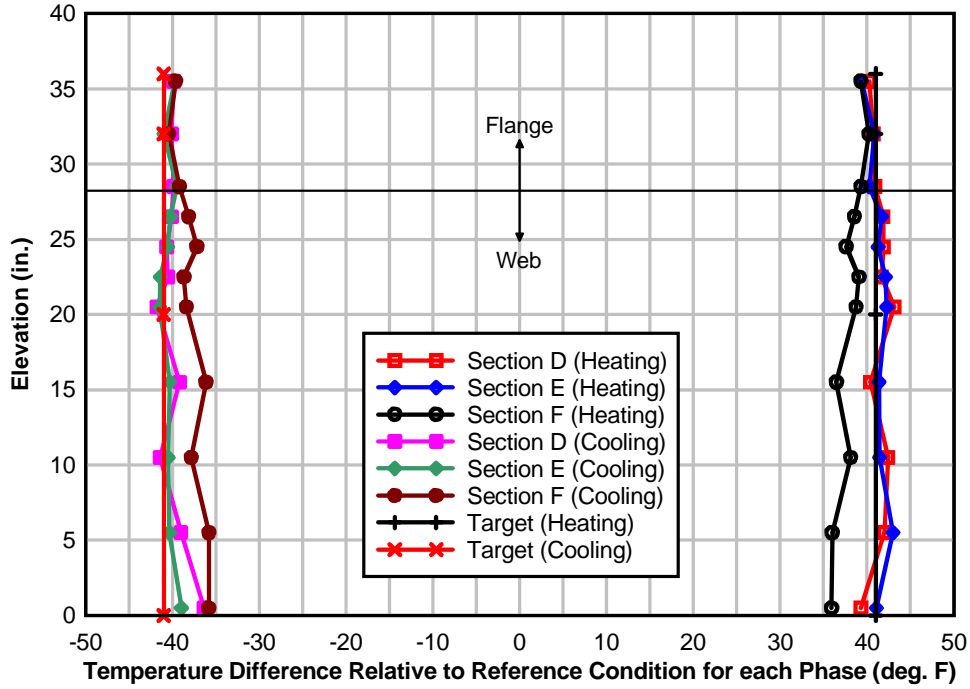


Figure 12-3. Laboratory imposed temperature changes on Segment 3

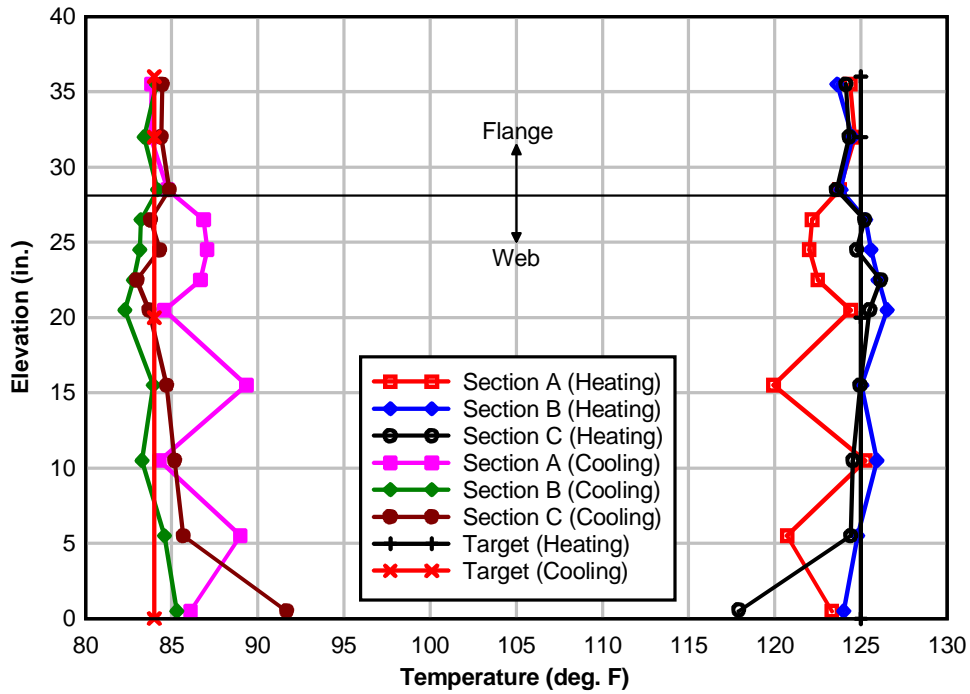


Figure 12-4. Measured concrete temperatures in Segment 2

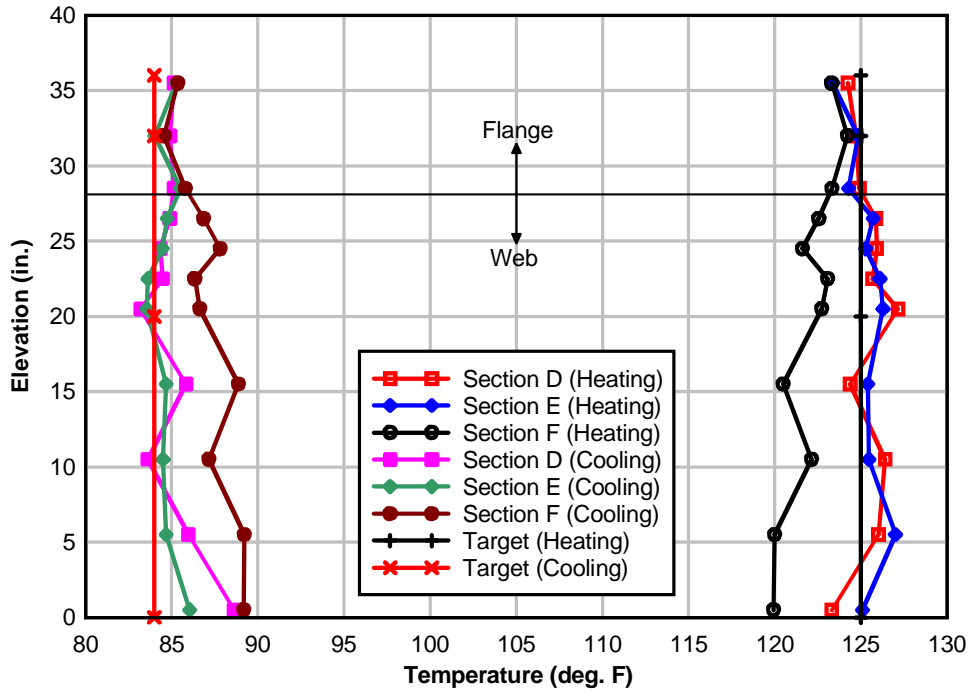


Figure 12-5. Measured concrete temperatures in Segment 3

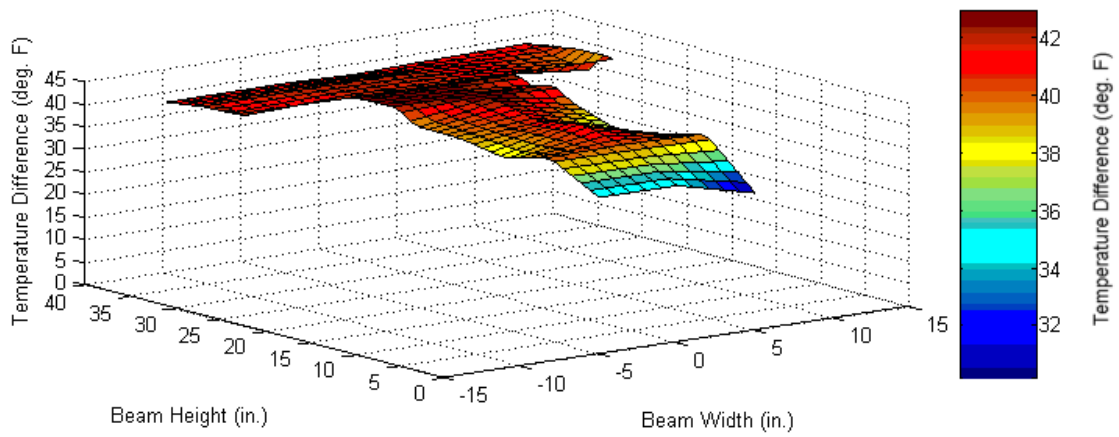


Figure 12-6. Measured temperature changes at Section C (Heating phase)

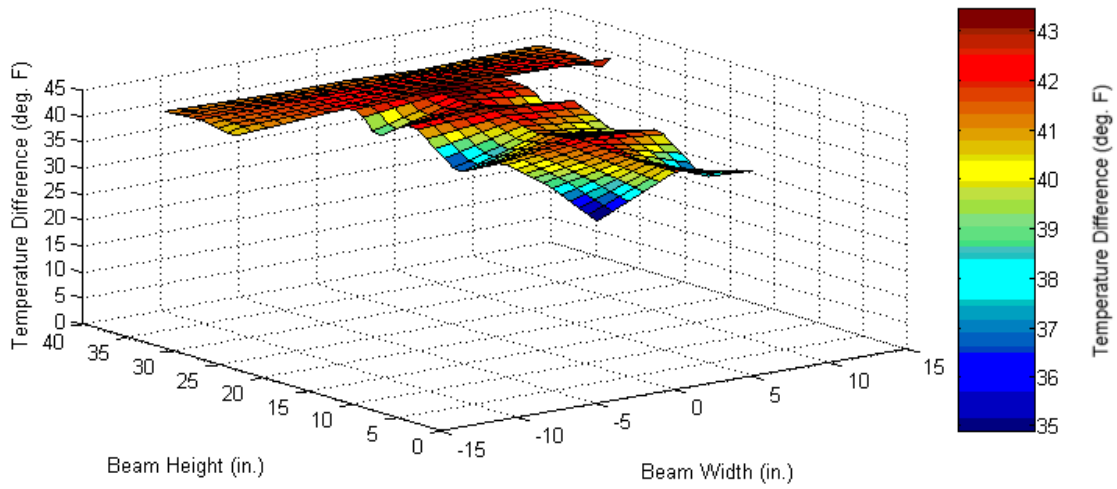


Figure 12-7. Measured temperature changes at Section D (Heating phase)

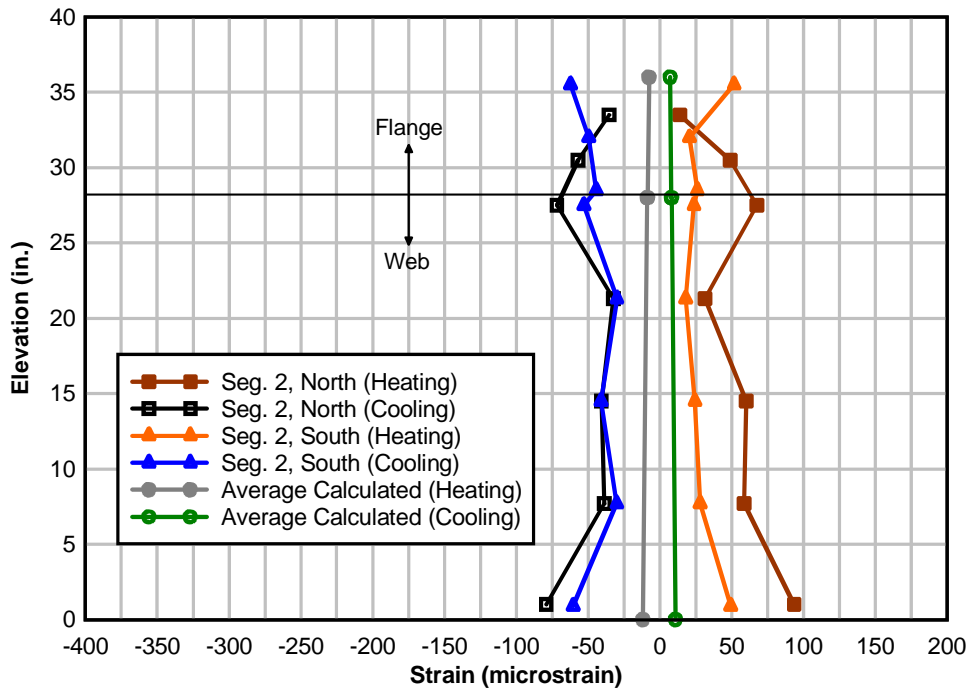


Figure 12-8. Measured strain distribution on Segment 2 (Section C) due to temperature changes

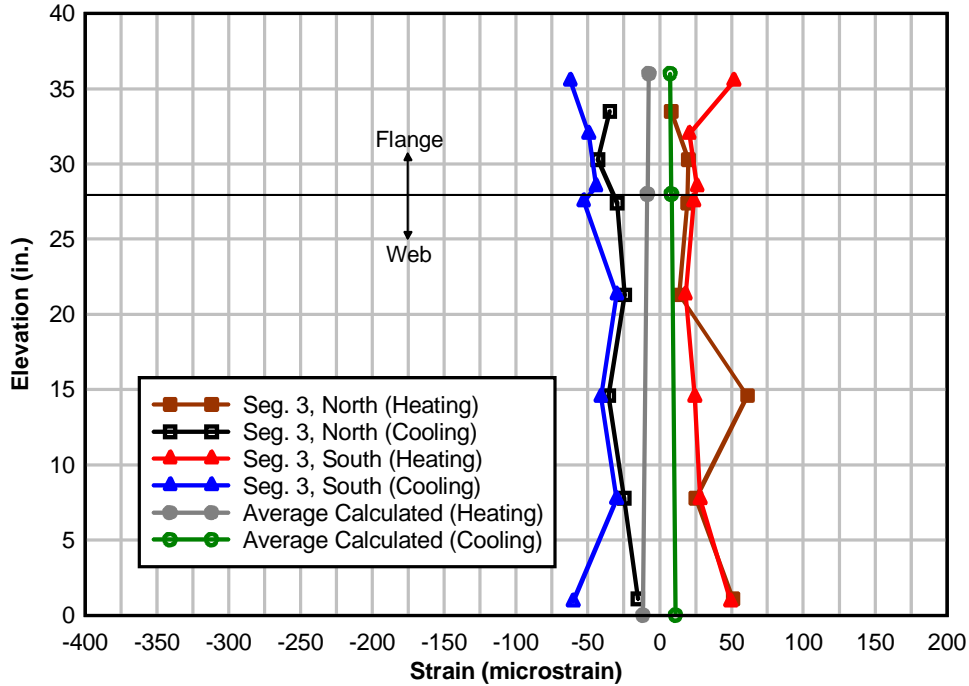


Figure 12-9. Measured strain distribution on Segment 3 (Section D) due to temperature changes

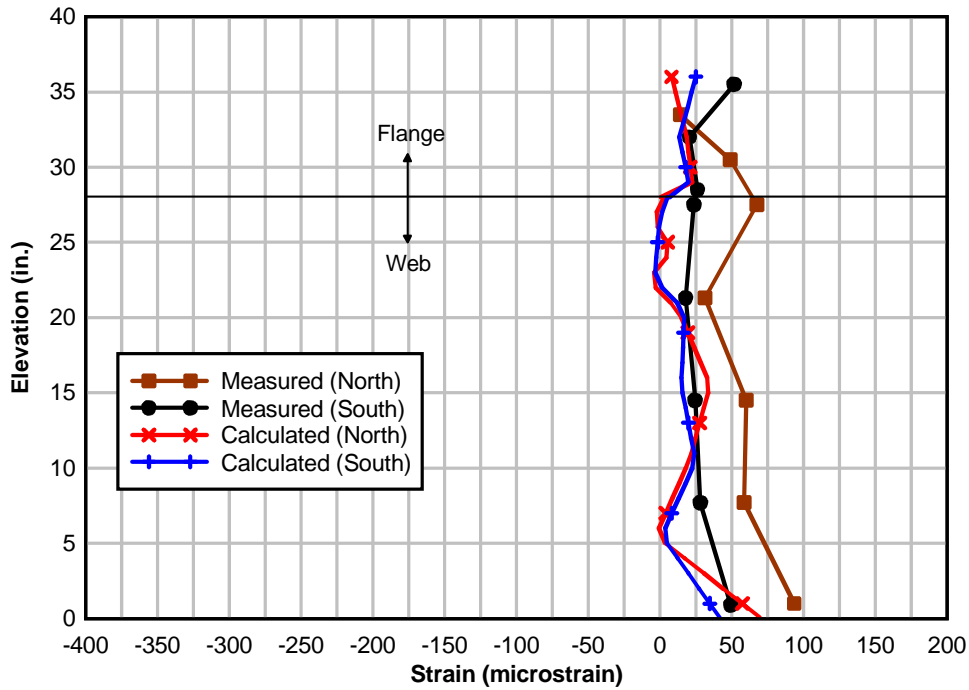


Figure 12-10. Comparison of measured and calculated strains at Section C due to moderately nonuniform temperature distribution (Segment 2, Heating)

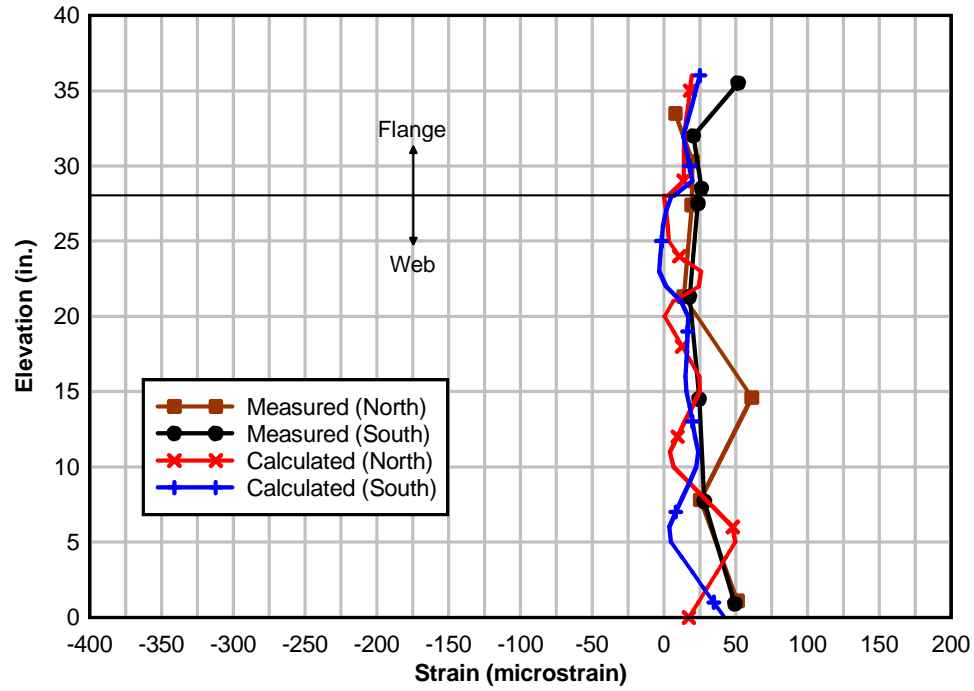


Figure 12-11. Comparison of measured and calculated strains at Section D due to moderately nonuniform temperature distribution (Segment 3, Heating)

CHAPTER 13 RESULTS – AASHTO POSITIVE THERMAL GRADIENT

Results from the application of mechanical loading in combination with the AASHTO positive thermal gradient are presented and discussed in this chapter. The objective of the mechanical-thermal load tests was to experimentally quantify the self-equilibrating thermal stresses caused by the AASHTO nonlinear positive thermal gradient in the top 4 in. of the combined flanges of segments 2 and 3. Two independent methods were used to quantify stresses. The first was to convert measured strains using the elastic modulus, which was determined from tests on cylinders made from the same concrete that was used to construct the beam. Stresses determined using this method will be referred to as elastic modulus derived stresses (E stresses). This is the method most often used to determine stresses, but may be subject to variation from local strain contributions in the concrete surrounding the strain gauge, size effect between cylinder and specimen, or creep and shrinkage. The second method was a more direct measure of stress using the known stress state at incipient joint opening. Stresses determined in this manner will be referred to as joint opening derived stresses (J stresses). In both methods, concrete behavior was assumed to be linear elastic.

Figure 13-1 illustrates the test sequence that was used. Before mechanical or thermal loads were applied, the forces acting on the beam consisted of prestress and self-weight. The test sequence started with partial opening and closing of the joint at midspan (joint J2) with the beam at a constant reference temperature (about 80 °F). As indicated in the figure, strain data from this step were used to establish a reference stress state at joint J2. The AASHTO positive thermal gradient was then imposed on segments 2 and 3. After achieving and maintaining the steady state thermal gradient on the heated segments for 30 to 45 minutes, joint J2 was again partially opened and closed. Strains at this stage were used to determine the thermal stress state. The

heated segments were then cooled to the original reference temperature at the start of the test, after which joint J2 was again partially opened and closed, completing the load cycle.

Joint-opening loads and contact areas at joint J2, as the joint was gradually opened, which were determined from data collected from steps 1 and 3 of the load sequence, were used to calculate self-equilibrating stresses caused by the nonlinear gradient (J stresses). Note that neither the elastic moduli nor the coefficients of thermal expansion of segments 2 and 3 were used in the calculation of the J stresses.

Elastic modulus derived thermal stresses calculated from measured thermal strains close to joint J2 (E stresses) and joint opening derived thermal stresses (J stresses) are presented and discussed in the following sections.

Elastic Modulus Derived Stresses (E stresses)

The nonlinear positive thermal gradient imposed on the heated segments of the laboratory beam (see Figure 13-2) in Step 2 of the load sequence is shown in Figure 13-3. For comparison, Figure 13-3 also shows the AASHTO design positive gradient. Though it did not exactly match the AASHTO gradient, the shape of the laboratory gradient was more representative of typical field measured gradients (see Figure 13-4). Measured temperatures in the heated segments after the positive thermal gradient was imposed are shown in Figure 13-5.

Temperature data for the laboratory-imposed thermal gradient profile was available up to an elevation of 35.5 in. (0.5 in. below the top surface of the flange): the elevation of the topmost thermocouples embedded in the heated segments. Thus the concrete temperature at the top surface of the flanges (at an elevation of 36 in.) was not measured. Because the segments were heated from the inside, rather than externally from solar radiation, it is likely that the top flange surface temperature was equal to or even slightly less than the measured temperature at 35.5 in. For the purpose of calculating theoretical stresses and strains caused by the laboratory gradient,

the magnitude of the thermal gradient at the top surface of the flange was obtained by extrapolating from measured thermal gradient magnitudes at elevations 32 in. and 35.5 in.

Figure 13-6 shows an ideal representation of the components of strains induced in the laboratory beam by the AASHTO design gradient. These strains were calculated according to the procedure outlined in the AASHTO (1989a) guide specifications and the coefficients of thermal expansion given in Table 12-1 (see Chapter 12) using the equation:

$$\varepsilon_T = \alpha \cdot \delta T(z) + \varepsilon_{SE} \quad (13-1)$$

where the unrestrained thermal strain profile ($\alpha \cdot \delta T(z)$) represents the strains that the section would undergo if the section were layered and the layers were free to deform independently. The total strains (ε_T) are generated when compatibility between the layers is enforced. Assuming that plane sections remain plane under the action of flexural deformations, this strain distribution is linear. The total strain (ε_T) includes components caused by axial and flexural restraint, which were not present in the laboratory set-up. The self-equilibrating strains (ε_{SE}), which are the only strains measurable with temperature compensating strain gauges (see Chapter 3 for a complete discussion), make up the final component of the total strains.

The change in strain between the beginning and end of Step 2 at joint J2 are plotted in Figure 13-7 through Figure 13-9. Figure 13-7 and Figure 13-8 show the strain differences along the height of segments 2 and 3, respectively. Figure 13-9 shows a plan view of the strain differences on the top flange near the same joint. Also shown in the figures are two sets of strain changes predicted using the AASHTO design procedure: one using the AASHTO design thermal gradient, and the other using the laboratory-imposed thermal gradient. Because the strain gauges were self-temperature compensating (STC) gauges, and because there was no axial or flexural restraint on the beam, the measured strains consisted only of the self-equilibrating component of

the total strains. The average laboratory-imposed thermal gradient profile (average of profiles at Section A through Section F (see Figure 13-3)) was used in calculating the ‘laboratory gradient’ strains in Figure 13-7 through Figure 13-9.

No marked difference is apparent between measured and predicted strains below approximately 20 in. elevation. Compressive strains were present in the bottom of the section up to an elevation of approximately 10 in. Tensile strains arose in the section mid-height from about 10 in. to 32 in. elevation. A maximum predicted tensile strain (due to the laboratory gradient) of about $52 \mu\epsilon$ was predicted at elevation 28 in., whereas a maximum measured tensile strain of about $65 \mu\epsilon$ occurred at elevation of 27.5 in. The maximum predicted tensile strain due to the AASHTO design gradient, of magnitude about $53 \mu\epsilon$, occurred at an elevation of 20 in.

The difference between locations of maximum predicted tensile strains due to the imposed laboratory gradient and the AASHTO design gradient was due to the difference in the shape of the laboratory and AASHTO design thermal gradients. In each case maximum tensile strain occurred at the location where the change in slope (in units of $^{\circ}\text{F}/\text{in.}$) of the thermal gradient profile was algebraically at a maximum. This occurred between elevations of 27.5 in. and 28.5 in. for the laboratory gradient and at an elevation of 20 in. for the AASHTO design gradient. Compressive strains also occurred above the mid-thickness of the flange with a gradient steeper than that of the remainder of the profile.

Some additional differences between the measured and predicted strains are also notable. Measured compressive strains were significantly smaller in magnitude than predicted at the top of the section in both segments (see Figure 13-9). This was also the case during prestressing (see Chapter 10) and mechanical load tests (see Chapter 11). One explanation for the lower measured compressive strains at the top of the section is the shape of the thermal gradient in the top 4 in. of

the flange. The placement of copper tubes in the flange allowed for a linear gradient between elevations of 32 in. and 35.5 in. The shape and magnitude of the thermal gradient in the top 0.5 in. of the flange was, however, not known. To predict top fiber strains, the magnitude of the thermal gradient in the top flange was obtained by extrapolating from the linear thermal gradient between elevations 32 in. and 35.5 in.

Another possibility is that differential shrinkage on top of the flange at joint J2 contributed to the lower measured strains. Between elevations of 32 in. and 35.5 in., the measured compressive strains more or less followed a linear distribution as did the predicted strains. The measured strains were, however, generally larger than predicted strains between elevations 32 in. and 34 in. and smaller than predicted strains above 34 in. This was attributed to variations between the measured thermal gradients at sections A through F, and the average of these gradients (see Figure 13-10), which was used to predict strains per the AASHTO design procedure.

The uniform and linear sub-components of the overall nonlinear thermal gradient were expected to lead to additional stresses in the concrete as segments 2 and 3 were heated during Step 2. Expansion of the segments relative to the prestressing caused a net increase in prestressing force. However, the measured peak increase was only 0.4% of the initial prestress and was therefore considered negligible.

Elastic modulus derived stresses (E stresses) were the self-equilibrating thermal stresses caused by the positive thermal gradient, and were determined by multiplying the measured strains in Figure 13-7 and Figure 13-8 by the elastic moduli of Segment 2 (4760 ksi) and Segment 3 (4760 ksi), respectively. The elastic moduli were calculated by linearly interpolating

cylinder modulus of elasticity data between test ages of 28 and 360 days. At the time of the test, the ages of segments 2 and 3 were 232 and 219 days, respectively.

Figure 13-11 and Figure 13-12 show E stress distributions near joint J2 on Segment 2 and Segment 3, respectively. For comparison, self-equilibrating thermal stresses were also calculated using the AASHTO recommended procedure discussed in Chapter 3, the laboratory thermal gradient, and the AASHTO design gradient. CTEs from Table 12-1 and the segment MOEs noted above were used in these calculations.

Table 13-1 compares E stresses computed at the top of the flanges of segments 2 and 3 with similar stresses obtained by extrapolating from the linear E stress distributions between elevations 32 in. and 35.5 in. (see Figure 13-11 and Figure 13-12) on the sides of the segment flanges. E stresses in the extreme top flange fibers were significantly lower than stresses extrapolated to the same location. This condition follows from the relatively smaller stress-inducing thermal strains that were measured at the top surfaces of the flanges (see Figure 13-9). As discussed previously, the smaller strains were attributed to differential shrinkage at joint J2 and to a lower thermal gradient magnitude than was targeted for the top of the flanges of the segments. At an elevation of 32 in., E stresses in segments 2 and 3 (see Figure 13-11 and Figure 13-12) were compressive whereas predicted stresses were tensile. This was attributed to the difference in magnitude of the laboratory thermal gradients at sections A through F (from the average thermal gradient used in predicting stresses) at that elevation; the location of the maximum slope change in the thermal gradients (see Figure 13-13).

E stresses and predicted stresses caused by the laboratory-imposed thermal gradient in the top 4 in. of the flanges of segments 2 and 3 are compared in Table 13-2. Predicted stresses in the extreme top flange fibers (where the maximum compressive stresses were expected to occur had

the gradient been linear in the top 4 in. of the flanges) are not shown in the table because the shape and magnitude of the thermal gradient at that location were not measured. E stresses 0.5 in. below the top flange (maximum E stresses) were approximately 3% and 8% less than corresponding predicted stresses in Segment 2 and Segment 3, respectively. Taking into consideration the possible effects of differential shrinkage at joint J2, these differences were considered to be within the limits of experimental error.

Joint – Opening Derived Stresses (J Stresses)

The known stress state at incipient joint opening was used to determine stresses caused by the laboratory positive thermal gradient without converting measured strains to stresses using the elastic moduli of the concrete segments. The magnitude of stresses caused by the thermal gradient in the top 4 in. of segments 2 and 3 at joint J2 were quantified using data collected from steps 1 and 3 of the load sequence shown in Figure 13-1. This was accomplished by loading the specimen until joint J2 began to open. At the condition of joint opening, it is known that the normal concrete stress near the joint face is zero (due to lack of contact). Assuming linear elastic behavior for subsequent short-term loads (thermal or mechanical), it was possible to extrapolate concrete stresses from the known (zero) stress state. Section properties of the contact area at joint J2, after joint opening, were used to calculate these stresses (J stresses).

Figure 13-14 and Figure 13-15 illustrate the J stress calculation procedure using component stress blocks. Stresses at joint J2 prior to Step 1 of the load sequence consisted of stresses caused by prestress (P) and the self-weight (SW) of the beam. In Step 1, joint J2 was opened and closed at the reference temperature of the beam. The state of stress in the contact area at the joint caused by the joint-opening load, Q_R , will be referred to as the reference stress state (see Figure 13-14). In Step 2 the positive thermal gradient was applied. Stresses at joint J2 consisted of stresses caused by prestress (P), self-weight (SW), and the nonlinear positive

thermal gradient (PG). In Step 3 of the load sequence, joint J2 was again opened and closed. The state of stress in the contact area at the joint caused by the joint-opening load, Q_T , will be referred to as the thermal stress state (see Figure 13-15). At incipient joint opening, flexural stresses caused by Q_R and Q_T in the extreme top flange fibers were equal, but opposite, to the existing normal stresses caused by $(P + SW)$ and $(P + SW + PG)$, respectively, at the same location. This condition was used to quantify self-equilibrating thermal stresses caused by the nonlinear positive thermal gradient. Though the concept of creating a zero stress condition at joint J2 is illustrated for the extreme top flange fibers, it is generally applicable to any shape of contact area. A general discussion of joint-opening and its uses in quantifying self-equilibrating thermal stresses follows.

Figure 13-16 shows uniform opening of joint J2 to a known depth 'h' below the extreme top flange fibers. Because the joint opens uniformly across the width of the section, the boundary (referred to as the contact boundary in the figure) between open and closed parts of the joint is perpendicular to the sides of the segments. The joint opens in this manner when the line of action of the joint-opening load passes through the axis of symmetry of the contact area, and normal stresses existing prior to opening the joint are a function of depth only (i.e. uniformly distributed across the width of the section at all depths). If these conditions hold true for load cases without the thermal gradient $(P + SW)$ and with the thermal gradient $(P + SW + PG)$, then the contact area at the reference and thermal stress states is the same (Figure 13-16 (B)). If the distribution of existing normal stresses at the joint caused by $(P + SW)$ and/or $(P + SW + PG)$ varies across the depth and width, the depth of joint opening would not be uniform across the width of the segments, as was found to be the case for the laboratory beam. As shown in Figure

13-17, the contact areas at the reference and thermal stress states are in general not the same under these conditions.

The zero stress condition created by superimposing stresses caused by the joint-opening loads Q_R and Q_T (see Figure 13-14 and Figure 13-15) on existing normal stresses along corresponding contact boundaries is shown mathematically in the following equations:

$$f_p(y, z) + f_{sw}(y, z) + f_R(y, z) = 0, \{(y, z) \in R\} \quad (13-2)$$

$$f_p(y, z) + f_{sw}(y, z) + f_J(y, z) + f_T(y, z) = 0, \{(y, z) \in T\} \quad (13-3)$$

Then,

$$f_J(y, z) = f_R(y, z) - f_T(y, z), \{(y, z) \in R \cap T\} \quad (13-4)$$

where f_p is the concrete stress in the contact area due to prestressing force, f_s is the stress caused by self-weight, f_J is the J stress (self-equilibrating concrete stress caused by nonlinear positive thermal gradient), f_R is the reference stress state, f_T is the thermal stress state, R is the contact boundary at the reference stress state, T is the contact boundary at the thermal stress state, and y and z are vertical and horizontal coordinates of points on contact boundaries, respectively.

These equations are valid only along the contact boundary corresponding to each stress state. For example, Equation 13-2 and Equation 13-3 are applicable along line AB in Figure 13-16. In Figure 13-17, however, Equation 13-2 is applicable along line AB while Equation 13-3 is applicable along line AC. Equation 13-4, which is obtained by taking the difference between the reference stress state and thermal stress state, is valid only at point A in Figure 13-17, where the contact boundary at the reference stress state is at the same elevation as the contact boundary at the thermal stress state. Equation 13-4 shows that self-equilibrating thermal stresses caused by the nonlinear positive thermal gradient at the points of intersection of the contact boundaries can be determined if stresses caused by Q_R and Q_T are known.

The load that caused joint J2 to open at a known depth 'h' at the reference and final stress states was determined from load vs. strain curves of strain gauges adjacent to the joint. Because the laboratory beam was statically determinate, the bending moment at joint J2 was determined from the joint-opening load without taking the change in stiffness of the beam, caused by opening the joint, into account. Assuming that plane sections remained plane under the actions of the forces and moments acting at the joint, stresses caused by joint-opening loads at the reference and final stress states along corresponding contact boundaries were determined with the aid of stress-strain diagrams of the concrete segments and equations of statics. Assuming further that the behavior of the beam was linear elastic under the action of the applied loads, it became possible to determine stresses without measuring strain.

For stresses due to joint-opening loads to be determined without explicitly using the elastic/tangent modulus of concrete (i.e. without the stress-strain curve), the material behavior of concrete within the load ranges considered had to be linear elastic. Furthermore, the distribution of strain through the depth of the contact area at joint J2 (after opening the joint) had to be a linear function of curvature (i.e. plane sections remain plane). It was assumed that concrete was homogeneous and isotropic. Linear elastic material behavior of the beam segments within the range of mechanical loads applied during testing was supported by data from cylinder tests, which showed that the beam segments were linear elastic up to stresses of about 6000 psi (uniaxial compression). Distributions of measured concrete strain through the depth of evolving contact areas near joint J2 were approximately linear as the joint was opened. This was evidence of plane sections remaining plane, within the contact area, under flexure. Data collected from in-situ CTE tests conducted on the heated segments showed that, within the temperature ranges to which the segments were subjected during testing, plane sections remained plane and thermal

strains were a linear function of temperature difference. Based on these observations flexural stresses due to joint-opening loads were determined using classical flexural stress formulas.

Figure 13-18 and Figure 13-19 show variations of concrete strain with applied load near joint J2 on the North side of Segment 3 at the reference stress state (reference temperature) and thermal stress state (with positive thermal gradient), respectively. Similar plots near the same joint on the South side of Segment 3 are shown in Figure 13-20 and Figure 13-21, respectively. The variation of concrete strain with applied load on top of the flanges of segments 2 and 3 near joint J2 at the reference and thermal stress states are shown in Figure 13-22 and Figure 13-23, respectively. Data collected from strain gauges near joint J2 on Segment 2 (which were similar to those from Segment 3), LVDTs mounted across joint J2 on top of the flanges of segments 2 and 3, and LVDTs mounted across the same joint on the South side can be found in Appendix D. The variation of measured strains and measured displacements with load near joint J2 on the South side, North side, and on top of the flanges of segments 2 and 3 was discussed in detail in Chapter 11.

Two general observations can be made when measured concrete strains at the same side of joint J2 and LVDT readings at the reference and thermal stress states are compared. These observations are illustrated in Figure 13-24 with data from the strain gauges at elevations 33.5 in. and 35.3 in. on the North and South sides of joint J2, respectively. The first is that at the same elevation in the top 4 in. of the flange, the joint opened at higher loads at the thermal stress state than it did at the reference stress state (i.e. $Q_{TN} > Q_{RN}$ and $Q_{TS} > Q_{RS}$). This is also evident in the top flange strains shown in Figure 13-22 and Figure 13-23, and LVDT data (see Figure D-5 through Figure D-8 in Appendix D). Opening of joint J2 at higher loads at the thermal stress

state was consistent with the development of compressive strains in the top concrete fibers caused by the positive thermal gradient.

The second observation is that although smaller strains were recorded on the South side of the joint than on the North side (i.e. $\epsilon_{RS} < \epsilon_{RN}$ and $\epsilon_{TS} < \epsilon_{TN}$ in Figure 13-24), the strain difference between vertical portions of strain diagrams at the reference and thermal stress states ($\Delta\epsilon_S$ and $\Delta\epsilon_N$) was independent of the side of the joint on which strain gauges were located. The strain difference was, however, dependent on the distribution of stress-inducing concrete strains caused by the positive thermal gradient at joint J2 (and therefore the elevation of gauges). In Figure 13-24 the strain difference on the North side at elevation 33.5 in. ($\Delta\epsilon_N$) was less than the strain difference on the South side of the joint at elevation 35.3 in. ($\Delta\epsilon_S$). This was because the gauge on the South side was at a higher elevation than the gauge on the North side.

Since the strain difference between vertical portions of strain curves at the reference and thermal stress states represented strains caused by the positive thermal gradient at joint J2, it was evident that within the top 4 in. of the flange, these strains (and corresponding stresses) decreased in compression, with the maximum strains and stresses occurring in the top fibers of the section. This was consistent with the expected distribution of self-equilibrating thermal stresses within the top 4 in. of the flange (see predicted strains and stresses in the discussion of E stresses)

Loads that caused joint J2 to open at the reference and thermal stress states were detected using load vs. strain data (detection of joint-opening loads using strain gauges was discussed in Chapter 11). LVDT data were mainly used to check joint-opening loads determined with strain gauges, especially on top of the flange, where very low strains were recorded at the reference stress state. Applied loads at the cantilevered-end of the test beam, that caused joint J2 to open at

various depths, are shown in Figure 13-25. Each point in the figure shows the average load (determined from gauges on segments 2 and 3 on the same side (North or South) of the joint) at which the change in strain at that location became zero. These points were used to define the boundary of the contact area at varying loads. The sign convention for moments and curvatures is shown in Figure 13-26. Tensile stresses caused by joint-opening loads are positive and compressive stresses are negative. Recall that tensile stresses are actually reductions of the initial compressive stresses caused by prestressing.

Figure 13-27 through Figure 13-29 show estimated contact areas at joint J2 at the reference and thermal stress states just as opening of the joint was detected from strain gauges at elevations of 35.5 in. (South), 33.5 in. (North), and 32.0 in. (South), respectively. Contact boundaries are indicated by dashed lines. Contact areas were estimated by interpolating between joint-opening loads and the positions of the strain gauges from which the loads were determined (see Figure 13-25). Total stresses caused by moments at joint J2 due to joint-opening loads and changes in prestress were determined using the contact area cross sections and Equation 13-5 through Equation 13-11.

$$f(z, y, M_z, M_y, I_z, I_y, I_{zy}, \Delta p, A) = \frac{(M_y \cdot I_z + M_z \cdot I_{zy}) \cdot z - (M_z \cdot I_y + M_y \cdot I_{zy}) \cdot y}{I_y \cdot I_z - I_{zy}^2} - f_N(\Delta p, A) \quad (13-5)$$

$$M_y = -\Delta M_{P_v} \quad (13-6)$$

$$M_z = M_Q - \Delta M_{P_h} \quad (13-7)$$

$$f_N(p, A) = \frac{-\left(\sum_{i=1}^4 P_i\right)}{A} \quad (13-8)$$

$$\Delta M_{P_h}(\Delta p, e_y) = \sum_{i=1}^4 (\Delta p_i \cdot e_{i_y}) \quad (13-9)$$

$$\Delta M_{P_v}(\Delta p, e_z) = \sum_{i=1}^4 (\Delta p_i \cdot e_{i_z}) \quad (13-10)$$

$$M_Q = x_{J2} \cdot Q \quad (13-11)$$

Where, f is the total stress caused by the joint-opening load (Q), f_N is the stress caused by changes in prestress at load Q, M_Q is the moment of joint-opening load (Q) at joint J2, Δ_p is the change in prestress at load Q, e_{iy} is the vertical eccentricity of post-tensioning bar 'i', e_{iz} is the horizontal eccentricity of post-tensioning bar 'i', ΔM_{P_y} is the moment about the vertical axis due to changes in prestress, ΔM_{P_h} is the moment about the horizontal axis due to changes in prestress, I_z is the moment of inertia of the section about the horizontal axis, I_y is the moment of inertia of the section about the vertical axis, I_{zy} is the product of inertia of the section, z is the horizontal coordinate of the point at which stress is calculated, y is the vertical coordinate of point at which stress is calculated, and x_{J2} is the moment arm of the joint-opening load from joint J2.

Though data from strain gauges and LVDTs on top of the flanges of segments 2 and 3 were useful in estimating contact areas, top flange stresses could not be determined with these equations. This was because the condition of the joint at the top of the flanges (see Figure 11-6) violated the assumptions under which the equations could be used.

Table 13-3 shows calculated J stresses at the locations of strain gauges on the sides of the beam within the top 4 in. of the flange. Though the total stresses (stresses determined from Equation 13-5 are positive, indicating tension, they actually represent relief of prestressing-induced compressive stresses at J2 that were present prior to the application of joint-opening loads. The J stresses were then determined by taking the difference between total stresses at the reference stress state and total stresses at the final stress state.

In Equation 13.5, the total stress is made of two components; the stress component due to the joint opening load and the stress component due to changes in prestress. Changes in prestress (determined from measured prestress forces and section properties) accounted for less

than 0.5% of total stresses. The calculated total stresses were therefore essentially dependent on the magnitude of joint opening loads. J stresses, however, were dependent only on the difference between the joint-opening loads at the reference and thermal stress states. For example, the loads initiating opening of joint J2 on the North side at an elevation of 33.5 in. were greater than on the South side at an elevation of 35.5 in. as can be seen from the magnitudes of the moments in Table 13-3. However, calculated J stresses at an elevation of 33.5 in. were lower than J stresses at an elevation of 35.5 in. This was expected since the distribution of self-equilibrating thermal stresses within the top 4 in. of the flanges of segments 2 and 3 was expected to increase linearly (in compression) from a minimum magnitude at an elevation of 32 in. to a maximum magnitude at the top flange (elevation 36 in.).

J stresses and predicted stresses in the top 4 in. of the flange are compared in Table 13-4. J stresses 0.5 in. below the top of the flange (maximum J stresses) were approximately 10% and 15% less than corresponding predicted stresses in Segment 2 and Segment 3, respectively. At elevation 32 in., J stresses were about 82% less than predicted stresses. Both predicted and J stresses were, however, tensile. As was the case for E stresses, this was attributed mainly to the difference in magnitude between the measured thermal gradients and the average thermal gradient (with which stresses were predicted).

J stresses and E stresses in the top 4 in. of the flange are compared in Table 13-5. Both sets of stresses compared well except at elevation 32 in. A possible reason for this discrepancy was noted above. Maximum J stresses (at elevation 35.5 in.) were about 7% and 8% less than maximum E stresses on Segment 2 and Segment 3, respectively.

Table 13-1. Comparison of E stresses and extrapolated stresses on top of segment flanges near joint J2 (laboratory positive thermal gradient)

	Measured (psi)	Extrapolated (psi)	Measured/Extrapolated
Segment 2, North	-307	-786	0.391
Segment 2, South	-438	-732	0.598
Segment 3, North	-463	-772	0.600
Segment 3, Middle	-518	-751	0.690
Segment 3, South	-499	-729	0.684

Table 13-2. Comparison of E stresses and predicted self-equilibrating thermal stresses caused by laboratory positive thermal gradient near joint J2

Segment 2			
Elevation (in.)	Average E Stress (psi)	Average Predicted (psi)	E Stress/Predicted
36	-373	N/A	N/A
35.5	-671	-693	0.968
33.5	-320	-219	1.461
32	-57	137	-0.416
Segment 3			
Elevation (in.)	Average E Stress (psi)	Average Predicted (psi)	E Stress/Predicted
36	-493	N/A	N/A
35.5	-674	-729	0.925
33.5	-369	-230	1.604
32	-140	144	-0.972

Table 13-3. J stresses in top 4 in. of flange

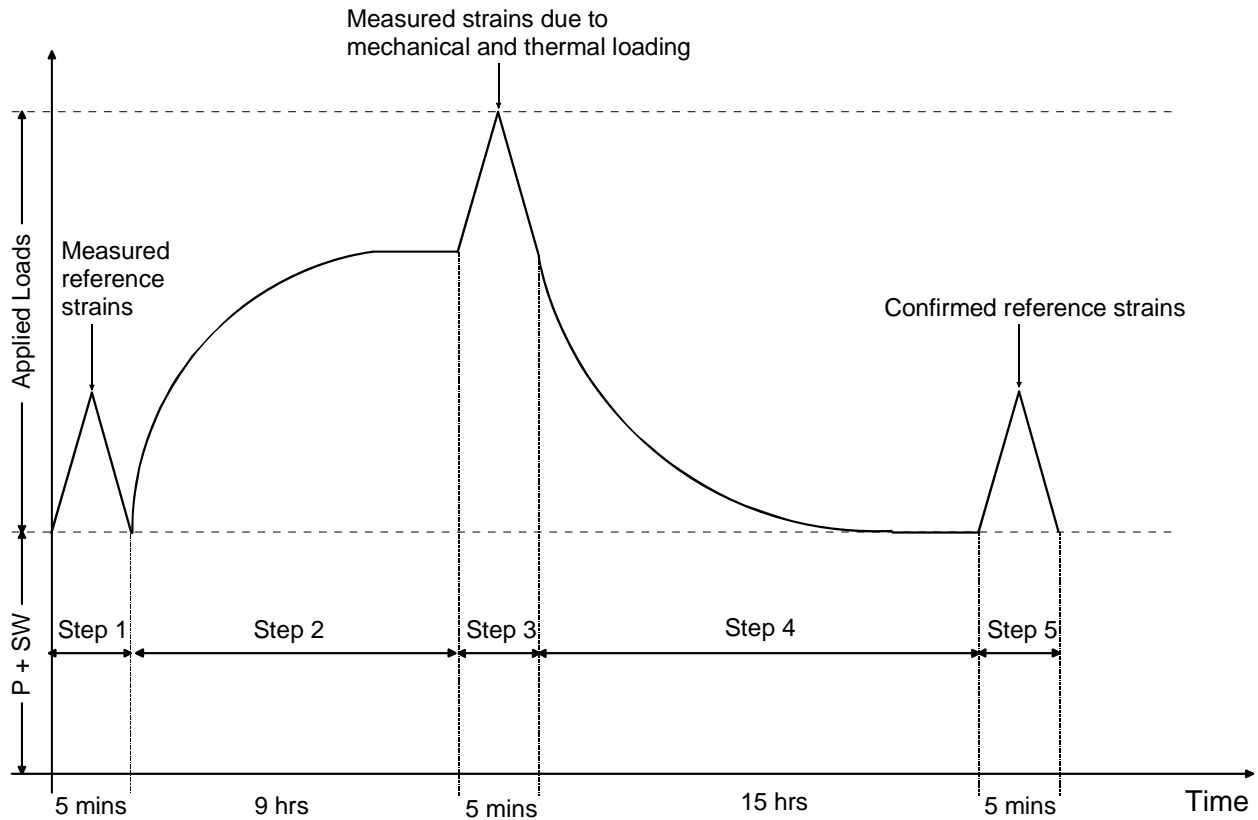
Gauge Elevation	Moments due to Joint-opening Loads (kip-in.)		Total Stresses (psi)		J Stress (psi)
	Reference	Thermal	Reference	Thermal	
35.5 in. S	1399	2889	366	989	-623
33.5 in. N	2790	4063	801	1124	-323
32.0 in. S	1833	2645	558	533	25

Table 13-4. Comparison of J stresses and predicted stresses in top 4 in. of flange

Segment 2			
Gauge Elevation	J Stress (psi)	Predicted Stress (psi)	J Stress/Predicted Stress
35.5 in. S	-623	-693	0.899
33.5 in. N	-323	-219	1.475
32.0 in. S	25	137	0.182
Segment 3			
Gauge Elevation	J Stress (psi)	Predicted Stress (psi)	J Stress/Predicted Stress
35.5 in. S	-623	-729	0.855
33.5 in. N	-323	-230	1.404
32.0 in. S	25	144	0.174

Table 13-5. Comparison of J stresses and E stresses in top 4 in. of flange

Segment 2			
Gauge Elevation	J Stress (psi)	E Stress (psi)	J Stress/E Stress
35.5 in. S	-623	-671	0.928
33.5 in. N	-323	-320	1.009
32.0 in. S	25	-57	-0.439
Segment 3			
Gauge Elevation	J Stress (psi)	E Stress (psi)	J Stress/E Stress
35.5 in. S	-623	-674	0.924
33.5 in. N	-323	-369	0.875
32.0 in. S	25	-140	-0.179

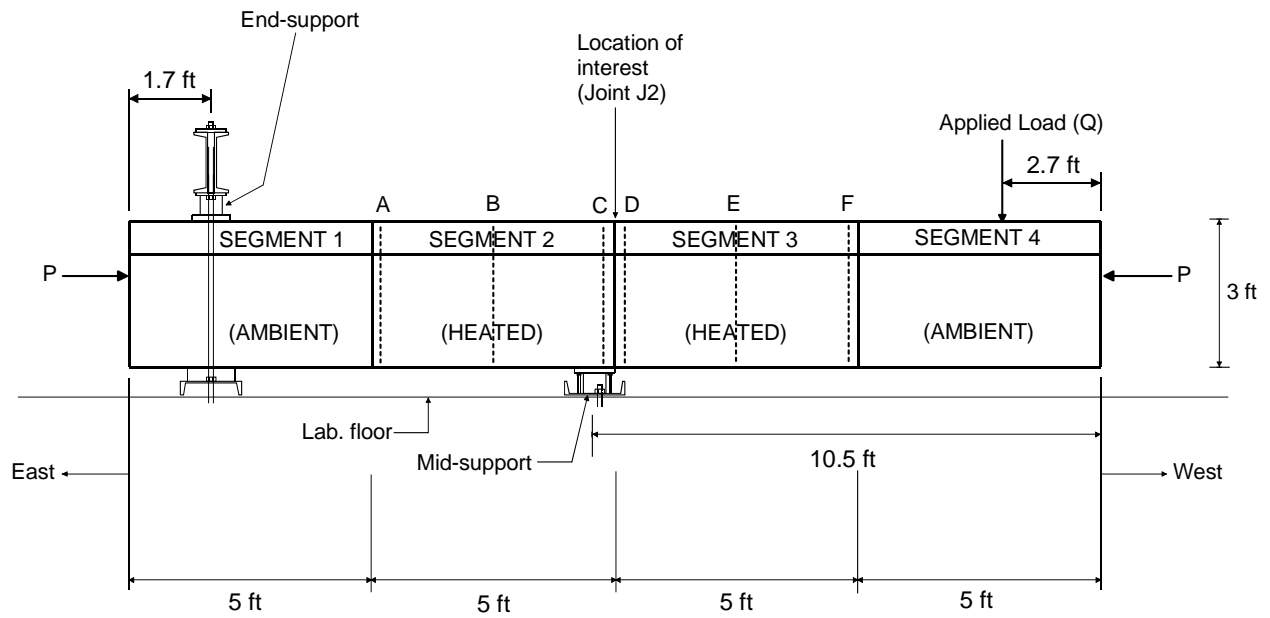


P + SW: Pretress + Self-weight

Applied Loads:

- Step 1: Opening and closing of joint J2 (application and removal of mechanical loads)
- Step 2: Positive thermal gradient (application of thermal load)
- Step 3: Opening and closing of joint J2 (application and removal mechanical loads)
- Step 4: Cooling to reference temperature at start of test (removal of thermal loads)
- Step 5: Opening and closing of joint J2 (application and removal of mechanical loads)

Figure 13-1. Sequence of load application (positive gradient test)



P: Post-tensioning force

Figure 13-2. Laboratory beam

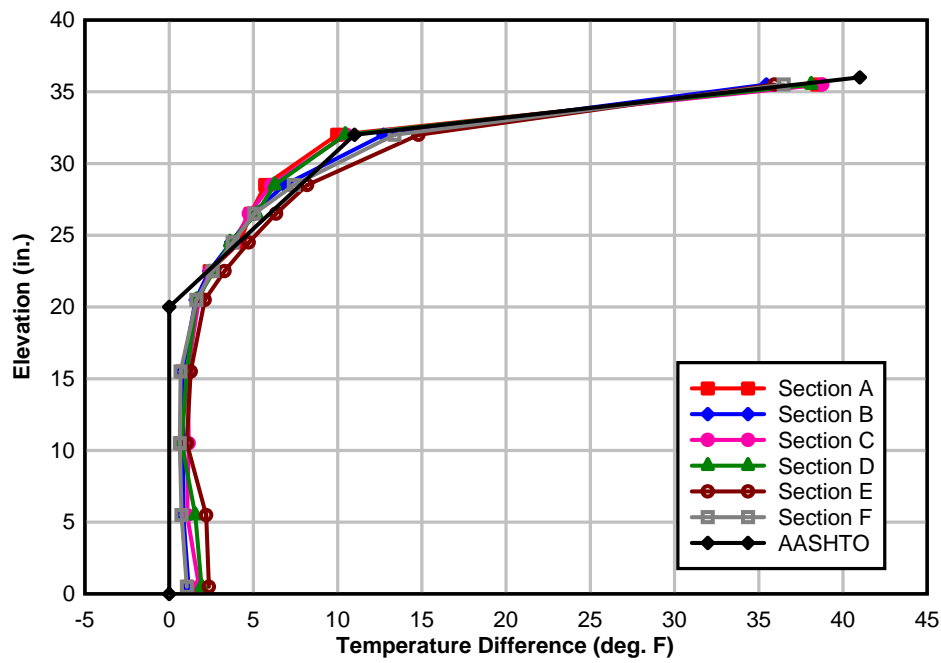


Figure 13-3. Laboratory imposed positive thermal gradient

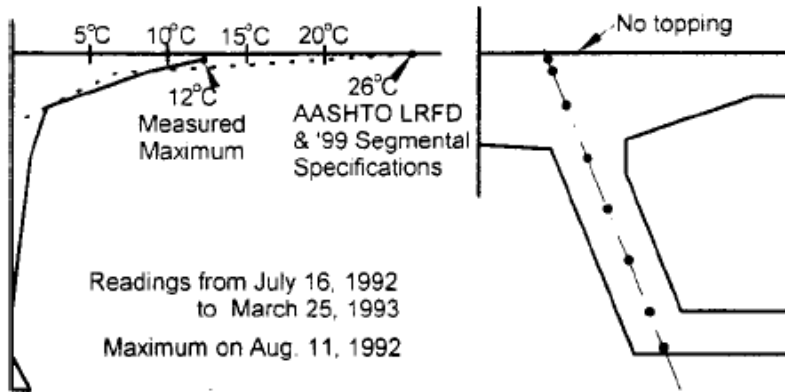


Figure 13-4. Typical field measured positive thermal gradient (Roberts, C. L., Breen, J. E., Cawrse J. (2002)., "Measurement of Thermal Gradients and their Effects on Segmental Concrete Bridge," ASCE Journal of Bridge Engineering, Vol. 7, No. 3, Figure 4a, pg. 168)

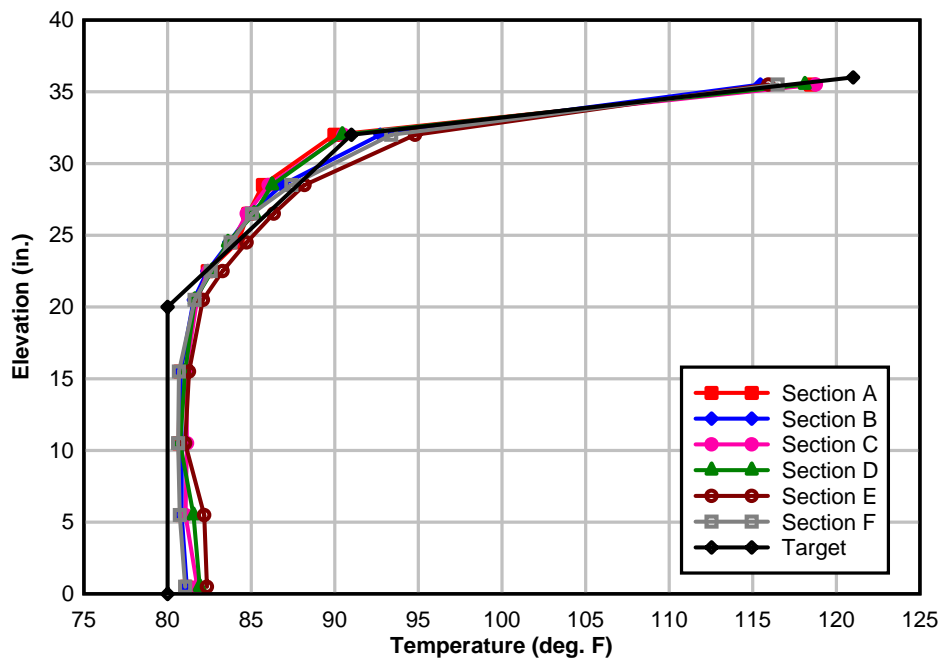


Figure 13-5. Measured temperatures in heated segments (positive thermal gradient)

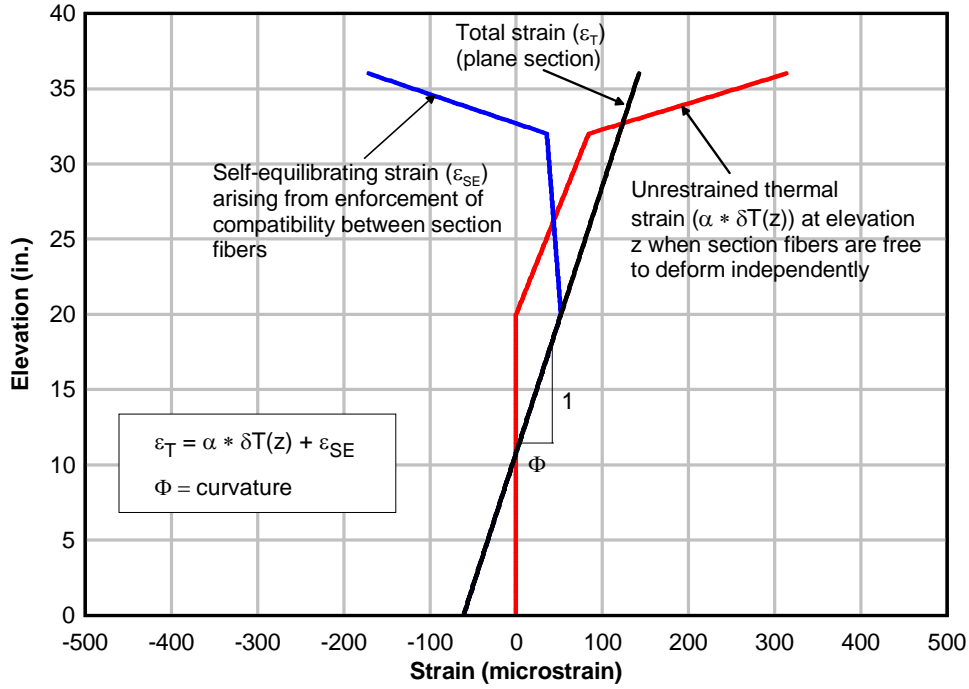


Figure 13-6. Calculated strain components of the AASHTO positive thermal gradient

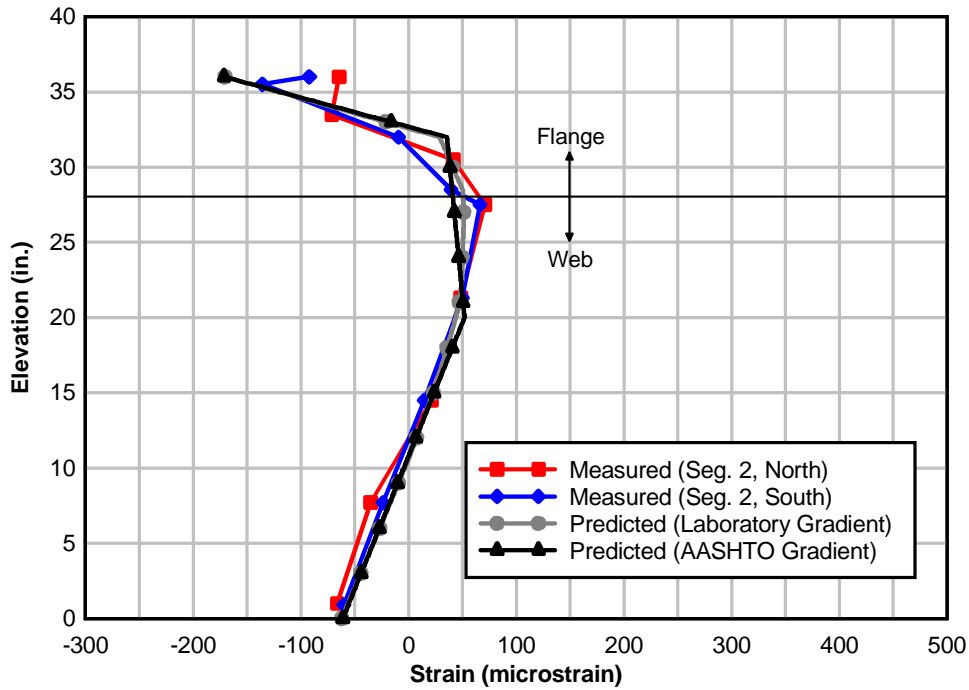


Figure 13-7. Measured and predicted strains near joint J2 (Segment 2)

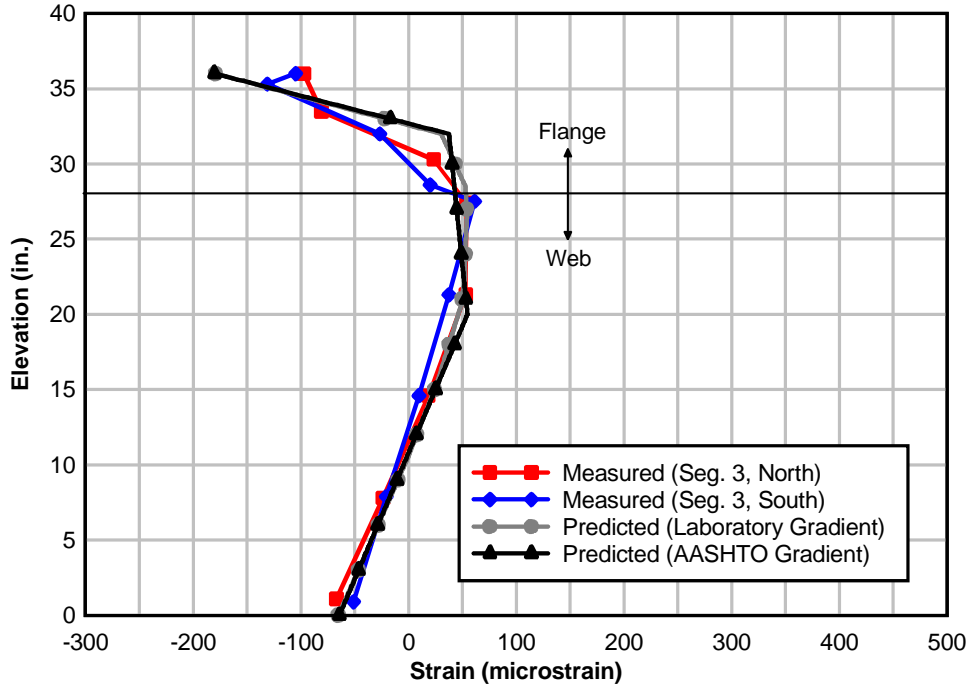


Figure 13-8. Measured and predicted strains near joint J2 (Segment 3)

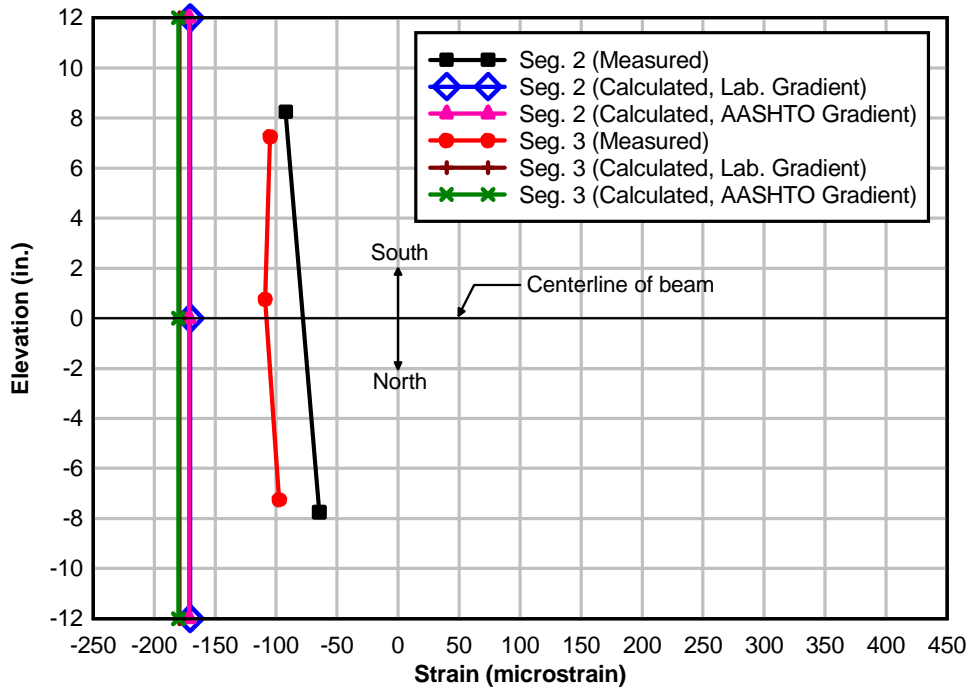


Figure 13-9. Plan view of measured and predicted strains near joint J2 (Top Flange)

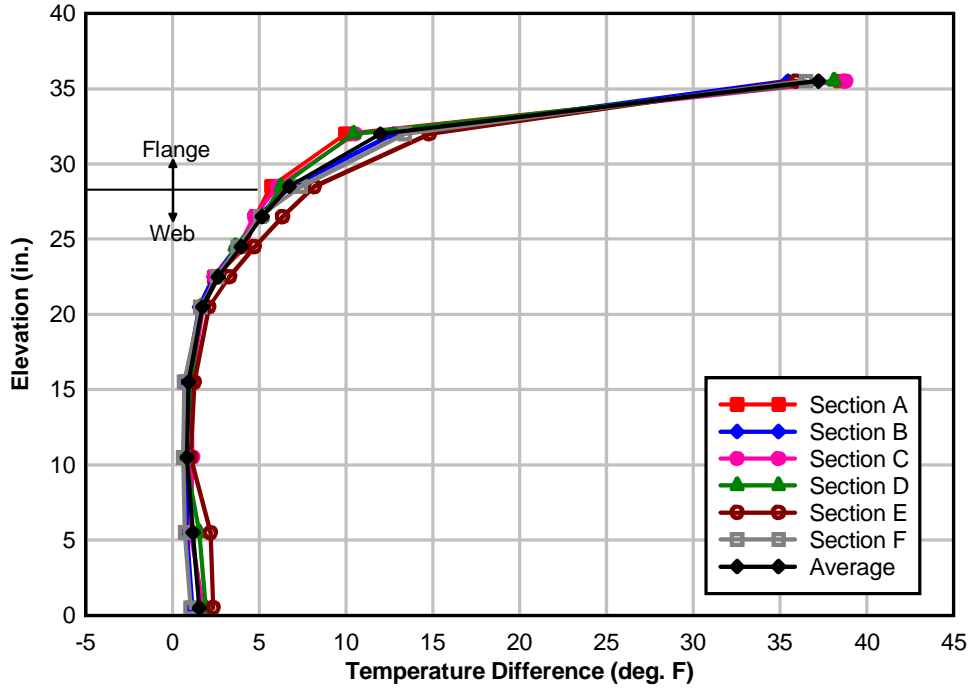


Figure 13-10. Comparison of measured thermal gradient profiles with average

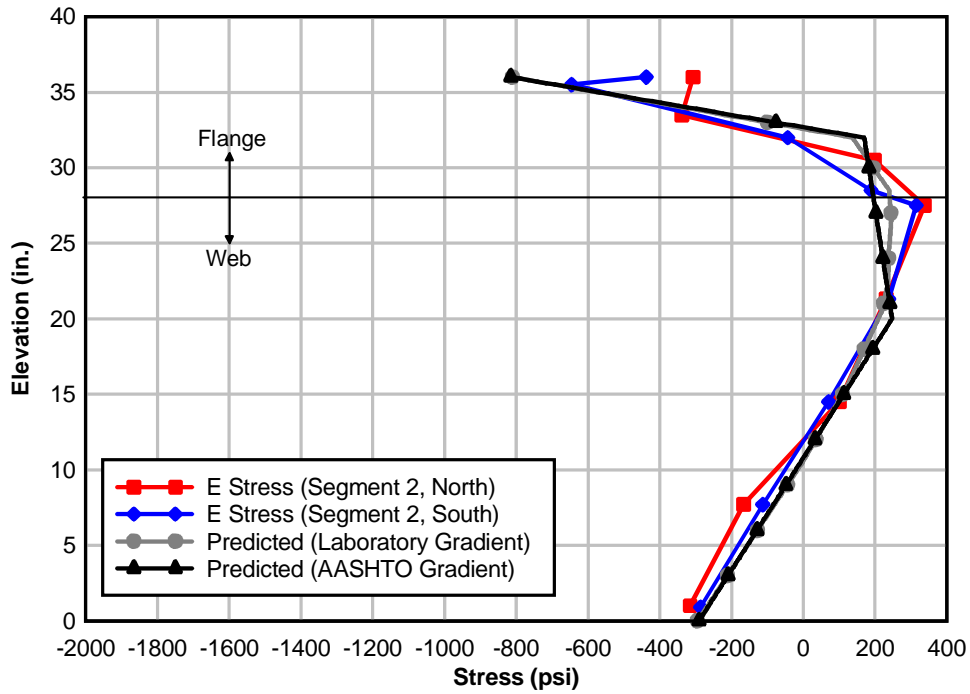


Figure 13-11. E stresses near joint J2 (Segment 2)

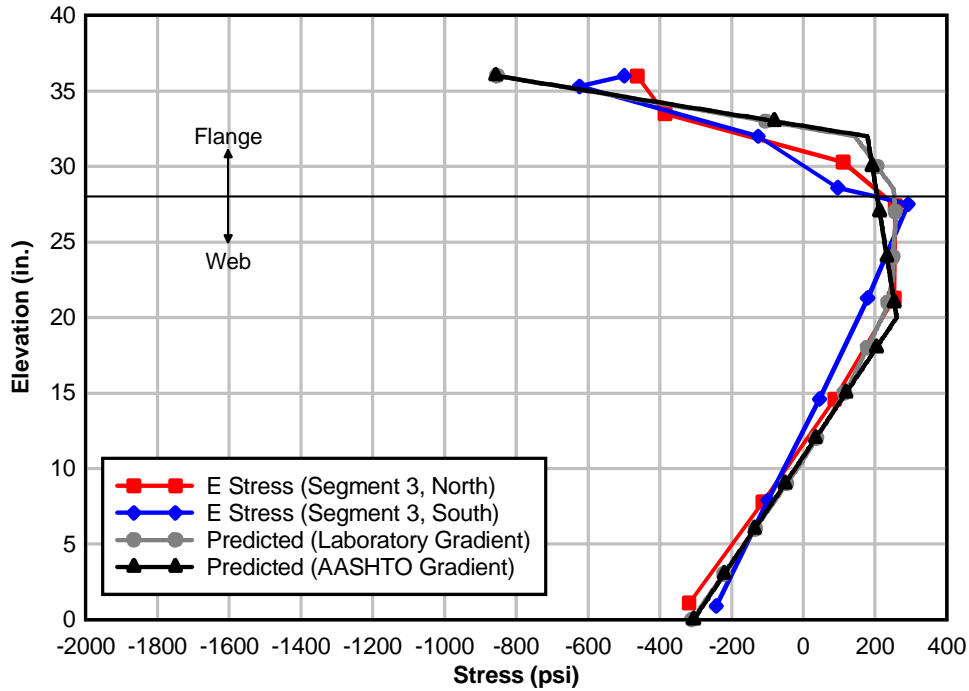


Figure 13-12. E stresses near joint J2 (Segment 3)

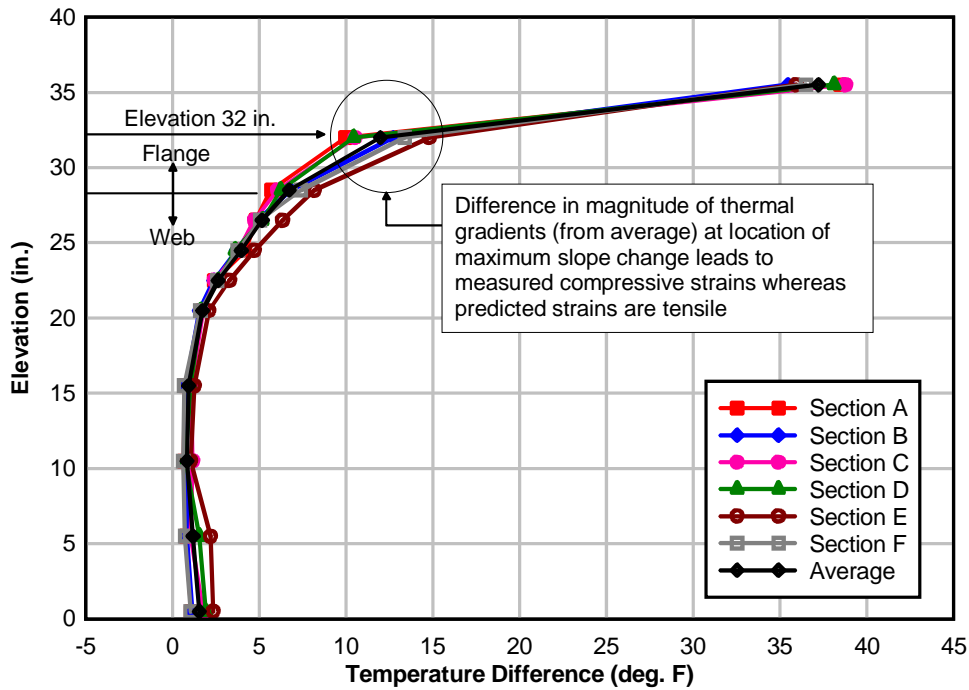


Figure 13-13. Difference in magnitude of imposed thermal gradients at location of maximum slope change (elevation 32 in.)

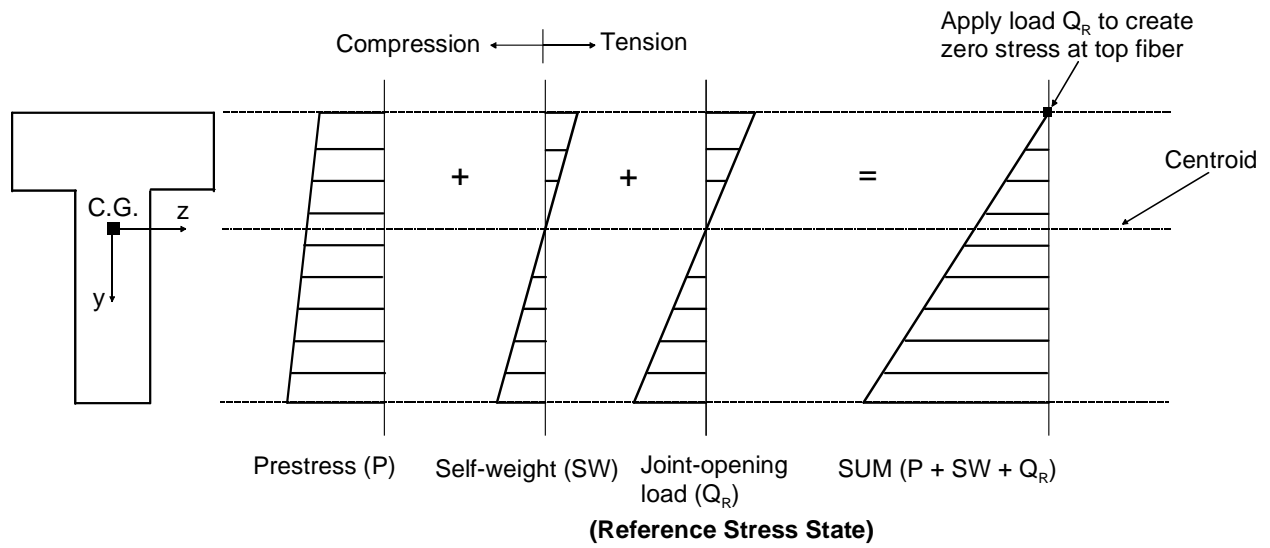


Figure 13-14. Superposition of component stress blocks (Mechanical loads only)

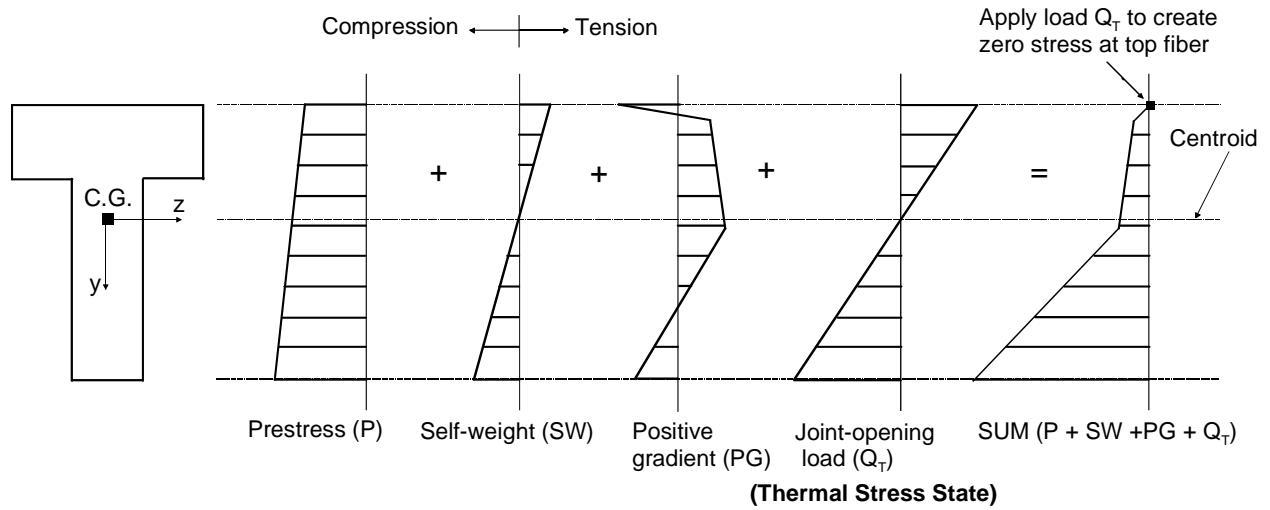


Figure 13-15. Superposition of component stress blocks (Mechanical loads with positive thermal gradient)

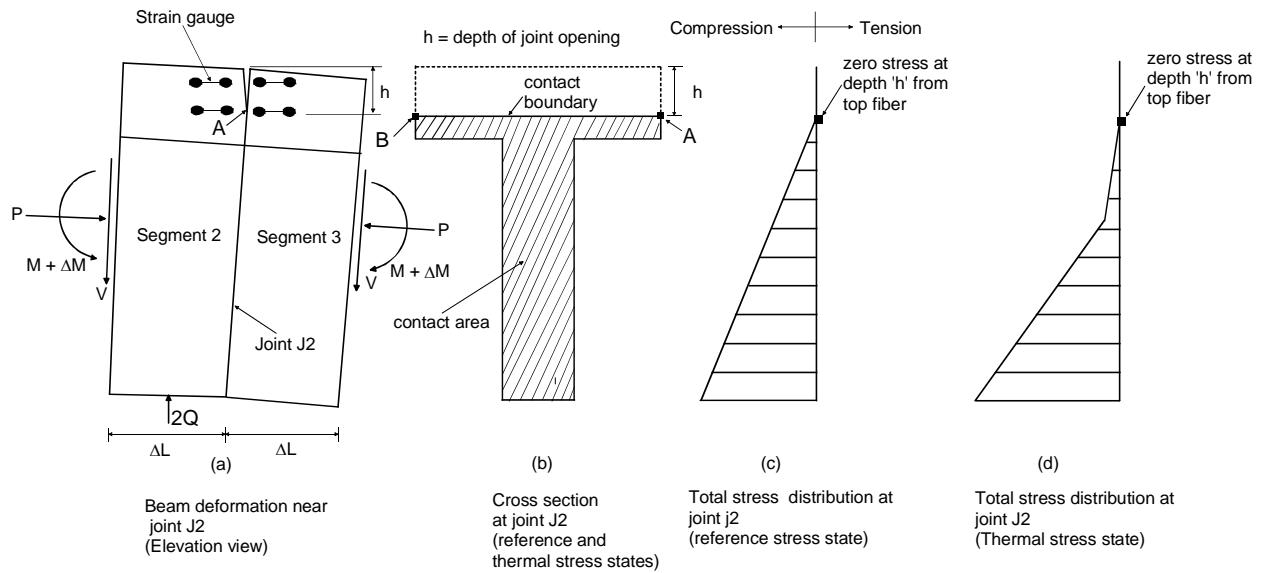


Figure 13-16. Uniform opening of joint across section width

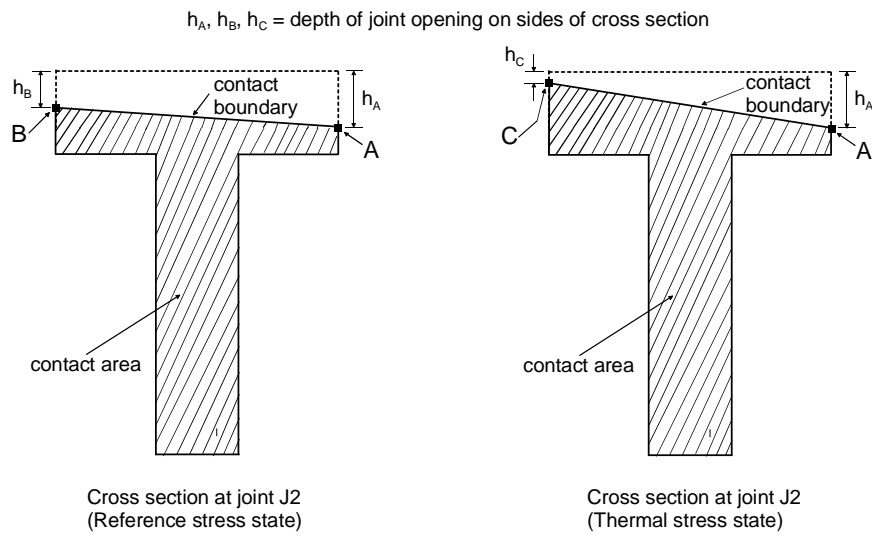


Figure 13-17. Non-uniform opening of joint across section width

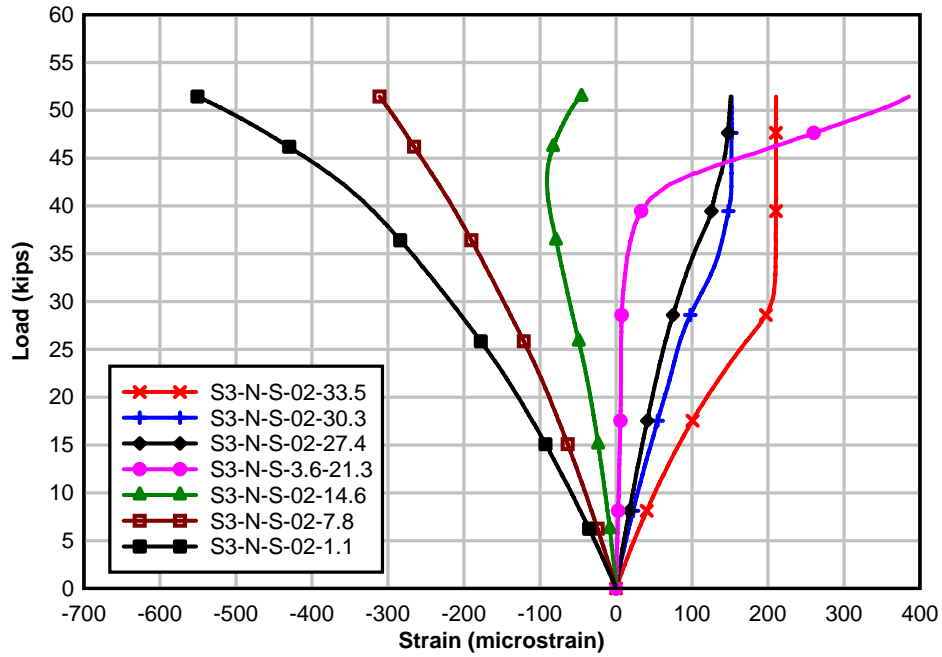


Figure 13-18. Load vs. strain at reference temperature (Segment 3, North)

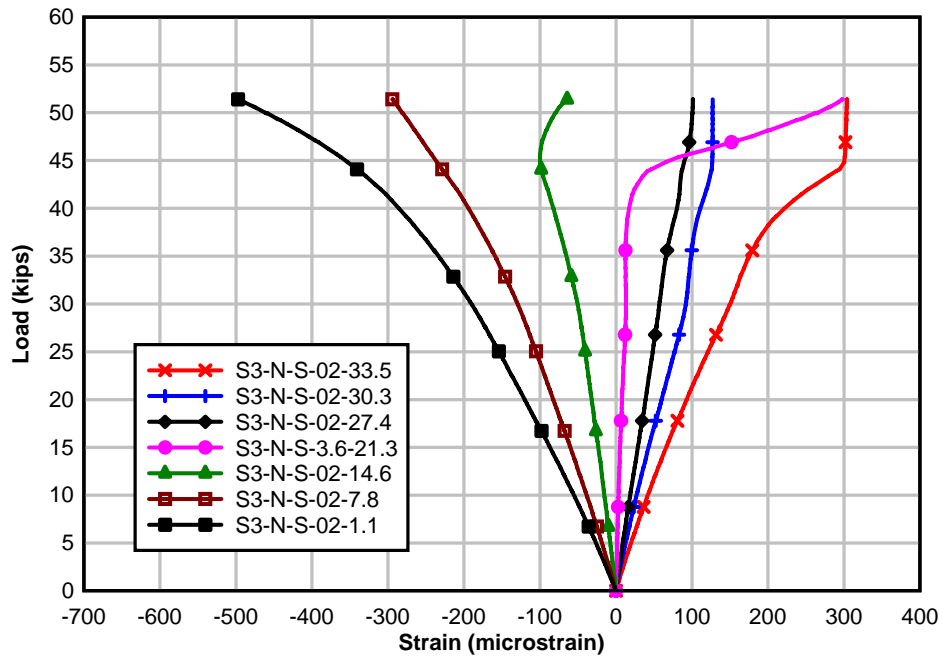


Figure 13-19. Load vs. strain with positive thermal gradient (Segment 3, North)

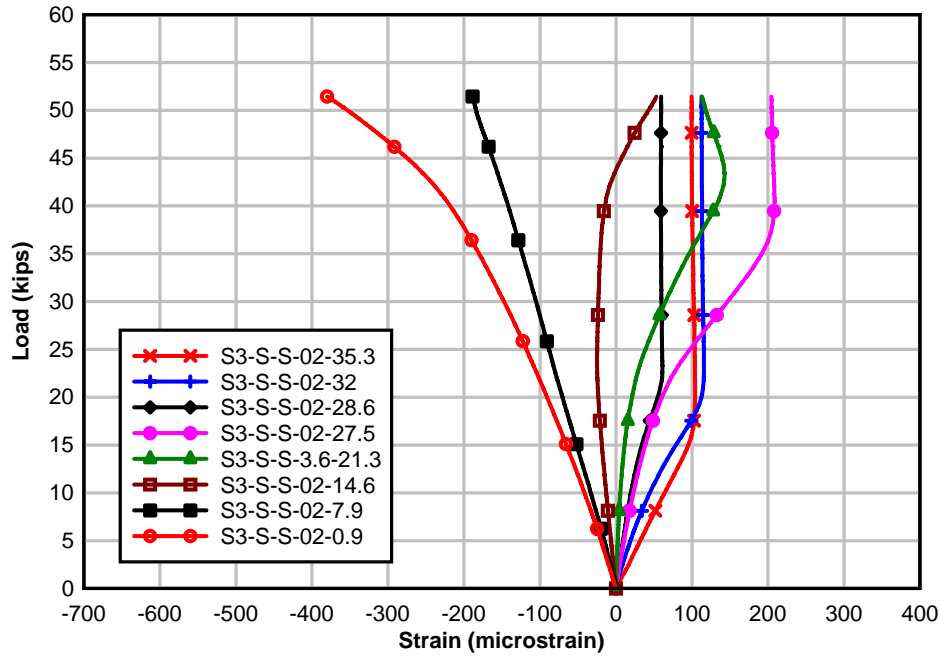


Figure 13-20. Load vs. strain at reference temperature (Segment 3, South)

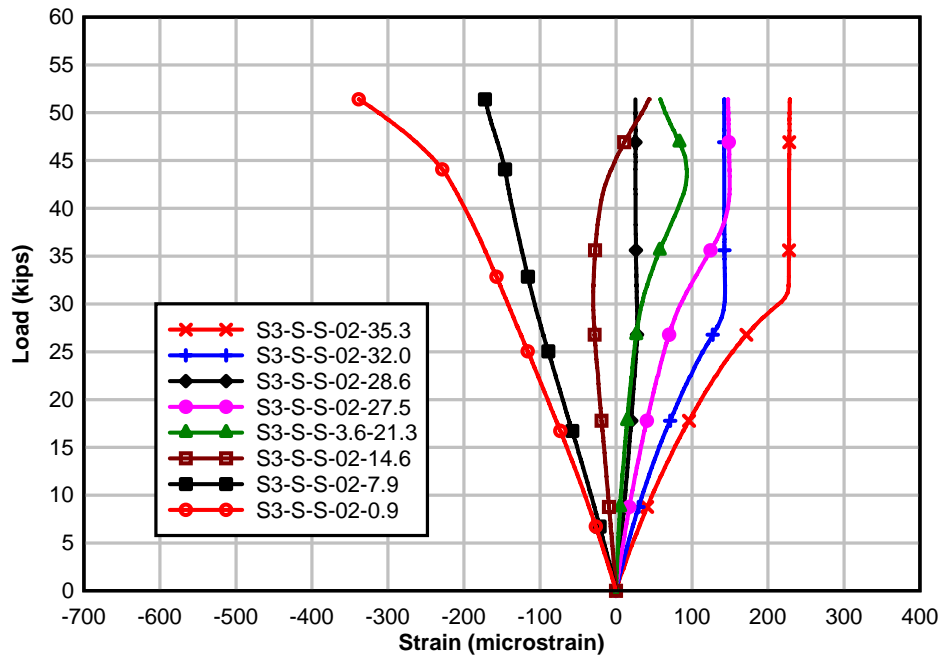


Figure 13-21. Load vs. strain with positive thermal gradient (Segment 3, South)

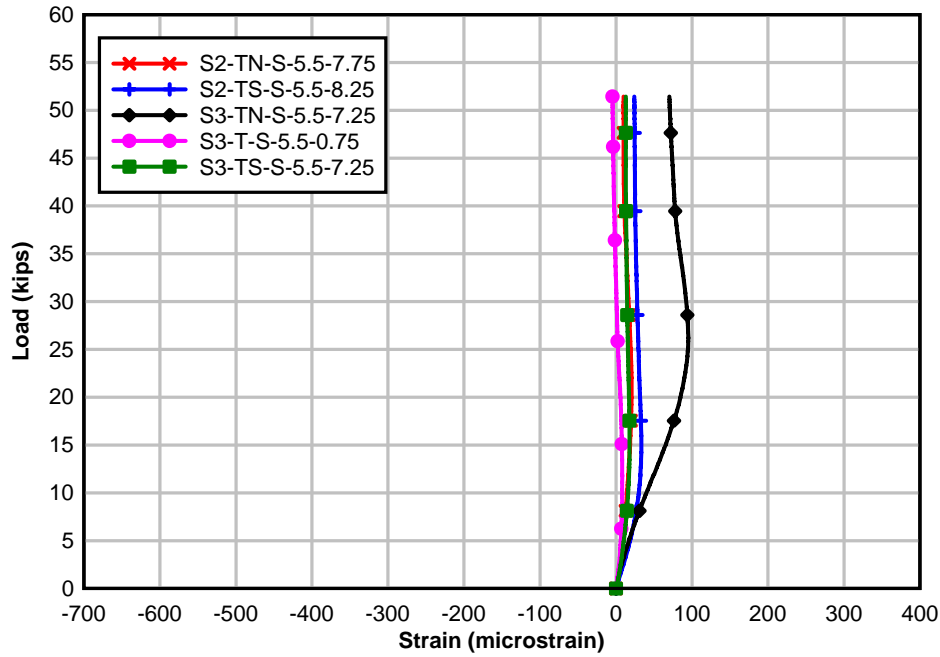


Figure 13-22. Load vs. strain at reference temperature (Top flange)

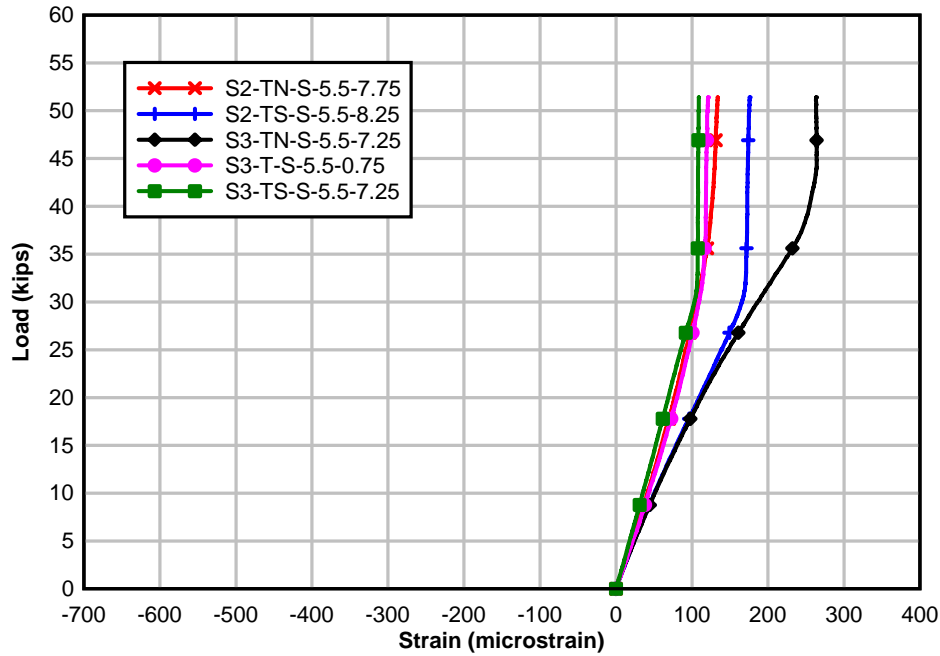


Figure 13-23. Load vs. strain with positive thermal gradient (Top flange)

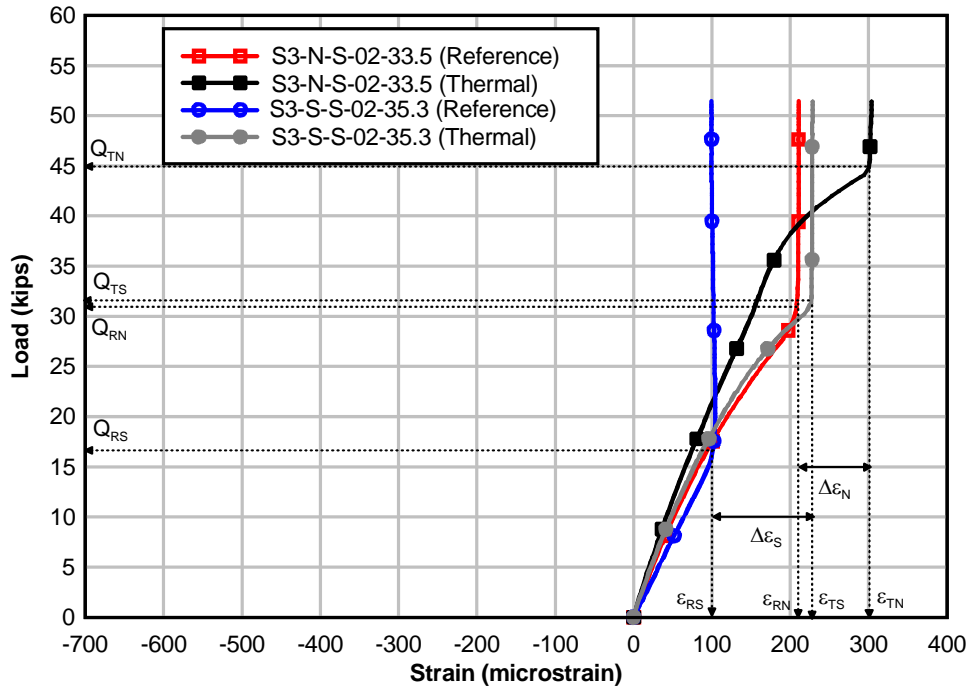


Figure 13-24. Comparison of strain differences on North and South sides of joint J2 (Positive thermal gradient)

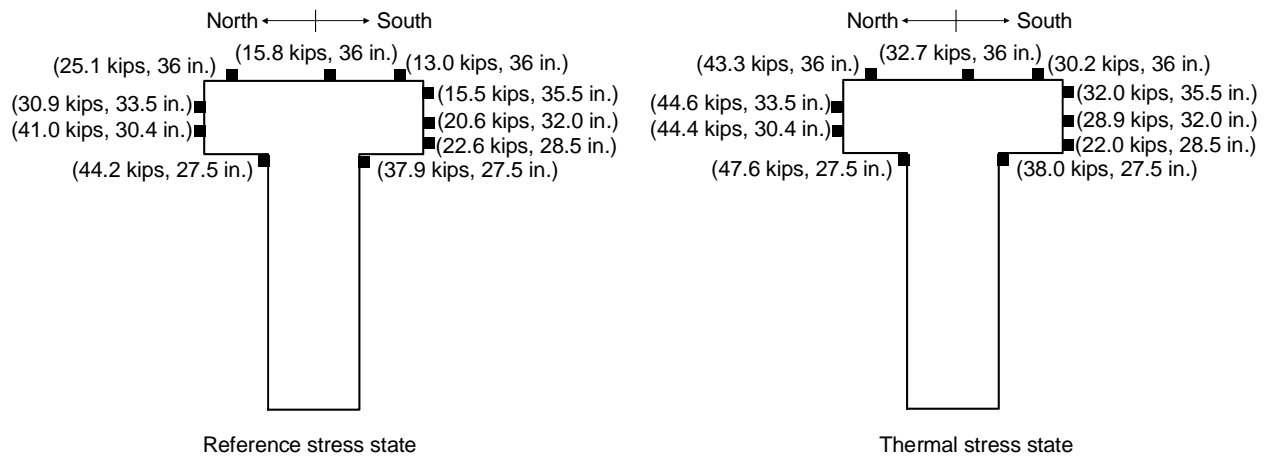


Figure 13-25. Joint opening loads detected from strain gauges near joint J2

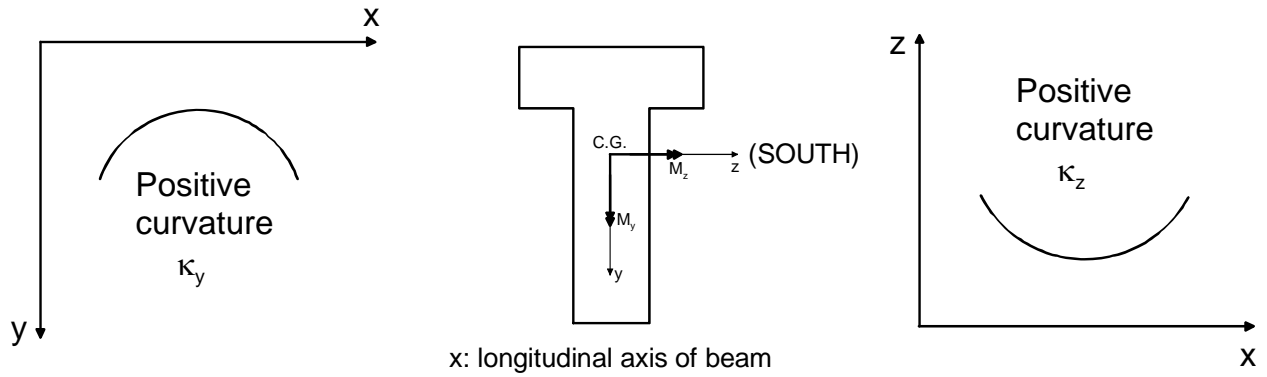


Figure 13-26. Sign convention for moments and curvature

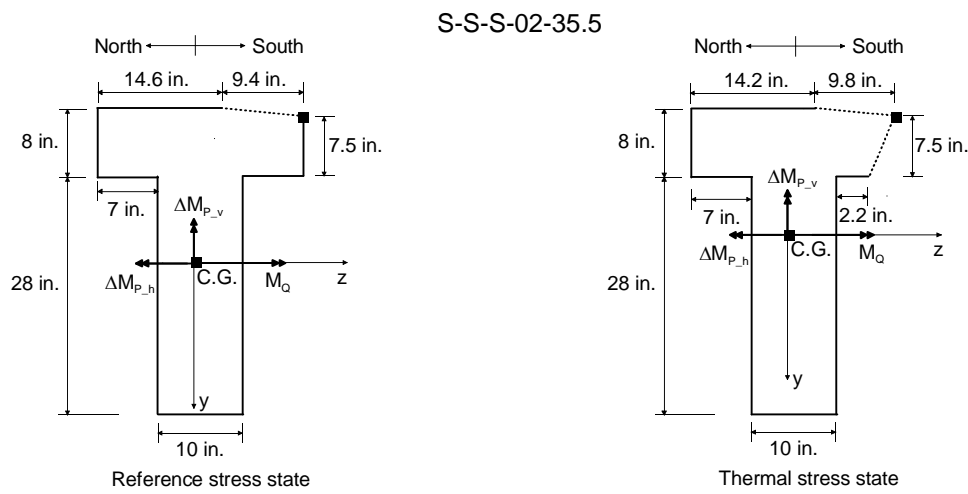


Figure 13-27. Contact areas at joint J2 at incipient opening of joint on South side at elevation 35.5 in.

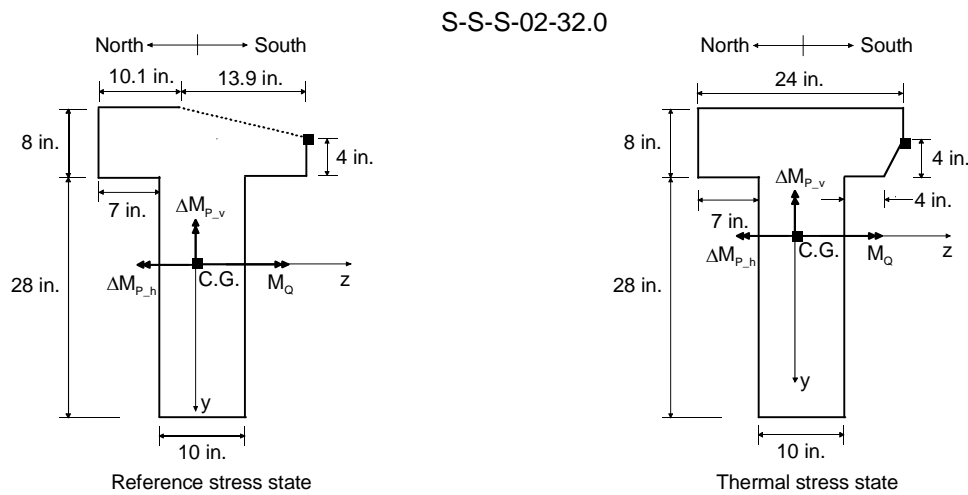


Figure 13-28. Contact areas at joint J2 at incipient opening of joint on North side at elevation 33.5 in.

S-N-S-02-33.5

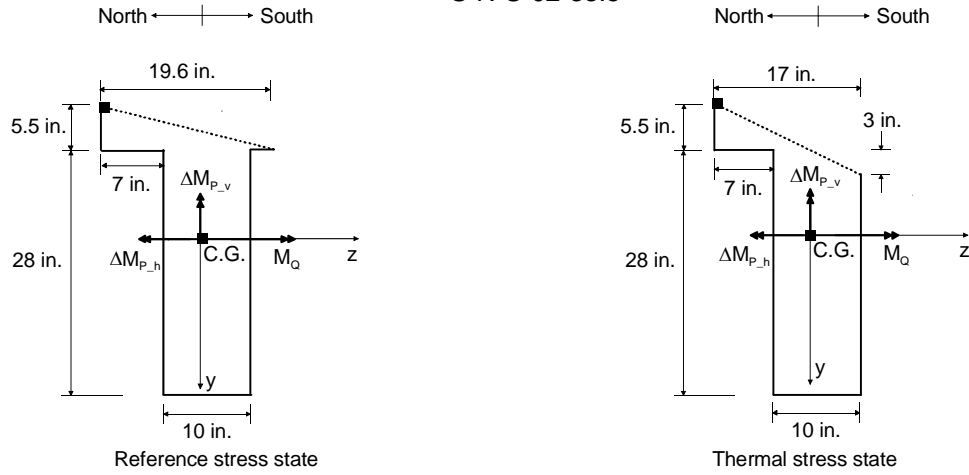


Figure 13-29. Contact areas at joint J2 at incipient opening of joint on South side at elevation 32.0 in.

CHAPTER 14 RESULTS – AASHTO NEGATIVE THERMAL GRADIENT

Results from the application of mechanical loading in combination with the AASHTO negative thermal gradient are presented and discussed in this chapter. The objective of the mechanical-thermal load tests was to experimentally quantify the self-equilibrating thermal stresses caused by the AASHTO nonlinear negative thermal gradient in the top 4 in. of the flanges of segments 2 and 3. As with the positive gradient, two independent methods were used to quantify stresses. Elastic modulus derived stresses (E stresses) were determined by converting measured strains into stresses using the elastic modulus of concrete. Independently, joint opening derived stresses (J stresses) were determined using the known stress state at incipient joint opening. In both methods concrete behavior was assumed to be linear elastic.

The test sequence, illustrated in Figure 14-1, shows that before mechanical or thermal loads were applied, the only forces acting on the beam were prestress and self-weight. The test sequence started with partial opening and closing of the joint at midspan (joint J2) with the beam at the ambient temperature of the laboratory (about 80 °F). This was followed by application of a uniform temperature increase of about 45 °F on segments 2 and 3 of the beam, after which the top portion of the segments could be cooled to impose the negative thermal gradient (see Chapter 8). Joint J2 was partially opened and closed after achieving and maintaining the steady state uniform temperature increase on the heated segments for 30 to 45 minutes. Data from this step of the load sequence were used to establish a zero reference stress state at joint J2. The top of the segments were then cooled to impose the AASHTO negative thermal gradient. After achieving and maintaining the steady state negative thermal gradient on the heated segments for 30 to 45 minutes, joint J2 was partially opened and closed to determine the thermal stress state.

The heated segments were then cooled to the reference temperature (tap water temperature) at the start of the test, after which joint J2 was again opened and closed, completing the load cycle.

Data collected from steps 3 and 5 of the load sequence were used to quantify self-equilibrating thermal stresses caused by the laboratory-imposed negative thermal gradient. Joint-opening loads and contact areas at joint J2, as the joint was gradually opened, were used to calculate self-equilibrating stresses caused by the nonlinear gradient (J stresses). Neither elastic moduli, nor coefficients of thermal expansion of segments 2 and 3 were used in the calculation of J stresses.

Elastic modulus derived thermal stresses calculated from measured thermal strains close to joint J2 (E stresses) and joint opening derived thermal stresses (J stresses) are presented and discussed in the following sections.

Elastic Modulus Derived Stresses (E stresses)

The nonlinear negative thermal gradient imposed on the heated segments of the laboratory beam (see Figure 14-2) in Step 4 of the load sequence is shown in Figure 14-3. For comparison, Figure 14-3 also shows the AASHTO design negative gradient. Measured temperatures in the heated segments after imposing the negative thermal gradient are shown in Figure 14-4.

As was done for the positive gradient (described in Chapter 13) temperature on top of the flange was obtained by extrapolating the measured temperature data from elevations 32 in. and 35.5 in. The idealized strain components induced by the AASHTO design negative thermal gradient are shown in Figure 14-5 (A detailed description of the strain components is given in Chapter 3 and Chapter 13).

The change in measured strain between Step 3 and 5 at joint J2 are plotted in Figure 14-6 through Figure 14-8. Figure 14-6 and Figure 14-7 show the strain difference along the height of segments 2 and 3, respectively. Figure 14-8 shows a plan view of the strain differences on the

top flange near the same joint. Also shown in the figures are the two sets of strain changes predicted using the AASHTO design procedure: one using the AASHTO design thermal gradient, and the other using the laboratory-imposed thermal gradient. Because the strain gauges installed on the beam were self-temperature compensating (STC) gauges, and because there was no axial or flexural restraint on the beam, the measured strains consisted only of the self-equilibrating strain component of the total strains. The average laboratory-imposed thermal gradient profile (average of profiles at Section A through Section F (Figure 14-3)) was used in calculating the ‘laboratory gradient’ strains in Figure 14-6 through Figure 14-8.

No marked difference is apparent between measured and predicted strains due to the laboratory gradient below approximately 28 in. elevation. Tensile strains were present in the bottom of the section up to an elevation of about 10 in. Compressive strains arose in the section mid-height from about 10 in. to 32 in. elevation. A maximum compressive strain (due to the laboratory gradient) of about $21 \mu\epsilon$ was predicted at elevation 27.5 in. whereas a maximum measured compressive strain of about $26 \mu\epsilon$ occurred at the same elevation. The maximum predicted tensile strain due to the AASHTO design gradient, of magnitude about $15 \mu\epsilon$, occurred at an elevation of 20 in.

The difference between locations of maximum predicted compressive strains due to the imposed laboratory gradient and the AASHTO design gradient was due to the difference in the shape of the laboratory and AASHTO design thermal gradients. In each case, the maximum compressive strain occurred at the location where the change in slope (in units of $^{\circ}\text{F}/\text{in.}$) of the thermal gradient profile was algebraically at a maximum. This occurred at an elevation of 27.5 in. for the laboratory gradient and at an elevation of 20 in. for the AASHTO design

gradient. Tensile strains also occurred above the mid-thickness of the flange with a steeper gradient than that of the remainder of the profile.

Some additional differences between the measured and predicted strains are also notable. Measured tensile strains were significantly smaller than predicted at the top of the section in both segments except for the North top flange of Segment 3 (see Figure 14-8). As with the positive thermal gradient, the smaller measured tensile strains on top of the section were thought to be caused by a likely discontinuity in the shape of the thermal gradient in the top 0.5 in. of the flange. Although not measured, it is probable that the temperature at the top surface of the flange was less than that of the temperature of the topmost thermocouples (located at an elevation of 35.5 in.). In determining predicted strains, however, the magnitude of the thermal gradient in the top flange was obtained by extrapolating the linear thermal gradient between elevations of 32 in. and 35.5 in. The approximately 53% difference between strains measured on the North and South top flange of Segment 3 was attributed to the condition at the top surface of the flange at joint J2 shown in Figure 11-6.

Measured concrete strains on the North side at midspan (joint J2) and at mid-segment of segments 2 and 3 are compared in Figure 14-9 and Figure 14-10, respectively. The distributions of measured strain on the side of the flange at mid-segment did not match the predicted strain profile as well as the measured strains at midspan because only two strain gauges were located on the side of the flange at mid-segment. Additionally, measured tensile strains on top of the flange at mid-segment were significantly less than predicted strains at the same locations. Measured strains on top of the flange at mid-segment were, however, generally greater than corresponding measured tensile strains at joint J2. This observation reinforces the possibility that differential shrinkage at joint J2 led to a greater discrepancy between measured and

predicted strains at the joint. Between elevations 32 in. and 35.5 in., measured tensile strains followed a linear distribution as did the predicted strains. The measured strains were, however, generally larger than predicted strains between elevations 32 in. and 33 in. and smaller than predicted strains above 33 in. As discussed in Chapter 13, a possible reason for the difference between measured and predicted strains in this region of the flange was a variation between measured thermal gradients and the average thermal gradient (see Figure 14-11), which was used to predict strains per the AASHTO design procedure.

The uniform and linear sub-components of the overall negative thermal gradient were expected to lead to additional stresses in the concrete as the top portions of segments 2 and 3 were cooled during Step 4. Contraction of the segments relative to the prestressing caused a net reduction in prestressing force, however the measured peak reduction was only 0.2% of the initial prestress and was therefore considered negligible.

Elastic modulus derived stresses (E stresses) were the self-equilibrating thermal stresses caused by the negative thermal gradient, and were determined by multiplying the measured strains in Figure 14-6 and Figure 14-7 by the elastic moduli of Segment 2 (4850 ksi) and Segment 3 (4850 ksi), respectively. The elastic moduli were calculated by linearly interpolating between cylinder modulus of elasticity data between test ages of 28 and 360 days. At the time of the test, the ages of segments 2 and 3 were 251 and 238 days, respectively.

Figure 14-12 and Figure 14-13 show E stress distributions near joint J2 on Segment 2 and Segment 3, respectively. E stresses at midspan and mid-segment on the North side of segments 2 and 3 are compared in Figure 14-14 and Figure 14-15, respectively. Also for comparison, self-equilibrating thermal stresses due to the laboratory thermal gradient and the AASHTO design gradient were calculated using the AASHTO recommended procedure discussed in

Chapter 3, and are shown in the figures. CTEs from Table 12-1 and the segment MOEs noted above were used in these calculations.

Table 14-1 compares E stresses computed at the top of the flanges of segments 2 and 3 with similar stresses obtained by extrapolating from the linear E stress distributions between elevations 32 in. and 35.5 in. (see Figure 14-12 and Figure 14-13) on the sides of the segment flanges. E stresses in the extreme top flange fibers were significantly lower than stresses extrapolated to the same location. This condition follows from the relatively smaller stress-inducing thermal strains that were measured at the top surfaces of the flanges (see Figure 14-8). As discussed previously, the smaller strains were attributed to differential shrinkage at joint J2 and to a lower thermal gradient magnitude than was targeted (as prescribed by the AASHTO gradient) for the top of the flanges of the segments. At an elevation of 32 in., the E stress on Segment 2 was about 88% less than the predicted stress. Both stresses were compressive. The E stress on Segment 3 at the same elevation, however, was tensile whereas the predicted stress was compressive. As was the case for the positive thermal gradient, this was attributed to the difference in magnitude of the laboratory thermal gradients at sections A through F (from the average thermal gradient used in predicting stresses) at that elevation; the location of the maximum slope change in the thermal gradients (see Figure 14-16).

E stresses and predicted stresses caused by the laboratory-imposed nonlinear negative thermal gradient in the top 4 in. of the flanges of segments 2 and 3 are compared in Table 14-2. Predicted stresses in the extreme top flange fibers (where the maximum tensile stresses were expected to occur, had the gradient been linear in the top 4 in. of the flanges) are not shown in the table because the shape and magnitude of the thermal gradient in this region were not measured. E stresses 0.5 in. below the top of the flange (maximum E stresses) were

approximately 25% and 14% less than corresponding predicted stresses in Segment 2 and Segment 3, respectively. E stresses caused by the positive thermal gradient (see Chapter 13) at the same location were 3% and 8% less than corresponding stresses predicted in Segment 2 and Segment 3, respectively. Beam response was more sensitive to small errors in thermocouple readings in the negative thermal gradient case than in the positive thermal gradient case because of the relatively lesser magnitude (temperature change) of the negative thermal gradient. This was thought to be the reason for the greater discrepancy between maximum E stresses and corresponding predicted stresses due to the negative gradient. Taking into consideration the effects of differential shrinkage at joint J2, small errors in measuring strain gauge elevations, and differences between measured thermal gradients (at sections A through F) and the average thermal gradient within the top 4 in. of the segment flanges, these differences were considered to be within the limits of experimental error.

Joint – Opening Derived Stresses (J Stresses)

Joint-opening derived stresses (J stresses) were determined using the procedure outlined in Chapter 13 and data collected from steps 3 and 5 of the load sequence shown in Figure 14-1. For the thermal loading sequence used in the negative gradient tests, Eqns. 13-1 and 13-2 were modified as follows:

$$f_P(y, z) + f_{sw}(y, z) + f_{UT}(y, z) + f_R(y, z) = 0, \{(y, z) \in R\} \quad (14-1)$$

$$f_P(y, z) + f_{sw}(y, z) + f_{UT}(y, z) + f_J(y, z) + f_T(y, z) = 0, \{(y, z) \in T\} \quad (14-2)$$

where, f_{UT} represents stresses caused by the expansion of the concrete segments (against the restraint of the prestress bars) due to a uniform temperature increase (see Figure 14-17 and Figure 14-18) and all other quantities are as described in Chapter 13. The f_{UT} term was added to account for the fact that the negative gradient was imposed by first heating the entire section and then cooling the top portion.

Figure 14-19 and Figure 14-20 show variations of concrete strain with applied load near joint J2 on the North side of Segment 3 at the reference stress state (reference temperature) and thermal stress state (with negative thermal gradient), respectively. Similar plots near the same joint on the South side are shown in Figure 14-21 and Figure 14-22, respectively. The variation of concrete strain with applied load on top of the flanges of segments 2 and 3 near joint J2 at the reference and thermal stress states are shown in Figure 14-23 and Figure 14-24, respectively. Data collected from strain gauges near joint J2 on Segment 2, LVDTs mounted across joint J2 on top of the flanges of segments 2 and 3, and LVDTs mounted across the same joint on the South side can be found in Appendix E.

A comparison of concrete strains at same side of joint J2 at the reference and thermal stress states shows that at identical elevations in the top 4 in. of the flange, the joint opened at lower loads at the thermal stress state than it did at the reference stress state. This is illustrated in Figure 14-25 with data taken from the strain gauges at elevations 33.5 in. on the North and 35.3 in. on the South side of the joint. The same is true of the top flange strains shown in Figure 14-23 and Figure 14-24. LVDTs on the sides and top of the flange (see Appendix E) also show the joint opening at lower loads at the thermal stress state than at the reference stress state. This was indicative of the development of tensile stresses in the top concrete fibers at joint J2 due to the negative thermal gradient. It is also evident in Figure 14-25 that, similar to the positive thermal gradient, the strain difference between vertical portions of strain diagrams, at the reference and thermal stress states, was dependent only on the elevation of the gauge and not on the side (North/South) of the joint on which the gauge was located.

Loads that caused joint J2 to open at the reference and thermal stress states were detected using the strain data shown in Figure 14-19 through Figure 14-24 above, and Figure E-1 through

Figure E-8 in Appendix E. Applied loads at the cantilevered-end of the test beam, which caused joint J2 to open at various depths, are shown in Figure 14-26. The sign convention for moments and curvatures, which is the same as that used in Chapter 13, is shown (for convenience) in Figure 14-27.

Figure 14-28 through Figure 14-30 show estimated contact areas at joint J2 at the reference and thermal stress states just as opening of the joint was detected from strain gauges at elevations of 35.5 in. (South), 33.5 in. (North), and 32.0 in. (South), respectively. These plots were developed using the same approach detailed in Chapter 13.

In Table 14-3 calculated J stresses are presented for the locations of strain gauges on the sides of the beam within the top 4 in. of the flange. As for the positive thermal gradient, the total stresses (stresses determined from Equation 13-5) though positive, indicating tension, actually represent relief of existing compressive stresses at J2 prior to the application of joint-opening loads. J stresses were determined by taking the difference between total stresses at the reference stress state and total stresses at the final stress state.

Changes in prestress (as the beam was mechanically loaded and joint J2 opened) accounted for less than 1% of total stresses (see Equation 13.5). Calculated total stresses were, therefore, essentially dependent on the magnitude of joint-opening loads. J stresses, however, were dependent on the difference between the joint-opening loads at the reference and thermal stress states. For example, the loads initiating opening of joint J2 on the North side at an elevation of 33.5 in. were greater than they were on the South side at an elevation of 35.5 in. as can be seen from the magnitudes of the moments in Table 14-3. However, calculated J stresses at an elevation of 33.5 in. were lower than J stresses at an elevation of 35.5 in. because the difference

in joint-opening moments at elevation 33.5 in. was lower than the difference in moments required to open the joint at elevation 35.5 in.

J stresses and stresses predicted with the AASHTO procedure using the laboratory thermal gradient, in the top 4 in. of the flange, are compared in Table 14-4. J stresses 0.5 in. below the top of the flange (maximum J stresses) were approximately 17% and 23% less than corresponding predicted stresses in Segment 2 and Segment 3, respectively. At elevation 32 in., J stresses were about 82% less than predicted stresses. Both predicted and J stresses compressive.

J stresses and E stresses in the top 4 in. of the flanges are compared in Table 14-5. Maximum J stresses were within 11% of maximum E stresses. J stresses were, in general, higher than E stresses on Segment 2 and lower than E stresses on Segment 3. This could possibly be due to small errors in estimating contact areas and determining joint-opening loads. Another possibility is that J stresses represented the average stress between segments 2 and 3 at joint J2 whereas E stresses represented stresses on each segment about 2 in. away from joint J2.

Table 14-1. Comparison of E stresses and extrapolated stresses on top of segment flanges near joint J2 (laboratory negative thermal gradient)

	E Stress (psi)	Extrapolated (psi)	Measured/Extrapolated
Segment 2, North	38	252	0.151
Segment 2, South	71	191	0.372
Segment 3, North	255	277	0.921
Segment 3, Middle	69	265	0.260
Segment 3, South	120	252	0.476

Table 14-2. Comparison of E stresses and predicted self-equilibrating thermal stresses caused by laboratory negative thermal gradient near joint J2

Segment 2			
Elevation (in.)	Average E Stress (psi)	Average Predicted (psi)	E Stress/Predicted
36	55	N/A	N/A
35.5	193	258	0.748
33.5	79	80	0.994
32	-6	-54	0.116
Segment 3			
Elevation (in.)	Average E Stress (psi)	Average Predicted (psi)	E Stress/Predicted
36	148	N/A	N/A
35.5	235	272	0.865
33.5	118	84	1.413
32	31	-57	-0.539

Table 14-3. J stresses in top 4 in. of flange

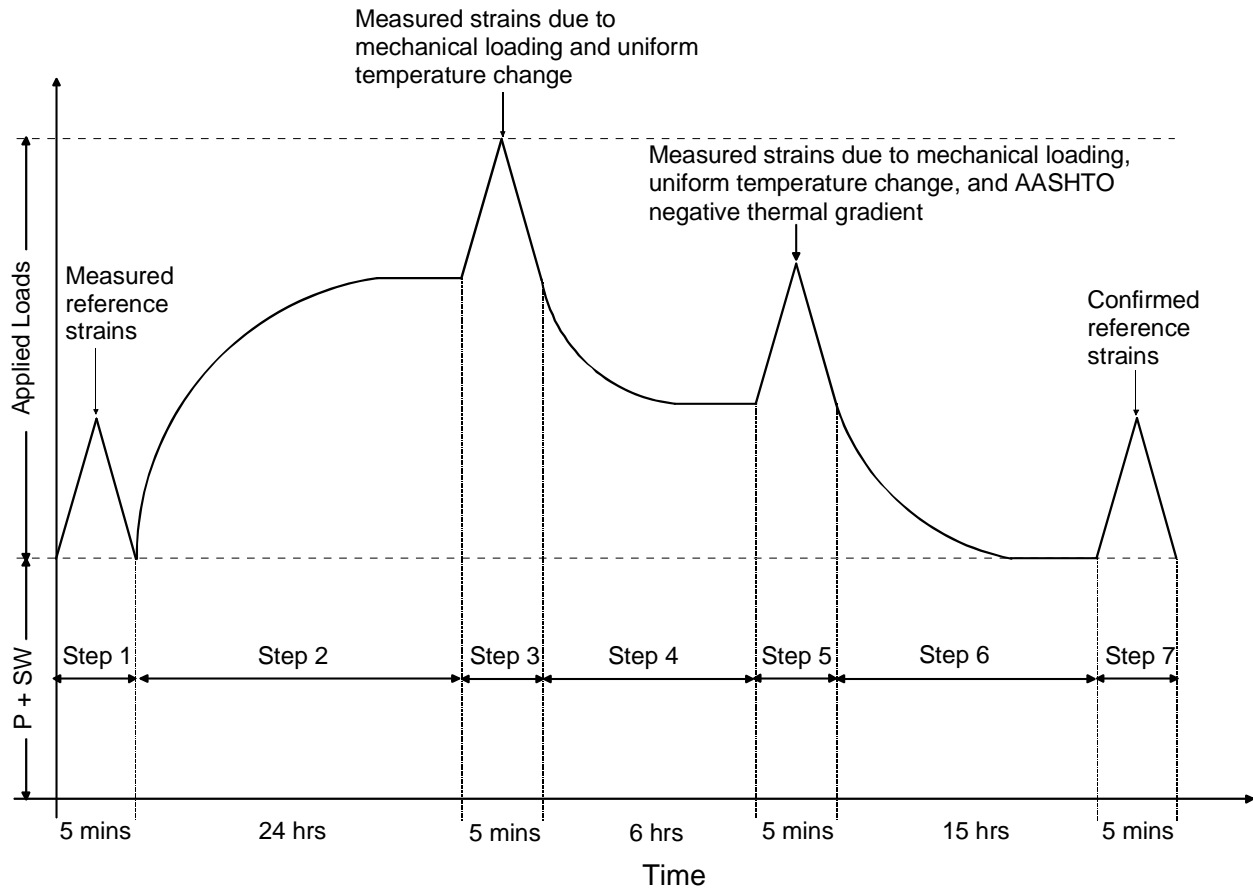
Gauge Elevation	Moments due to Joint-opening Loads (kip-in.)		Total Stresses (psi)		J Stress (psi)
	Reference	Thermal	Reference	Thermal	
35.5 in. S	1679	885	443	229	214
33.5 in. N	2961	2510	861	740	121
32.0 in. S	1986	1896	625	635	-10

Table 14-4. Comparison of J stresses and predicted stresses in top 4 in. of flange

Segment 2			
Gauge Elevation	J Stress (psi)	Predicted Stress (psi)	J Stress/Predicted Stress
35.5 in. S	214	258	0.829
33.5 in. N	121	80	1.500
32.0 in. S	-10	-54	0.185
Segment 3			
Gauge Elevation	J Stress (psi)	Predicted Stress (psi)	J Stress/Predicted Stress
35.5 in. S	214	272	0.787
33.5 in. N	121	84	1.440
32.0 in. S	-10	-57	0.175

Table 14-5. Comparison of J stresses and E stresses in top 4 in. of flange

Segment 2			
Gauge Elevation	J Stress (psi)	E Stress (psi)	J Stress/E Stress
35.5 in. S	214	193	1.109
33.5 in. N	121	79	1.532
32.0 in. S	-10	-6	1.667
Segment 3			
Gauge Elevation	J Stress (psi)	E Stress (psi)	J Stress/E Stress
35.5 in. S	214	235	0.911
33.5 in. N	121	118	0.975
32.0 in. S	-10	31	-0.323

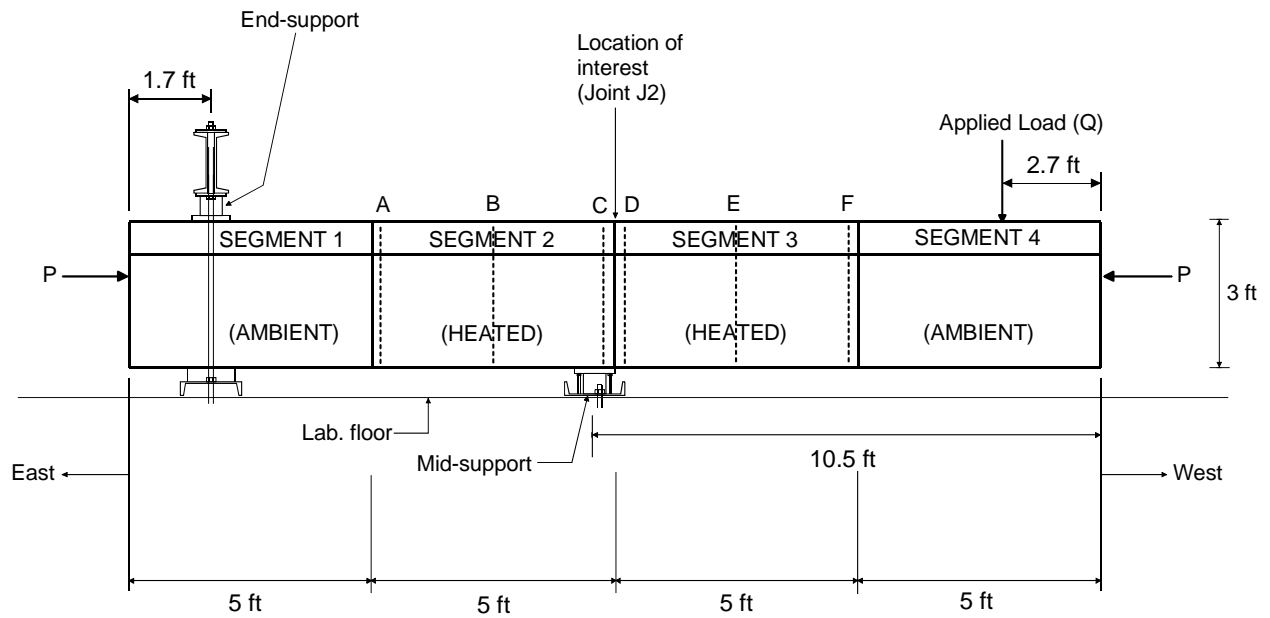


P + SW: Prestress + Self-weight

Applied Loads:

- Step 1: Opening and closing of joint J2 (application and removal of mechanical loads)
- Step 2: Uniform temperature change (application of thermal load)
- Step 3: Opening and closing of joint J2 (application and removal mechanical loads)
- Step 4: Negative thermal gradient (application of thermal load)
- Step 5: Opening and closing of joint J2 (application and removal of mechanical loads):
- Step 6: Cooling to reference temperature at start of test (removal of thermal loads)
- Step 7: Opening and closing of joint J2 (application and removal of mechanical loads)

Figure 14-1. Sequence of load application (negative gradient test)



P: Post-tensioning force

Figure 14-2. Laboratory beam

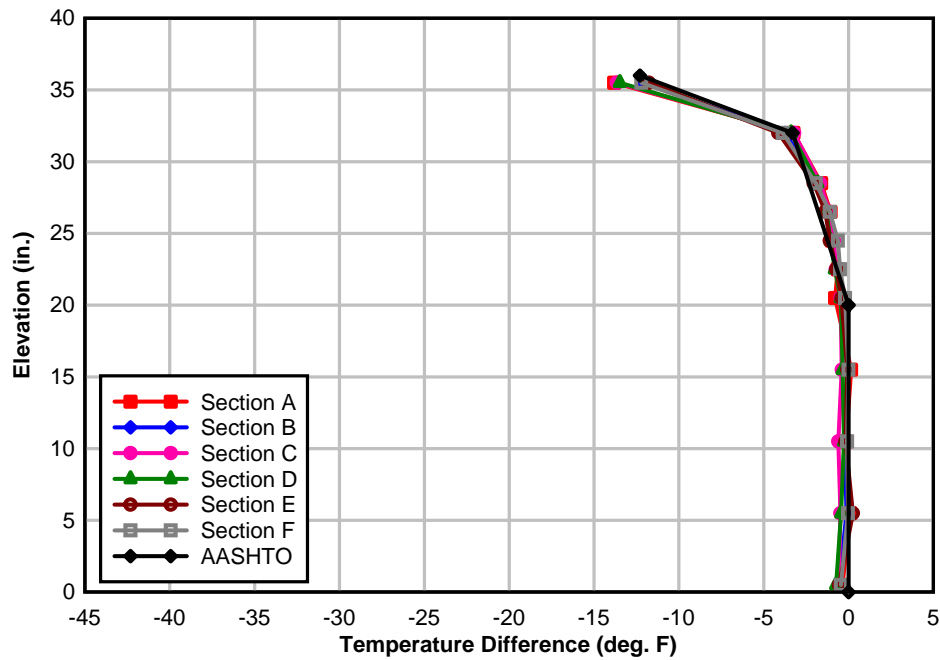


Figure 14-3. Laboratory imposed negative thermal gradient

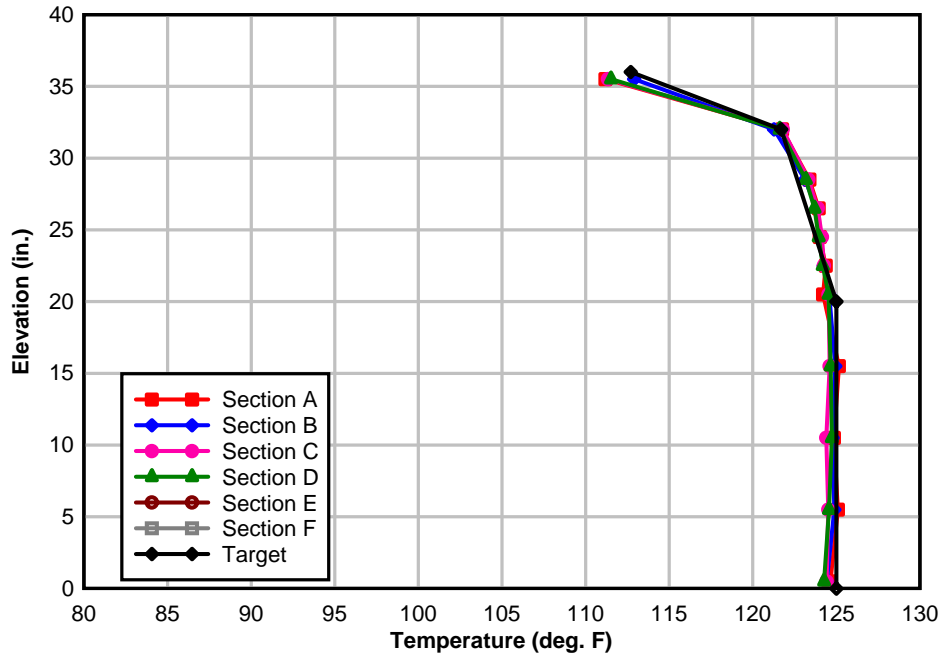


Figure 14-4. Measured temperatures in heated segments (negative thermal gradient)

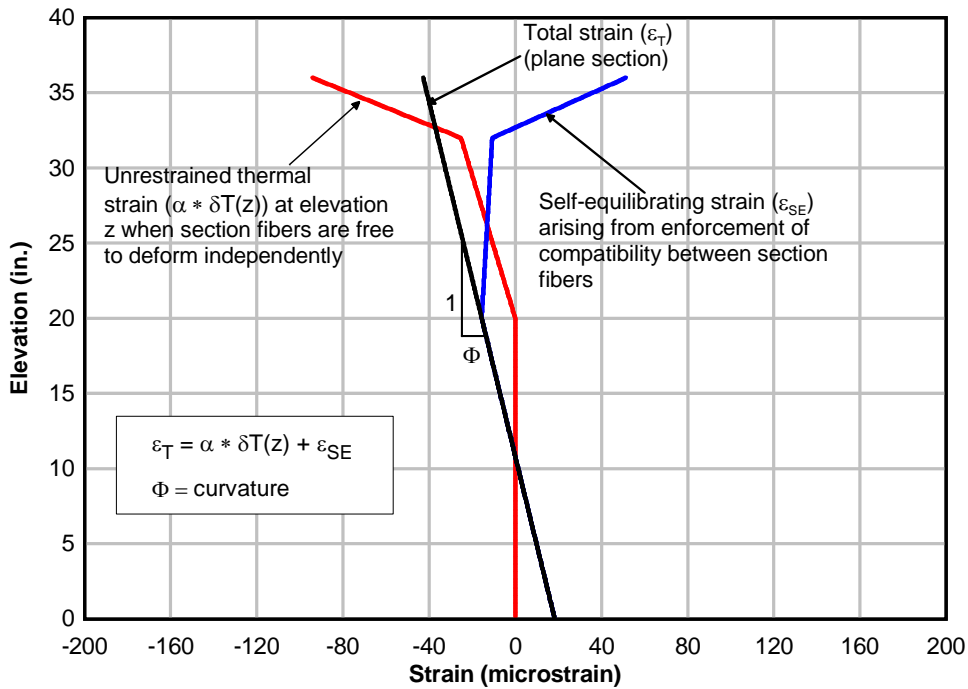


Figure 14-5. Calculated strain components of the AASHTO negative thermal gradient

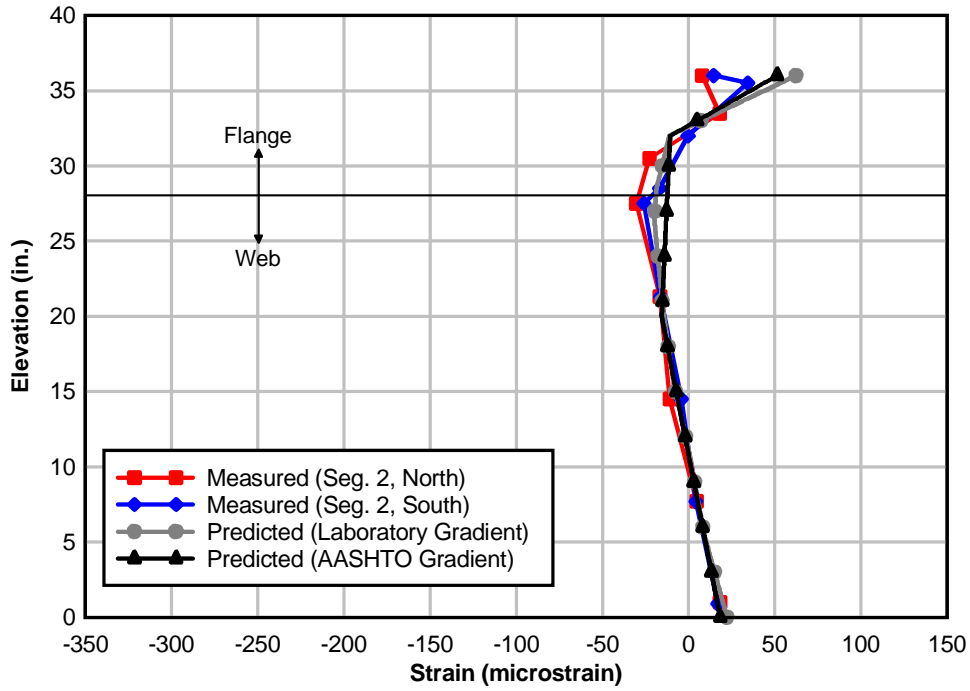


Figure 14-6. Measured and predicted strains near joint J2 (Segment 2)

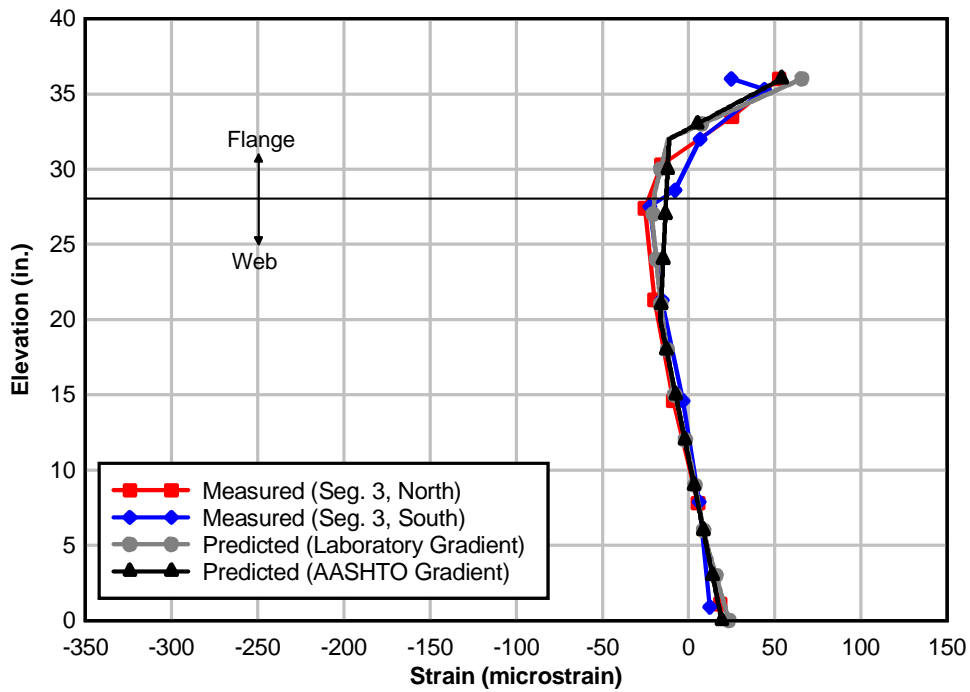


Figure 14-7. Measured and predicted strains near joint J2 (Segment 3)

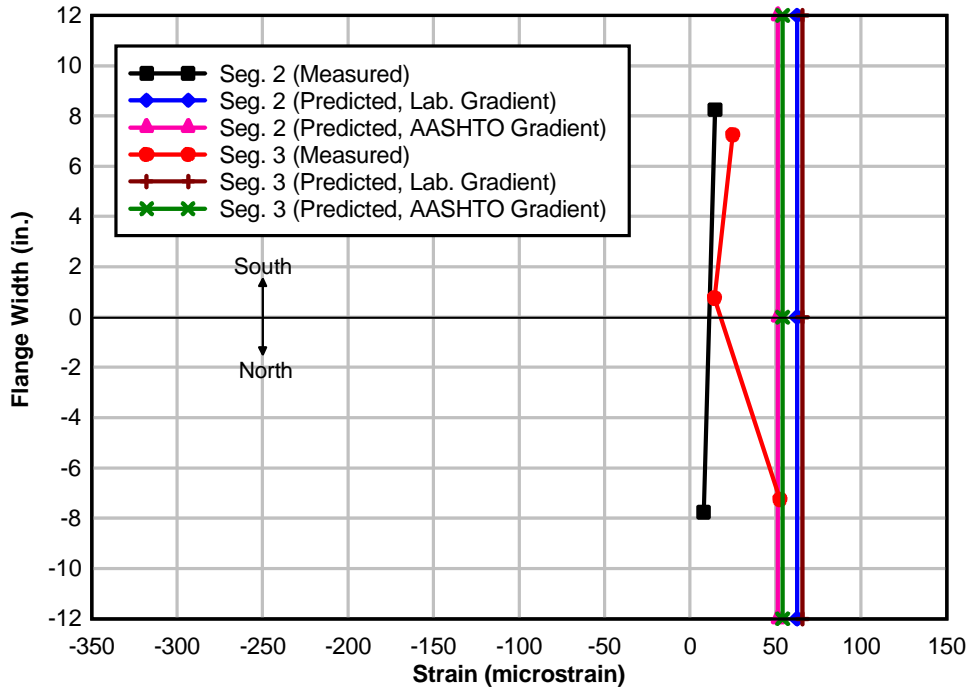


Figure 14-8. Plan view of measured and predicted strains near joint J2 (Top Flange)

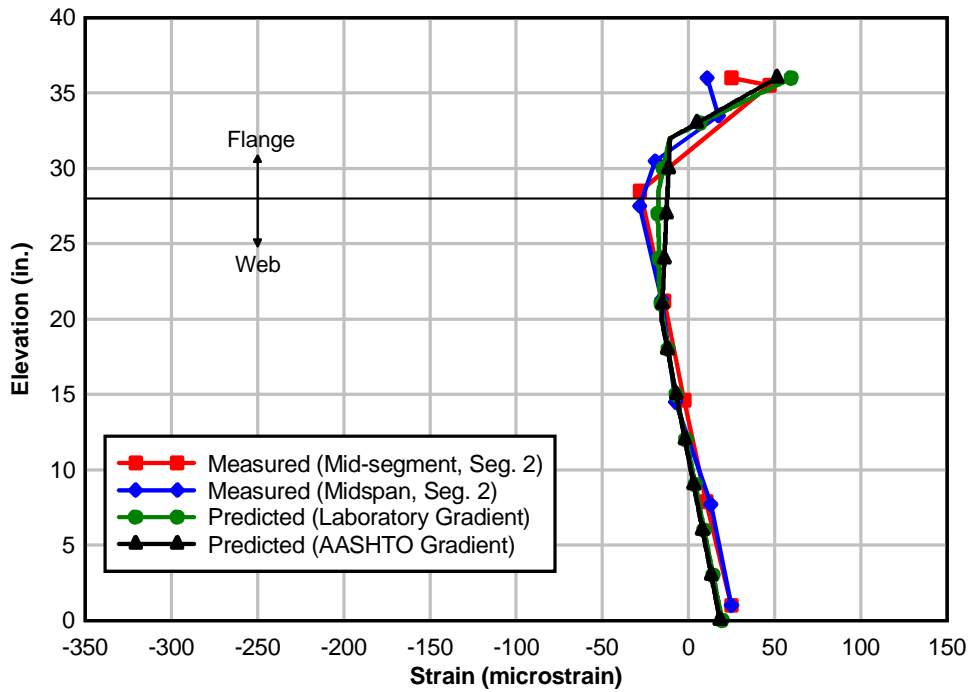


Figure 14-9. Measured and predicted strains at midspan and mid-segment (Segment 2, North)

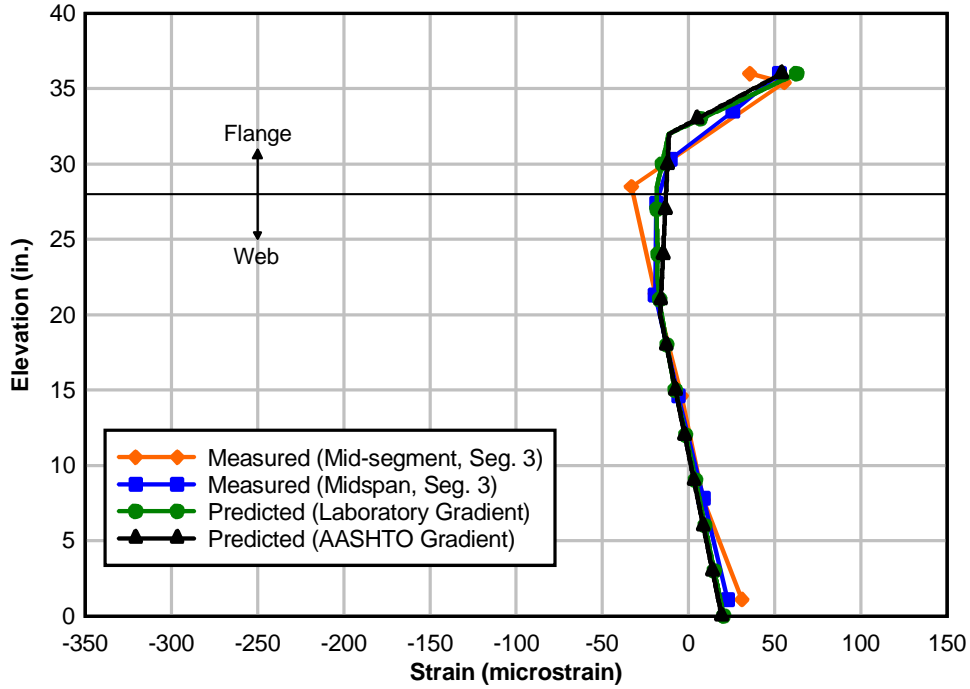


Figure 14-10. Measured and predicted strains at midspan and mid-segment (Segment 3, North)

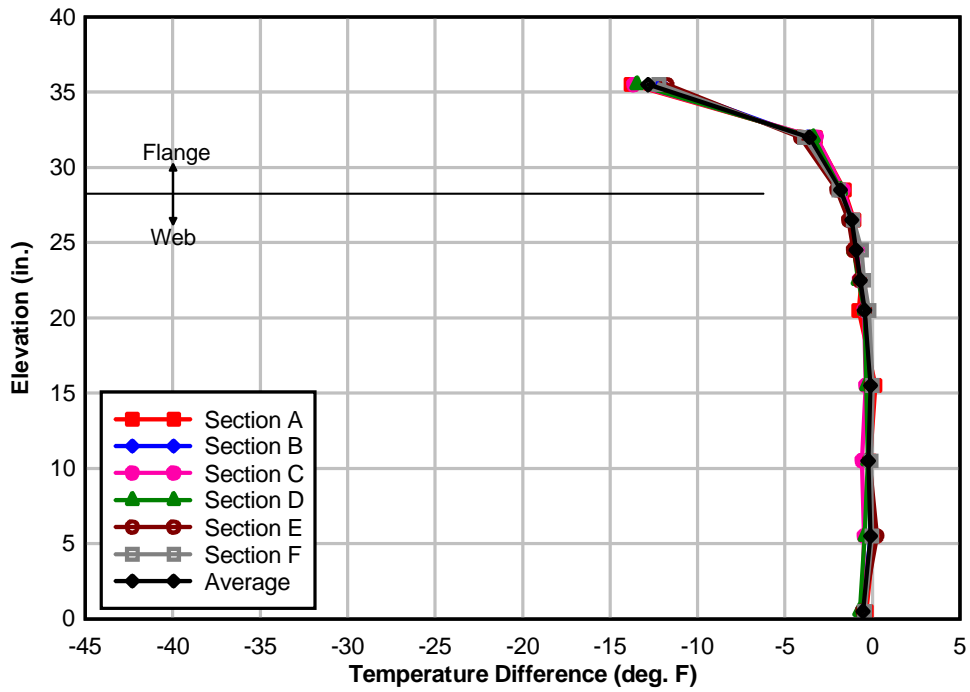


Figure 14-11. Comparison of measured thermal gradient profiles with average profile

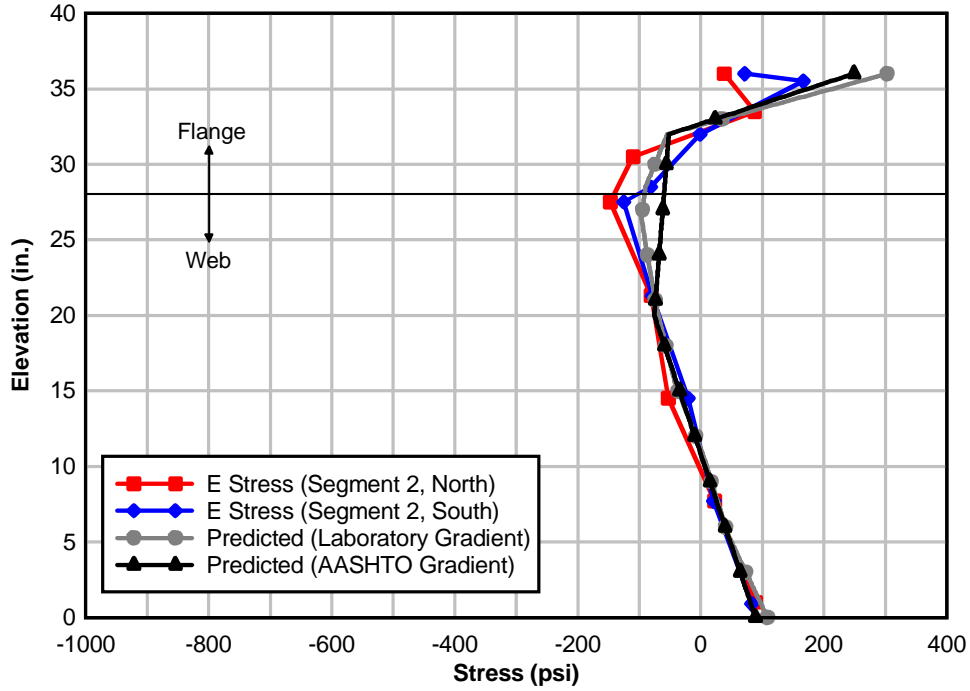


Figure 14-12. E stresses near joint J2 (Segment 2)

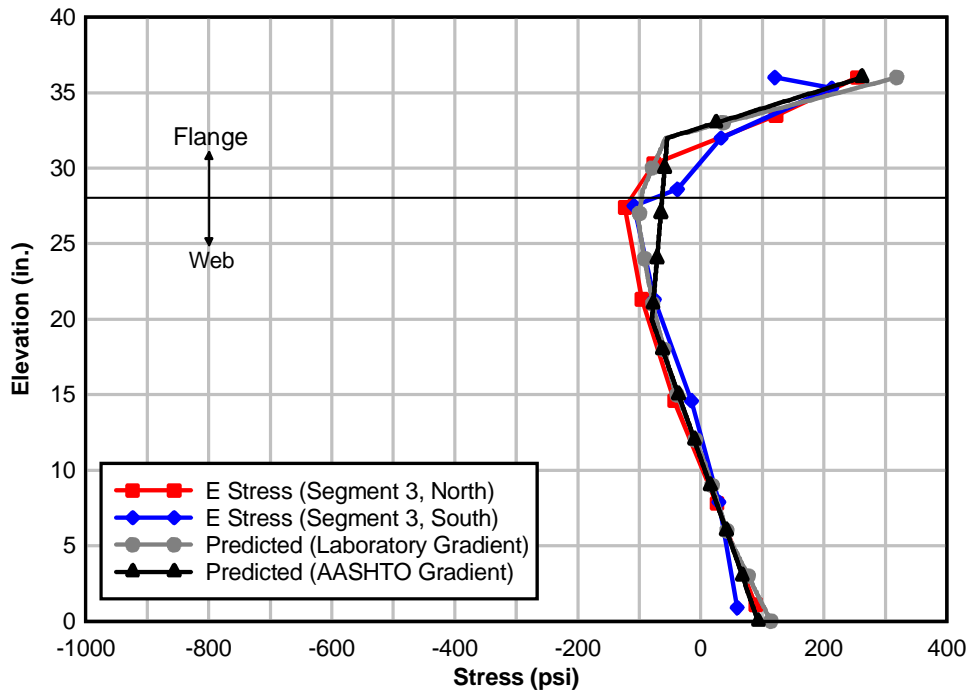


Figure 14-13. E stresses near joint J2 (Segment 3)

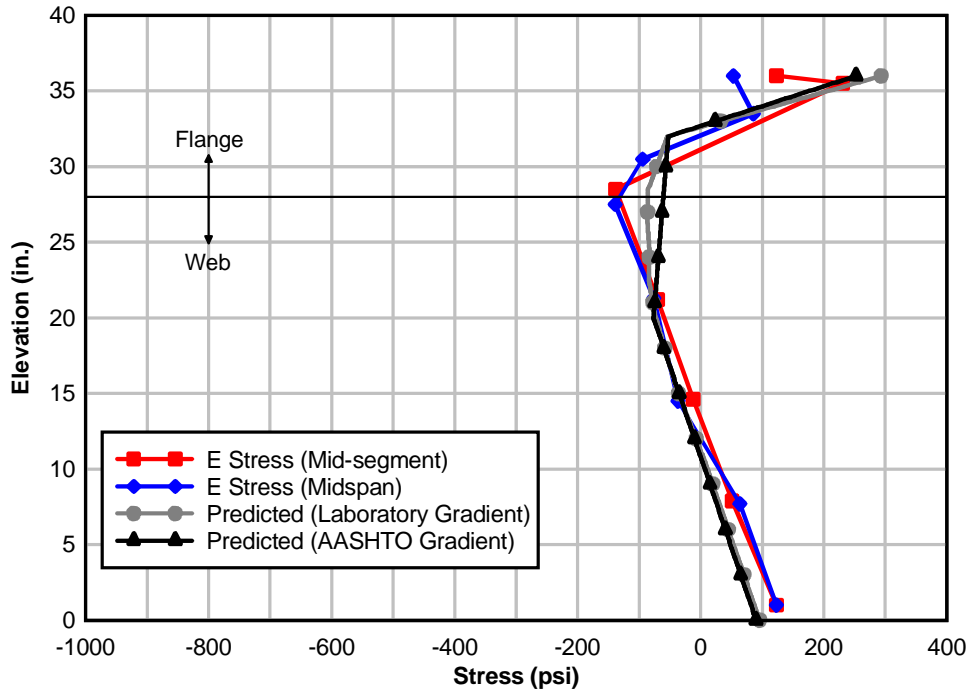


Figure 14-14. E stresses at mid-segment and midspan (Segment 2, North)

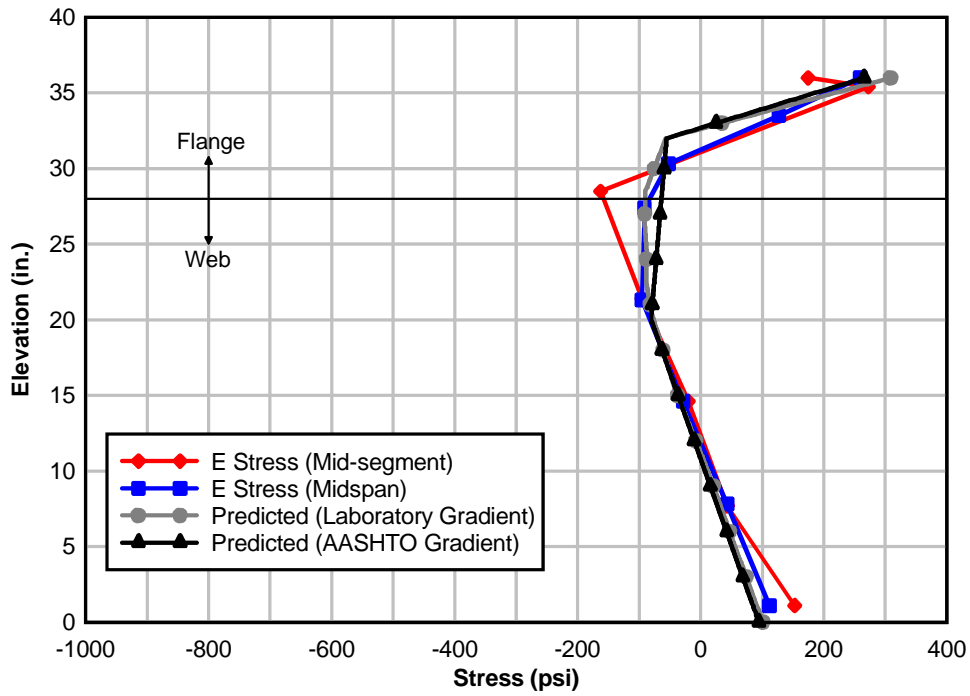


Figure 14-15. E stresses at mid-segment and midspan (Segment 3, North)

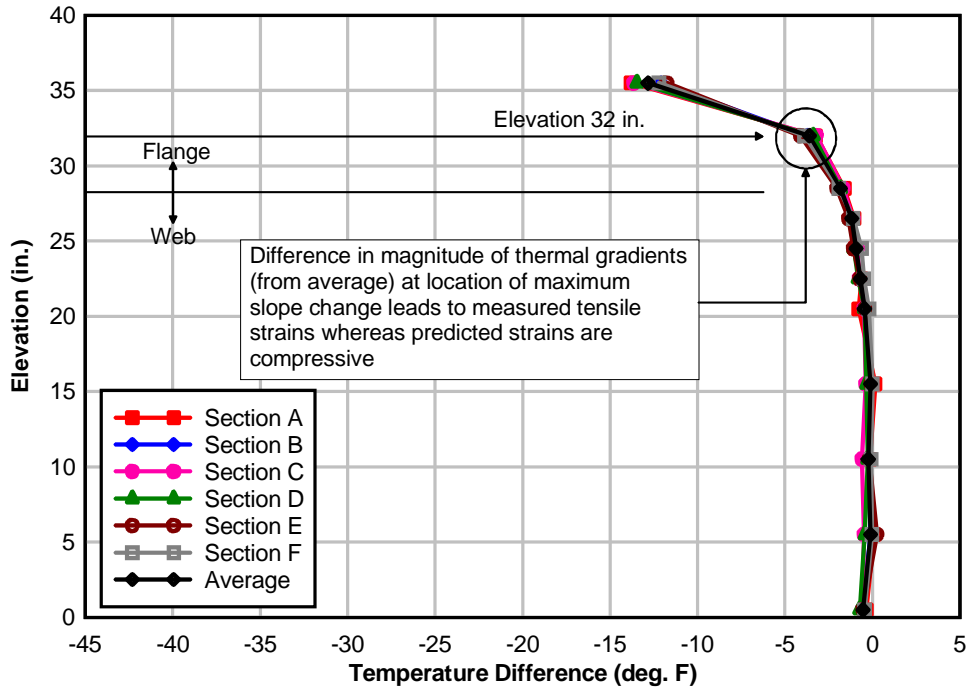


Figure 14-16. Difference in magnitude of imposed thermal gradients at location of maximum slope change (elevation 32 in.)

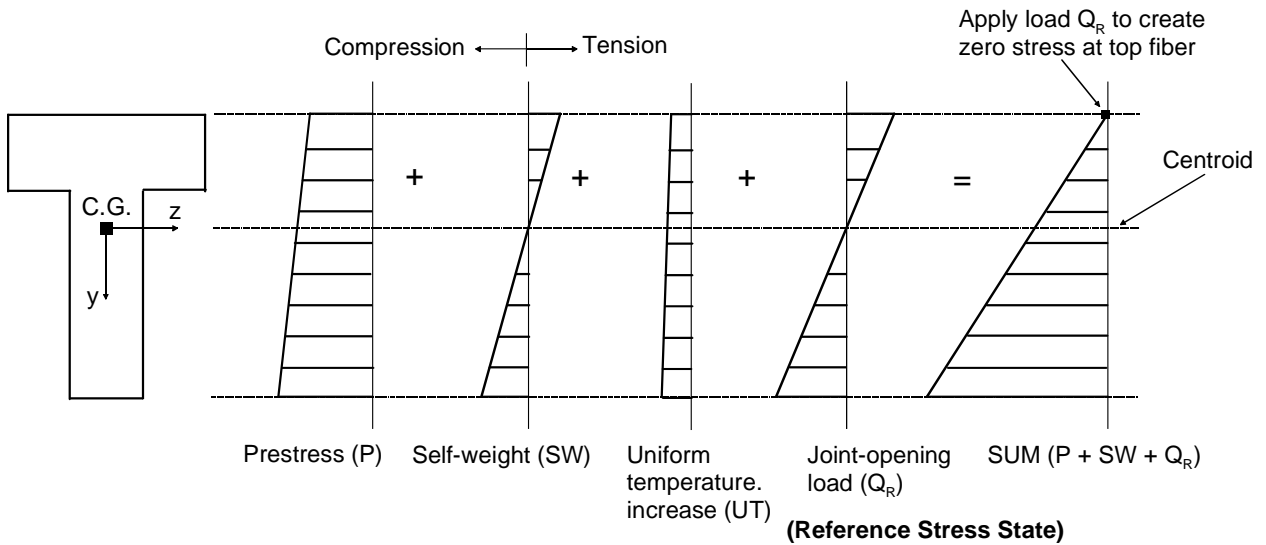


Figure 14-17. Superposition of component stress blocks (mechanical with uniform temperature increase)

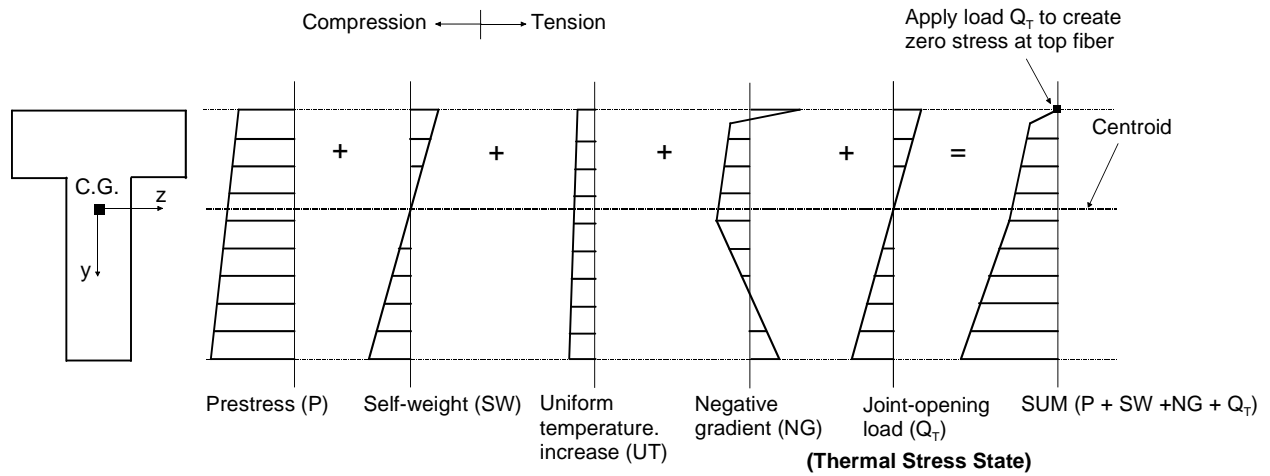


Figure 14-18. Superposition of component stress blocks (mechanical with uniform temperature increase and negative thermal gradient)

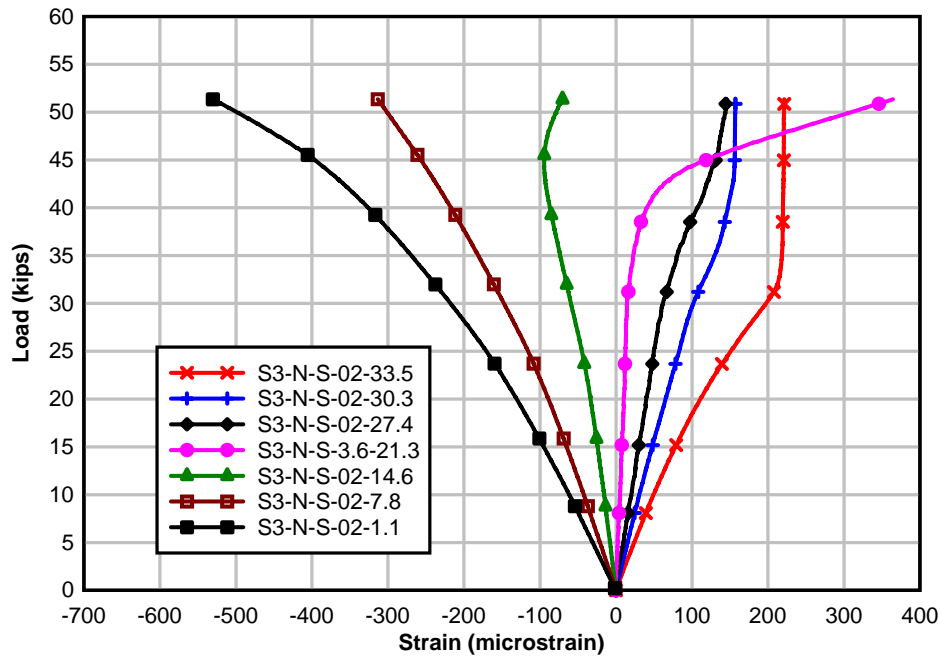


Figure 14-19. Load vs. strain at reference temperature (Segment 3, North)

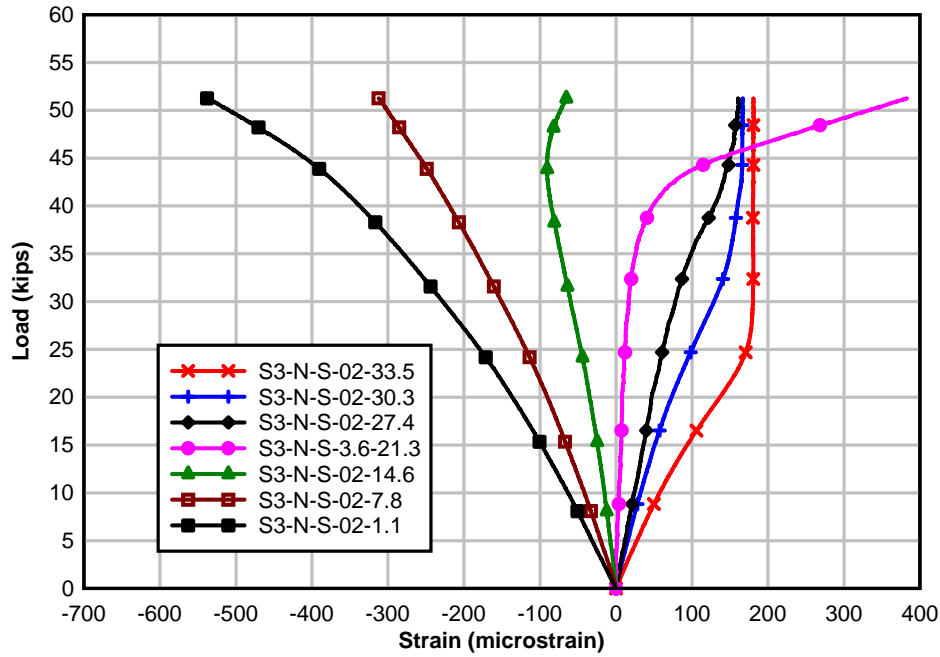


Figure 14-20. Load vs. strain with negative thermal gradient (Segment 3, North)

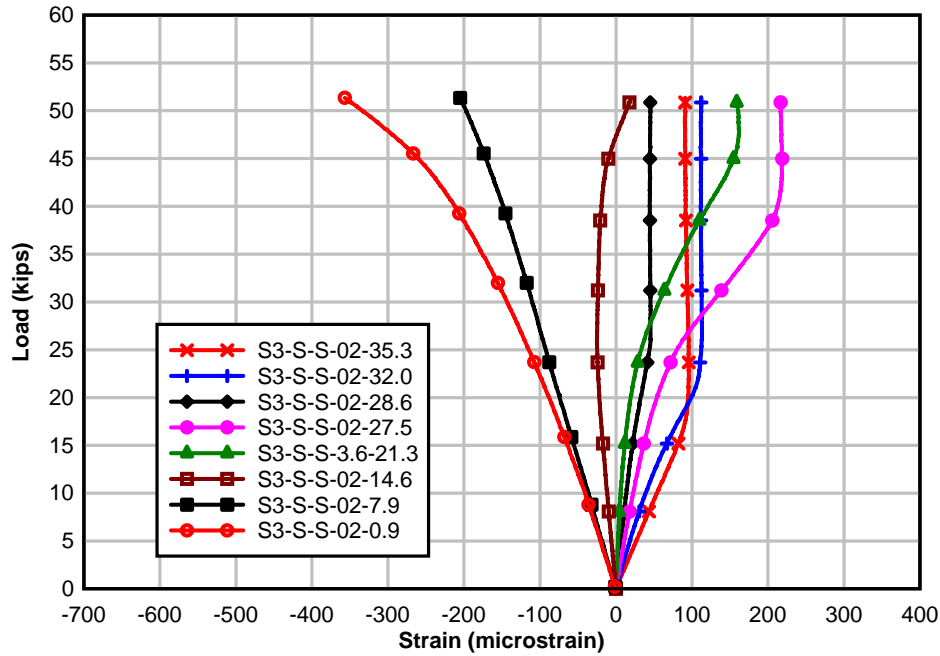


Figure 14-21. Load vs. strain at reference temperature (Segment 3, South)

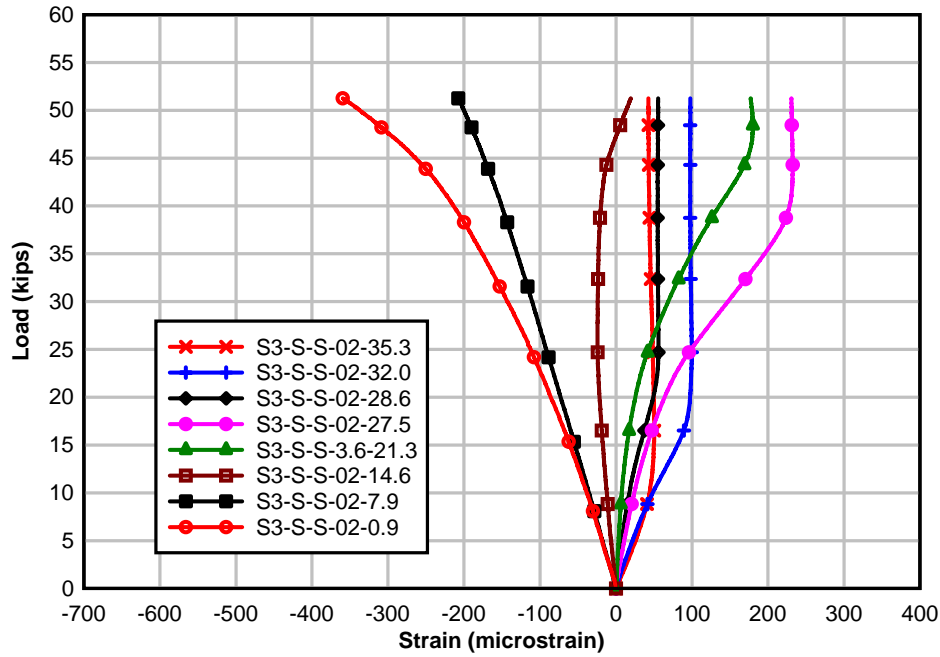


Figure 14-22. Load vs. strain with negative thermal gradient (Segment 3, South)

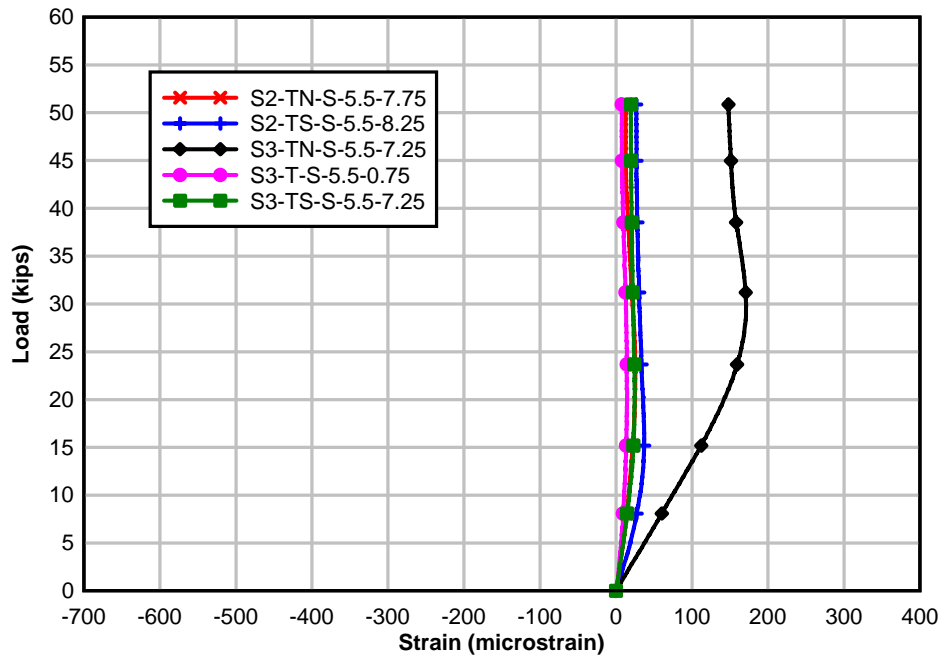


Figure 14-23. Load vs. strain at reference temperature (Top flange)

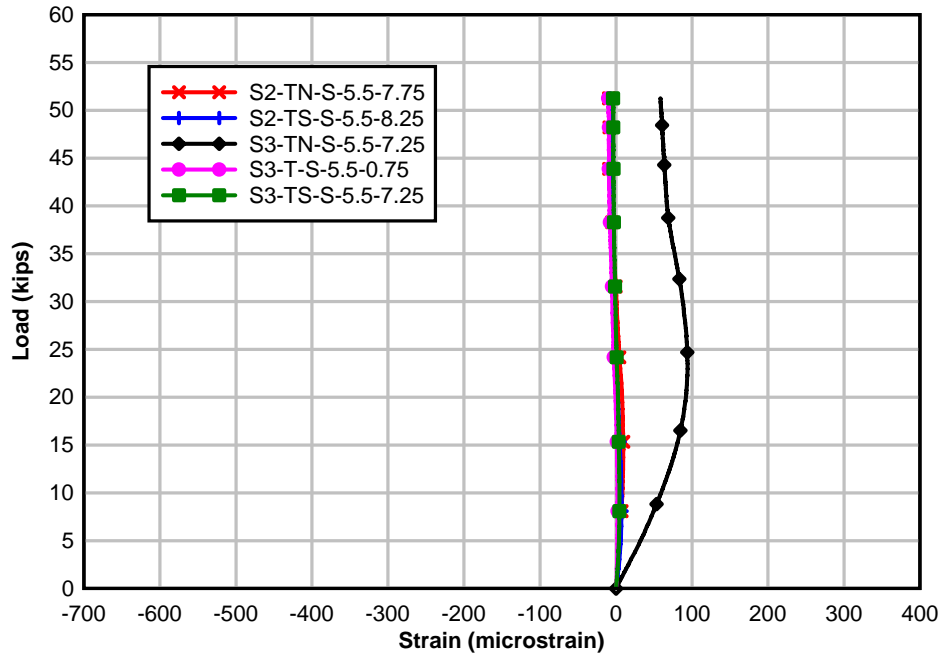


Figure 14-24. Load vs. strain with negative thermal gradient (Top flange)

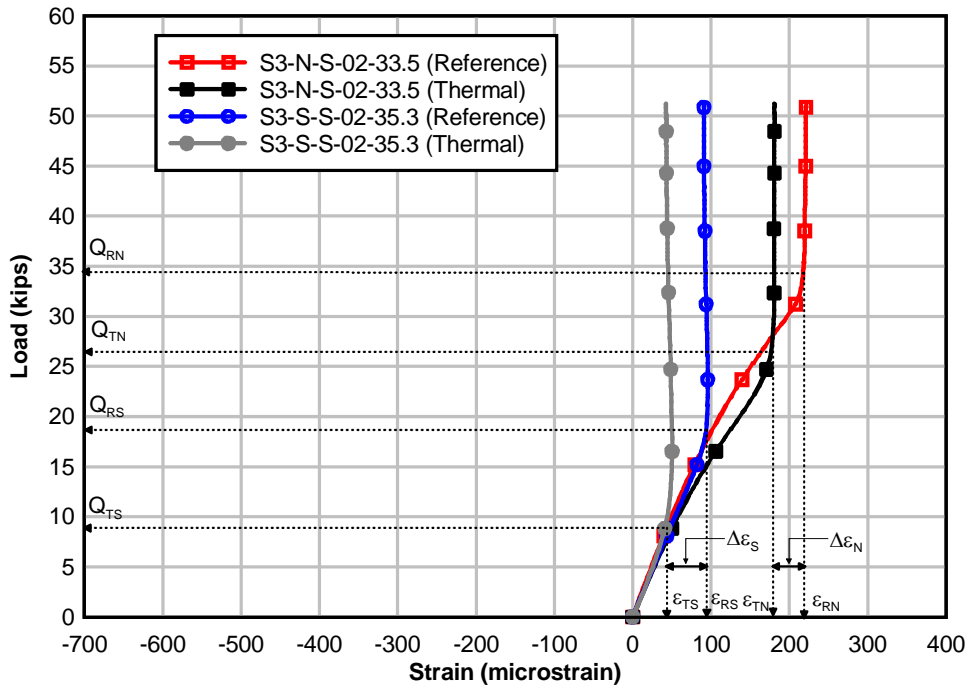


Figure 14-25. Comparison of strain differences on North and South sides of joint J2 (Negative thermal gradient)

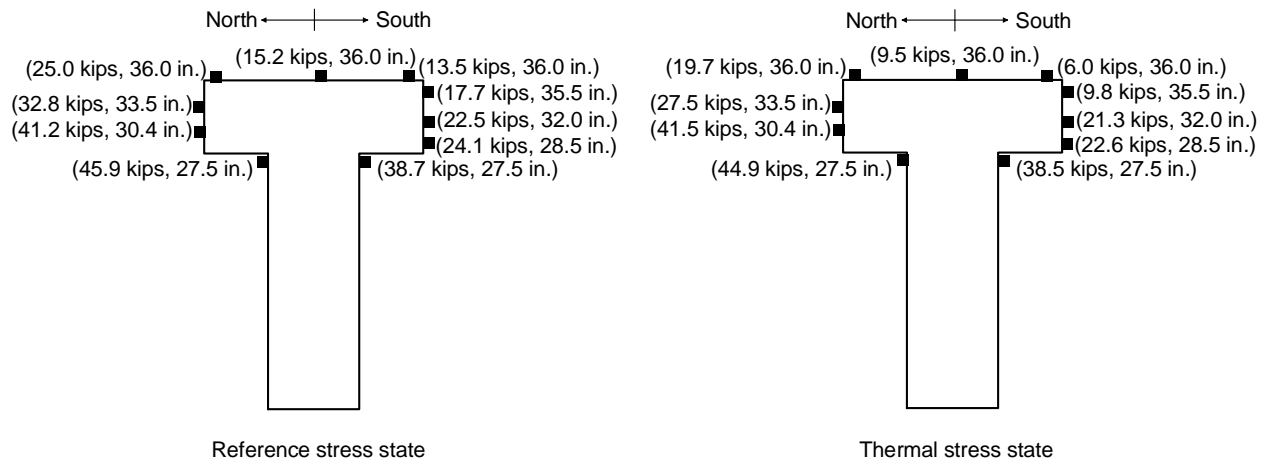


Figure 14-26. Joint opening loads detected from strain gauges near joint J2

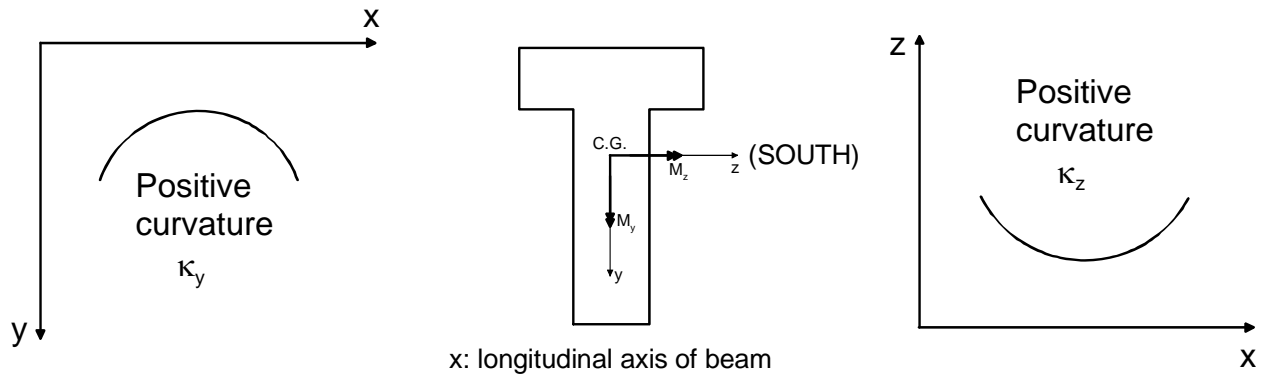


Figure 14-27. Sign convention for moments and curvature

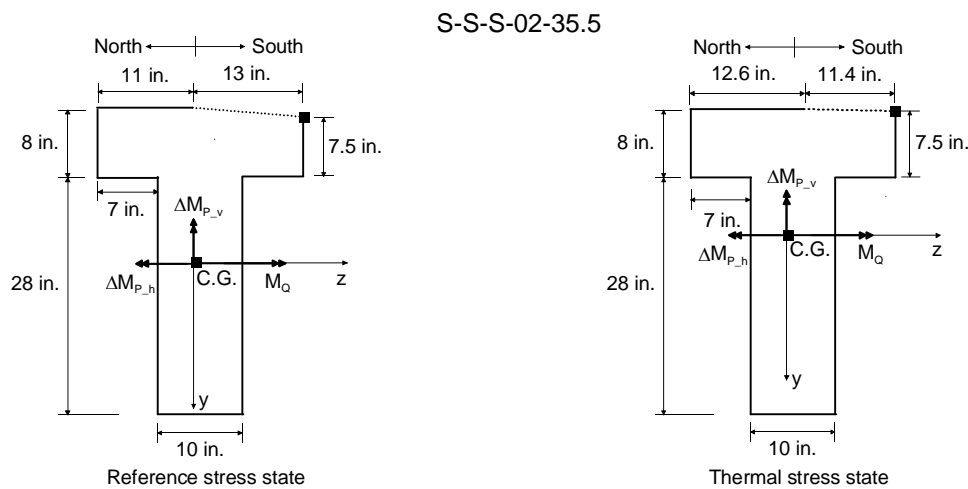


Figure 14-28. Contact areas at joint J2 at incipient opening of joint on South side at elevation 35.5 in.

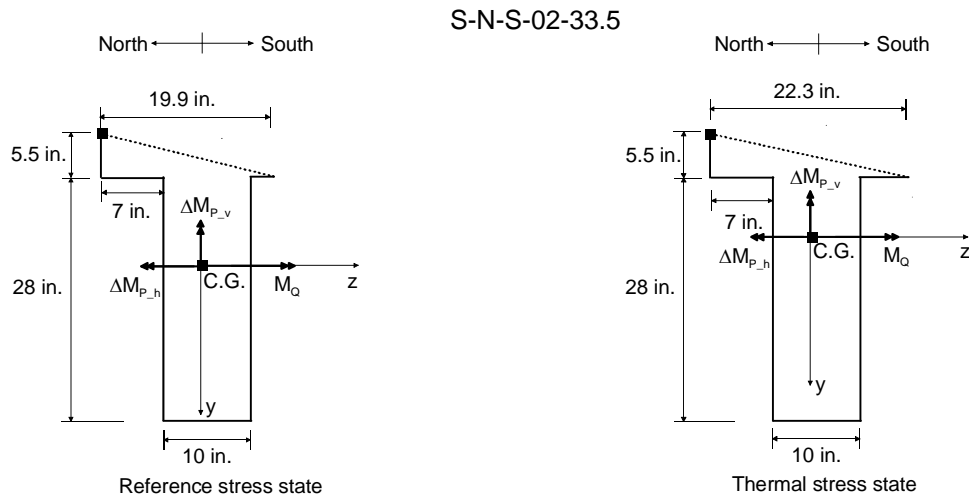


Figure 14-29. Contact areas at joint J2 at incipient opening of joint on North side at elevation 33.5 in.

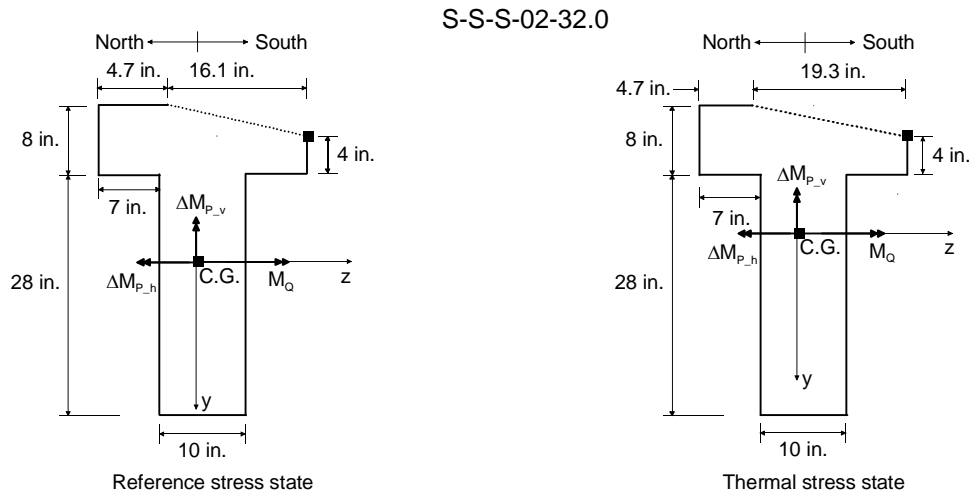


Figure 14-30. Contact areas at joint J2 at incipient opening of joint on South side at elevation 32.0 in.

CHAPTER 15 SUMMARY AND CONCLUSIONS

Results from a series of tests conducted on a 20 ft-long 3 ft-deep segmental concrete T-beam, aimed at quantifying self-equilibrating thermal stresses caused by AASHTO design nonlinear thermal gradients, have been presented and discussed. The beam consisted of four 5 ft long segments that were post-tensioned together. Layers of copper tubes, which would later carry water, were embedded in the middle two segments of the beam (Segments 2 and 3), designated “heated” segments. Thermocouples were also cast into the heated segments to monitor the distribution of temperature. The two end segments of the beam (Segments 1 and 4), which were designated “ambient” segments, were strengthened using steel reinforcing bars to carry loads at the prestress anchorage zones. The beam was vertically supported at midspan and at the end of one ambient segment. Mechanical loads were applied at the cantilevered end and thermal profiles were imposed on the heated segments by passing water at specific temperatures through each layer of copper tubes. The region of interest in the experimental program was the dry joint between the two heated segments of the beam (designated joint J2), which was heavily instrumented with surface strain gauges and LVDTs. Detection of opening of the joint was of primary importance in quantifying stresses caused by the application of AASHTO nonlinear thermal gradients.

The experimental program consisted of determining the in-situ coefficient of thermal expansion (CTE) of the heated segments; investigating the behavior of the beam under the action of mechanical loads; applying a uniform temperature change on the heated segments to investigate the free expansion behavior of the beam; and imposing the AASHTO design nonlinear thermal gradients in combination with mechanical loads for the purpose of quantifying self-equilibrating thermal stresses due to the thermal gradients.

In-situ CTEs of Segments 2 and 3 were determined by imposing uniform and linear temperature distributions on each segment. The CTE of Segment 3 was also determined using a procedure specified by AASHTO. Good agreement was found between the in-situ CTEs determined using uniform and linear thermal profiles for both segments. Good agreement was also found between the CTE determined using the AASHTO method and the average in-situ CTE of Segment 3. AASHTO CTE testing was not conducted for Segment 2 because the cylinders required for the test were not cast for this segment.

Mechanical load tests indicated that strain gauges mounted on the side surfaces of the beam close to the joint at midspan (joint J2) were the most reliable instruments in detecting opening of the joint. However, strain gauges mounted on the top surfaces of the segment flanges near the joint showed little change in strain with increasing applied load. This was attributed to an imperfect fit (despite match-casting of the segments) at the joint, and differential shrinkage in the top flange fibers which were unsealed and exposed to the laboratory environment during curing of the segments. Strain distributions through the height of the contact area at the joint (before and after the joint opened) were generally found to be linearly dependent on applied load, which allowed for the use of classical flexural stress formulas in quantifying stresses due to the AASHTO nonlinear thermal gradients. Observations and conclusions that were drawn from the directly measured experimental data are as follows:

- A uniform temperature increase of 41 °F increased the prestress force by about 6% of the initial prestress due to differential movement and heating between the bars and concrete segments. The measured change in prestress compared well with predicted values determined using in-situ CTEs and laboratory determined concrete elastic moduli.
- Measured concrete strains caused by the uniform temperature increase were generally tensile, whereas predicted strains (determined using the AASHTO recommended procedure) were compressive. The difference was attributed primarily to slight variations in temperature between the inner core and the outer perimeter of the heated segments.

- Measured stress-induced concrete strains caused by the laboratory-imposed nonlinear thermal gradients on top of the flanges of the heated segments near joint J2 were significantly less than predicted for both positive and negative thermal gradients. For the positive thermal gradient, average measured strains on top of the flanges of segments 2 and 3 were about 56% and 39% less than predicted strains, respectively. For the negative thermal gradient, average measured strains at the same locations on segments 2 and 3 were about 81% and 53% less than predicted. The differences were attributed both to differential shrinkage in the top flange fibers and a probable discontinuity in the thermal gradients (positive and negative) within the top 0.5 in. of the flanges of the heated segments.
- At elevations below 0.5 in. from the top surface of the segment flanges near joint J2, measured stress-induced concrete strains caused by the laboratory-imposed nonlinear thermal gradients agreed well with strains predicted using the AASHTO recommended method for the analysis of nonlinear thermal gradients. Maximum measured stress-induced concrete strains (which occurred at elevation 35.5 in.) under the action of the positive thermal gradient were about 3% and 7% less than predicted strains on segments 2 and 3, respectively. For the negative thermal gradient, maximum measured stress-induced concrete strains (at the same location as for the positive thermal gradient) were about 25% and 14% less than predicted strains on segments 2 and 3, respectively.

Two independent methods were also used to quantify concrete stresses caused by the laboratory-imposed nonlinear thermal gradients at the joint between the heated segments. The first method involved multiplying measured thermal stress-induced concrete strains by elastic moduli (E stresses) whereas the second method involved determining stresses at the joint using the known stress state at incipient joint opening (J stresses). E stresses were determined throughout the height of the heated segments at a distance of about 2 in. away, the location of strain gauges from joint J2. J stresses were quantified within the top 4 in. of the flanges of the heated segments at joint J2. Conclusions from quantifying the E stresses and J stresses are as follows:

- J stresses in the extreme top flange fibers at the joint, where the maximum stresses caused by the nonlinear thermal gradients were expected to occur, could not be quantified because of the effects of differential shrinkage and because pieces of concrete had broken off the top surface during transportation and handling of the segments. Though E stresses on top of the flanges of the heated segments near joint J2 were determined, they did not agree well with predicted stresses because of reasons given in the third bulleted paragraph above.

- Maximum E stresses caused by the positive thermal gradient, which occurred at elevation 35.5 in. (i.e. 0.5 in. below the top surface of the segment flanges), were about 3% and 8% less than corresponding predicted self-equilibrating thermal stresses in Segment 2 and Segment 3, respectively. Maximum J stresses caused by the positive thermal gradient (also at elevation 35.5 in.) were about 10% and 15% less than the predicted self-equilibrating thermal stresses in segments 2 and 3, respectively.
- In the case of the negative thermal gradient, maximum E stresses (which also occurred at elevation 35.5 in.) were about 25% and 14% less than corresponding predicted self-equilibrating thermal stresses in segments 2 and 3, respectively. Maximum J stresses (at the same elevation) were about 17% and 23% less than predicted stresses in segments 2 and 3, respectively.
- The percentage difference between maximum measured and maximum predicted negative gradient stresses was higher than that for the positive thermal gradient because the negative thermal gradient was more sensitive to local deviations of temperature from the width-wise average temperatures that were used in predicting the self-equilibrating thermal stresses. The difference in sensitivity was due to the magnitude of the negative thermal gradient being only 30% the magnitude of the positive thermal gradient.

E stresses and J stresses in the top few inches of the flanges of segments 2 and 3 were in general lower than stresses predicted using the AASHTO recommended procedure. In particular, the maximum quantified stresses due to the negative thermal gradient were on the average about 20% less than corresponding predicted stresses (at the same location). These differences between quantified and AASHTO predicted stresses could, however, not be attributed to any flaws in the AASHTO method. They were considered to be likely the result of experimental error. Based on the effects of differential shrinkage at joint J2, and the slight damage to the top flange surfaces of the segments at the joint on the magnitude of quantified stresses, it is possible that self-equilibrating thermal stresses in the top section fibers at dry joints in segmental concrete bridges may be smaller in magnitude than stresses predicted using the AASHTO method.

This study focused mainly on quantifying self-equilibrating stresses caused by the AASHTO nonlinear thermal gradients. Some suggestions on future research are proposed:

- The current AASHTO nonlinear thermal gradients are computationally inconvenient and do not work well with most structural analysis software. Furthermore, the stresses of importance in design are the stresses in the top 4 in. of box-girder flanges. A study on

simplifying the nonlinear thermal gradients into a combination of linear gradients, such that stresses of equal magnitude (especially the maximum stresses) caused by the nonlinear gradients in the top 4 in. are generated by the combination of linear gradients, would greatly simplify the computational effort that currently goes into calculating self-equilibrating stresses in complex box-girder sections.

- The effect on concrete durability of tensile stresses generated by the AASHTO negative thermal gradient in the top few inches of the flanges of segmental concrete bridges needs investigation. Though tensile stresses have been known to cause damage to concrete, this damage has been difficult to quantify. A study into the effect of the relatively steep self-equilibrating stress gradient in the top few inches of concrete (compared to typical bending stresses) on the potential for cracking would lead to a better understanding of the level of damage that gradient-induced tensile stresses may cause.

APPENDIX A BEAM SHOP DRAWINGS

In this appendix, design plans for the construction of the laboratory segmental beam are presented. Steel reinforcement in prestress anchorage zones, thermocouple cages, copper tube locations, plans for the loading mechanism, and shear keys are shown.

Date: JUL 2008 Drawn: L.A.M. D.W. Checked: D.M. Project: 029 Client: U.S. Army Corps of Engineers Contract: W91133-00-2-0000 Project # 029 Sheet 2 OF 3	RESEARCH TEAM: M.F., D.W., & C.A. PROJECT #S: H.M.H. & G.R.C. THERMAL GRADIENT RESEARCH PROPOSED TEST BEAM FOR	UNIVERSITY OF FLORIDA STRUCTURES DEPARTMENT 1616 UNIVERSITY BLVD. GAINESVILLE, FL 32611-8440 PHONE: 352/392-2934 FAX: 352/392-2934 WWW: WWW.UFL.EDU
--	---	---

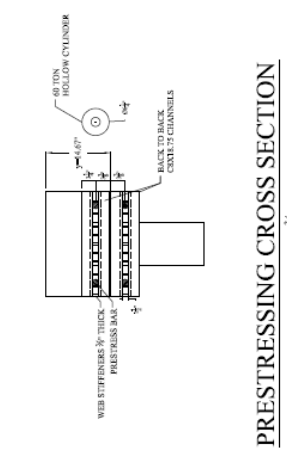
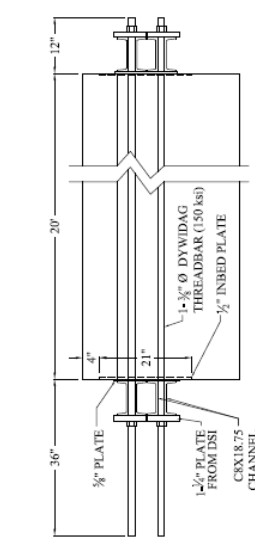
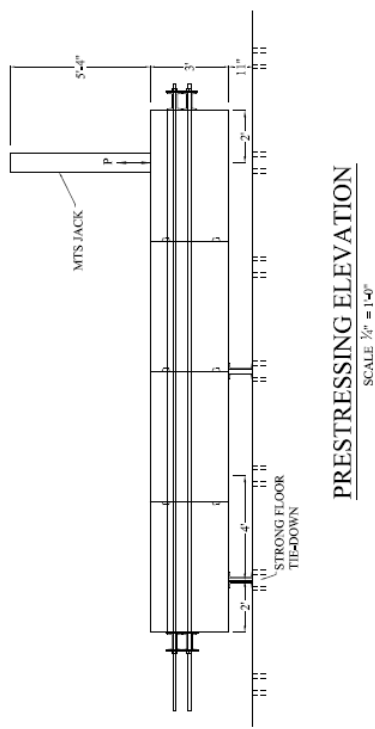
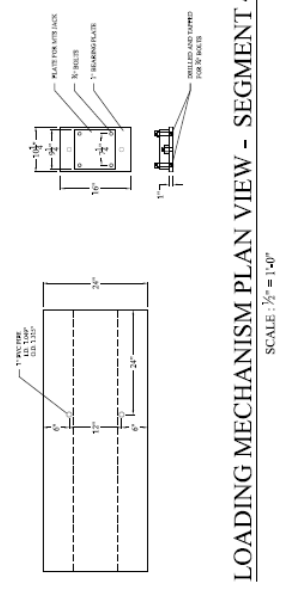
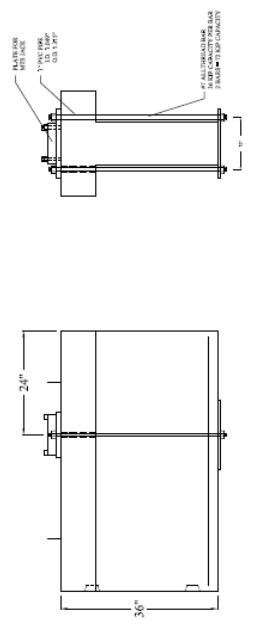
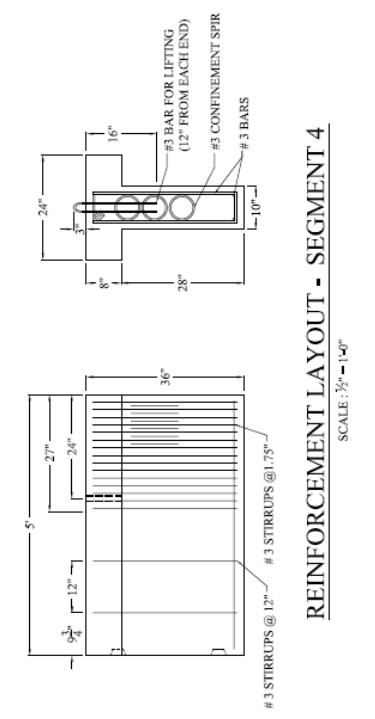
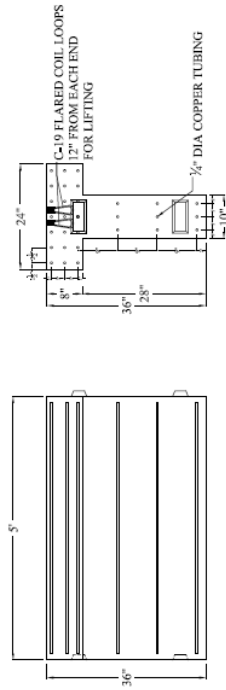
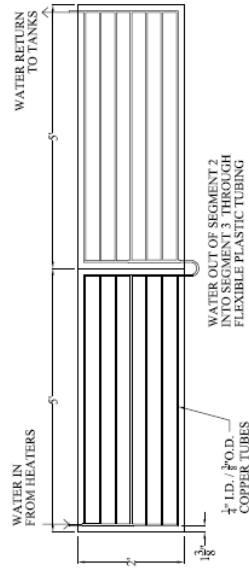


Figure A-1. Prestress reinforcement details

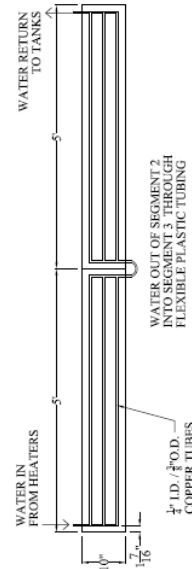
RESEARCH TEAM: M.F., D.W., & G.A.C. PROJECT #S: HRH & G.R.C. THERMAL GRADIENT RESEARCH PROPOSED TEST BEAM FOR	UNIVERSITY OF FLORIDA STRUCTURES DEPARTMENT 1600 GENE SMITH DRIVE GAINESVILLE, FL 32611 PHONE: (352) 392-3000 FAX: (352) 392-3004 WWW: WWW.UFL.EDU	Project # : Date : Drawn by : Checked by : Scale :	SHEET 1 OF 3
--	--	--	-----------------



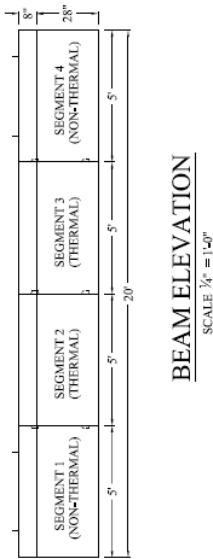
TUBING LAYOUT - SEGMENTS 2 & 3
SCALE: 1/2" = 1'-0"



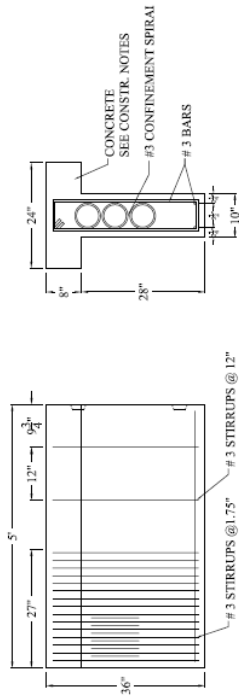
PLAN VIEW MANIFOLD SYSTEM - FLANGE
SCALE: 1/2" = 1'-0"



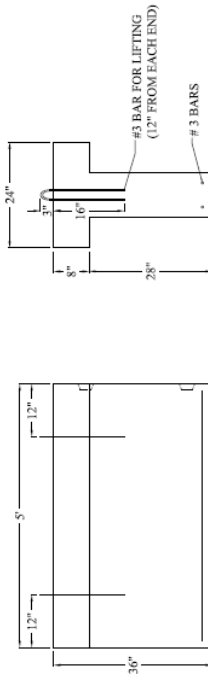
PLAN VIEW MANIFOLD SYSTEM - WEB
SCALE: 1/2" = 1'-0"



BEAM ELEVATION
SCALE: 1/4" = 1'-0"



REINFORCEMENT LAYOUT - SEGMENT 1
SCALE: 1/2" = 1'-0"



LIFTING REINFORCEMENT LAYOUT - SEGMENT 1
SCALE: 1/2" = 1'-0"

Figure A-2. Manifold and copper tube details

APPENDIX B LOADING FRAME DRAWINGS

Details of the loading frame which was used to apply mechanical loads at the cantilevered end of the test beam are shown in this appendix.

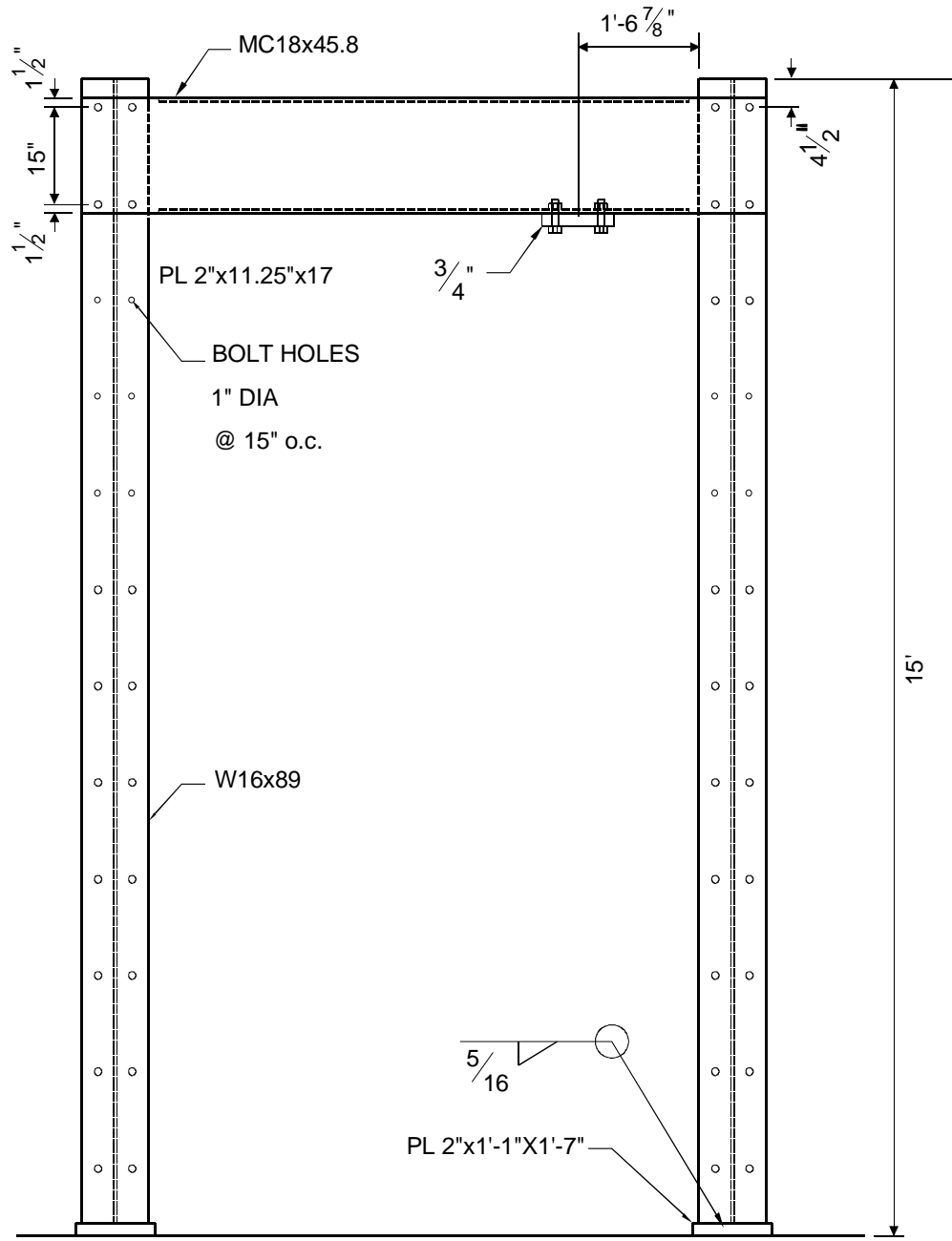


Figure B-1. Loading frame details

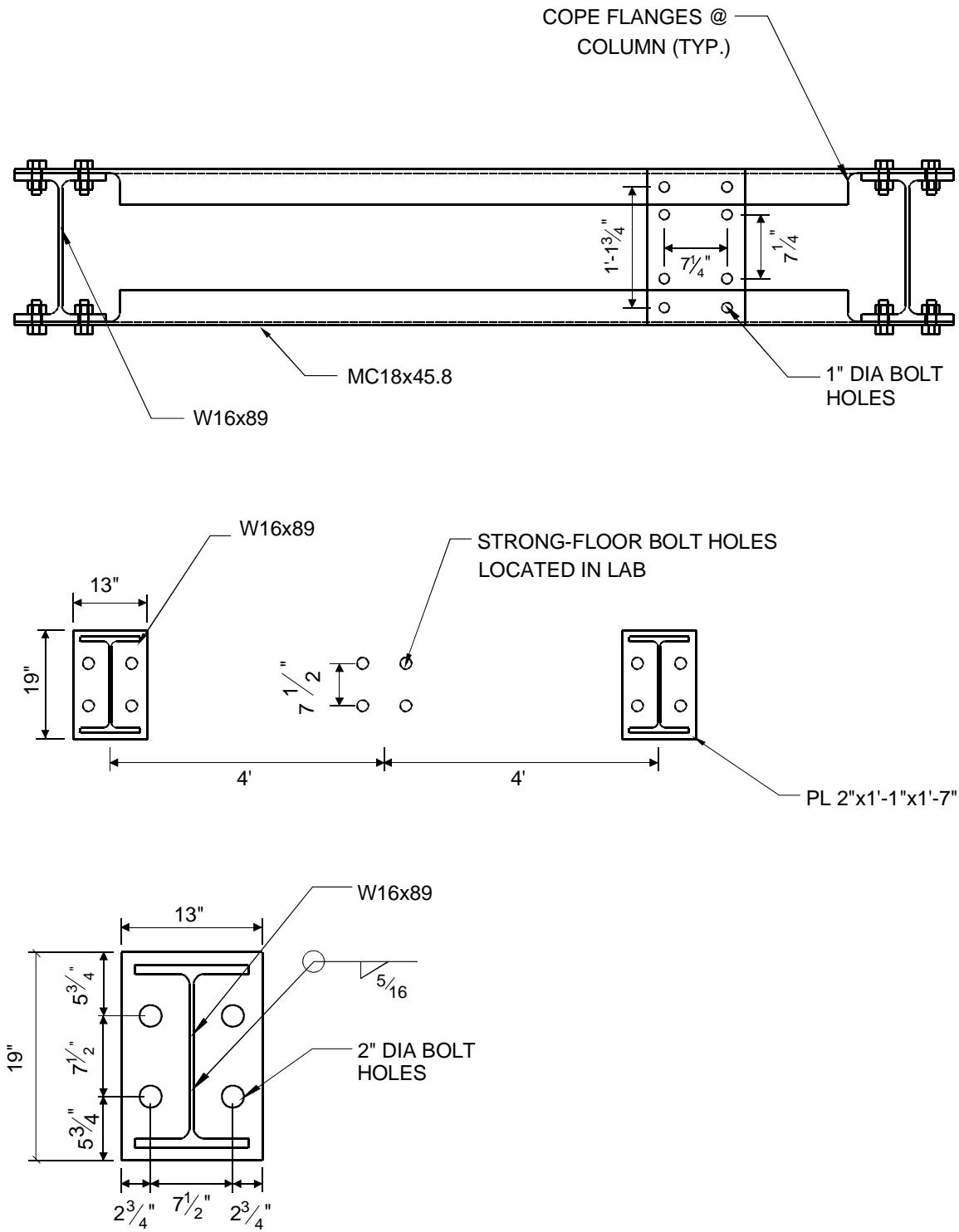


Figure B-2. Details of cross channels

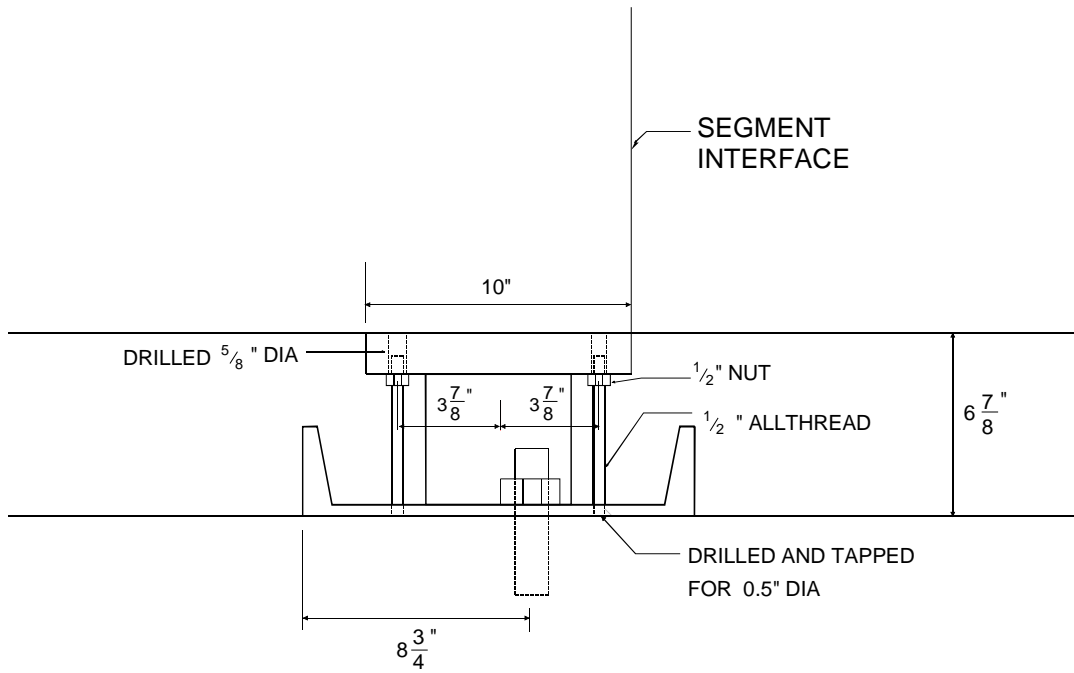
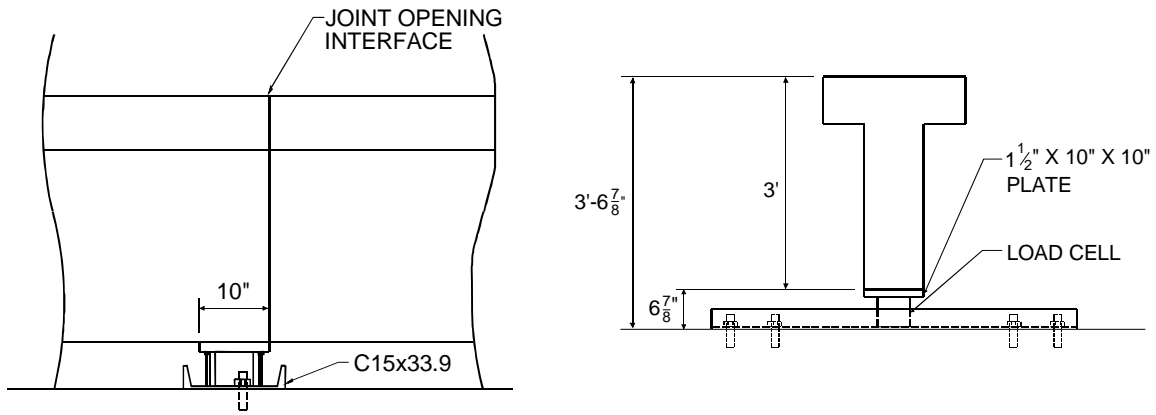


Figure B-3. Mid-support details

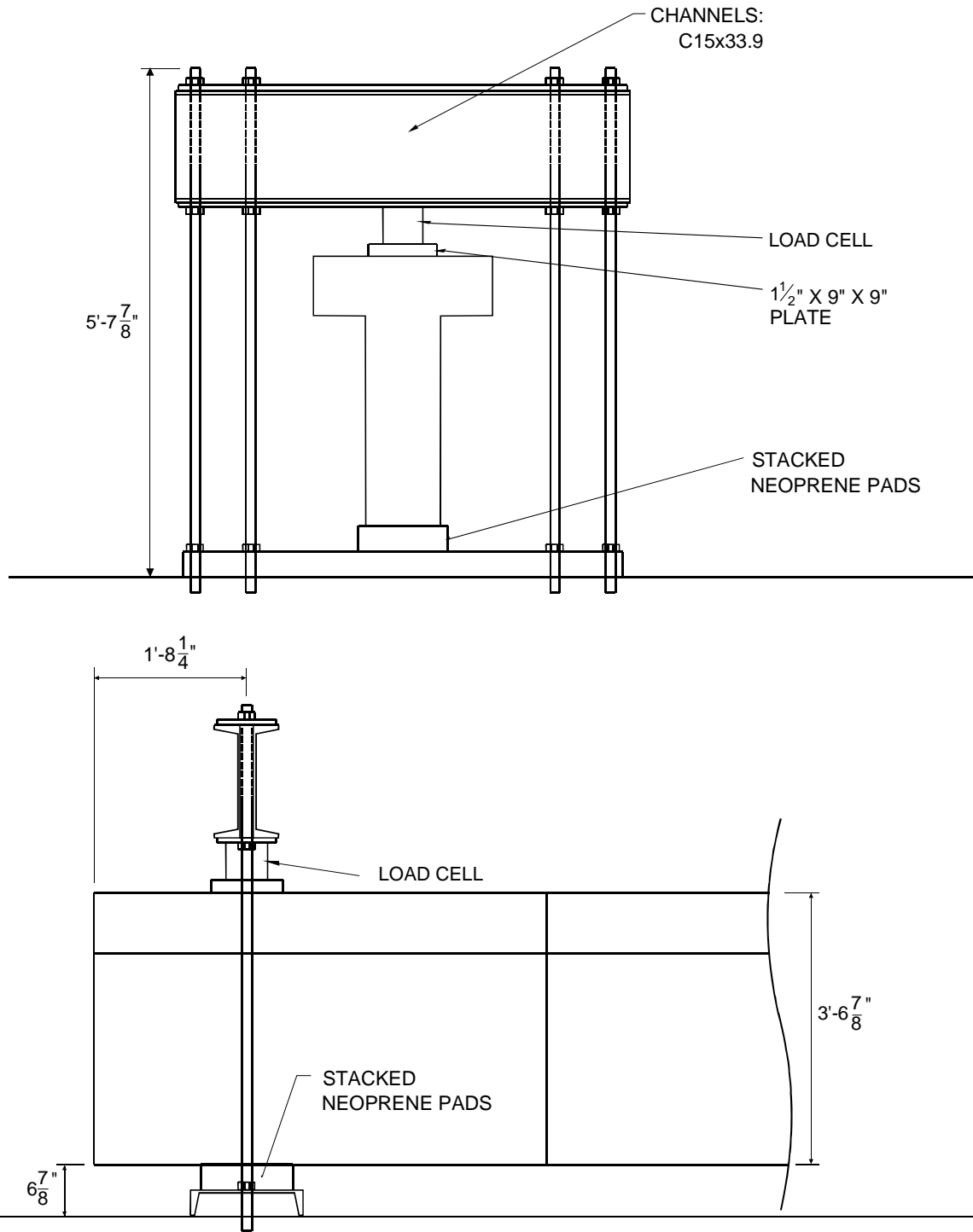


Figure B-4. End-support details

APPENDIX C
LOAD RESPONSE CURVES AT MID-SEGMENT (MECHANICAL LOADING)

In this appendix load versus strain response curves at the middle of Segment 2 and Segment 3 (30 in. away from joint J2) are presented.

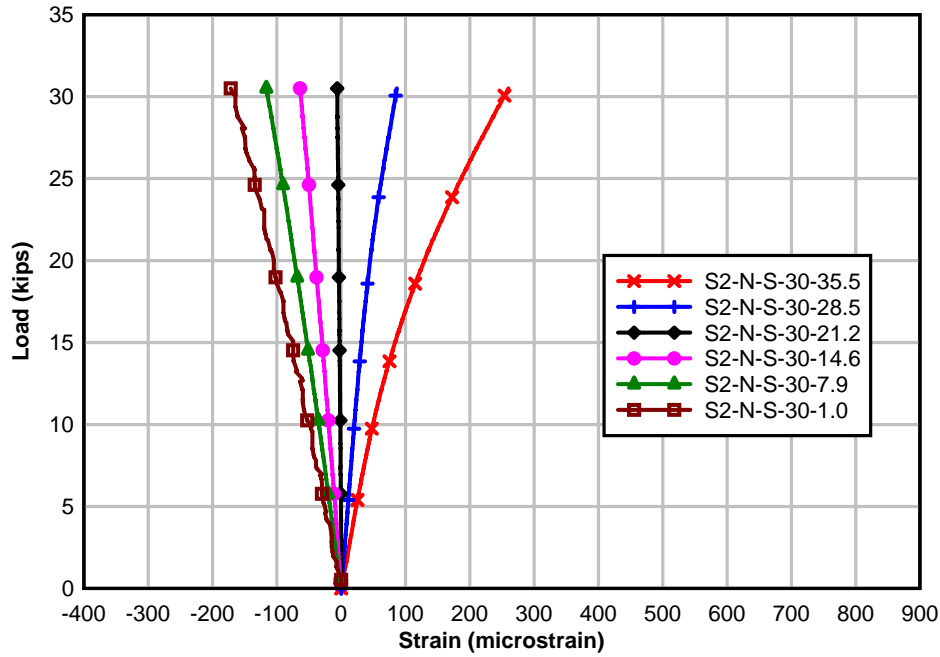


Figure C-1. Load vs. strain at middle of Segment 2 on North side

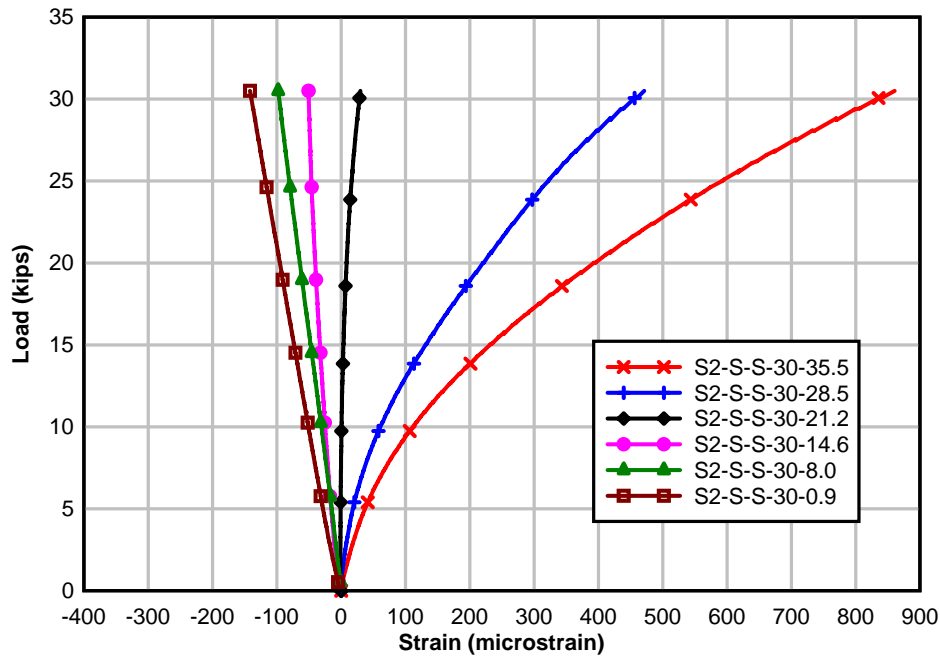


Figure C-2. Load vs. strain at middle of Segment 2 on South side

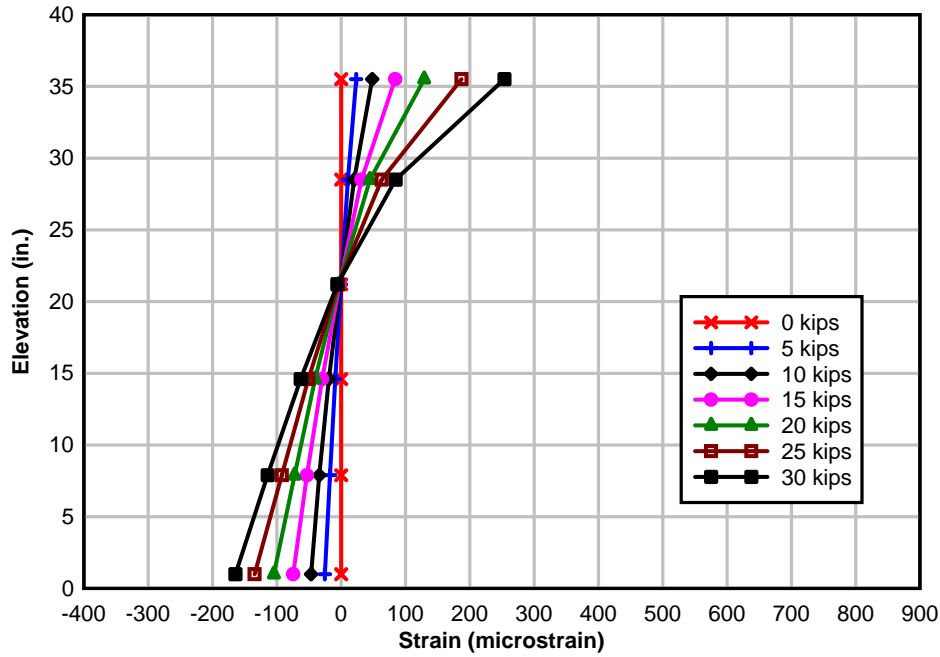


Figure C-3. Measured strain distributions at middle of Segment 2 on North side

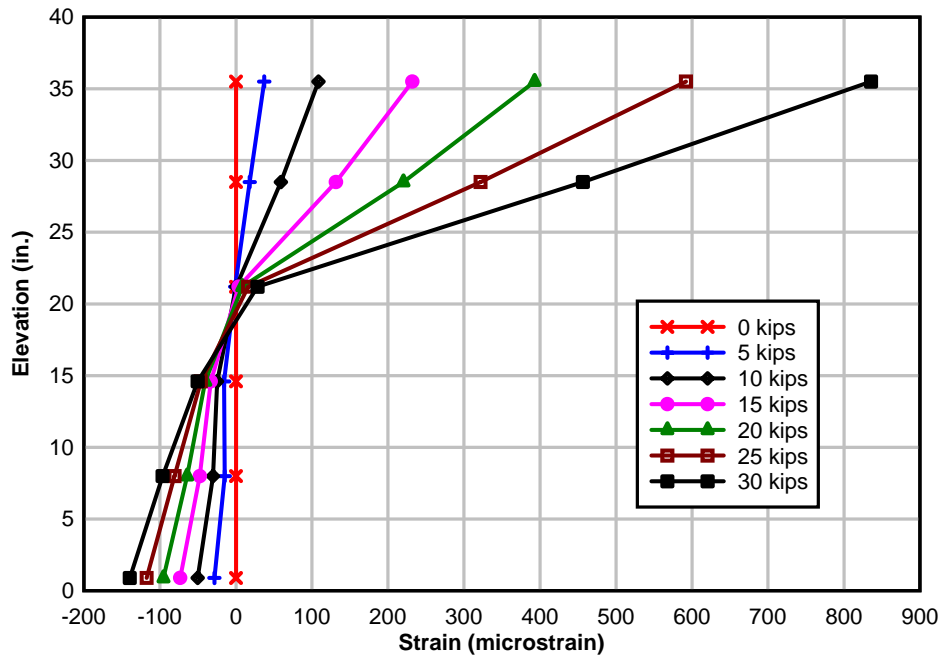


Figure C-4. Measured strain distributions at middle of Segment 2 on South side

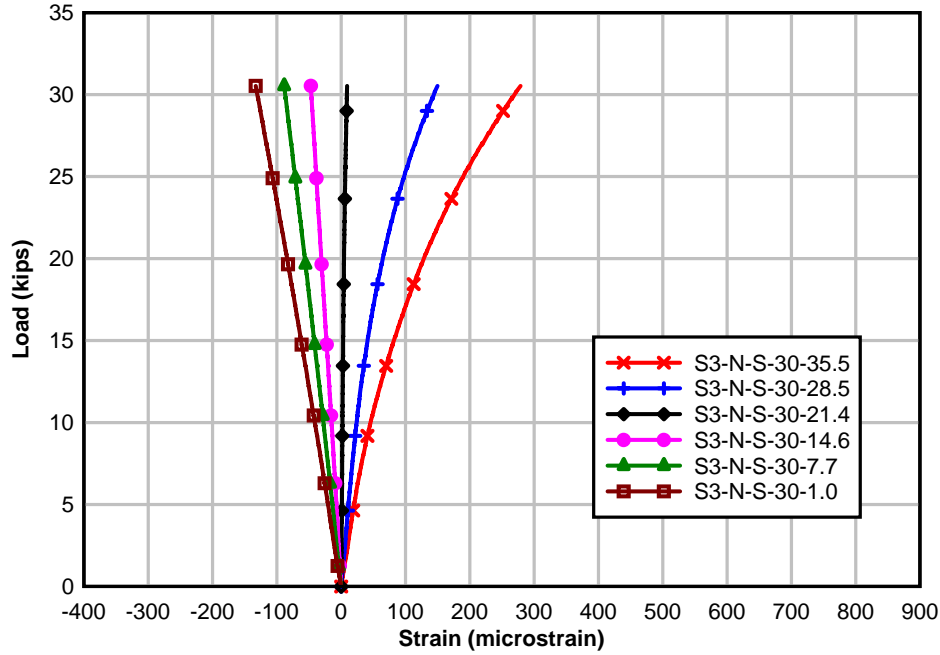


Figure C-5. Load vs. strain at middle of Segment 3 on North side

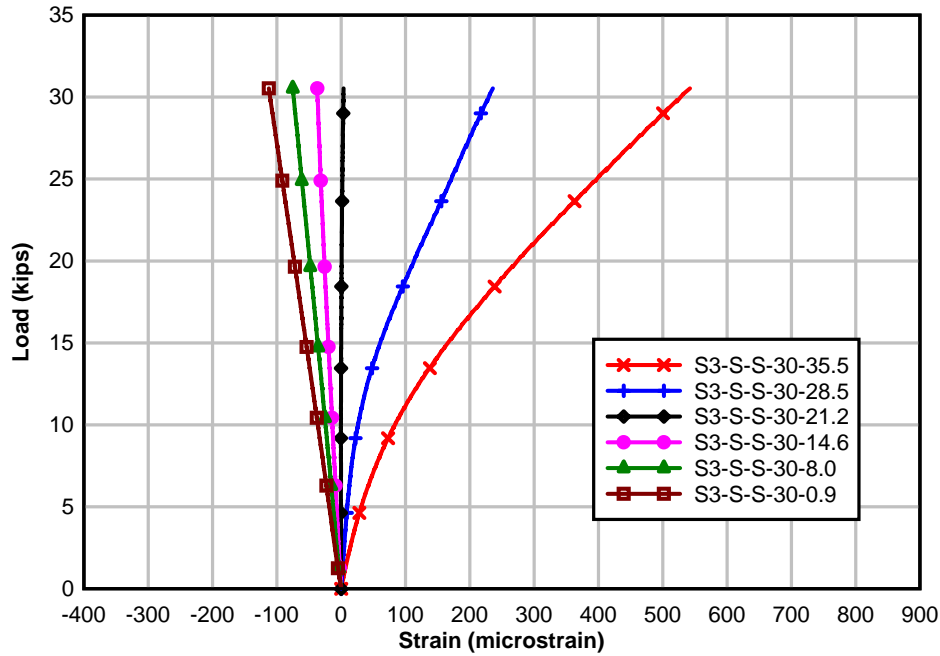


Figure C-6. Load vs. strain at middle of Segment 3 on South side

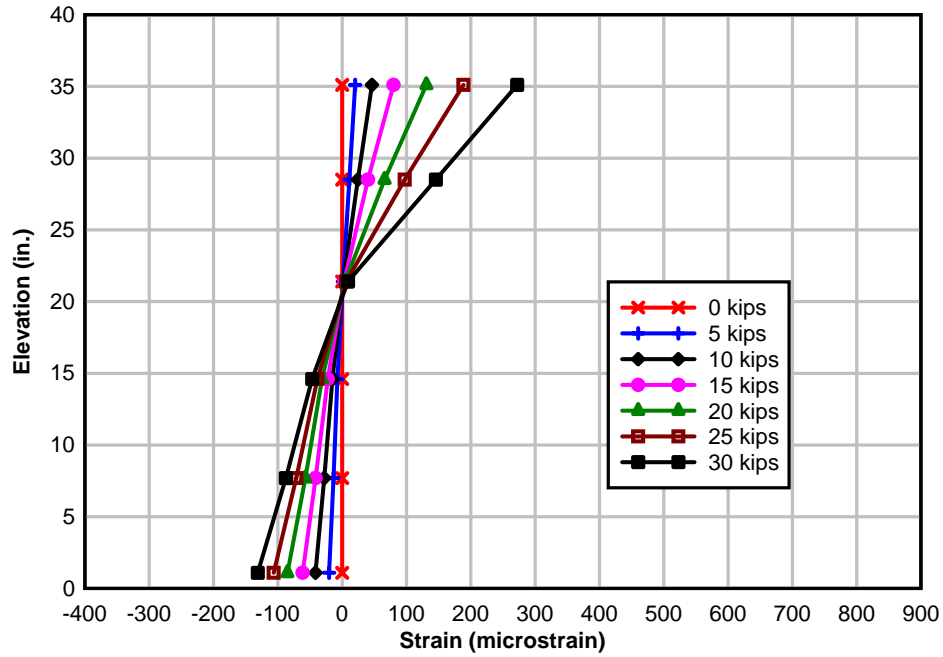


Figure C-7. Measured strain distributions at middle of Segment 3 on North side

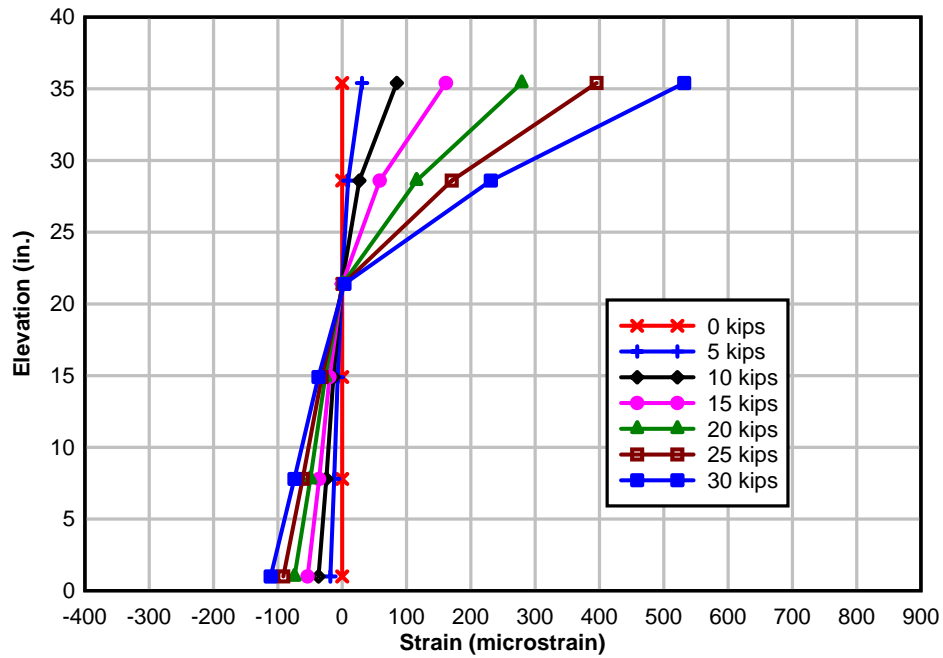


Figure C-8. Measured strain distributions at middle of Segment 3 on South side

APPENDIX D
LOAD RESPONSE CURVES (POSITIVE THERMAL GRADIENT)

Load vs. beam response curves which were derived from strain gauge and LVDT data are shown here. These curves were used to determine loads at which the joint at midspan (designated joint J2) opened. The curves were also used to determine effective concrete contact areas at joint J2, which were then used to quantify J stresses due to the AASHTO nonlinear positive thermal gradient.

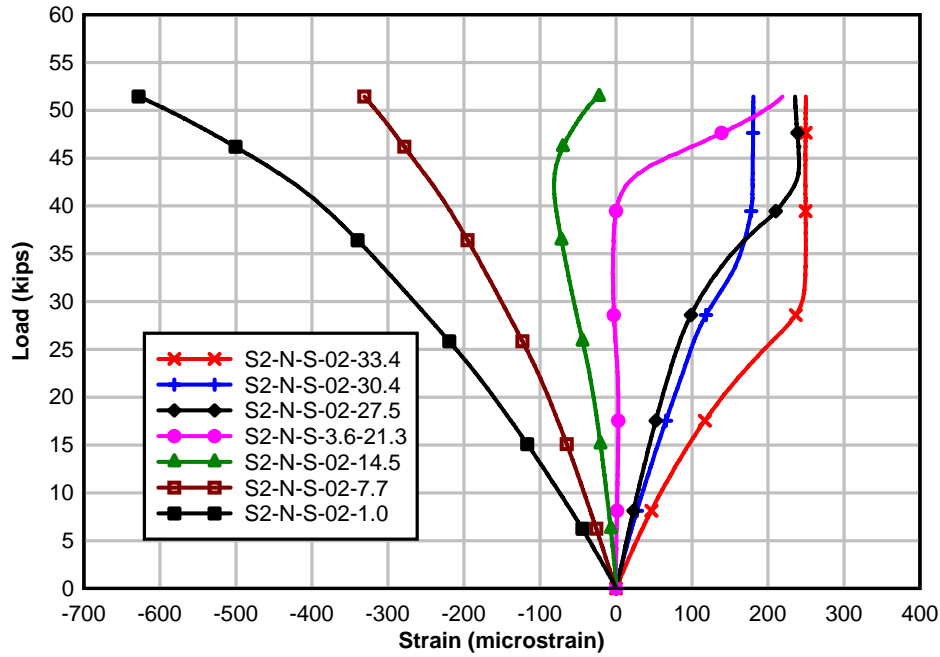


Figure D-1. Load vs. strain at reference temperature (Segment 2, North)

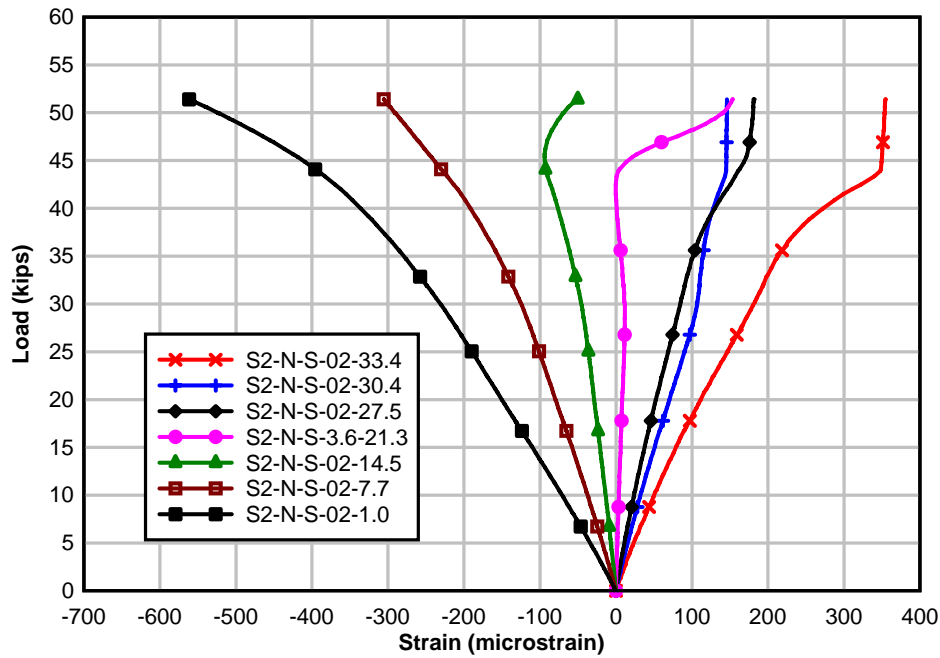


Figure D-2. Load vs. strain with positive thermal gradient (Segment 2, North)

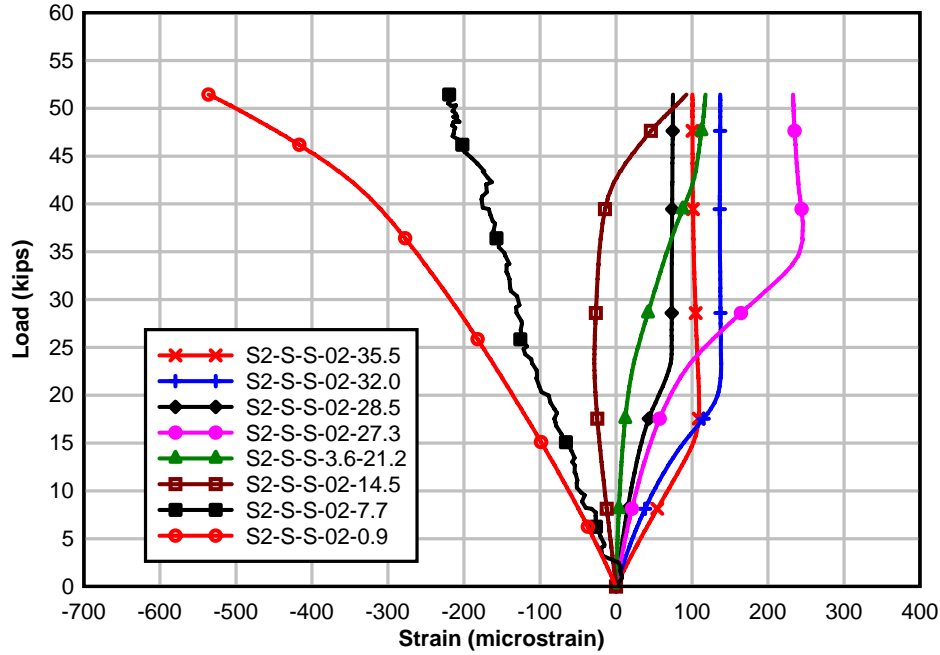


Figure D-3. Load vs. strain at reference temperature (Segment 2, South)

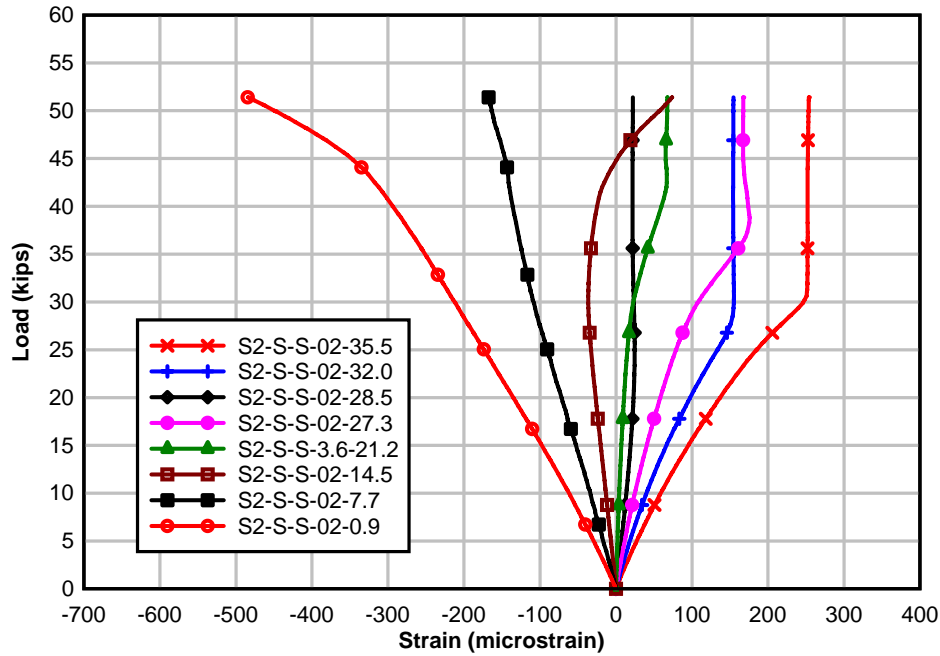


Figure D-4. Load vs. strain with positive thermal gradient (Segment 2, South)

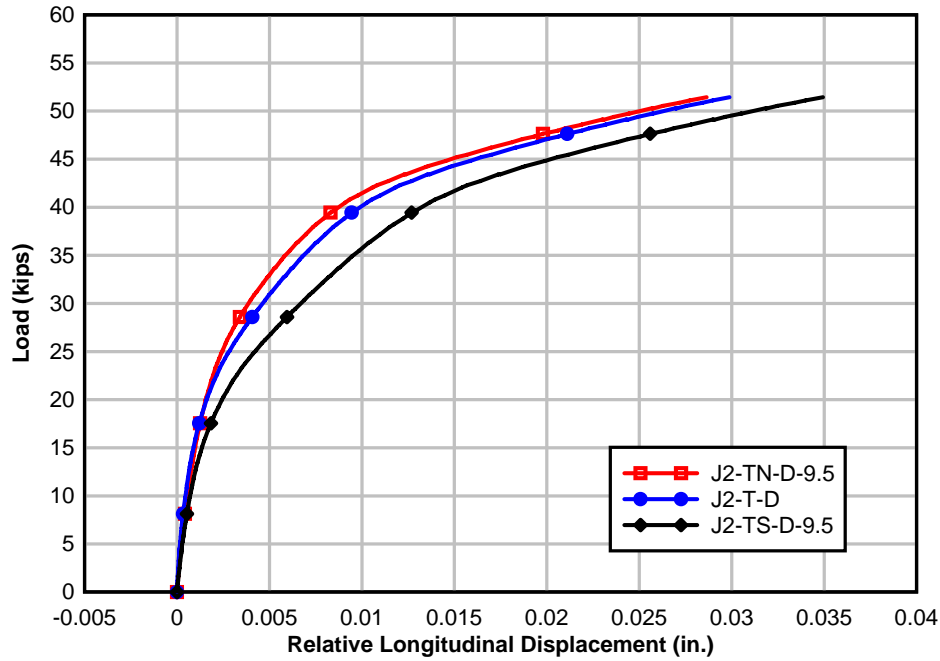


Figure D-5. Load vs. joint opening at reference temperature (Top flange)

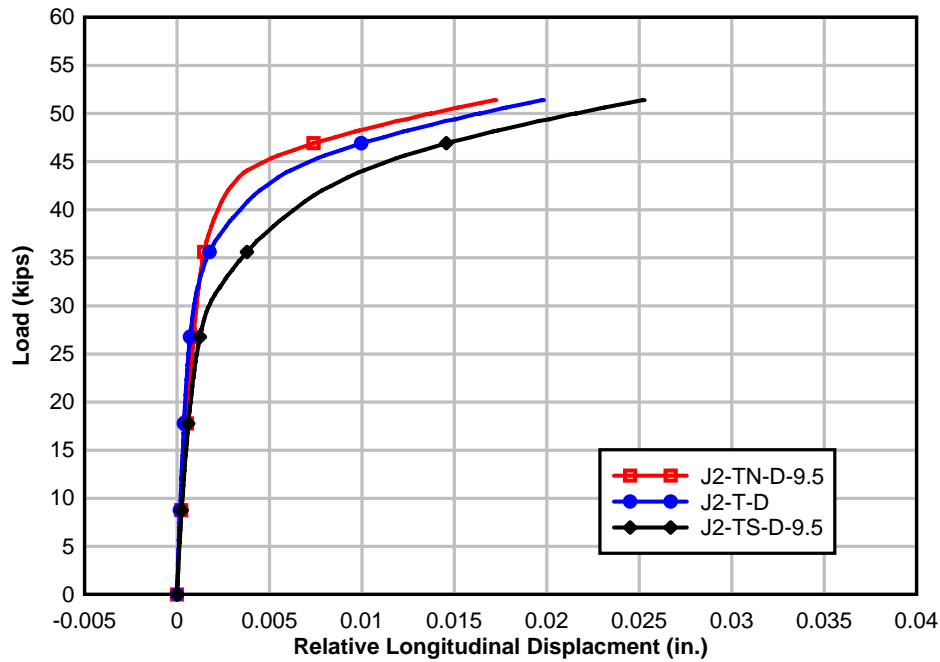


Figure D-6. Load vs. joint opening with positive thermal gradient (Top flange)

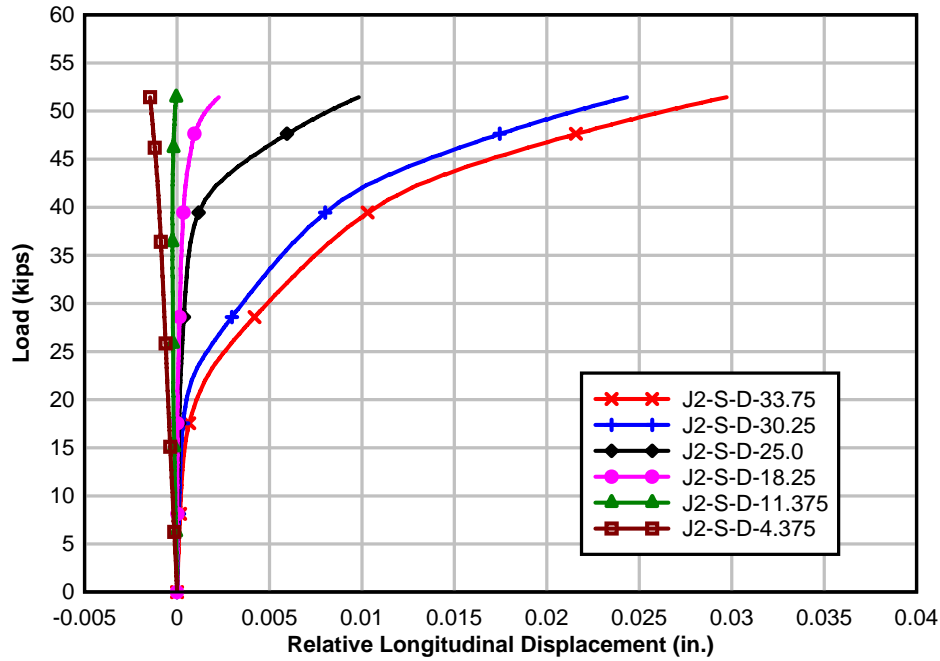


Figure D-7. Load vs. joint opening at reference temperature (South side)

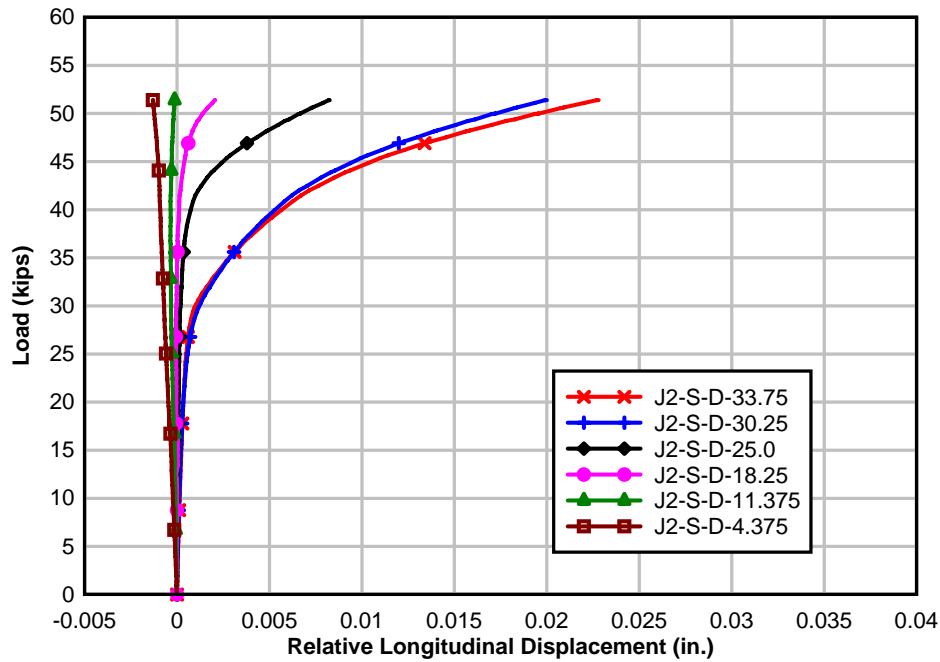


Figure D-8. Load vs. joint opening with positive thermal gradient (South side)

APPENDIX E
LOAD RESPONSE CURVES (NEGATIVE THERMAL GRADIENT)

Load vs. beam response curves which were derived from strain gauge and LVDT data are shown here. These curves were used to determine loads at which the joint at midspan (designated joint J2) opened. The curves were also used to determine effective concrete contact areas at joint J2, which were then used to quantify J stresses due to the AASHTO nonlinear negative thermal gradient.

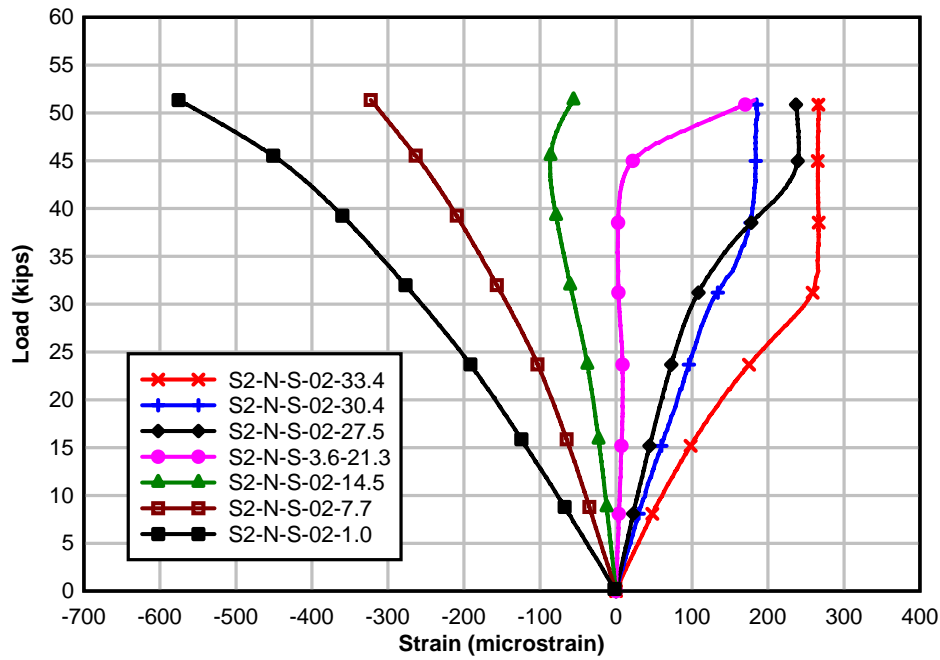


Figure E-1. Load vs. strain at reference temperature (Segment 2, North)

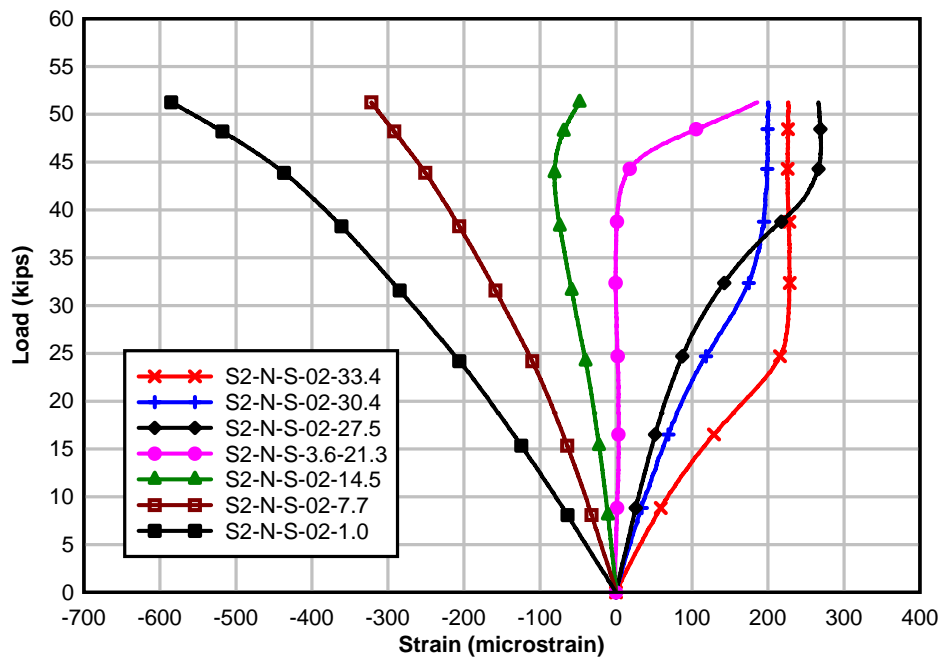


Figure E-2. Load vs. strain with negative thermal gradient (Segment 2, North)

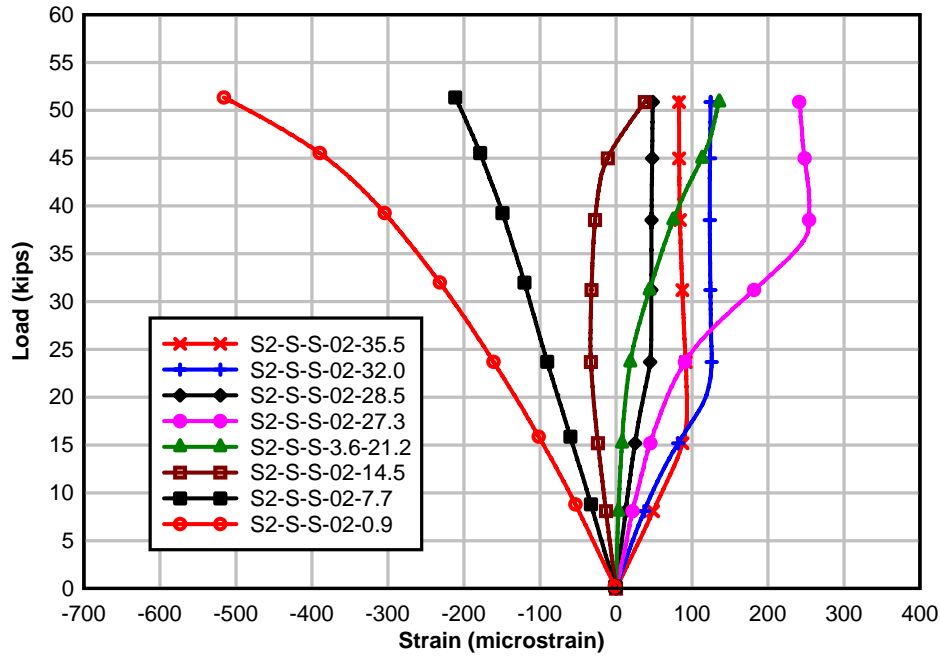


Figure E-3. Load vs. strain at reference temperature (Segment 2, South)

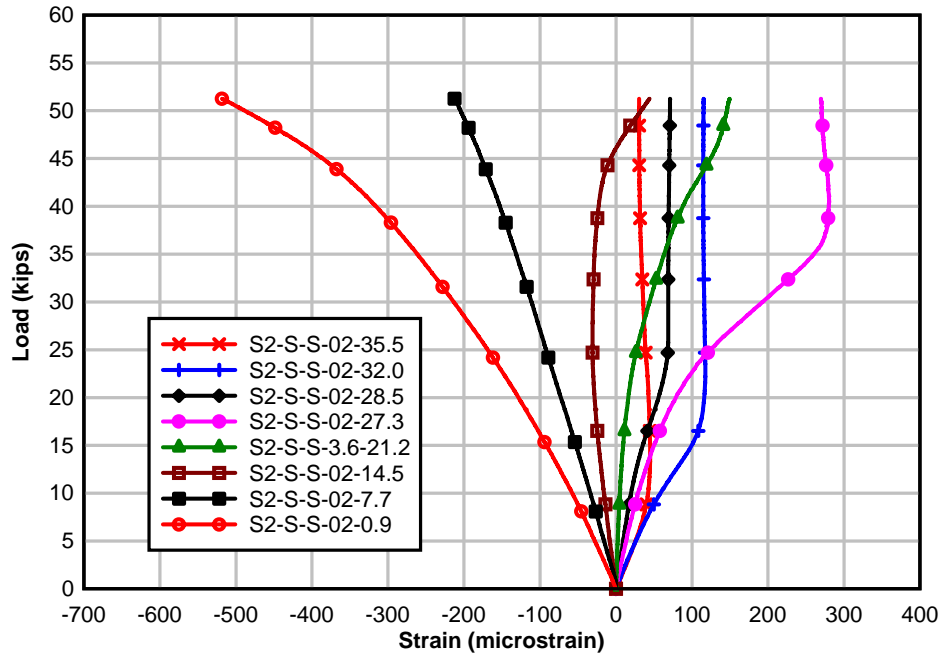


Figure E-4. Load vs. strain with negative thermal gradient (Segment 2, South)

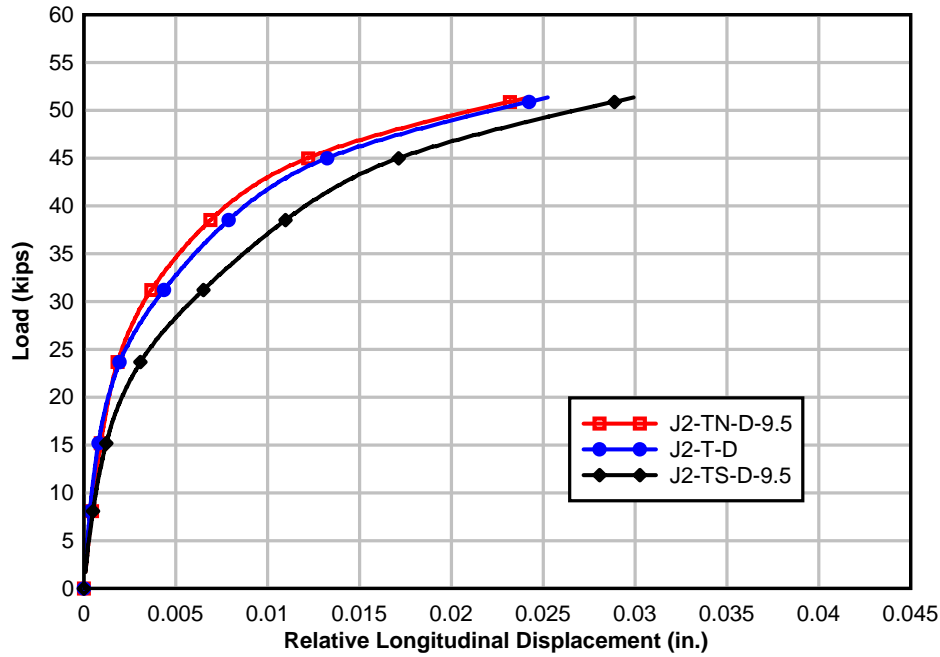


Figure E-5. Load vs. joint opening at reference temperature (Top flange)

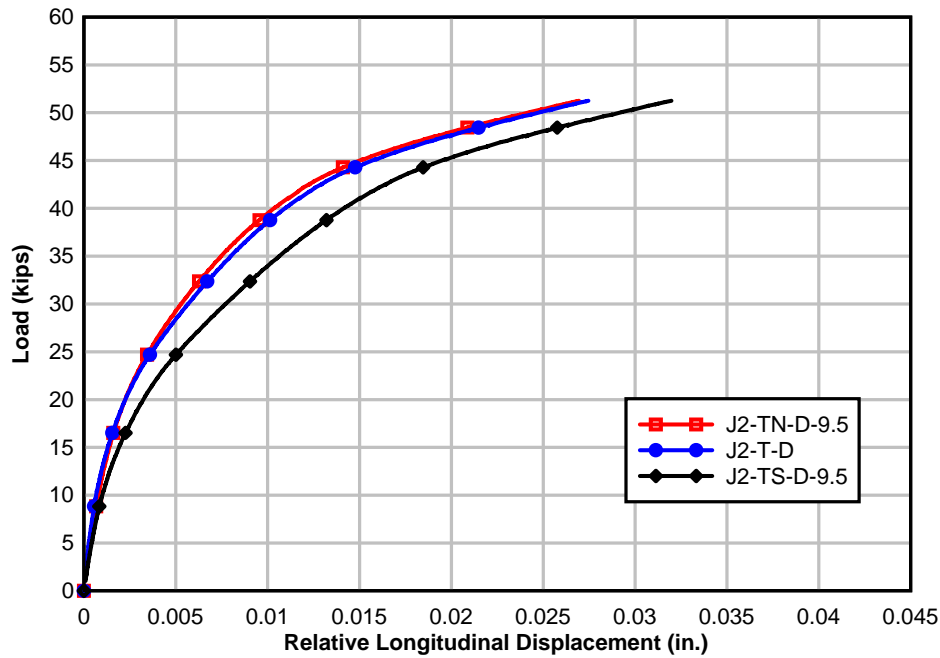


Figure E-6. Load vs. joint opening with negative thermal gradient (Top flange)

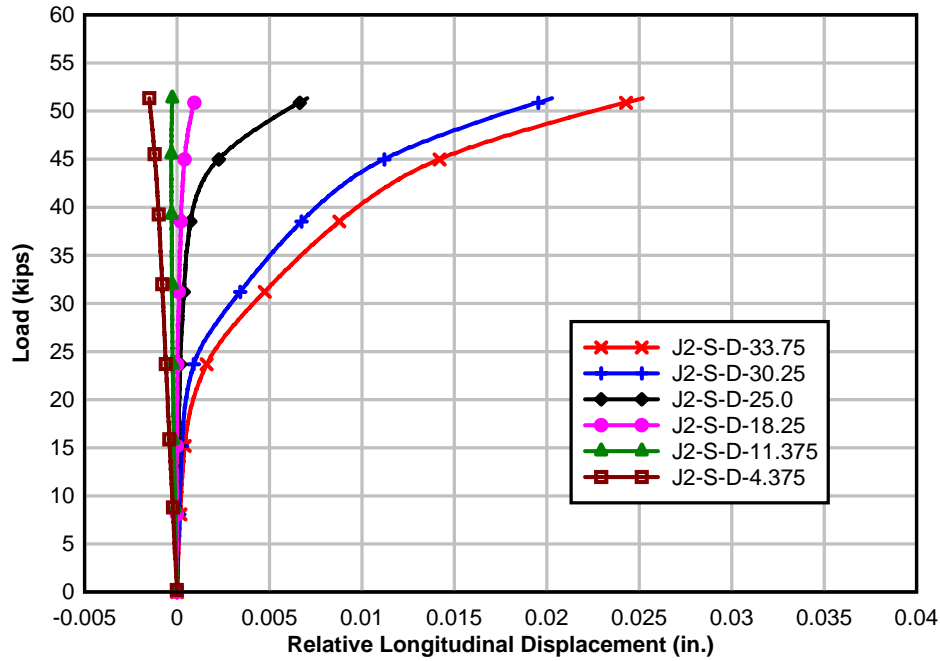


Figure E-7. Load vs. joint opening at reference temperature (South side)

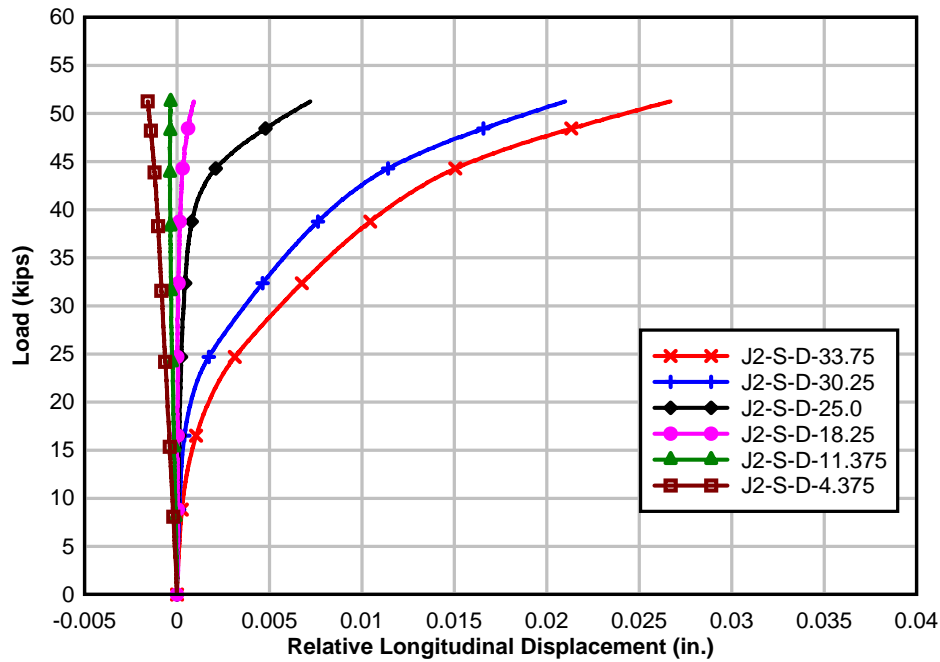


Figure E-8. Load vs. joint opening with negative thermal gradient (South side)

LIST OF REFERENCES

- AASHTO (1989a)., "AASHTO Guide Specifications, Thermal Effects in Concrete Bridge Superstructures," Washington D.C.
- AASHTO (1989b)., "Guide Specifications for Design and Construction of Segmental Concrete Bridges," 1st Ed., Washington, D.C.
- AASHTO (1994a)., "AASHTO LRFD Bridge Design Specifications," Washington, D.C
- AASHTO (1994b)., "Interim Specifications for the Guide Specifications for Design and Construction of Segmental Concrete Bridges," 1st Ed., Washington, D.C.
- AASHTO (1998a)., "AASHTO LRFD Bridge Design Specifications," Washington, D.C.
- AASHTO (1998b)., "Guide Specifications for Design and Construction of Segmental Concrete Bridges," Proposed 2nd Ed., Washington, D.C.
- AASHTO (1999)., "Guide Specifications for Design and Construction of Segmental Concrete Bridges," 2nd Ed., Washington, D.C.
- AASHTO (2004)., "AASHTO LRFD Bridge Design Specifications," 3rd Ed., Washington, D.C.
- AASHTO TP 60-00. (2004), "Standard Method of Test for Coefficient of Thermal Expansion of Hydraulic Cement Concrete," Washington, D.C.
- ACI Committee 318 (2002)., "Building Code Requirements for Structural Concrete (318-02) and Commentary (318R-02)." American Concrete Institute, Farmington Hills, Michigan.
- ASTM C 469-94 (1994), "Standard Test Method for Static Modulus of Elasticity and Poisson's Ratio of Concrete in Compression," American Society of Testing and Materials, West Conshohocken, PA.
- ASTM C 39-01 (2001)., "Standard Test Method for Compressive Strength of Concrete Cylinders Cast in Place in Cylindrical Molds," American Society of Testing and Materials, West Conshohocken, PA.
- Imbsen, R. A., Vandershof, D. E., Schamber, R. A., and Nutt, R.V. (1985)., "Thermal Effects in Concrete Bridge Superstructures," NCHRP 276, Transportation Research Board, Washington, D.C.
- Potgieter, I. C., and Gamble, W. L. (1983)., "Response of Highway Bridges to Nonlinear Temperature Distributions," Rep. No. FHWA/IL/UI-201, University of Illinois at Urbana-Champaign, Urbana-Champaign, Ill.
- Priestley, M. J. N. (1978)., "Design of Concrete Bridges for Thermal Gradients," ACI Journal, 75(5), 209-217.

- Roberts, C.L., Breen, J. E., and Kreger, M.E. (1993)., “Measurement Based Revisions for Segmental Bridge Design and Construction Criteria,” Research Rep. 1234-3F, Center for Transportation Research, Univ. of Texas at Austin, Austin, Texas.
- Roberts, C. L., Breen, J. E., Cawrse J. (2002)., “Measurement of Thermal Gradients and their Effects on Segmental Concrete Bridge,” ASCE Journal of Bridge Engineering, Vol. 7, No. 3, 166-174.
- Shushkewich, K.W. (1998)., “Design of Segmental Bridges for Thermal Gradient,” PCI Journal, 43(4), 120-137.
- “Steel, Concrete and Composite Bridges, Part I, General Statement.” British Standard BS 5400. British Standards Institution. Crowthorne, Berkshire, England (1978).
- Thompson, M. K., Davis, R. T., Breen, J. E., and Kreger, M. E. (1998)., “Measured Behavior of a Curved Precast Segmental Concrete Bridge Erected by Balanced Cantilevering,” Research Rep. 1404-2, Center for Transportation Research, Univ. of Texas at Austin, Texas.

BIOGRAPHICAL SKETCH

The author began his undergraduate education in 1997 at Orta Dogu Teknik Universitesi in Ankara, Turkey. On graduating with a Bachelor of Science degree in civil engineering in June 2001, he moved to Ohio where he obtained a Master of Science in civil engineering at The University of Akron in August, 2003. Later in August 2003 the author began studying at the University of Florida towards obtaining a Doctor of Philosophy degree in civil engineering, with a concentration in structural engineering. The author anticipates obtaining this degree in December, 2007. Upon graduating, the author plans to pursue a career in structural engineering at a design firm.